

# Interactions of light and mirrors: Advanced techniques for modelling future gravitational wave detectors

Daniel David Brown

A thesis submitted for the degree of  
*Doctor of Philosophy*



Astrophysics and Space Research Group  
School of Physics and Astronomy  
College of Engineering and Physical Sciences  
University of Birmingham  
Compiled: Friday 12<sup>th</sup> February, 2016

UNIVERSITY OF  
BIRMINGHAM

**University of Birmingham Research Archive**

**e-theses repository**

This unpublished thesis/dissertation is copyright of the author and/or third parties. The intellectual property rights of the author or third parties in respect of this work are as defined by The Copyright Designs and Patents Act 1988 or as modified by any successor legislation.

Any use made of information contained in this thesis/dissertation must be in accordance with that legislation and must be properly acknowledged. Further distribution or reproduction in any format is prohibited without the permission of the copyright holder.



# Abstract

As of yet, a direct observation of gravitational waves has eluded science's best efforts to detect them. The second generation of ground based interferometric gravitational wave detectors, offering ten times the sensitivity of their predecessors, are now just beginning to come online. With these fully operational the community expects that within the next few years we will finally observe the first direct detection of a gravitational wave.

To achieve this feat, the interferometers must reach a displacement sensitivity of  $\sim 10^{-20} \text{ m } \sqrt{\text{Hz}}^{-1}$  around 100Hz. The second generation of detectors aiming to reach this, such as Advanced LIGO in the USA, employ a variety of techniques to overcome the limits of previous detectors, for example improved interferometer mirrors and better seismic isolation systems. The new optical designs rely on using multiple coupled optical cavities whose primary aim is to increase the laser power interacting with the gravitational wave signal. This comes at the cost of creating a more complex system. The suspended optical components in the presence of high laser powers produce a complex optomechanical system involving thermal distortion of the optics and radiation pressure effects. Furthermore, imperfections in the detector, such as mirror surface defects or misaligned optics, can have a significant impact on its behaviour and sensitivity. To design and operate these detectors the combination of the aforementioned effects must be understood and prepared for. Numerical models are vital to this effort, allowing us to explore new parameter spaces for designs and troubleshooting unexpected results as the detectors are commissioned. The work presented in this thesis is aimed at using numerical models to improve the designs of future gravitational wave detectors and for a more effective commissioning of current ones, with a particular focus on the Advanced LIGO detectors.

The main tool used throughout this work is FINESSE; a program originally developed more than 10 years ago and already popular within the gravitational wave community. Its primary aim was to provide a tool to better understand the behaviour of the first generation of gravitational wave detectors. However, neither FINESSE nor other simulation packages provided the means to model realistic second generation detectors. In particular none of the tools could effectively model all of the following key effects: radiation pressure effects, distortions of the laser beam, quantum fluctuations of the optical fields, interferometer control signal and noise projections. As part of my work I have implemented these features into FINESSE for the benefit of the wider gravitational wave community and other interested parties.

With these new features I have used FINESSE to directly support the Advanced LIGO project including a study into the interferometer behaviour in the presence of a combination of beam clipping and mode-mismatch experienced at one of the LIGO detectors. I also studied how similar imperfections in the system leads to an effect called 'mode hopping'.

The effectiveness of numerical modelling of realistic systems is in many cases limited by the computation time. I have investigated the use of a reduced-order quadrature technique to reduce the computational cost of calculating spatial overlap integrals of Hermite-Gaussian mode. This technique was successfully applied to optical mode coupling calculations in FINESSE and resulted in a speed improvement of around three orders of magnitude. This significant reduction allows for new parameter spaces to be efficiently explored. The described method is generic and could also be applied to other numerical models using Gaussian modes or beam shapes.

One of the challenges in the design of future gravitational wave detectors are unstable mechanical oscillations of the test masses: also known as parametric instabilities. These are present due to the use of low loss mirror substrate materials and a high intracavity laser power inducing an undesirable optomechanical feedback. I have shown a new method to reduce these parametric instabilities by using purely optical means—previously only mechanically damping has been successfully demonstrated and explored. The described method opens up new avenues to explore advanced optical configurations with higher circulating power.

Finally, the susceptibility of waveguide grating mirrors to lateral displacement phase shifts coupling in to the reflected beam was investigated. Waveguide grating mirrors offer reduced thermal noise that limits the mid-range of many detectors' sensitivities. These devices incorporate grating structures that typically exhibit a strong coupling between lateral displacements to the phase of diffracted orders. It was demonstrated using a finite-difference time-domain model to solve Maxwell's equations that such a coupling does not affect waveguide grating mirrors, to the level of numerical errors.

## Acknowledgements

Over the last four years I have met some fantastic people. Whether you were guiding me to become a better physicist, sympathising with me when having yet another missing conjugate or minus sign in FINESSE to hunt down, or distracting me from it all: you have my thanks.

None of this would have been possible without my supervisor Andreas Freise. You have given me the opportunity to work on exciting problems and projects I would have never even considered, and the chance to travel around the world presenting my work in the process. You have been a great supervisor, and no doubt we will continue making computer games long into the future.

Paul Fulda and Charlotte Bond, thank you for battling FINESSE with me! It has been a both great fun and a privilege working with you both on all the various projects over the years; and all the fun times had outside of work. You both taught me a great deal and if it was not for your bug reports (no matter how late at night they came in) and feature requests FINESSE would be half the tool it is today.

My thanks also goes out to all my colleagues, past and present, at Birmingham; it has been a pleasure to work with you all and you have made the group here a great place to work. David Stops, thanks for the countless times you have helped me with all manner of computer based problems—whether it was the computers at fault or me for breaking things. To Jan Harms, Rebecca Palmer and Haixing Miao, your knowledge of physics and abilities to teach me about all manner of complex problems amazes me to this day. Without your help the quantum features of FINESSE would have taken much longer to surface. A big thanks must also go to Rory Smith who opened my eyes to the seemingly ‘magical’ abilities of reduced order modelling techniques.

The LIGO-VIRGO collaboration has been a great team of international scientists to work with. I have many great memories of all the interesting conferences (both content and destinations) and being able to be part of one of the most exciting experiments being undertaken in the world today. My thanks is also extended to Garilynn Billingsley for all the help with LIGO maps over the years for all our simulations at Birmingham.

To my friends: Simon ‘Weasel’ Jones, Stas ‘Brains’ Kuzmierkiewicz, Chris ‘El rat’ Bradley, Emily ‘Gnasher’ Nash, Charlotte ‘Chops’ Roberts, Lilly ‘the pink’ Pye, Jamie ‘Curtains!’ Pugh and Sayo ‘Lemon drizzle’ Taiwo. Thank you for all the distractions from work, the Snobs escapades, and all the horrendous in-jokes—all of which I am sure there will be plenty more of in the future.

I would not be where I am today without my family. To my Mum who has always been there to offer guidance and help me out (especially with proof reading this thesis), Dad for the terrible puns and jokes but always sound advice, to my Brother, and the extended stepfamily: I have come along way with all your support and encouragement.

Finally, my little sister, Sofia. Thank you for all the late night chats on dinosaurs, hamsters and endangered animals, and generally keeping me young at heart. I hope that one day—when you are grown up—you can look over all this and understand some of the seemingly strange science I was always getting up to!

# Statement of Originality

This thesis reports on my own research work conducted during my PhD at the University of Birmingham between September 2011 and September 2015.

Chapter 1 begins with a brief introduction to gravitational wave detectors. This provides background on interferometer optics and the noise sources relevant to the work reported in this thesis.

Chapter 2 outlines the use of a technique called reduced order quadrature for computing the optical scattering in interferometers. This work was carried out by myself and Rory Smith and as of September 2015 has been submitted for publication under the name *Fast simulation of Gaussian-mode scattering for precision interferometry*.

Chapter 3 presents a new idea using optical feedback to provide a broadband reduction in unstable mechanical modes (parametric instabilities) in the mirrors of gravitational wave detectors. This idea is explored both analytically and numerically. This work is currently being prepared for publication. This chapter also provides a detailed explanation of how radiation pressure effects can be modelled within a steady-state modal model. This forms the mathematical basis for the my implementation of radiation pressure in FINESSE, which was used to explore the optical feedback method for parametric instability suppression.

Chapter 4 presents a selection of tasks from the Advanced LIGO commissioning modelling and design work I participated in as a member of the Advanced LIGO FINESSE simulation team. These examples highlight the necessity for the development and implementation of key features to FINESSE.

Chapter 5 departs from FINESSE related work and reports on simulation work I carried out during my first year. This work was published in: *Daniel Brown, Daniel Friedrich, Frank Brückner, Ludovico Carbone, Roman Schnabel, and Andreas Freise, "Invariance of waveguide grating mirrors to lateral displacement phase shifts," Opt. Lett. 38, 1844-1846 (2013)*. This work relies on a Finite-Difference Time-Domain simulation software (developed by myself during my masters project) to study the susceptibility of waveguide grating mirrors to a displacement-based noise coupling. In this work I show that such structures, unlike diffraction gratings, do not suffer from this noise coupling and can thus be considered for interferometric high-precision experiments.

Appendix A provides a development overview of FINESSE and the changes made that were required for the modelling work of realistic advanced detectors.

Appendix B provides an overview of the Python based wrapper for FINESSE called PYKAT. This was developed to enable efficient modelling of complex interferometers, through automation and post-processing.

Appendix C provides some analytic mathematics for the yaw and pitch degrees of freedom with radiation pressure coupling. These equations are those that were used in FINESSE.

Appendix D provides a description of the quantum noise model used in FINESSE. Part of this is taken from the text I wrote for the Living Review article *Interferometer Techniques for Gravitational-Wave Detection*. This article is a major update to the article originally written by Andreas Freise and Kenneth Strain (Living Rev. Relativity 13, 2010) and has recently been submitted for review. This appendix also describes an alternative and efficient approach to calculating the full quantum noise limited spectrums that accounts for higher order optical modes, losses and squeezed states of light.

Appendix E shows one of the Advanced LIGO parameter files for the FINESSE simulation. This file is based on the Advanced LIGO design parameters. Similar files exist for both LIGO Hanford and LIGO Livingston detectors; these are regularly updated based on the real parameters measured at the detector sites. The files can be found at the LIGO DCC [1, 2, 3]. The LIGO files represent the most complicated use of FINESSE today, the files were developed by myself and the Advanced LIGO FINESSE modelling team over the last year.

# Contents

<b>Contents</b>	<b>vii</b>
<b>List of Figures</b>	<b>xi</b>
<b>1 Modelling interferometers for advanced gravitational wave detectors</b>	<b>1</b>
1.1 Thesis overview . . . . .	6
1.2 Interferometric gravitational wave detectors . . . . .	7
1.3 Optics for gravitational wave detectors . . . . .	17
1.3.1 Propagation of optical fields . . . . .	17
1.3.2 The paraxial approximation . . . . .	20
1.3.2.1 Hermite-Gaussian modes . . . . .	24
1.3.3 Optical couplings with components . . . . .	25
1.3.3.1 Multiple optical frequencies . . . . .	29
1.3.3.2 Higher order modes . . . . .	32
1.3.4 Optical cavities . . . . .	37
1.3.4.1 Transforming beams with ABCD matrices and beam tracing . . . . .	40
1.3.4.2 Stability . . . . .	42
1.3.5 Optical readout and sensing . . . . .	44
1.4 Conclusion . . . . .	48
<b>2 Fast simulation of Gaussian-beam mode scattering</b>	<b>51</b>
2.1 Efficiently computing scattering matrices: integration by interpolation	55
2.1.1 The empirical interpolation method . . . . .	56
2.1.2 Affine parameterization . . . . .	57
2.1.3 The empirical interpolation method algorithm (Offline) . . . . .	59
2.1.4 Error bounds on the empirical interpolant . . . . .	62
2.1.5 Reduced order quadrature (Online) . . . . .	63
2.2 Exemplary case: near-unstable cavities and control signals . . . . .	64
2.3 Application and performance of new integration method . . . . .	68
2.3.1 Computing the ITM and ETM empirical interpolants . . . . .	68
2.3.2 Producing the ROQ weights . . . . .	69
2.3.3 Performance . . . . .	73
2.4 Conclusion . . . . .	75

<b>3</b>	<b>Optomechanics and parametric instabilities</b>	<b>77</b>
3.1	Radiation pressure effects . . . . .	79
3.1.1	Mechanics and vibrational modes . . . . .	80
3.1.2	Surface motions to optical field couplings . . . . .	88
3.1.3	Optical field to surface motion coupling . . . . .	92
3.1.4	Optical springs . . . . .	97
3.1.5	The parametric gain: the measure of instability . . . . .	102
3.1.6	Conditions for instability . . . . .	106
3.2	Optical suppression of parametric instabilities . . . . .	109
3.2.1	Extraction cavities . . . . .	110
3.2.2	Numerical experiment . . . . .	122
3.2.3	Results of PI suppression with the ECM . . . . .	126
3.3	Conclusion . . . . .	134
<b>4</b>	<b>Commissioning and design modelling</b>	<b>137</b>
4.1	Lock-dragging modelling technique . . . . .	139
4.2	Mode Hopping in the LHO SRC . . . . .	146
4.3	Beam clipping in the LLO PRC . . . . .	150
4.4	Active wavefront control modelling . . . . .	157
4.5	Conclusion . . . . .	164
<b>5</b>	<b>Waveguide phase noise invariance</b>	<b>165</b>
5.1	Waveguide grating mirrors . . . . .	167
5.2	Numerical experiment . . . . .	169
5.3	Conclusion . . . . .	173
<b>6</b>	<b>Summary and conclusions</b>	<b>175</b>
6.1	Outlook . . . . .	178
<b>A</b>	<b>Interferometer simulation tool: FINESSE</b>	<b>181</b>
<b>B</b>	<b>PYKAT: Python wrapper for FINESSE</b>	<b>187</b>
<b>C</b>	<b>Rotational radiation pressure</b>	<b>191</b>
<b>D</b>	<b>The quantum kat</b>	<b>197</b>
<b>E</b>	<b>aLIGO FINESSE file</b>	<b>215</b>
	<b>List of publications</b>	<b>229</b>
	<b>References</b>	<b>233</b>

# Nomenclature

## Acronyms

aLIGO Advanced LIGO

AR Anti-reflective

ASC Alignment sensing control

AWC Active wavefront control

CARM Common arm length

DARM Differential arm length

DOF Degree of Freedom

EC Extraction cavity

EI Empirical interpolant

EIM Empirical interpolant method

ET Einstein Telescope

FC Filter cavity

FEM Finite element model

FSR Free-spectral range

FWHM Full width half maximum

HG Hermite-Gaussian

HOM Higher order modes

HR High-reflective

IFO Interferometer

IMC Input mode cleaner

LHO LIGO Hanford Observatory  
LIGO Laser interferometer gravitational wave observatory  
LLO LIGO Livingston Observatory  
LSC Length sensing control  
MICH Short Michelson length  
OMC Output mode cleaner  
PI Parametric instability  
ppm parts per million  
PRC Power recycling cavity  
PRCL Power recycling cavity length  
RB Reduced basis  
RHS Right-hand-side vector  
ROC Radius of curvature  
ROQ Reduced order quadrature  
SRC Signal recycling cavity  
SRCL Signal recycling cavity length  
TCS Thermal compensation system

# List of Figures

1.1	<i>Stretch-and-squash</i> : A passing gravitational wave will stretch and ...	3
1.2	<i>Global reach</i> [24]: Since I took over development of FINESSE, we ...	5
1.3	<i>aLIGO-like Sensitivity</i> : The main fundamental noise sources are ...	11
1.4	<i>General advanced detector optical layout</i> : On top of the base ...	14
1.5	<i>Gaussian beam parameters</i> : A Gaussian beam is defined by its beam ...	21
1.6	<i>Hermite-Gaussian modes</i> : Shown are the transverse intensity shapes ...	25
1.7	<i>Optical fields at a mirror</i> : Shown are the four incoming and ...	26
1.8	<i>Interferometer matrix</i> : An arbitrary interferometer setup can be ...	29
1.9	<i>Mirror map</i> [50, 51]: The surface height variation around the ...	34
1.10	<i>Optical cavity</i> : The fields in an optical cavity can be broken down ...	37
1.11	<i>Cavity resonances</i> : The reflected, transmitted and circulating fields ...	38
1.12	<i>Resonance features</i> : There are several descriptive parameters ...	39
1.13	<i>Beam parameter transformations</i> : In a modal model the beam ...	41
1.14	<i>aLIGO length sensing</i> : An overview of the aLIGO length sensing ...	45
1.15	<i>Error signal example</i> : An error signal for an optical cavity length as ...	47
2.1	<i>Uncoated LIGO mirror maps</i> [64]: Measured surface distortions for ...	55
2.2	<i>Intracavity beam sizes</i> [64]: The beam size on the ITM and ETM of ...	64
2.3	<i>Near-unstable cavity scan with ROQ</i> [64]: As the RoC of the ITM and ...	66
2.4	<i>Near-unstable cavity error signal</i> [64]: The Pound-Drever-Hall error ...	67
2.5	<i>ROQ parameter space</i> [64]: Range of beam parameters needed to ...	67
2.6	<i>Reduced order model of surface maps</i> [64]: Absolute and argument ...	70
2.7	<i>Coupling coefficient error</i> [64]: Relative error in the scattering ...	71
2.8	<i>ROQ parameter space accuracy and extrapolation</i> [64]: Maximum ...	72
2.9	<i>Empirical interpolant error</i> [64]: EI error as a function of the ...	73
2.10	<i>ROQ method timing</i> [64]: Time taken to run FINESSE to model the ...	74
2.11	<i>ROQ speedup</i> [64]: The speed-up achieved using ROQ compared to ...	75
3.1	<i>Components of radiation pressure</i> : An overview of the separate ...	79
3.2	<i>Mirror motion degrees of freedom</i> : The full six degrees of freedom, ...	80
3.3	<i>Suspensions and mirror mesh</i> : Shown is a picture depicting the ...	82
3.4	Example of the surface displacement for two mechanical mode ...	88
3.5	<i>Static optical spring</i> : Illustrative example of the circulating power ...	97
3.6	<i>Components of radiation pressure, detailed</i> : A generic view of a ...	99
3.7	<i>Optical spring resonance</i> : Analytic v.s. numeric (FINESSE) ...	101

## Nomenclature

---

3.8	<i>Corbitt's experimental PI comparison</i> : Using data on the parametric ...	105
3.9	<i>Conditions for parametric instabilities</i> : Depending on the cavity ...	108
3.10	<i>Simple extraction cavity</i> : The basic components required to extract ...	110
3.11	<i>Coupled cavity fields</i> : To compute how a field injected into a coupled ...	112
3.12	<i>Long vs short extraction cavity suppression</i> : Using Eq.(3.78) the ...	115
3.13	<i>Coupled cavity frequency split</i> : Using Eq.(3.87) the frequency ...	118
3.14	<i>Frequency split vs. cavity lengths</i> : Shown are the resonances of a ...	119
3.15	<i>Optical mode resonances and parametric gains</i> : Using FINESSE the ...	123
3.16	<i>Equal length frequency split parametric gain</i> : For an equal length ...	125
3.17	<i>Short cavity frequency gain parametric gain</i> : For a short length ratio ...	126
3.18	<i>Equal length extraction cavity tuning</i> : For an equal length ratio ...	127
3.19	<i>Short extraction cavity tuning</i> : For short length ratio between the ...	128
3.20	<i>Two mechanical modes and an extraction cavity</i> : The two modes ...	129
3.21	<i>ETM parametric instability reduction</i> : Applying the 800 mechanical ...	130
3.22	<i>ITM parametric instability reduction</i> : The same as figure 3.21 but ...	132
3.23	<i>Layouts to explore</i> : When a mechanical mode scatters sidebands at ...	133
4.1	<i>aLIGO DOF fields</i> : This plot shows how these powers and ...	141
4.2	<i>aLIGO length error signals</i> : Shown are the main length sensing error ...	142
4.3	<i>Lock-Dragging lock changes</i> : Shown is the behaviour of the FINESSE ...	144
4.4	<i>Lock-Dragging mirror position changes</i> : The desired output from the ...	145
4.5	<i>SRCL error signal with BS tilt</i> : Shown is how a yaw tilt of the BS ...	148
4.6	<i>SRCL error signal with ITMX tilt</i> : Similar to figure 4.5, shown is how ...	149
4.7	<i>HR and AR BS clipping</i> [52, 53]: Each beam interacting with the ...	152
4.8	<i>Beam clipping at LLO BS</i> [52, 53]: From the beamsplitters ...	154
4.9	<i>Contrast defects and apertures</i> [52, 53]: By tuning the ITMX radius ...	155
4.10	<i>Baffles and centring at LLO BS</i> [52, 53]: The clipping loss present ...	157
4.11	<i>Filter cavity mismatching</i> : Mismatching the filter cavity to both the ...	159
4.12	<i>Filter cavity mismatching</i> : Mismatching both the squeezer and FC ...	160
4.13	<i>Mode-matching of aLIGO cavities</i> : The AWC aLIGO FINESSE file was ...	161
4.14	<i>OM1 beam parameter trajectory</i> : Beam parameter traces can show ...	162
4.15	<i>SR3 beam parameter trajectory</i> : Similar to figure 4.14 but varying ...	163
5.1	<i>The ray picture</i> [129]: The incident beam (black) is coupled into ...	167
5.2	<i>Simulation setup</i> [129]: Schematic layout of 2D FDTD simulation ...	171
5.3	<i>Waveguide displacement phase shifts</i> [129]: Central plot shows ...	173
5.4	<i>Numerical noise floor</i> [129]: Maximum change in phase at beam ...	173
A.1	<i>Flow of FINESSE</i> : A general overview of the operation when running ...	183
D.1	<i>Ball on a stick</i> [27]: Phasor diagram of equation D.4 depicting the ...	198
D.2	<i>Quantum noise sideband spectrum</i> [27]: This diagram depicts a ...	201
D.3	<i>Demodulated quantum noise spectrum</i> : Shown is a frequency ...	204

# Chapter 1

## Modelling interferometers for advanced gravitational wave detectors

Gravitational waves, as predicted by Einstein in his theory of general relativity, are ripples in the curvature of space-time. They are strongly emitted by heavy objects accelerating at near the speed of light, such as the inspiralling and collision of compact binaries like neutron stars and black holes [4]. Decoding the information contained in the gravitational waves emitted by such events is the ultimate goal of a multiple decade long quest to detect them. Access to this information has the potential to revolutionise our understanding of the universe and the cosmic bodies that reside in it.

The effect of a passing gravitational wave is often described as a *stretching-and-squashing* [5] of space-time. The effect can be visualised by imagining how a ring of free test masses placed in a plane perpendicular to the propagation of a gravitational wave are displaced, as shown in figure 1.1. The space between the masses is stretched in one direction whilst, orthogonal to it, space is squashed. The amplitude and fre-

## 1. MODELLING INTERFEROMETERS

---

quency of this stretching-and-squashing motion is determined by the amplitude and frequency of the gravitational wave. The principle aim of interferometric gravitational wave detectors is to then measure the relative displacement of several test masses as a gravitational wave passes by. The amplitude of the strain a gravitational wave emitted from a source induces is given by [4]:

$$h(r) = \frac{2G}{c^4 r} \frac{d^2 I}{dt^2} \quad (1.1)$$

where  $G$  is the gravitational constant,  $c$  the speed of light,  $r$  the distance to the source and  $I$  is the source's quadrupole moment. From an observer's point of view the distance between them and a test mass  $L$  metres away will then change by  $\Delta L = h(r)L \cos(\omega_{\text{gw}} t)$ , assuming such a passing wave is optimally orientated. For a cosmic source megaparsecs away,  $r \approx 10^{22}$  m, along with the  $\frac{G}{c^4} \approx 10^{-46}/r \text{ s}^2\text{kg}^{-1}\text{m}^{-1}$  scaling term means it must have a very large quadrupole moment to produce a measurable strain in a detector.

Cosmic sources that emit gravitational waves span a wide frequency range. The second generation of ground based detectors aim to detect sources within the 10 – 1000 Hz frequency band. The four types of sources are continuous, burst, inspiral and stochastic. Continuous sources are those oscillating with a stable frequency, such as spinning pulsars that are not perfectly spherical. Inspiral signals are those formed when binary systems coalesce. Such systems will lose energy via the emission of gravitational radiation, reducing the distance and speeding up the orbit the binary objects. Eventually these bodies will merge together producing a single compact object that will then ringdown. The detectors are expected to witness each of these three stages. Bursts of gravitational wave are also expected to be seen, produced by events such as unsymmetrical supernova or sources we might have never considered before. Finally, stochastic sources are those where many unresolvable sources form a background of

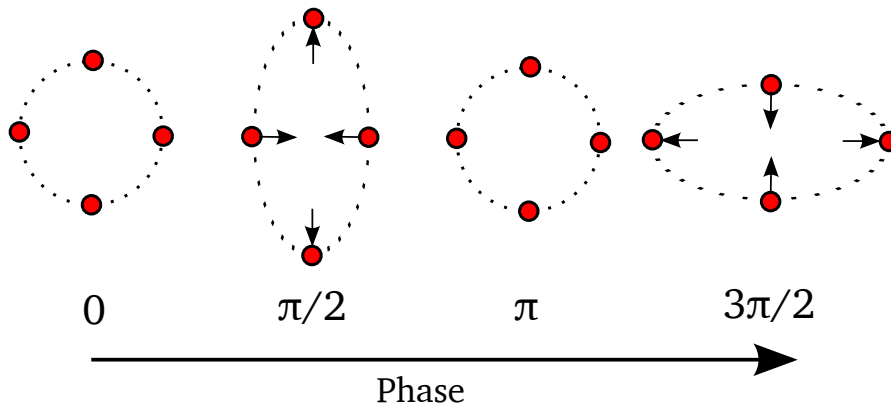


**Figure 1.1:** *Stretch-and-squash:* A passing gravitational wave will stretch and squash the space between free masses. Here the effect of such a wave on a ring of free masses is shown at different points in the cycle of the wave. This depicts the *plus polarisation* of a gravitational wave. A *cross polarisation* is also possible, which induces the same stretch-and-squash effect but rotated by  $45^\circ$  from the plus polarisation.

signal that can be measured. The binary coalescence rate at which events will be seen varies greatly: for the second generation of detectors operating at designed sensitivities it is expected between 0.4–400 Neutron star, 0.4–1000 blackhole and 0.2–10 neutron-blackhole binary coalescences will be seen per year [6]. Expected continuous sources, such as the Crab and Vela pulsars, allow for targeted searches in the data that have so far have only placed upper limits on the amount of radiation such sources emit [7].

Thus far, the first generation of gravitational wave detectors have been constructed and operated but have yet to detect any gravitational waves: GEO600 [8] based in Germany, LIGO [9] in Livingston (LLO) and Hanford (LHO) and VIRGO [10] in Italy. Advanced LIGO [11] (aLIGO) and Advanced VIRGO [12] has already begun extensive *second generation* upgrades with the aim to provide a ten-fold improvement in sensitivity. A new detector in Japan called KAGRA [13] is currently under construction with another LIGO detector having been proposed for construction in India. At the heart of all the above is a Michelson interferometer which measures the differential change in length of space over several kilometres. Such long distances are used to maximise the change in length as  $\Delta L \propto L$ .

## 1. MODELLING INTERFEROMETERS

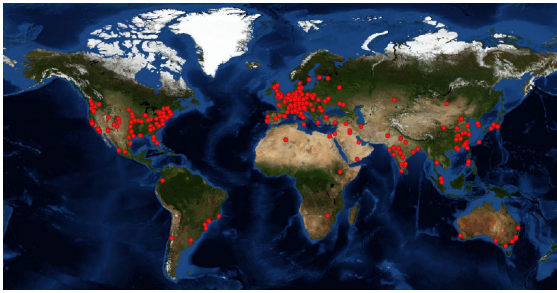
---

The LIGO detectors aim to measure the distance between two test masses placed 4 km apart. The typical strains expected from cosmic sources that it aims to detect are very small [4]. For example, the signal from the coalescence of a binary neutron star system  $\approx 100$  Mpc away is expected to have a strain amplitude of  $h \approx 10^{-22}$ . The resulting change in distance between these two test masses from such a source would then be of the order  $\Delta L = h \cdot 4 \text{ km} \approx 4 \cdot 10^{-19} \text{ m}$ : a truly minute quantity. As will be discussed in the following sections, such small changes in length are easily masked by a variety of noise sources.

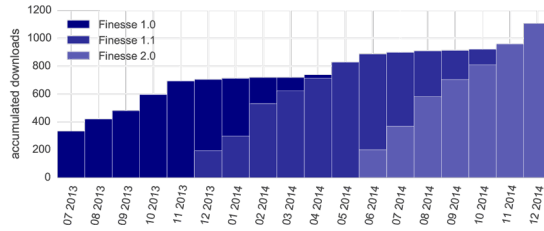
The span of expertise required to construct a detector with such unprecedented sensitivity requires a worldwide effort. The LIGO scientific collaboration aims to do just that. It brings together groups with knowledge from small quantum fluctuations of light to the cosmic reach of colliding black holes to develop, construct and operate these detectors with which we can view the universe through. This thesis is concerned with just a few aspects of this wide range of topics: the advancement of optical modelling software used for current and future generations of gravitational wave detectors and improving the detector's performance.

### Interferometric simulations

The central aim for using interferometric simulations are to the study important physical features of increasingly complex systems for improving their sensitivity and operation. The first optical propagation codes begun to appear in 1988, written by Jean Yves-Vinet [14]. This foundation was used in 1990 to study how deformations in the optical components affected the interferometer [15]. These codes gradually expanded into ever more complex simulation tools attempting to combine not only the optics but also control system feedback and mechanical suspensions of the experimental setups [16, 17]. As the interest and utility of these simulations tools began to grow a series of workshops called *Software tools for advanced interferometer con-*



(a) Unique IP download locations



(b) Unique IP downloads of FINESSE versions

**Figure 1.2:** *Global reach* [24]: Since I took over development of FINESSE, we have seen a steady increase in the number of unique downloads. Using a GEOIP lookup a rough location of each download was found. The downloads are clustered around gravitational wave research groups but appear on every continent, except for Antarctica, which remains a future goal.

*figurations* [18] were held to focus efforts and further their development. To date, simulations have played crucial role in every step of bringing the detectors from ideas on paper to fully functioning systems, and as their complexity grows these tools will only ever become more important.

Several branches of simulation tools exist in the gravitational wave community today. Firstly, the full system simulations (typically time-domain models) enable optic, suspension and electronic components to be combined and studied. Two such tools were developed at LIGO and VIRGO, End-2-End [16] and SIESTA [17]. These are heavy weight simulations. They require significant understanding of the software and can be both complex in practice and computationally costly to run. The second branch consists of steady state optical simulations. These are in general simpler to manipulate and understand as a user; this is because many non-linear and transient behaviours which the user might not be interested in are assumed away. Despite the simplification they are still incredibly powerful tools and the most widely used. Those that are in use today are OPTICKLE [19], MIST [20], SIS [21], OSCAR [22] and FINESSE [23]; a webpage is available ([gwic.ligo.org/simulations](http://gwic.ligo.org/simulations)) that keeps track of the more popular tools.

The simulation tool that will feature heavily throughout this thesis is FINESSE: the

## 1. MODELLING INTERFEROMETERS

---

Frequency domain INtErferometer Simulation SoftwarE. I took over the development and responsibility of FINESSE around the beginning of 2013 from Andreas Freise, its original creator; download statistics can be seen in figure 1.2 over this period. For version 1.0 the source code was open sourced under the GPL v2 license. Since then many physical, ergonomic and performance additions have been made ensuring that FINESSE is capable of tackling current and future modelling tasks. The task of producing a usable simulation tool in any field is not an easy one—and the level of work required often underestimated. From the Git statistics, approximately 1000 commits altering 270k lines of *C* code have been made by myself over the years. The actual features this resulted in are outlined in more detail in appendix A.

The development and features implemented in FINESSE were driven by needs of the community for design and commissioning tasks for LIGO, GEO and third generation detectors such as the Einstein Telescope [25]. This thesis reports on these features and the modelling tasks I have undertaken for advanced detectors, in particular for aLIGO. For those readers looking for more details on FINESSE and optical simulations I recommend the FINESSE manual [26], the review article on gravitational wave interferometry [27] and the optical simulation book chapter [28], all of which I am a co-author of. For those readers who are interested in seeing FINESSE used in practice I would suggest exploring the freely available aLIGO FINESSE Git repository [29] that contains vast amounts of the modelling scripts and results undertaken for commissioning activities.

### 1.1 Thesis overview

In this chapter I will provide an overview of the detector and its relevant components. Then a more detailed description of the relevant optics involved in such interferometers. These sections form the basis of required knowledge for later chapters that delve

---

into more specific problems.

In chapter 2 a new computational technique is applied to optical scattering calculations used to model precision interferometers. This is based on a near-optimal approach to solving overlap integrals which significantly improves simulation runtimes. Here both the method and an example case are provided.

In chapter 3 a new method using purely optical means of reducing parametric instabilities is proposed and analysed. Here the methods for computing radiation pressure effects in interferometers are outlined and how such instabilities are modelled. This is followed by both analytics and numerical experiments undertaken to investigate it further. It is then demonstrated how the use of additional cavities can be used to suppress parametric instabilities.

In chapter 4 I hope to provide an overview of the modelling work conducted for the commissioning for one of the most advanced detector to date, Advanced LIGO.

Chapter 5 outlines the modelling undertaken to study the susceptibility of waveguide grating mirrors to a problematic noise coupling for grating like structures. Grating structures couple any relative transverse displacement to an incident beam into higher diffracted orders. A rigorous solver of Maxwell's equations was used to study this problem for Gaussian beams. These results of this show that waveguide grating mirrors should not be affected by this coupling, thus removing one potential barrier to their future use in precision interferometers.

## **1.2 Interferometric gravitational wave detectors**

The first and second generation of gravitational wave detectors (GEO, LIGO, VIRGO and KAGRA) are all based on Michelson interferometers. These aim to be sensitive to gravitational waves over a wide frequency range from 10 Hz to several kilohertz. A Michelson layout requires an incoming laser to be split into two parts at a beamsplitter.

## 1. MODELLING INTERFEROMETERS

---

The beamsplitter has four ports: the incoming port, the Y-arm port, the X-arm port and the outgoing port. The incoming light field is split by the beamsplitter and will propagate along the two *arms* of the Michelson, X-arm and Y-arm. At the end of each arm the light is reflected back from the *test mass*, the returned light will then propagate back along the arm to be interfered at the beamsplitter. Whether the interference of the returned beams is constructive, destructive or something in between will depend on how the light was distorted in the arms.

One basis in which these distortions can be described in are those which are common to both arms and those which are differential; these are also known as *common mode* and *differential mode* effects or distortions. Common mode effects will alter each beam in the same way; for example, if both of the arms are elongated the same additional phase will be seen in each of the returned beams. Thus any common mode effects do not alter the interference of the returned beams. Differential mode effects are those where the effect is not the same in each arm, for example, if one arm gets longer and the other shorter; these types of effects will alter how the beams interfere.

The amount of differential changes the light experiences in each arm will determine whether it interferes constructively, destructively or somewhere in between at the incoming and outgoing ports. The power of the field at the outgoing port is

$$P = P_0 \cos^2(\Delta\phi + \phi_{\text{off}}), \quad (1.2)$$

where  $P_0$  is the power of the input laser,  $\Delta\phi$  is the differential phase difference between each of the light fields recombining at the beamsplitter and  $\phi_{\text{off}}$  being a specially chosen static phase offset, which shall be elaborated on more shortly.

The Michelson has different *operating points* at which it can be setup to run. An operating point is the particular collective positioning of an interferometer's mirrors that allows it to behave in given manner. For gravitational wave detectors the Michel-

---

son is setup to operate close to what is called the *dark fringe* [27],  $\phi_{\text{off}} \approx \pi/2$ . The dark fringe is where the returned light from the arms interferes destructively at the outgoing port and constructively at the incoming port. When operating in this state the output port is also referred to as the *dark port*. The light power at the output is now

$$P = P_0 \sin^2(\Delta\phi). \quad (1.3)$$

Thus, if there is no differential phase differences between the arms all the light that goes into the Michelson is returned back out of the incoming port, and  $P = 0$  for the dark port. This operating point is chosen so that all common mode noises, such as laser frequency and amplitude noise which are significant noise sources, are reflected back towards the laser and do not reach the output photodiode where the gravitational wave signal is measured. Any differential signal

A passing gravitational wave will stretch-and-squash the arms of the Michelson, or one arm becomes shorter whilst the other longer—if the polarisation of the wave is aligned to the detector. The light will then accumulate a different phase in each arm due to the displacement of the end mirrors relative to the beamsplitter

$$\Delta\phi \propto Lh \cos(\omega_{\text{gw}}\tau), \quad (1.4)$$

where  $\omega_{\text{gw}}$  is the frequency of the gravitational wave and  $\tau$  is time,  $L$  is the length of the arm and  $h$  the strain of the wave. This differential phase accumulated in the arms results in these differentials fields interfering constructively at the dark port and destructively at the bright, opposite to that of common mode fields. These fields with a differential phase signal are then measured with a photodiode at the dark port, the output of which then contains the strain signal from the gravitational wave.

The amount of power in light that contains the gravitational wave signal that reaches the photodiode is very small as  $Lh \ll 1$ . To efficiently extract the signal a

## 1. MODELLING INTERFEROMETERS

---

technique called DC readout [30] is used (which is used in all current generation detectors). Mentioned previously was that the detector is operated close to a perfect dark fringe. In fact,  $\phi_{\text{off}} = \pi/2 + k\delta_{\text{off}}$  where  $\delta_{\text{off}}$  is a static (DC) differential arm length offset chosen by us and  $k$  is the wavenumber. This DC offset allows a small amount of carrier light to *leak* out to the dark port which beats with the field containing the signal. By demodulating this beat the signal can be efficiently extracted. The signal power using DC readout is [27]

$$P_s \propto \delta_{\text{off}} P_0 \frac{\omega_0^2 h}{\omega_{gw} c} \sin\left(\frac{\omega_{gw} \bar{L}}{c}\right) \cos\left(\omega_{gw} \left[\tau - \frac{\bar{L}}{c}\right]\right), \quad (1.5)$$

where  $\omega_0$  is the angular frequency of the laser light and  $\bar{L}$  is the average length of the two arms. For signals up to a kilohertz and arm lengths of the order of several kilometres it can be assumed  $\frac{\omega_{gw} \bar{L}}{c} \ll 1$ , the amount of signal at the output is then

$$P_s \sim \delta_{\text{off}} P_0 \frac{\omega_0^2 \bar{L} h}{c^2} \cos(\omega_{gw} \tau). \quad (1.6)$$

The metric used to quantify the performance of a detector is the *noise-to-signal* ratio over the detector bandwidth (10 – 5000Hz). This ratio states the sensitivity of the detector to differential length changes of the arms. The sensitivity is improved by increasing the amount of signal at the output photodiode or reducing noise sources; design improvements for the second-generation detectors aim for both.

The noise that limits the sensitivity of detectors can be described as either fundamental or technical in nature. The main fundamental noises sources are:

- *Seismic noise*: The vibration of the ground is the limiting source of noise at very low frequency ranges as ground motion displaces the test masses in each arm. These displacements are not coherent between the arms due to geographical separation, thus it appears as a differential signal. In practice the test masses

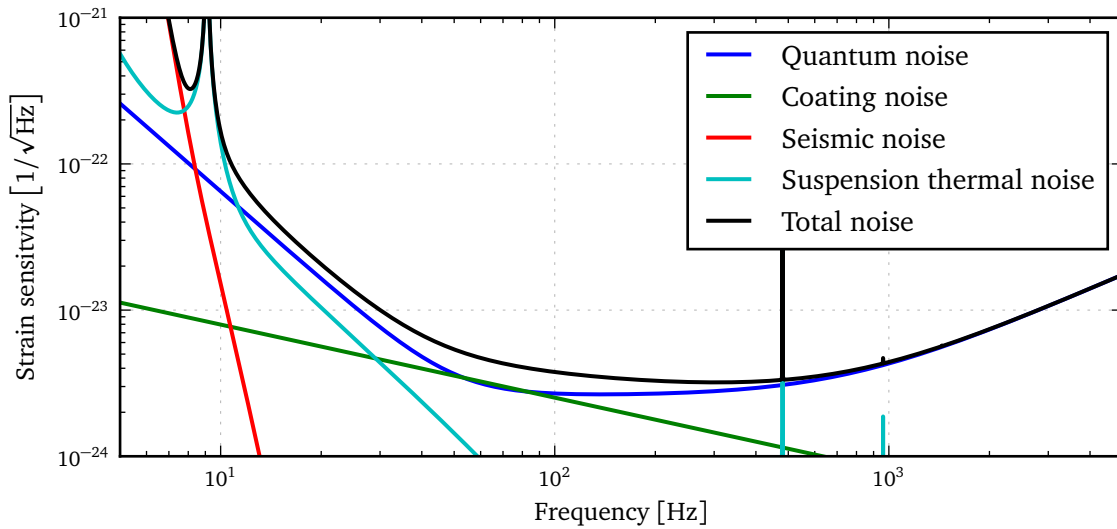


**Figure 1.3:** *aLIGO-like Sensitivity:* The main fundamental noise sources are seismic noise, coating thermal noise, suspension thermal noise and quantum noise. These create the typical *bucket* like shape of the sensitivity common to all ground based interferometric gravitational wave detectors. These curves were computed with the *GWINC noise curve calculator* [31].

are isolated from seismic motion using both passive systems, like multi-stage pendulums [32], and active, such as the hydraulic external pre-isolators used in aLIGO [33].

- *Thermal noise:* At low frequencies in the range of 10 to a few hundred Hz the thermal vibrations of the atoms excite the vibrational modes of the suspension wires [34, 35] and the internal modes of the test masses [36]. To reduce thermal noise high quality low loss materials are used in structures whose resonance frequencies are either much lower or higher than the signal bandwidth. The high quality factor ensures much of the vibrational energy is contained within a narrow band around the resonance frequency reducing it in the signal bandwidth. Coating thermal noise is also inversely proportional to the size of the incident laser beam; as an increased beam size averages over a larger area of the mirror surface vibrations [37].
- *Quantum noise:* Heisenberg's uncertainty principle places a limit on the knowl-

## 1. MODELLING INTERFEROMETERS

---

edge of both the phase and amplitude of the light fields. This noise in the optical field then translates into noise in the photocurrent of the output photodiode. Quantum noise can be limiting across the signal bandwidth, which can broadly be broken down into two effects: Shot noise at high frequencies and radiation pressure noise at low. Shot noise is a frequency independent noise that (semi-classically) is due to the finite number of photoelectrons in the output signal thus is subjected to counting statistics. The power spectral density (see appendix D) of shot noise for a field with power  $P$  and frequency  $f_0$  is

$$S_s = 2hf_0P. \quad (1.7)$$

At low frequencies the amplitude fluctuations in the light exerts a radiation pressure force on the test masses shaking them. This becomes problematic when a high laser power is used to reduce shot noise, as the radiation pressure scales with power. The power spectral density of this noise for a Michelson with free mass mirrors of mass  $M$  at a signal frequency  $f$  Hz is

$$S_{rp}(f) = \left( \frac{2P}{Mc(2\pi f)^2} \right)^2 hf_0P. \quad (1.8)$$

Radiation pressure noise can be reduced by using heavier test masses, or even removed if using a speed meter interferometer configuration instead of a Michelson [38, 39].

These listed fundamental noise sources are shown in figure 1.3. This shows how sensitive a dual-recycled Michelson detector is to a differential strain signal over the interested bandwidth. The aim of the second generation of LIGO detectors is to reach a designed amplitude spectral density strain sensitivity similar to that depicted in figure 1.3, with a peak in sensitivity at  $\approx 300$  Hz of  $\sim 3 \cdot 10^{-24} \sqrt{\text{Hz}}^{-1}$ .

---

Even if all other noise sources could be removed using improved technology the quantum fluctuations of the optical field at the output will always persist. The power spectral density of the quantum noise limited sensitivity of a suspended Michelson is

$$\text{NSR}(f) = \frac{S_s + S_{\text{rp}}(f)}{P_s(f)} \propto \frac{1}{L^2} \left[ \frac{1}{P_0} + \frac{4P_0}{(Mc f^2)^2} \right]. \quad (1.9)$$

From this we can see that the overall sensitivity of the detector is improved with longer arms due to an increased amount of signal. At high frequencies we benefit from using higher laser power reducing shot noise. However, at low frequencies increasing the laser power decreases the sensitivity as radiation pressure effects become substantial. Using heavier test masses can combat this radiation pressure noise

Technical noise sources include aspects such as fluctuations in the frequency and amplitude of the main laser, or fluctuations in the position or misalignments of the laser field. The primary reason of using a Michelson interferometer is actually for its *common mode rejection* [27]. For example, laser frequency noise is common to both arms. Assuming the arms are perfectly matched and the detector is operating on the dark fringe, these fluctuations do not reach the output port and do not degrade the sensitivity. In practice imperfections between the cavities will always exist, which couples common mode noise into the output port.

To reach levels of strain sensitivity required advanced detectors make use of optical cavities to enhance the field. The key elements are the Fabry-Perot *arm cavities* (X-arm and Y-arm), the *power recycling cavity* (PRC) and the *signal recycling cavity* (SRC). An overview of the layout of an aLIGO interferometer is shown in figure 1.4.

## **Fabry-Perot arm cavities**

Fabry-Perot cavities consist of two slightly transparent mirrors. The laser beam is injected into the cavity through the input test mass (ITM). It propagates to the end

## 1. MODELLING INTERFEROMETERS

---

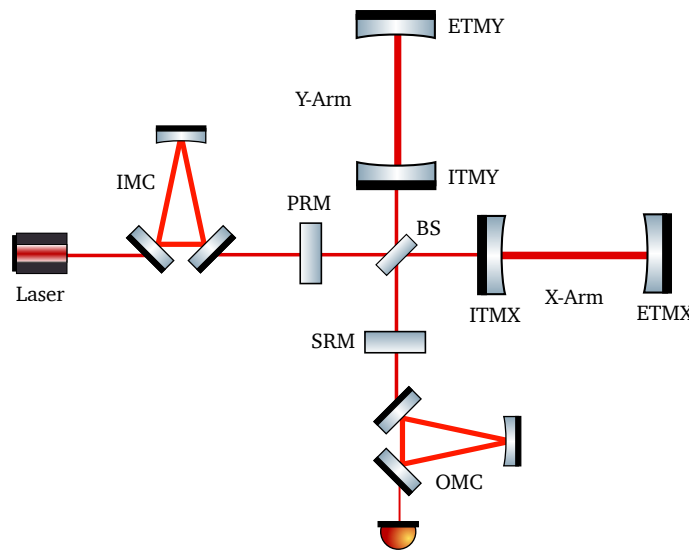


**Figure 1.4:** *General advanced detector optical layout:* On top of the base Michelson layout extra cavities are included to improve the sensitivity. The notation is input test mass (ITM), end test mass (ETM), power recycling mirror (PRM), signal recycling mirror (SRM), main beamsplitter (BS), input mode cleaner (IMC) and output mode cleaner (OMC)

test mass (ETM) from which it is reflected back. If the mirrors are aligned the laser will bounce back and forth between the mirrors. If the length of the cavity is an integer number of the laser wavelength the optical field will resonate and the injected power is multiplied significantly.

Increasing the length of the detector's arms proves difficult beyond more than 4 km due to the curvature of the Earth. By using cavities along the arms the light is made to take multiple round trips, thus spending longer interacting with a passing gravitational wave.

### **Power recycling cavity**

To increase the effective power of the laser a power recycling cavity is used. This is achieved by placing a mirror (The power recycling mirror, PRM) between the laser and the beamsplitter. When the Michelson is operating at the dark fringe, all the common mode light will be returned back toward the laser. Using a high reflectivity PRM the optical field is then returned back into the Michelson. The PRC actually forms two

---

cavities, from the PRM to the ITMY and PRM to ITMX, also known as PRX and PRY respectively. If these cavities are kept on resonance the laser power is multiplied by a factor known as the *power recycling gain*, which for aLIGO is  $\approx 45$ . By combining the gain of the PRC and that of the arm cavities the input power is magnified greatly. The target aLIGO input laser power is 125 W, this with the gains of the PRC and arms this will reach approximately 800 kW in the arm cavities.

### **Signal recycling cavity**

Like power recycling for the common mode light, signal recycling aims to enhance any differential signals created in the interferometer. Primarily this is aimed at enhancing the gravitational wave signal by placing a mirror between the beamsplitter and the output photodiode. This creates a coupled cavity between the SRC and the arms where the gravitational wave interacts with the optical field. Two modes of operation are available here: the signal can be resonantly enhanced at a particular frequency (signal recycling) or the coupled cavity system can be setup so that the signal is anti-resonant (resonant sideband extraction, RSE) which broadens the bandwidth of the detector; the latter is used in aLIGO. An SRC operating with RSE sacrifices peak sensitivity to allow a broader linewidth, thus the detector is less sensitive to a particular signal frequency but better at a wider range of signals.

### **Mode cleaners**

The spatial shape of the laser beams in these interferometers are well described by a Gaussian beam, with perturbations to the shape described using Hermite-Gaussian modes, which are discussed in more details in later sections. The frequency content of the beam is also well described as a dominant single-frequency component with sidebands describing perturbations to the beam's phase and amplitude. The optical field at any point in the interferometer is then described by a sum of these spatial

## 1. MODELLING INTERFEROMETERS

---

and frequency modes. When such an optical field is presented to a cavity only the spatial and frequency modes that are also eigenmodes of the cavity will resonate. Thus cavities can be designed to select particular modes of a beam and reject others: this process is referred to as *mode cleaning*. Mode cleaners are just specially designed cavities to achieve the degree of cleaning required. The two important mode cleaners are the input mode cleaner (IMC) and output mode cleaner (OMC). The former cleans the beam before entering the core of the interferometer and ensures a spatially and frequency stable laser beam is used. The output mode cleaner is used to remove the modes that do not contain any gravitational wave signal before reaching the output photodiode. Any modes that reach it that do not contain any signal just increase the noise and decreases the detector's sensitivity.

### **Input laser**

The input lasers used for gravitational wave detectors are required to be ultra-stable and output a high power for reducing shot-noise. The pre-stabilised lasers used for LIGO consist of a master laser whose output is amplified and stabilised before being injected into the interferometer [40, 41]. The master laser is a commercial non-planar ring Nd:YAG laser initially outputting 2 W, the wavelength of which is 1064 nm. This is then boosted to  $\approx 200$  W in two stages using a single pass medium power amplifier from 2 W to 35 W consisting of four Nd:YVO<sub>4</sub> crystals and finally a high power ring oscillator containing four further Nd:YAG crystals.

The laser output is then stabilised in frequency, power and pointing (alignment and displacement) to achieve the required noise limits [42]. These noise sources couple to the output photodiode measuring the gravitational wave signal, thus can limit the sensitivity. Differential imperfections in the arms—such as absorption, scattering, and mode-mismatching—allow these noise sources to couple directly to the output port. Using DC readout also couples these noises to the output by purposefully allow-

---

ing a small amount of carrier light through, though this level can be chosen so that these noises are not limiting. A pre-mode cleaner is used to suppress both pointing and power fluctuations, the output of which is directed into the IMC of the main interferometer. Further, power stabilisation is achieved by monitoring fluctuations on transmission of the IMC and fed back to an amplitude modulator before the pre-mode cleaner. Frequency stabilisation is achieved using a monolithic reference cavity and fed back into the master laser and a phase modulator. Overall this reaches the design requirements in the gravitational wave detection frequency band: relative power noise of  $2 \cdot 10^{-8} \sqrt{\text{Hz}}^{-1}$ ; frequency noise  $0.1 \text{ Hz} \sqrt{\text{Hz}}^{-1}$ ; and relative beam pointing noise  $10^{-7} \sqrt{\text{Hz}}^{-1}$  [40, 41].

## 1.3 Optics for gravitational wave detectors

The principal optics required for modelling gravitational wave detectors is the propagation, interference and scattering of electromagnetic waves throughout the interferometer. The model must account for how these fields propagate on scales of centimetres to kilometres between mirrors and through cavities, whilst including how the beam is perturbed by imperfections in the system. A complete description of the whole theory is not possible here. I will try to highlight the important aspects required for this thesis, where further information on the optics relevant to gravitational wave detectors can be found in [27].

### 1.3.1 Propagation of optical fields

A rigorous description of how light behaves is described by Maxwell's equations as the co-propagation of both an electric and magnetic field. The propagation of such light throughout a gravitational wave detector typically involves passing through mediums like vacuum, air, and materials such as fused silica; these materials are assumed to

## 1. MODELLING INTERFEROMETERS

---

be isotropic, homogeneous and non-dispersive. Continuous stable lasers are used as the main light source this propagates between successive optical components. For this a full Maxwellian description of the optical field is often excessive and not easily solvable for generic interferometers. In such cases, describing light as a scalar field and its propagation using *scalar diffraction theory* suffices.

Scalar diffraction describes the manner in which waves propagate and diffract from objects in its path. As a scalar theory, it does not handle the vector nature of light. The propagation of either the electric or magnetic field of light can be described by scalar diffraction. For the systems that are considered in this work only the electric field,  $\xi$ , is required to be computed; the magnetic field in such cases is always perpendicular to the electric field with a magnitude  $\xi/c$ , where  $c$  is the speed of light.

In scalar diffraction theory the propagation of the electric field is described by the wave equation:

$$\left( \nabla^2 - \frac{1}{v^2} \frac{d^2}{d\tau^2} \right) E(\vec{r}, \tau) = 0, \quad (1.10)$$

where  $E(\vec{r}, \tau)$  is a complex valued scalar function describing the amplitude and phase of the electric field:

$$\xi(\vec{r}, \tau) = \text{Re} \{ E(\vec{r}, \tau) \}. \quad (1.11)$$

The speed of the wave being  $v = c/n$  with  $n$  being the refractive index of the medium it is propagating through. One potential solution to this is that of a plane-wave propagating in the direction  $\hat{z}$ , or what will be commonly referred to as the *beam axis*:

$$E(z, \tau) = E_0(\tau) e^{i\omega\tau + ikz + i\Phi(\tau)}, \quad (1.12)$$

where  $E_0$  and  $\Phi$  are the amplitude and phase of the electric field,  $\omega$  is the optical angular frequency,  $\omega = 2\pi c/\lambda$  and the wavenumber  $k = \omega/c$ . Gravitational wave detectors make use of several wavelengths of laser light, however the primary laser is produced using an Nd:YAG crystal whose wavelength is  $\lambda = 1064\text{nm}$ ; this will be

---

the default wavelength assumed throughout this thesis. Propagating the beam from one point,  $z$ , to another,  $z'$ , along the beam axis depends only upon the time delay between them:

$$E'(z' - z, \tau) = E(\tau - (z' - z)/c) = E_0(\tau - (z' - z)/c)e^{i\omega\tau - ik(z' - z)}. \quad (1.13)$$

As the frequency of the optical fields in question are very high,  $\omega/(2\pi) \approx 10^{15}$  Hz. Directly observing  $E$  at these frequencies is not possible; instead the measured property is the power in the optical field which is physically achieved using either photodiodes or CCDs. As a photodiode cannot respond to the terahertz oscillations in the optical field the time-averaged values of terms with the optical frequency in the power are taken. Using the Poynting vector of  $E$ , for a plane-wave the power is:

$$P(\tau) = \frac{\epsilon_0 c}{2} \int_A |E(\tau)|^2 dA \quad [\text{W}] \quad (1.14)$$

where the optical field has unit of  $\text{V m}^{-1}$ . To simplify calculations the unit of  $E$  are rescaled to  $\sqrt{W} \text{m}^{-1}$ , which will be assumed from this point onwards. This then sets the relationship between the  $E$  and the real electric field  $\xi$  as

$$\text{Re}\{E(\vec{r}, \tau)\} = \sqrt{\frac{\epsilon_0 c}{2}} \xi(\vec{r}, \tau). \quad [\sqrt{W} \text{m}^{-1}] \quad (1.15)$$

After this rescaling the power of a plane-wave optical field is

$$P(\tau) = A|E(\tau)|^2, \quad (1.16)$$

where  $A$  is the cross sectional area of the beam considered. When the shape of the beam is an important feature a finite-beam size must be considered and the field in-

## 1. MODELLING INTERFEROMETERS

---

tensity must be integrated over the measured area:

$$P(\tau) = \int_A |E(\tau)|^2 dA. \quad (1.17)$$

### 1.3.2 The paraxial approximation

The aim of the paraxial approximation is to describe a beam of finite size propagating along straight axis. Finite here means the beam is of a finite size in the transverse plane orthogonal to the propagation axis. It is assumed the beam is like that of a plane-wave propagating along the beam axis,  $\hat{z}$ , but with a shape described by a time-independent function  $u(\vec{r})$ . The field is then of the form

$$E(\vec{r}, \tau) = u(\vec{r})e^{i\omega\tau - ikz}. \quad (1.18)$$

Substituting this into Eq.(1.10), a beam in a vacuum becomes

$$\left( \frac{d^2}{dx^2} + \frac{d^2}{dy^2} \right) u(\vec{r})e^{-ikz} + \frac{d^2}{dz^2} [u(\vec{r})e^{-ikz}] + k^2 u(\vec{r})e^{-ikz} = 0. \quad (1.19)$$

The  $z$  derivative here expands to

$$\frac{d^2}{dz^2} [u(\vec{r})e^{-ikz}] = \left( \frac{d^2}{dz^2} u(\vec{r}) + 2ik \frac{d}{dz} u(\vec{r}) - k^2 u(\vec{r}) \right) e^{-ikz}. \quad (1.20)$$

Expanding and simplifying Eq.(1.19) further

$$\left( \frac{d^2}{dx^2} + \frac{d^2}{dy^2} + \frac{d^2}{dz^2} \right) u(\vec{r}) + 2ik \frac{d}{dz} u(\vec{r}) = 0. \quad (1.21)$$

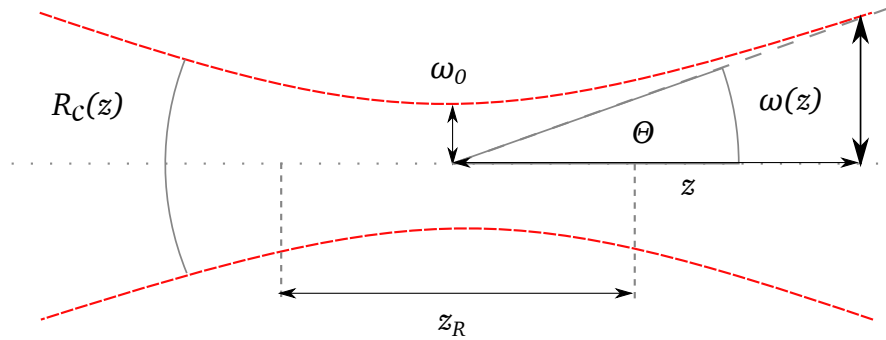


**Figure 1.5:** *Gaussian beam parameters:* A Gaussian beam is defined by its beam waist  $w_0$  and the wavelength of the light. The beam diverges from this waist as it propagates along the beam axis. This gives rise to a wavefront curvature,  $R_c$ , and far-field divergence angle  $\Theta$ . The spot size at some point along the axis is  $w(z)$ . The boundary which defines the near and far field is the Rayleigh range  $z_R$ .

The paraxial approximation assumes that the beam shape does not vary quickly in shape in the transverse plane as it propagates along the beam axis:

$$2k \frac{du(\vec{r})}{dz} \gg \frac{d^2u(\vec{r})}{dz^2}. \quad (1.22)$$

Using this approximation the paraxial wave equation is given as

$$\left( \frac{d^2}{dx^2} + \frac{d^2}{dy^2} + 2ik \frac{d}{dz} \right) u(\vec{r}) = 0. \quad (1.23)$$

In practice, the paraxial approximation breaks down when describing the optical field that diverge very quickly away from the beam axis, or similarly when trying to describe the field at large angles from a source. Thus the paraxial approximation is not suited for describing beams with a small source area at large distances. For describing larger beams with small divergences that are present in gravitational wave interferometers this approximation is a valid as it introduces minimal errors. In an aLIGO like arm cavity the error in the total power of a beam is  $\approx 10^{-3}$  ppm [43] using this description compared to more rigorous approaches, whereas typical design requirements set losses from absorption or clipping of mirrors are of the order of 10–100 ppm.

## 1. MODELLING INTERFEROMETERS

---

Various solutions exist for  $u(\vec{r})$  in Eq.(1.23). The most prominent for optical systems is the Gaussian beam equation, which is shown in figure 1.5 with its various defining features. This type of beam well describes the typical shape of lasers used in gravitational wave detectors. It defines a beam whose maximal intensity is at its center which drops off exponentially away from the beam axis. These beams are defined by the wavelength of the laser light and the smallest size of the beam, known as the *beam waist*,  $w_0$ . The shape of a Gaussian beam is parameterised by the complex *beam parameter* [44]:

$$q = z + i \frac{\pi w_0^2}{\lambda}, \quad (1.24)$$

where  $\lambda$  is the wavelength of the light and  $z$  is the distance along the beam axis from the beam's waist.

In this work the beam will be described in Cartesian coordinates. The mathematical form of a Gaussian beam is given by [44]:

$$u(x, y; \mathbf{q}) = \sqrt{\frac{2}{\pi w_x(z) w_y(z)}} e^{i(\Psi_x(z) + \Psi_y(z))/2} e^{-ik\left(\frac{x^2}{2q_x} + \frac{y^2}{2q_y}\right)}, \quad (1.25)$$

where  $w_x$  and  $w_y$  are the beam spot sizes in the  $x$  and  $y$  directions, and  $\mathbf{q} = \{q_x, q_y\}$  are the beam parameters in the  $x$  and  $y$  directions.

The beam has several features that are a result of the diffraction of the beam as it passes through its narrowest width. The beam diverges as it propagates away from the beam waist. The spot size at some point along the axis is

$$w(z) = w_0 \sqrt{1 + \left(\frac{z}{z_R}\right)^2}. \quad (1.26)$$

The point at which the area the beam covers has doubled is known as the Rayleigh range

$$z_R = \frac{\pi w_0^2}{\lambda}. \quad (1.27)$$

---

A Gaussian beam also has a curved wavefront. The radius of curvature of a beam is given by:

$$R_c(z) = z + \frac{z_R}{z} \quad (1.28)$$

where  $z > z_R$  the wavefront is essentially spherical. Below the Rayleigh range the wavefront becomes flat at the beam waist.

The beam parameter can also be reformulated in terms of the Rayleigh range

$$q(z) = z + iz_R. \quad (1.29)$$

Its inverse also contains the radius of curvature and spot size:

$$\frac{1}{q(z)} = \frac{1}{R_c(z)} - i \frac{\lambda}{\pi w(z)^2}. \quad (1.30)$$

Thus it can be seen that the individual  $q$  values offer a great deal of simplification when stating the shape of a beam at a particular point along the axis, as all of the descriptive parameters can be derived from it.

In equation 1.25,  $\Psi(z)$  is the *Gouy phase* of the beam in either the  $x$  or  $y$  directions. This is an additional longitudinal phase shift that finite beams accumulate as they propagate compared to a plane-wave:

$$\Psi(z) = \arctan\left(\frac{z}{z_R}\right). \quad (1.31)$$

This additional phase plays an important role in how Gaussian beams behave in an optical cavity as will be discussed later in this section.

## 1. MODELLING INTERFEROMETERS

---

### 1.3.2.1 Hermite-Gaussian modes

Although the interferometers are constructed and designed to a high precision imperfections still exist: misaligned mirrors, defects on the surface of optics, thermally distorted mirrors, to name but a few. One of the main uses of interferometer modelling is to study how small defects can alter the behaviour of the entire interferometer. This is predominantly the type of work that is conducted for commissioning simulations as shown later in chapter 4. Therefore, it is important to be able to describe how a beam is perturbed from the fundamental Gaussian beam described previously for realistic models.

Perturbations to the transverse spatial shape of the beam are described with the addition of higher-order Gaussian modes (HOMs), in this work the Hermite-Gaussian (HG) modes [45] which are solutions to the paraxial wave equation will be used. These modes are based on the complete and orthonormal Hermite polynomials. The complex transverse spatial amplitude of a HG modes is given by

$$u_{nm}(x, y, \mathbf{q}) = u_n(x, q_x)u_m(y, q_y). \quad (1.32)$$

The shape of the beam in the  $x$  direction can be written in terms of  $q_x$  as

$$u_n(x, q) = \left(\frac{2}{\pi}\right)^{1/4} \left(\frac{1}{2^n n! w_0}\right)^{1/2} \left(\frac{q_0}{q}\right)^{1/2} \left(\frac{q_0 q^*}{q_0^* q}\right)^{n/2} H_n\left(\frac{\sqrt{2}x}{w(z)}\right) \exp\left(-i \frac{kx^2}{2q}\right), \quad (1.33)$$

where the  $y$  direction shape is the same but given by  $u_m(y, q_y)$ . Here  $n$  defines the order of the Hermite polynomials  $H_n$  in the  $x$  direction and  $m$  for  $y$ . The order of the optical mode is defined as  $\mathcal{O} = n + m$ , with individual modes referenced to as  $\text{TEM}_{nm}$ .  $\text{TEM}_{00}$ , the only order zero mode, reduces to the fundamental beam. Higher order modes typically refer to any with  $\mathcal{O} > 0$ . The intensity of these modes is shown in figure 1.6 for various orders. The above can also equivalently be written in terms of

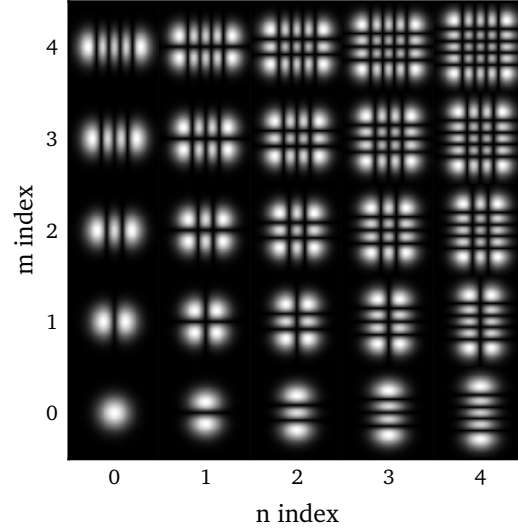


**Figure 1.6:** *Hermite-Gaussian modes:* Shown are the transverse intensity shapes of the Hermite-Gaussian modes up to a maximum modal index of 5.

the actual beam properties:

$$u_{nm}(x, y, \mathbf{q}) = \frac{e^{i(n+0.5)\Psi_x(z)+i(m+0.5)\Psi_y(z)} e^{-i\frac{k(x^2)}{2R_{cx}(z)} - i\frac{k(y^2)}{2R_{cy}(z)} - \frac{x^2}{w_x^2(z)} - \frac{y^2}{w_y^2(z)}}}{\sqrt{w_x(z)w_y(z)} 2^{n+m-1} n! m! \pi} H_n\left(\frac{\sqrt{2}x}{w_x(z)}\right) H_m\left(\frac{\sqrt{2}y}{w_y(z)}\right). \quad (1.34)$$

A finite Gaussian beam can then be described as a sum of numerous higher order modes:

$$E(x, y, \tau; \mathbf{q}) = \sum_{n=0, m=0}^{n+m \leq \mathcal{O}_{max}} a_{nm} u_{nm}(x, y; \mathbf{q}) e^{i\omega\tau} \quad (1.35)$$

where  $a_{nm}$  is a complex value describing the amplitude and phase of a mode  $TEM_{nm}$  and  $\mathcal{O}_{max}$  being the maximum order of modes included in the expansion.

### 1.3.3 Optical couplings with components

The key behaviours that will be required to model is how the optical field interacts with the many mirrors and other optical components that make up a gravitational wave interferometer. Optical couplings here refer to how some incoming beam, inci-

## 1. MODELLING INTERFEROMETERS

dent on an imperfect component, are interfered, distorted and eventually propagate away as the outgoing beam. Provided here is an overview of the important physical features that are required for modelling problems tackled in later chapters of this thesis. More complete descriptions of these effects have been documented in the FINESSE manual [26], the Living review article [27] and the book chapter [28].

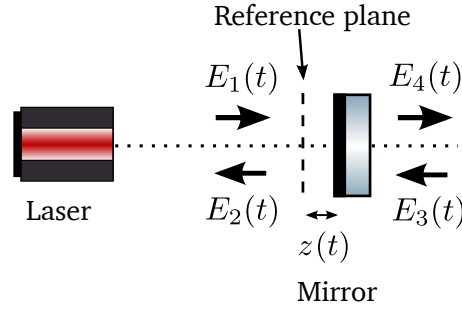


**Figure 1.7:** *Optical fields at a mirror:* Shown are the four incoming and outgoing optical fields at a mirror and a time dependent motion of the mirror along the beam axis.

The simplest component is a single mirror as shown in figure 1.7. Under normal incidence, there are four beams: two incoming and two outgoing. Depending on how reflective the mirror is for the given wavelength of light some light will be reflected, some transmitted and some lost due to imperfections in the mirror. The mirrors used for 1064nm light are made from fused silica with a dielectric coating stack applied to its faces to achieve the required reflectivity. For many mirrors a high-reflectivity (HR) coating applied to one side and an anti-reflective (AR) coating applied to the other. Thus a mirror is defined as having three inherent properties: A power reflectivity  $R$ , a power transmissivity  $T$ , a power loss  $L$  from absorption or scattering of the light. These values refer to how the *power* of the optical field changes when interacted with, this can also be expressed in terms of an *amplitude* coefficient:  $r = \sqrt{R}$  and  $t = \sqrt{T}$ .

The outgoing fields can be written in terms of the incoming fields:

$$E_2(\tau) = r e^{i\phi_{r1}} E_1(\tau) + t e^{i\phi_t} E_3(\tau), \quad (1.36)$$

$$E_4(\tau) = t e^{i\phi_t} E_1(\tau) + r e^{i\phi_{r2}} E_3(\tau), \quad (1.37)$$

---

where  $\phi_{r1}$  is the phase the fields picks up on reflecting from the one side,  $\phi_{r2}$  the other, and  $\phi_t$  on transmission. In practice the exact phase change will depend on the details of the coating stack, such as thicknesses and materials used. However, such information is not available to us. The important information is not the exact phase but the relative phases between the incoming and outgoing fields. The phases must be such that the incoming power equals that lost from scattering or absorption and the total outgoing power, so that  $1 = R + T + L$ . Power is conserved if in this case if [27]

$$\phi_{r1} + \phi_{r2} - 2\phi_t = \pi(2N + 1), \quad (1.38)$$

where  $N$  is any integer. The simplest choice here is that  $\phi_{r1} = \phi_{r2} = 0$  and that  $\phi_t = \pi/2$ . This choice means reflection is a symmetric process and only transmission receives a phase change. This phase relationship will be used throughout this thesis. Thus the coupling equations can be written as:

$$E_2(\tau) = rE_1(\tau) + itE_3(\tau), \quad (1.39)$$

$$E_4(\tau) = itE_1(\tau) + rE_3(\tau). \quad (1.40)$$

Note that the thickness of the mirror does not play a part here. The optical fields on both sides are in either vacuum or air; though the refractive index on either side could also differ.

The values  $E_{1-4}$  all represent the amplitude and phase of the optical field relative to a *reference plane* as shown in figure 1.7. The mirror can be displaced relative to this reference plane which will alter the phase of the incoming fields. This displacement,  $z$  as shown in the figure, is broken down into two different length scales: macroscopic shifts for anything larger than a wavelength, and the mirror *tuning*,  $\phi$ . The tuning is a microscopic change in the position of the mirror, on the order of the wavelength of

## 1. MODELLING INTERFEROMETERS

---

the light. Typically this is stated in units of phase  $\phi = kz$ , either in degrees or radians.  $360^\circ$  or  $2\pi$  being a displacement of one wavelength. The coupling equations for a field with identical refractive index on either side is then:

$$E_2(\tau) = rE_1(\tau)e^{i2\phi} + itE_3(\tau), \quad (1.41)$$

$$E_4(\tau) = itE_1(\tau) + rE_3(\tau)e^{-i2\phi}. \quad (1.42)$$

The optical fields that will be solved for in this thesis are steady state plane-wave or paraxial fields. For either the field is described as

$$E_{1-4}(\tau) = a_{1-4}e^{i\omega\tau} \quad (1.43)$$

with  $a$  being a complex value describing the phase and amplitude of the field. In the steady state the optical coupling equations are a set of linear equations:

$$a_1 = b_1, \quad (1.44)$$

$$a_2 = b_2 + ra_1e^{i2\phi} + ita_4, \quad (1.45)$$

$$a_3 = b_3, \quad (1.46)$$

$$a_4 = b_4 + ita_1 + ra_4e^{-i2\phi}, \quad (1.47)$$

where  $\vec{a} = \{a_1, a_2, a_3, a_4\}$  is the steady state amplitude of the optical field and  $\vec{b} = \{b_1, b_2, b_3, b_4\}$  and the RHS of the equations are the sources of optical field at each port. This is represented in a matrix form  $M\vec{a} = \vec{b}$ :

$$M = \begin{bmatrix} 1 & 0 & 0 & 0 \\ -r e^{i2\phi} & 1 & -it & 0 \\ 0 & 0 & 1 & 0 \\ -it & 0 & -r e^{-i2\phi} & 1 \end{bmatrix}. \quad (1.48)$$

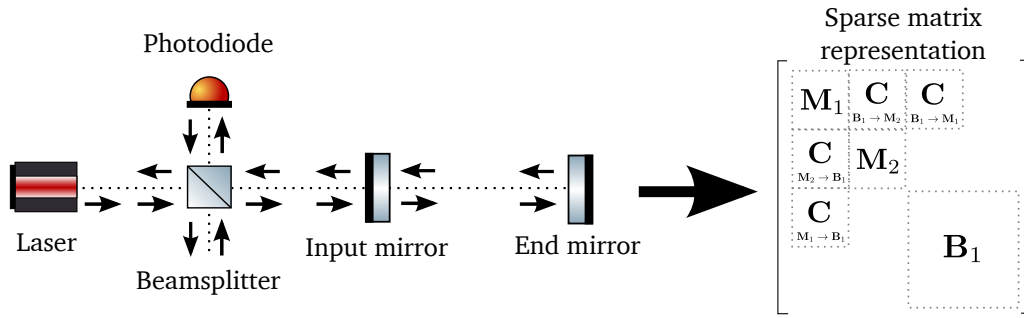


**Figure 1.8:** *Interferometer matrix:* An arbitrary interferometer setup can be described using coupling matrices for each components as building blocks. Shown is how the interferometer matrix for a Fabry-Perot cavity and a beamsplitter would look. Here  $M_1$ ,  $M_2$  and  $B_1$  are the input mirror, end mirror and beamsplitter coupling matrices. The spaces that connect these components then fill in off-diagonal elements represented by the connection matrices,  $C$ .

This is an optical coupling matrix for a mirror. For all the optical components that are of importance for modelling gravitational wave detectors they can all be represented in this matrix format; for a more complete list of components coupling matrices see [26].

These optical coupling matrices form the basic building blocks of an overall *interferometer matrix*,  $\mathbb{M}$ . This matrix describes the local coupling at each component in the model and how each of these components are connected together. A pictorial example of this is shown in figure 1.8. The steady state solutions of the optical fields throughout the entire interferometer,  $\vec{a}$ , can then be found by solving

$$\vec{a} = \mathbb{M}^{-1} \vec{b}, \quad (1.49)$$

where  $\vec{b}$  describes any source of optical fields in the interferometer, such as the main laser.

### 1.3.3.1 Multiple optical frequencies

The above only describes how a single optical frequency is coupled. Gravitational wave detectors make use of multiple optical fields at various frequencies for sensing and controlling mirror positions [46] and for heterodyne readout of the gravitational

## 1. MODELLING INTERFEROMETERS

---

wave signals; though this later gave way to DC readout which offered improved sensitivity [30]. Thus models of how an interferometer responds to different frequencies of light is crucial to simulating such control and readout problems.

Two types of modulation are important for the detectors: high frequency modulations of the optical fields phase or amplitude, usually in the MHz range, typically induced by either an electro-optic, acousto-optic modulators or dithering of an optics tuning; and lower frequency modulations of the order of kHz and less which describe smaller perturbations to an optical field's phase or amplitude, such as from a gravitational wave signal or thermal motion of a mirror surface. The former is typically referred to as *RF modulation* and the latter *audio modulation*, due to the typical frequency ranges used.

A phase modulated plane-wave optical field is described by

$$E(\tau) = a(\omega_0)e^{i\omega_0\tau + im\cos(\Omega\tau)} \quad (1.50)$$

where  $m$  is the *modulation index* describing the strength of the modulation,  $a(\omega_0)$  is the complex amplitude of the  $\omega_0$  frequency field and  $\Omega$  the frequency of the modulation. This is expanded using a Bessel function identity [47]

$$e^{im\cos(\psi)} = \sum_{k=-\infty}^{\infty} i^k J_k(m) e^{ik\psi}, \quad (1.51)$$

where  $J_k$  is the  $k^{\text{th}}$  Bessel function of the first kind. Thus a phase modulated field will be

$$E(\tau) = a(\omega_0) \sum_{k=-\infty}^{\infty} i^k J_k(m) e^{i(\omega_0 + k\Omega)\tau}. \quad (1.52)$$

There now exists multiple oscillating fields. The  $k = 0$  field is the *main carrier*, that produced by the main laser source. For fields with  $k \neq 0$  are known as *sidebands* to the main carrier whose frequency is shifted with  $\omega_0 + k\Omega$ . This process can also be

---

applied for amplitude modulation:

$$E(\tau) = a(\omega_0)(1 + m \cos(\Omega\tau))e^{i\omega_0\tau}, \quad (1.53)$$

$$= a(\omega_0)e^{i\omega_0\tau} \left[ 1 + \frac{m}{2}(e^{i\Omega\tau} + e^{-i\Omega\tau}) \right]. \quad (1.54)$$

The maximum order of sidebands required will depend on the strength of the modulation. First order sidebands are  $k = \pm 1$ , second order  $k = \pm 2$ , etc. For RF sidebands in aLIGO  $m \sim 0.2$ , thus one or two suffice. For audio sidebands which represent small perturbative modulations ( $m \ll 1$ ) only the first order sideband is required as  $J_k(m \ll 1) \rightarrow 0$  for  $|k| > 1$ . Such small modulations would adequately describe how a gravitational wave affects the optical field, for example [48]. For these small modulations the Bessel function is approximated as  $J_k(m) \approx (m/2)^k/k!$ .

The more frequencies that are included the more couplings will need to be considered. For  $N_f$  frequencies the reflected field on one side of the mirror will be:

$$E_2(\tau) = \sum_{j=0}^{N_f-1} a_2(\omega_j)e^{i\omega_j\tau} = \sum_{j=0}^{N_f-1} \left[ r a_1(\omega_j)e^{i2\phi\frac{\omega_j}{\omega_0}} + i t a_3(\omega_j) \right] e^{i\omega_j\tau}. \quad (1.55)$$

The coupling at each frequency is then described by the matrix

$$\mathbf{M}'(\omega) = \begin{bmatrix} 1 & 0 & 0 & 0 \\ -r(\omega)e^{i2\phi\frac{\omega}{\omega_0}} & 1 & -i t(\omega) & 0 \\ 0 & 0 & 1 & 0 \\ -i t(\omega) & 0 & -r(\omega)e^{-i2\phi\frac{\omega}{\omega_0}} & 1 \end{bmatrix}. \quad (1.56)$$

The mirror displacement now depends on the optical frequency, here  $\phi$  uses  $\omega_0$  as reference frequency is scaled appropriately. There could also be a frequency dependent  $r$  and  $t$ , however the range of modulation frequencies is much smaller than  $\omega_0$  over which the physical properties of the mirror should not vary. Thus the frequency de-

## 1. MODELLING INTERFEROMETERS

---

pendence here is typically ignored. The full mirror coupling matrix for all the optical fields is then constructed with Eq.(1.56) along the diagonals:

$$\mathbf{M} \Rightarrow \begin{bmatrix} \mathbf{M}'(\omega_0) & & & \\ & \mathbf{M}'(\omega_1) & & \\ & & \ddots & \\ & & & \mathbf{M}'(\omega_{N_f-1}) \end{bmatrix}. \quad (1.57)$$

The above describes a motionless mirror, which couples only between the same frequencies. A process known as mirror *dithering* is used to modulate the phase of reflected light. If the dithering frequency matches the difference between any two optical field frequencies additional non-diagonal terms will be required in the above matrix. Such techniques are used in generating sidebands for control and length sensing of the aLIGO OMC [49].

### 1.3.3.2 Higher order modes

As with the additional optical frequencies, each higher order mode is considered as a new optical field of which must be propagated throughout the interferometer. Each optical frequency in every beam has its own higher order modes. These must be included into the optical coupling matrix. The number of higher order modes that must be considered for a given maximum order is:

$$N_m = (\mathcal{O}_{max} + 1)(\mathcal{O}_{max} + 2)/2 \quad (1.58)$$

The process of adapting the original plane-wave coupling matrices can be visualised as replacing each element in the plane-wave coupling matrix with an  $N_M \times N_M$  sub-matrix.

---

For a mirror the plane-wave mirror matrix Eq.(1.56) this becomes:

$$\mathbf{M}'(\omega) \Rightarrow \begin{bmatrix} \mathbf{I} & \mathbf{0} & \mathbf{0} & \mathbf{0} \\ -r(\omega) e^{i2\phi} \frac{\omega}{\omega_0} \mathbf{K}_{11} & \mathbf{I} & -i t(\omega) \mathbf{K}_{12} & \mathbf{0} \\ \mathbf{0} & \mathbf{0} & \mathbf{I} & \mathbf{0} \\ -i t(\omega) \mathbf{K}_{21} & \mathbf{0} & -r(\omega) e^{-i2\phi} \frac{\omega}{\omega_0} \mathbf{K}_{22} & \mathbf{I} \end{bmatrix}. \quad (1.59)$$

Here  $\mathbf{I}$  is the identity matrix and the  $\mathbf{K}$  higher order mode *scattering matrices*:  $\mathbf{K}_{11}$  the scattering of modes that occurs on reflection on one side,  $\mathbf{K}_{22}$  the other,  $\mathbf{K}_{12}$  and  $\mathbf{K}_{21}$  describe how the modes are scattered on transmission. These matrices describe how the mapping from the incoming to the outgoing mode content of the beam.

When a field interacts with an optical component its mode content is typically changed due to imperfections. Here scattering is defined as the relationship between the mode content of the outgoing beam  $\bar{a}$ , with a beam shape  $\mathbf{q}$ , and the mode content of an incoming beam  $\bar{a}'$  described with a shape  $\mathbf{q}'$ . Further details on how these beam parameters are chosen can be found in section 1.3.4.1. Mathematically this is found with  $\bar{a} = \mathbf{K}\bar{a}'$  where  $\mathbf{K}$  is known as the *scattering matrix*.

Consider the spatial profile of a beam reflected from on an imperfect optic  $E'(x, y; \mathbf{q}') = A(x, y)E_{\text{in}}(x, y; \mathbf{q}')$ , where  $E_{\text{in}}$  is the incident beam and  $A(x, y)$  is complex function describing the perturbation it has undergone. For example, on reflection a beam will be clipped by the finite size of the mirror with radius  $R_{\text{ap}}$ :

$$\alpha(x, y; R_{\text{ap}}) = \begin{cases} 1, & \text{if } \sqrt{x^2 + y^2} \leq R_{\text{ap}} \\ 0, & \text{otherwise} \end{cases}. \quad (1.60)$$

It will also be reflected from the surface with some height variations  $z(x, y)$ . Thus,

## 1. MODELLING INTERFEROMETERS

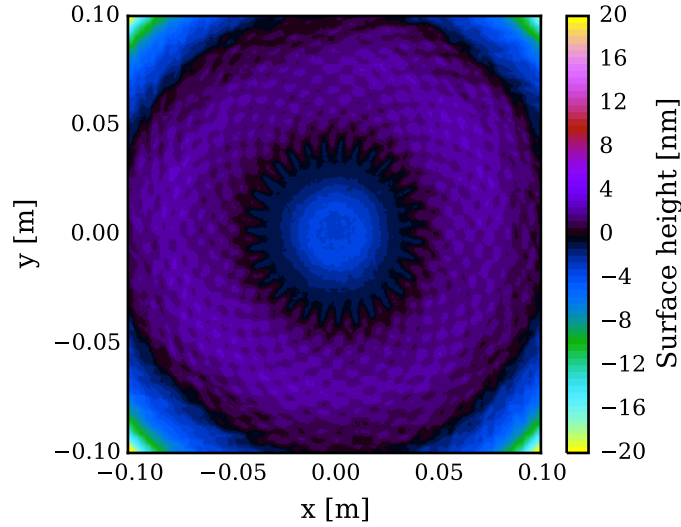


**Figure 1.9:** *Mirror map* [50, 51]: The surface height variation around the central region of ETM08 installed in the x-arm at LHO. The test mass mirrors have a diameter of 34 cm, though the central part as shown is typically that which the incident beam is perturbed by. This map has been processed to remove any piston, curvature and astigmatism modes, leaving behind the surface errors.

both the amplitude and phase of the beam will be affected with

$$A(x, y) = \alpha(x, y)e^{i2kz(x, y)}. \quad (1.61)$$

An example of the measured surface height variations present on an aLIGO test mass mirror can be seen in figure 1.9 [51].

The mode content of the outgoing beam  $E(x, y; \mathbf{q})$  is computed by projecting  $E'$  into the outgoing beam basis  $\mathbf{q}$ . For any incoming HOM  $u_{n'm'}$  the amount of outgoing  $u_{nm}$  can be computed via an overlap integral, this complex valued term is known as a *coupling coefficient*:

$$\mathbf{K}_{nm, n'm'}(q_x, q'_x, q_y, q'_y; A) = \iint_{-\infty}^{\infty} \mathcal{K}(\lambda_x; x)A(x, y)\mathcal{K}(\lambda_y; y) dx dy, \quad (1.62)$$

---

where the integral kernels  $\mathcal{K}(\boldsymbol{\lambda}_x; x)$  and  $\mathcal{K}(\boldsymbol{\lambda}_y; y)$  are given by

$$\mathcal{K}(\boldsymbol{\lambda}_x; x) = u_n^*(x, q_x)u_{n'}(x, q'_x), \quad (1.63)$$

$$\mathcal{K}(\boldsymbol{\lambda}_y; y) = u_m^*(y, q_y)u_{m'}(y, q'_y), \quad (1.64)$$

and the parameter vectors are given by  $\boldsymbol{\lambda}_x = (n, n', q_x, q'_x)$  and  $\boldsymbol{\lambda}_y = (m, m', q_y, q'_y)$ . There are two general cases when computing Eq.(1.62):  $q \neq q'$  which we refer to as *mode-mismatched* and  $q = q'$  as *mode-matched*.

Computing the scattering matrix  $\mathbf{K}$  requires evaluating the integral Eq.(1.62) for each of its elements. If couplings between modes up to and including order  $\mathcal{O}$  are considered then the number of elements in  $\mathbf{K}$  is  $N_k(\mathcal{O}) = (\mathcal{O}^4 + 6\mathcal{O}^3 + 13\mathcal{O}^2 + 12\mathcal{O} + 4)/4$  and the computational cost of evaluating such a large number of integrals can be very computationally expensive. In our experience [52, 53] a typical LIGO simulation task involving HOMs can be performed with  $\mathcal{O} = 6 - 10$  while in some cases, such as those that include strong thermal distortions or clipping, a higher maximum order is required.

In simple cases where  $A(x, y) = 1$  or  $A(x, y)$  represents a tilted surface, analytical results are available for both mode matched and mismatched cases [54, 55]. In general however  $A(x, y)$  is of no particular form and the integral in Eq.(1.62) must be evaluated numerically.

It is possible to split multiple distortions into separate scattering matrices for example if the distortion can be represented as  $A(x, y)B(x, y)$  and the coupling coefficients become a product of two separate matrices by inserting a complete basis with the parameter  $\tilde{q}$ :

$$\mathbf{K}_{nm, n' m'}(\mathbf{q}, \mathbf{q}'; AB) = \sum_{\tilde{n}, \tilde{m}=0}^{\infty} \mathbf{K}_{nm, \tilde{n} \tilde{m}}(\mathbf{q}, \tilde{\mathbf{q}}; A) \mathbf{K}_{\tilde{n} \tilde{m}, n' m'}(\tilde{\mathbf{q}}, \mathbf{q}'; B). \quad (1.65)$$

## 1. MODELLING INTERFEROMETERS

---

Thus our scattering matrix is just the product of the two separate effects

$$K(\mathbf{q}, \mathbf{q}'; AB) = K(\mathbf{q}, \tilde{\mathbf{q}}; A)K(\tilde{\mathbf{q}}, \mathbf{q}'; B). \quad (1.66)$$

By choosing  $\tilde{\mathbf{q}} = \mathbf{q}$  or  $\mathbf{q}'$  we can set the mode-mismatching to be in either one matrix or the other. This is ideal as a mode-matched  $\mathbf{K}$  is a Hermitian matrix whose symmetry can be exploited to only compute one half of the matrix. By ensuring that this matrix also contains any distortions that require numerical integration the computational cost can be nearly halved. It is then possible to benefit from the fast analytic solutions to Eq.(1.62) to account for mode-mismatching in the other matrix.

Care must be taken when separating the scattering matrices in this manner. By separating the matrices an ordering to the distortions applied to the beam is artificially implied. If the matrices do not commute an error will be present in the scattering calculation. This error should be reduced by using a higher  $\mathcal{O}_{max}$ , thus better satisfying the summation in Eq.(1.65). In practice, the types of mirror distortions seen from weakly clipped apertures and surface errors the commutation error did not appear to alter the results significantly.

Lastly, care must be taken when the two separated distortions are solved by numerical finite limited integrations. The finite limits introduce a clipping in both  $\mathbf{K}$ , and when combined will include twice the amount of clipping. To solve this, the integration limits must be large enough that clipping is not an issue. Or the inverse of the scattering matrix  $K(x, y; \alpha(x, y; R_{ap}))$  can be computed. Applying this inverted scattering matrix removes the clipping contribution from one of the separated  $\mathbf{K}$ . This can also be resolved by merging all of the applied maps into a single one and integrating over it.

Further details regarding these scattering matrices and how to efficiently compute them can be found in chapter 2.

### 1.3.4 Optical cavities

The upgrades put in place by many of the second generation of detectors use optical cavities to resonantly enhance the optical field for improved sensitivity. An optical cavity can be formed by two or more mirrors along a closed optical path. A linear cavity is shown figure 1.10 along with the important fields within it. Shown are the intracavity fields  $E_{1-4}(\tau)$ , the incident field  $E_I(\tau)$ , the reflected field  $E_R(\tau)$  and the transmitted field  $E_T(\tau)$ . Each mirror can also be displaced from its reference plane with a tuning of  $\phi_1$  or  $\phi_2$ , the differential displacement being  $\Delta\phi = \phi_1 - \phi_2$ . Their reflectivities and transmissivities are  $r_1$  and  $t_1$  for the input mirror and  $r_2$  and  $t_2$  for the output. The distance between the two mirrors, the cavity length, is  $L_{\text{cav}}$  metres.

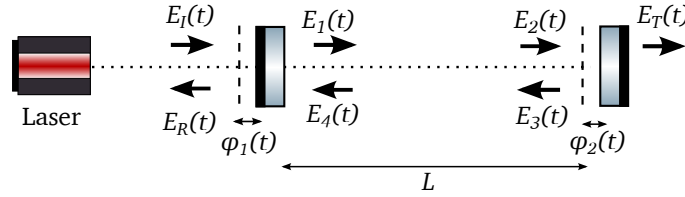


**Figure 1.10:** *Optical cavity:* The fields in an optical cavity can be broken down into those at each mirror.  $E_I$  being the a field incident on the input mirror and  $E_R$  that directly reflected combined with the transmitted intracavity field.  $E_T$  is that which is transmitted out of the end mirror. The intracavity fields are  $E_{1-4}$ .

The steady state fields can be found using the previous techniques for computing the optical coupling at the mirrors and propagating the field between them. The reflected, transmitted and circulating single frequency plane-waves are then:

$$E_4(\tau) = E_I(\tau) \frac{i t_1 r_2 e^{-i2kL_{\text{cav}} + i2\Delta\phi}}{1 - r_1 r_2 e^{-i2kL_{\text{cav}} + i2\Delta\phi}} \quad (1.67)$$

$$E_R(\tau) = E_I(\tau) \left( r_1 - \frac{T_1 r_2 e^{-i2kL_{\text{cav}} + i2\Delta\phi}}{1 - r_1 r_2 e^{-i2kL_{\text{cav}} + i2\Delta\phi}} \right) \quad (1.68)$$

$$E_T(\tau) = -E_I(\tau) \frac{t_1 t_2 e^{-i2kL_{\text{cav}} + i2\Delta\phi}}{1 - r_1 r_2 e^{-i2kL_{\text{cav}} + i2\Delta\phi}} \quad (1.69)$$

The power in each of these fields is plotted in figure 1.11. How the reflected, trans-

## 1. MODELLING INTERFEROMETERS

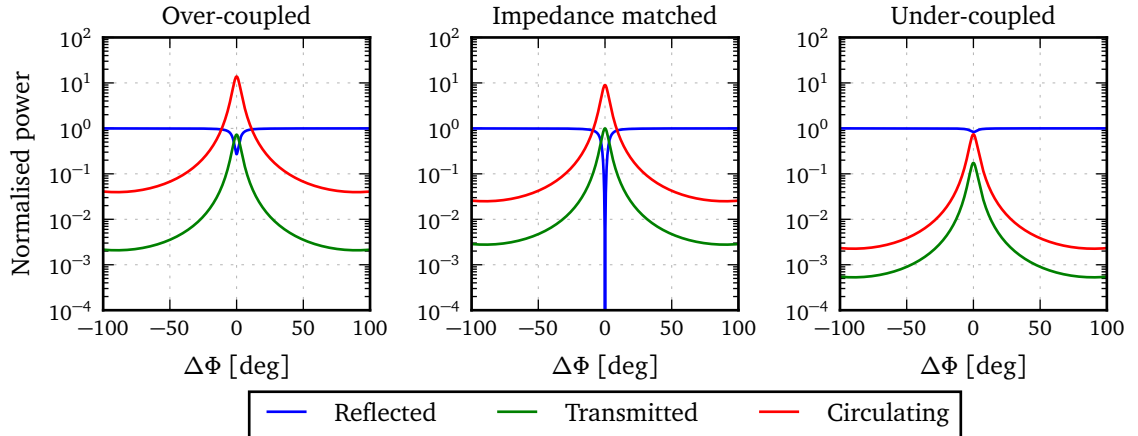


**Figure 1.11:** Cavity resonances: The reflected, transmitted and circulating fields differ in magnitude on resonance depending on the cavity parameters: Over-coupled ( $T_1 > T_2$ ), impedance matched ( $T_1 = T_2$ ) and under-coupled ( $T_1 < T_2$ ). The cavity power is scanned by varying the tuning of the cavity to change its length on a microscopic level.

mitted and circulating fields behave depend on the  $R$  and  $T$  of each of the cavity mirrors:  $R_1$  and  $T_1$  being that of the input mirror and  $R_2$  and  $T_2$  being that for the end. When the cavity mirrors have identical values the cavity is referred to as *impedance matched* ( $T_1 = T_2$ ). In this case it is possible to have all light being transmitted through the cavity; such setups are used for the IMC and OMC as minimal reflections from these cavities are desired. An over-coupled ( $T_1 > T_2$ ) refers to when the end mirror is more reflective than the input, such as the aLIGO arm cavities. Here most of the power is reflected but significant circulating power gains are possible. The other option is under-coupled, where the end mirror is less reflective than the input.

The intracavity field resonates when the round-trip path length is some integer  $N$  number of wavelengths. This can also be expressed in terms of which optical frequencies will resonate in the cavity. This occurs whenever the round-trip propagation phase is  $2N\pi$ :

$$2kL_{\text{cav}}N = 2N\pi f \left( \frac{2L_{\text{cav}}}{c} \right) = \frac{2N\pi f}{\text{FSR}}. \quad (1.70)$$

Here the free-spectral range (FSR) is the frequency separation between successive resonances. This is shown in figure 1.12. In this plot it can be seen that the resonances of

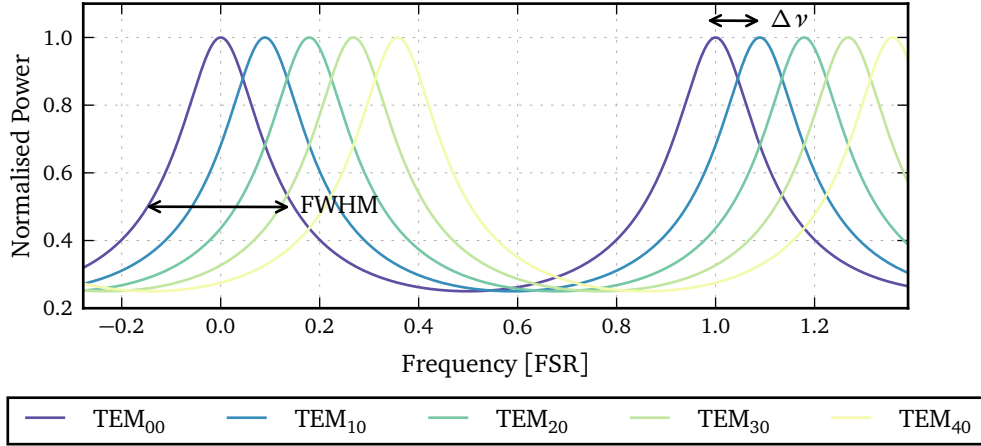


**Figure 1.12: Resonance features:** There are several descriptive parameters regarding the shape of the resonances. The FWHM highlighting the linewidth of the resonance. Also shown are how HOMs up to  $\mathcal{O}_{max} = 4$  resonate in the cavity. Here the Gouy phase of the HOMs ensures the modes resonate at different  $\Delta\phi$ . Here  $\Delta\nu$  is the mode separation frequency between successive HOM resonances.

the  $TEM_{00}$  mode aligns with zero tuning. To simplify models it is useful to breakdown lengths between optical components into two parts: a macroscopic  $\gg \lambda$  length which is always an integer number of wavelengths and the microscopic tuning. Then the tuning  $\Delta\phi$  is defined so that the main carrier is resonant when  $\Delta\phi = 0$ .

The shape of the resonance is described by its peak value and the full width half maximum (FWHM) as shown in figure 1.12. Another is the cavity's *finesse*

$$\mathcal{F} = \frac{FSR}{FWHM}. \quad (1.71)$$

The *finesse*, similar to the quality factor of a resonator, is defined by how narrow the linewidth of a resonance is compared to the free spectral range. It is also a measure of how lossy a cavity is: a cavity that has a high *finesse* loses less optical field loss. When the round-trip loss is small,  $\rho \ll 1$ , the *finesse* can be approximated as

$$\mathcal{F} \approx \frac{2\pi}{\rho}. \quad (1.72)$$

## 1. MODELLING INTERFEROMETERS

---

Loss here refers to any optical field that leaves the cavity, either from scattering, absorption, or transmitted through the mirrors. For example, the round-trip loss in a LIGO arm cavity is mostly through transmission of the ITM,  $\rho \approx T_{\text{itm}} \approx 0.014$  which means  $\mathcal{F} \approx 450$ .

### 1.3.4.1 Transforming beams with ABCD matrices and beam tracing

In order to compute the amplitude of the steady-state Hermite-Gaussian optical fields the beam parameters, both  $q_x$  and  $q_y$ , must be defined for all fields in the model. Without knowing the beam shape it is not possible to compute what Gouy phase is accumulated on propagation or what shape dependent scattering occurs. This is required whether for modelling a single cavity or a full interferometer.

How a Gaussian beam is transformed when propagating or interacting with an optical component is described using *ABCD matrices* [44]. For a known beam parameter  $q_1$  in a medium with refractive index  $n_1$  that is transformed by a matrix with components  $A$ ,  $B$ ,  $C$  and  $D$ , the new beam parameter is

$$q_2 = n_2 \frac{A \frac{q_1}{n_1} + B}{C \frac{q_1}{n_1} + D}, \quad (1.73)$$

where  $n_2$  is the output medium index. ABCD matrices exist for various components to describe how the  $x$  and  $y$  plane beam parameter is changed, these can be found in many sources such as [26, 44, 27].

As previously discussed in section 1.3.3.2, in order to compute the optical scattering we require both the incoming and outgoing beam parameters. When doing this it must be ensured that the correct beam parameters are used. The incoming beam is that which is the correctly transformed incident beam. This is demonstrated in figure 1.13 for both reflection and transmission at a mirror. The transformations are described by some ABCD matrices  $\mathbf{M}_R$  and  $\mathbf{M}_T$  respectively. There are two sides to

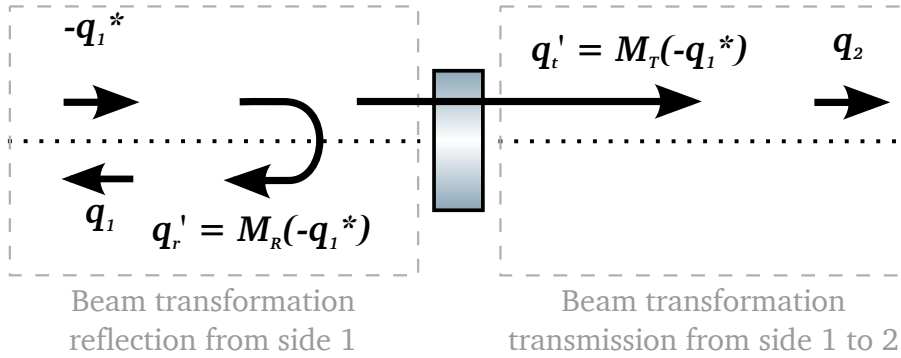


**Figure 1.13:** *Beam parameter transformations:* In a modal model the beam parameters must be set for every optical field to define its shape. In FINESSE it was chosen that at each node the incoming and outgoing field will have the same beam parameter but just reversed. On side 1 in this particular case  $q_1$  is the outgoing shape and  $-q_1^*$  that of the incoming, this is similar for side 2. Both  $q_r'$  and  $q_t'$  are the beam shapes after interacting with the mirror with ABCD matrices  $M_R$  and  $M_T$  on reflection and transmission from side 1 respectively.

the mirror here the reflection occurs on side 1 and the transmission is from side 1 to side 2. The outgoing beam on side 1 has a shape  $q_1$  and  $q_2$  on side 2. The untransformed beam incoming beams have a shape  $-q_{1/2}^*$ : this is the same shape beam as the outgoing but where it has been flipped from being either converging or diverging as it is travelling in the opposite direction. The scattering calculation on reflection then computes how the transformed beam shape,  $q_1' = M_R(-q_1^*)$ , projects into the outgoing beam. The situation is identical for the transmission case, just that  $M_T$  is used instead.

*Beam tracing* uses equation Eq.(1.73) to follow the beam from an initial position in the interferometer, where the beam parameter is defined, throughout the rest of the interferometer to fill in the unknown beam parameters. Although, the choice of what beam parameter to use is not a unique one. A good place to start is by using an optical cavity's *spatial eigenmode*. This spatial eigenmode is the steady state shape that builds up and is stable within the cavity. It is defined as the beam parameter  $q$  that is repeated after one round-trip of the cavity, thus is resonant. The properties of a cavity, such as the curvature of mirrors and its length, define this spatial eigenmode. As optical cavities dominate how advanced detectors behave, describing the beam shapes in the natural basis of these cavities is a sensible choice.

## 1. MODELLING INTERFEROMETERS

---

The above tracing works well for a single cavity, however in the case of multiple coupled cavities (like SRC, PRC, X-arm and Y-arm) the choice of beam parameter is neither unique or obvious. In many cases the beam parameter traced using the eigenmode of one cavity will not match that of another cavity once traced to it: this is known as a *mode-mismatch*. This term is used to describe whenever an optical field's  $q$  value does not match that of the target. If it does match, it is a *mode-matched* case. More information on how to effectively trace the beam in FINESSE can be found in the manual [26].

Mode-mismatching however is not just a numerical problem, this occurs in the detectors and is the focus of current research as discussed in section 4.4. When a beam is described in a mismatched basis additional higher order modes are required to fully describe the beam, thus the beam is scattered into higher order modes. A mismatched  $TEM_{00}$  beam is described with the addition of  $TEM_{20}/TEM_{02}$  modes for mismatches of a few percent, larger mismatches will require  $TEM_{40}/TEM_{04}$  or higher. The overlap between two beam parameters  $q_1$  and  $q_2$  can be compared with [56]

$$\mathbb{O}(q_1, q_2) = \frac{4|\text{Im}\{q_1\}\text{Im}\{q_2\}|}{|q_1^* - q_2|^2}, \quad (1.74)$$

with a value of 1 being a perfect match and 0 meaning none.

### 1.3.4.2 Stability

The stability of an optical cavity refers to how well it can contain a misaligned beam. A stable cavity will ensure that the beam is kept within the geometry of the cavity. An unstable one will eventually loose the beam after some number of round-trips. The Hermite-Gaussian modes are only eigenmodes of stable cavities with spherical mirrors, of which are used in gravitational wave detectors. Unstable resonators still possess a particular spatial eigenmode [57], however, they are not analytically available in many

---

cases.

The stability of a cavity can be determined using its round-trip ABCD matrix. With this it is possible to determine if after one round-trip the same beam shape is reproduced, if so a stable eigenmode exists. This is achieved using equation 1.73 by assuming  $q_1 = q_2 \equiv q$  (that the incoming beam is reproduced) and solving for  $q$ . If  $q$  has a real valued beam waist, a Hermite-Gaussian mode will describe the cavity eigenmode [27]. If such an eigenmode exists the cavity is referred to as *stable*. In the case where the solution  $q$  returns an imaginary value for the beam waist no stable eigenmode exists, thus the cavity is *unstable*. The condition for stability using the elements of the cavity's ABCD matrix is

$$0 \leq \frac{A+D+2}{4} \leq 1. \quad (1.75)$$

For a linear cavity this is more commonly shown as  $g$ -factors of the two mirrors:

$$g_1 = 1 - \frac{L_{\text{cav}}}{R_{c,1}}, \quad (1.76)$$

$$g_2 = 1 - \frac{L_{\text{cav}}}{R_{c,2}}, \quad (1.77)$$

$$g = g_1 g_2. \quad (1.78)$$

which is stable for  $0 \leq g \leq 1$ .

An important feature of a cavity's stability is how it affects higher order modes ability to resonate within it. As a cavity becomes more unstable the round-trip Gouy phase approaches an integer multiple of  $2\pi$  [58]:

$$\psi_{\text{RT}} = 2 \arccos \left( \text{sign}(B) \sqrt{\frac{A+D+2}{4}} \right). \quad (1.79)$$

In such cases all of the HOMs will experience the same round-trip phase, thus all are

## 1. MODELLING INTERFEROMETERS

---

resonant at the same time. The HOM separation frequency is

$$\Delta \nu = \frac{\psi_{\text{RT}}}{2\pi} \text{FSR}. \quad (1.80)$$

This states the frequency difference between successive orders of HOMs. An example of the resonances up to order four modes being separated is shown in figure 1.12.

Whether operating a cavity in a stable or unstable state depends on its function. It is typically desired that the mode separation frequency is higher than the linewidth of the cavity, which allows for a single order of HOM to be resonant at once. The aLIGO arm cavities are an example of this, where it should be ensured that the main carrier is resonant and no other scattered modes are. The PRC and SRC are also designed to be stable in aLIGO [59] to provide greater tolerance to scattered light, misalignments and radius of curvature differences in mirrors. Near unstable operation also has its uses as discussed in chapter 3 where an unstable cavity is used to manipulate multiple HOMs.

### 1.3.5 Optical readout and sensing

Optical readout refers to the process of measuring information from optical fields outputted by the interferometer. This is primarily achieved using photodiodes to measure a beam's power. The photocurrent generated by a photodiode will be proportional to the incident beam power

$$I(\tau) = \chi P(\tau) \quad (1.81)$$

where  $P(\tau)$  given by Eq.(1.16). Here  $\chi$  is the efficiency of the photodiode. It will be assumed that  $\chi = 1$  for this work being as it is a final scaling factor of an outputted signal.

The frequency spectrum of the beam power will consist of the optical beats between the various frequency components [27]. Optical modulators will act on the

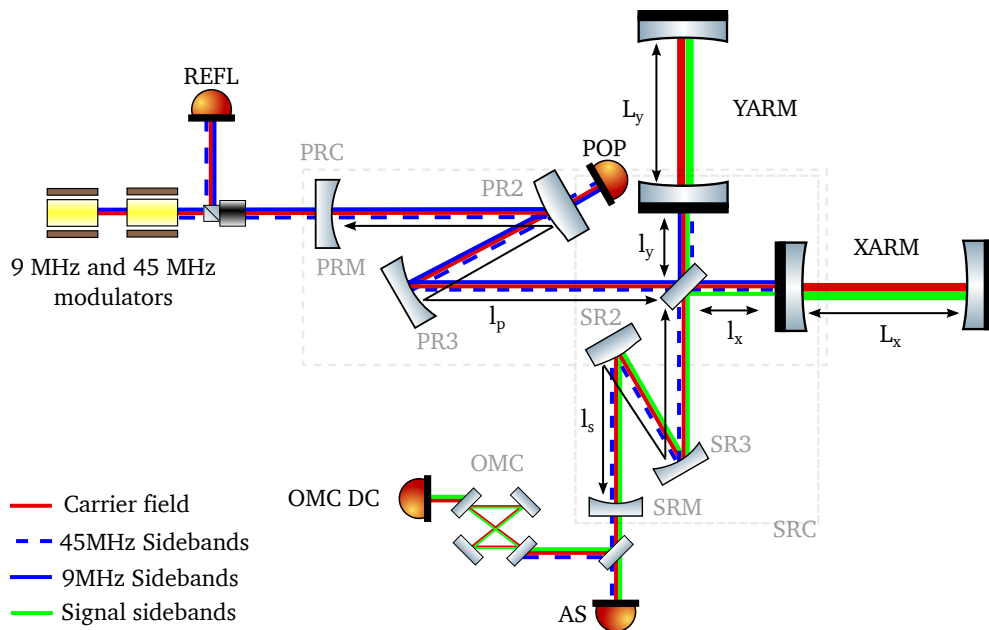


**Figure 1.14:** *aLIGO* length sensing: An overview of the *aLIGO* length sensing setup. Shown are the main photodiodes: REFL, POP, AS and OMC DC. Modulators are used to produce 9 and 45 MHz sidebands around the carrier field. The various cavities are designed so that particular frequencies resonant in certain areas to *sense* changes there. Also shown are the lengths which define the interferometer DOFs as listed in table 1.1.

main carrier before it enters the core interferometer, as shown in figure 1.14. In the case of *aLIGO* this is applies 9 MHz and 45 MHz phase modulation. These fields then propagate and resonate in particular cavities to *sense* them. Sensing here means that an optical field will be sensitive to changes in a particular cavity. The power in the optical fields are then measured at various points throughout the interferometer and phase or amplitude information is extracted by *demodulating* the photocurrent.

*aLIGO* length sensing and control design is outlined in [60]. Rather than discussing individual mirror positions, of which there are many, several length degrees of freedom can be defined:

- *CARM*: Common arm mode. This is any length changes that appears in both arm cavities in phase, e.g. both get longer or shorter.
- *DARM*: Differential arm mode. This is an out of phase change in the arm lengths,

## 1. MODELLING INTERFEROMETERS

---

e.g. one gets longer and one gets shorter.

- *MICH*: This is a differential motion of the *short Michelson*, between the BS and ITMs.
- *SRCL*: A change in the SRC length between the SRM and ITMX (SRX) and ITMY (SRY).
- *PRCL*: A change in the PRC length between the PRM and ITMX (SRX) and ITMY (SRY).

How each of these DOFs are defined in terms of actual lengths is shown in table 1.1. A diagram of where each frequency is resonant and the important lengths for the DOFs are shown in figure 1.14.

DOF	Definition	Output
PRCL	$(L_x - L_y)/2$	POP 9 MHz I
MICH	$(L_x + L_y)/2$	POP 45 MHz Q
CARM	$l_x - l_y$	REFL 9 MHz I
SRCL	$l_p + (l_x + l_y)/2$	REFL 45 MHz I
DARM	$l_s + (l_x + l_y)/2$	OMC DC

**Table 1.1:** *aLIGO* length definitions: Each length DOF is defined in terms of the physical lengths of the cavities as shown. These lengths are shown in figure 1.14. Also listed are the photodiode outputs and demodulations used for each DOF. Here REFL and POP refer to the photodiode locations and I and Q where the in-phase or quadrature of the error signal is used.

The carrier, 9 and 45 MHz sidebands are all resonant in the PRC. In the SRC the 45 MHz sidebands resonate but the main carrier and signal sidebands are anti-resonant to operate with resonant sideband extraction [61]. Neither of the RF sidebands resonate in the arm cavities. The photodiodes and demodulation frequencies used to generate an *error signal* for each DOF is shown in table 1.1. All apart from DARM are sensed using the RF sidebands. Unlike the others, DARM uses the DC power outputted by the diode, with some offset, on transmission of the OMC to produce its error signal. DARM can also be sensed using the AS photodiode demodulating at 45 MHz. The latter was used in the experiment before the OMC was commissioned.

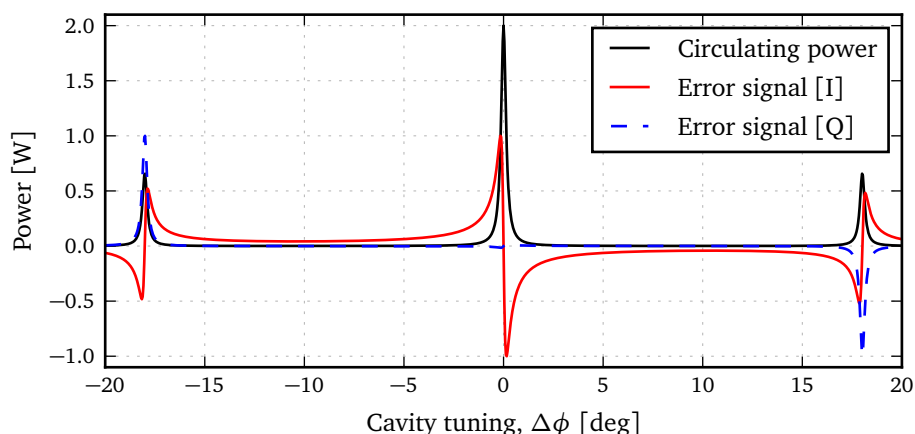


**Figure 1.15:** *Error signal example:* An error signal for an optical cavity length as would be used for the Pound-Drever-Hall technique. Here the intracavity power is plotted in relation to the error signal generated. Each resonance matches with a zero crossing in the error signal. The resonances away from  $\Delta\phi = 0$  are those of the RF sidebands matching the cavity. A linear range around the zero-crossing defines the control range of the error signal.

An error signal is an output from the interferometer that can be used to stabilise and control a particular parameter of the system. In this case, the signals outputted by the photodiodes are demodulated with the same RF signal used to modulate the optical fields. The error signals are used to control the cavities' length so that they are at the desired operating point. For optical cavities the operating point is typically defined as one that ensures the correct optical fields are resonant or anti-resonant within it, as noted above for each cavity.

An example of a typical shaped error signal is shown in figure 1.15. Here each of the resonances in the cavity coincides with a zero-crossing in the error signal, either side of which is an approximately linear change of the signal with length. This signal would be fed into an actuator of one of the cavity mirrors controlling its longitudinal position. A servo then keeps the error signal *zeroed* by displacing the mirror and keeping the cavity on resonance, or locked. The zero crossing is crucial for this as it provides the direction in which the actuation needs to act from the sign change. If the mirror is displaced beyond the linear range around the zero-crossing the lock will be lost as the servo will no longer be able to return to the resonant position.

## 1. MODELLING INTERFEROMETERS

---

Error signals can become distorted due to imperfections in the interferometer, such as mode-mismatches, misalignments or scattering. This leads to either the error signal being degraded until it is no longer usable with no zero crossing or a flat linear region. Distortions can also lead to undesirable shifts in the operating point which is followed by the servos. Modelling how these error signals can be designed and become distorted is one of the strongest abilities of frequency domain simulation tools like FINESSE.

More is discussed about operating points and finding them in numerical models in section 4.1. For interested readers, a more general overview on the aspects of length sensing and control can be found in [27]. Whilst more specific details on the aLIGO length and alignment can be found in [60] and [62] respectively.

### 1.4 Conclusion

In this chapter I have introduced what interferometric gravitational wave detectors are and their main components in relation to their second generation upgrades. Outlined was the core optical features that are required to construct a model that represents these physical detectors. This introduced the core optical features that are required to model interferometers in gravitational wave detector: propagation of lasers over small and large distances, coupling at optical components, describing how interferometer imperfections perturb the optical fields with HOMs, the handling multiple optical frequencies for sensing and control and reading out optical signals.

The theory described here will be revisited throughout the following chapters: chapter 2 will look at efficient computations of modal scattering; chapter 3 also relies on modal scattering but here combined with radiation pressure effects to study parametric instabilities. Chapter 4 outlines modelling work undertaken in relation to aLIGO commissioning and design. The optical theory presented here also forms the theoretical background of the simulation software FINESSE that I developed dur-

---

ing my PhD. An overview of FINESSE and the improvements implemented is given in appendix A.

## 1. MODELLING INTERFEROMETERS

---

## Chapter 2

# Fast simulation of Gaussian-beam mode scattering

This chapter outlines the research undertaken to speedup a major bottleneck in modal model simulations tools using a new quadrature technique, referred to as reduced order quadrature (ROQ) [63]. This work was reported in the paper *Fast simulation of Gaussian-mode scattering for precision interferometry* [64] and submitted for publication. My contributions to this work were the initial idea of using reduced order methods for such problems, the development of the Python and FINESSE implementation of the method and the numerical testing and validation of the method. The theoretical background of reduced order quadrature was contributed by Rory Smith who uses similar techniques in data analysis of gravitational waves. Plots and text have been used verbatim from this paper of which I was a principal author. The content has been modified to fit into the structure of this thesis with the introductory aspects of scattering being merged into chapter 1, hence some minor changes to the text have been made.

Numerical integration is a key computational element for many optical simula-

## 2. REDUCED ORDER QUADRATURE

---

tions. Typically this is in the form of solving the propagation of light via scalar diffraction integrals, which is the approach taken in FFT based simulation tools. Modal models take advantage of the analytic propagation of the orthogonal set of modes that describe the spatial eigenmodes of the cavities; thus removing the scalar diffraction integral. However, when using modes to describe an imperfect optical system, the distortions of the beam are represented by a sum of higher order optical modes. Which modes are present depend on the incoming beam's mode content and the imperfection. This scattering between the incoming mode and the outgoing mode content is evaluated using multiple overlap integrals between each mode (See Eq.(1.62)).

The computational cost of this is not an issue when a small number of optical modes are considered. Realistic models can require of order 100 modes resulting in the number of couplings between them ranging into the 1000s. This is a significant bottle neck in running modal simulations, like FINESSE, that include apertures, surface defects, thermal distortions and other potential scattering effects. The distortions present at a mirror usually come in a form that is colloquially referred to as a *mirror map*. This is a 2D grid of data that describes how the amplitude and phase of a beam is distorted. These maps can be based on physical measurements taken from the optics, or could be based on some theoretical equation. The map is then integrated with both the incoming and outgoing modes to compute the coupling between them, as shown in Eq.(1.62). An example of an actual and crucial modelling task which required the computation of 1000s of integrals was in the investigation of parametric instabilities. The work described in this chapter was necessary to perform the research presented in chapter 3.

The use of maps as seen in chapter 3 to describe distortions to a beam and how it affects an interferometer is typical of the type of modelling performed in the gravitational wave community. At hand is the task of understanding how various defects alter the behaviour and output of the interferometer. The wide range of possible param-

---

eters of the interferometer creates a high-dimensional parameter space within which different states must be explored. Thus, fast and lightweight numerical tools are crucial for providing quick feedback to the simulator as to whether they are modelling in a useful direction or simply to not waste time if a mistake was made.

Before ROQ, FINESSE used a basic implementation of scattering calculations. The integration of Eq.(1.62) was done using the simplest option of a Riemann summation. Various attempts were made at improving the performance of this using multithreading and caching results to save recomputing similar values. The best solution was found using the adaptive deterministic *Cuhre* routine provided in the *Cuba* library [65] along with caching as many of the computed results as possible for distortions that did not vary during the simulation. These additions proved much faster than the original Riemann summation. However, simulations could still take an excessively long time to run (on the order of days) when simulating distortions that changed during runtime, such as a varying thermal deformation of a mirror. At this stage Rory Smith, working on reduced order methods for the data analysis side of gravitational wave physics [66], and myself began exploring if such techniques could be used to optimise problems in optics.

The ROQ can be regarded as a near-optimal, application specific, downsampling of the integrands needed to compute the integrals for the scattering matrices. It is analogous to a Gaussian quadrature rule, but rather than being designed to provide exact results for polynomials of a particular degree, the ROQ produces nearly-exact results for an arbitrary parametric function. Importantly, it is possible to place tight error bounds on the accuracy of the ROQ for a particular application [63], thus making it an ideal technique to speed up costly integrals whilst remaining confident in the answer.

ROQ exploits an offline/online methodology in which the expensive integrals used to compute scattering matrices are recast into a more computationally efficient form

## 2. REDUCED ORDER QUADRATURE

---

during the *offline* stage. The offline/online methodology involves breaking the original computation into two parts: online refers to the computation done when the result is needed, e.g. when a FINESSE simulation is running; offline in our case refers to a single stage computation run separately from FINESSE which enables us to run the more a more efficient online computation. This is then used for the rapid *online* evaluation of the scattering matrices. The offline stage can itself be computationally expensive, however this step need only be performed once and is easily parallelisable for improved computation times. The data computed in the offline stage—that is needed by the ROQ—can be stored and shared with other simulators for particular modelling problems.

In this chapter the algorithm is shown in a general form and a working example is used to compare against previously used integration techniques. The implementation of the method described in this article is available as open source as part of the FINESSE source code and the Python based package PYKAT [67], which also contains the offline computed data to enable others to model Advanced LIGO like arm cavities. The particular implementation here is used to provide a simple, real-world example. However, the algorithm can be easily implemented in other types of simulation tools, for example, time domain simulations or grid based tools (also known as FFT simulations) that compare beam shapes. In all cases this algorithm can significantly reduce the computation time for evaluating overlap integrals of Gaussian modes with numerical data.

The outline is as follows: section 2.1 provides the mathematical background and algorithm for producing the ROQ (section 2.1 heavily relies on an additional mathematical technique known as the *empirical interpolation method* [68]); section 2.2 then highlights an exemplary case to demonstrate the method for modelling near-unstable optical cavities; and finally in section 2.3 the computational performance of the method is analysed.

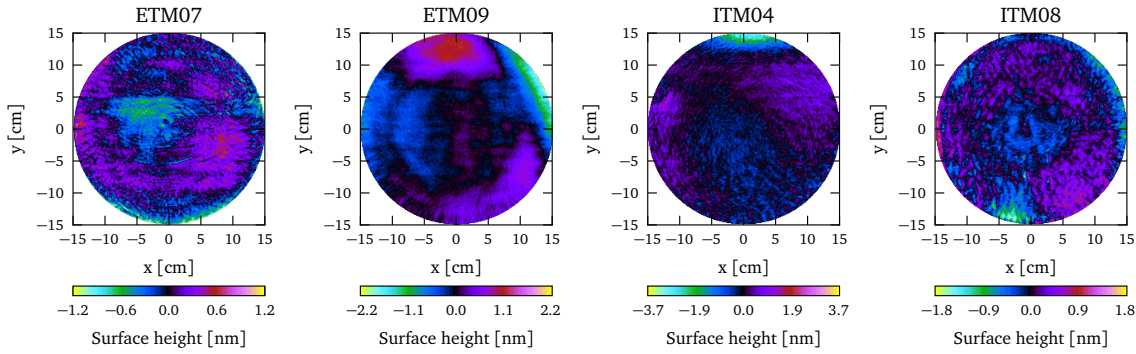


**Figure 2.1:** *Uncoated LIGO mirror maps* [64]: Measured surface distortions for the mirrors currently installed in the Livingston LIGO site (shown here are the distortions of the test masses before they were coated). ETM09 and ITM08 are installed in the x-arm and ETM07 and ITM04 in the y-arm [51]. These mirror maps have been processed to remove the overall mirror curvatures, offset and tilts.

## 2.1 Efficiently computing scattering matrices: integration by interpolation

For a discretely sampled mirror map with  $L$  sample points in both the  $x$  and  $y$  directions, the coupling coefficient Eq.(1.62) can be approximated using a composite Newton-Cotes quadrature rule:

$$k_{nm,n'm'}(q_x, q'_x, q_y, q'_y; A) \approx \sum_{k=1}^L \sum_{l=1}^L W_{kl} \mathcal{K}(\lambda_x; x_k) A(x_k, y_l) \mathcal{K}(\lambda_y; y_l), \quad (2.1)$$

where  $W$  is an  $L \times L$  matrix describing the 2D composite Newton-Cotes quadrature weights over the area of the map. Newton-Cotes rules is a term for the collection of quadrature rules for handling equally spaced samples of the integrand. Examples of such rules are the trapezium or Simpson's rule. The weighting matrix is found by taking the outer product of the 1D composite Newton-Cotes quadrature weights [69] in both  $x$  and  $y$  directions. This provides the weighting of each of the 2D samples towards the integration result. There are  $L^2$  terms in the double sum Eq.(2.1). When  $L^2$  is large,  $L \approx 1000$  for aLIGO mirrors, there are two major bottlenecks: (i) evaluation of the kernel at each discrete  $x_k, y_k$  and, (ii) evaluation of the double sum. With a set

## 2. REDUCED ORDER QUADRATURE

---

of  $M \ll L$  basis elements that accurately spans the kernel space, it is possible to replace the double sum Eq.(2.1) with a *reduced order quadrature* (ROQ) rule Eq.(2.11) containing only  $M^2$  terms, reducing the overall cost of the by a factor of  $\sim L^2/M^2$ , provided the kernel can be directly evaluated.

The reduced order quadrature scheme is implemented in three steps. The first two are carried out offline, while the final, mirror-map-dependent step is performed in preparation for the simulations; once per map. The steps are as follows: *Step 1* - Construct a reduced basis (offline); a set of  $M$  basis elements whose span describes the kernel space. *Step 2* - Construct an interpolant using the basis (offline) by requiring it to exactly match any kernel at  $M$  carefully chosen spatial subsamples  $\{X_k\}_{k=1}^M$  [70] (and similarly for  $y$ ). *Step 3* - Use the interpolant to replace the inner product evaluations in Eq.(2.1) with the ROQ Eq.(2.11) (online).

### 2.1.1 The empirical interpolation method

The empirical interpolation method is an efficient technique performing this offline/online procedure and has been demonstrated in the context of astronomical data analysis with LIGO [66]. Provided the kernels vary smoothly with  $\lambda_x$  over  $x$  and  $\lambda_y$  over  $y$  then there exists a set of kernels at judiciously chosen parameter values that represent any kernel - and hence any integral Eq.(1.62) - for an arbitrary parameter value. This set of kernels constitutes the reduced basis: Given any parameter value  $\lambda_x$  or  $\lambda_y$  the best approximation to the kernel at  $\lambda_x$  or  $\lambda_y$  as linear combination of the reduced basis can be found.

The ability to exploit the reduced basis to quickly evaluate Eq.(1.62) depends on being able to find an affine parameterisation of the integral kernels. In general, the kernels do not admit such a parameterisation. However, the empirical interpolation method finds a near-optimal affine approximation whose accuracy is bounded by the accuracy of the reduced basis [63]. This affine approximation is called the *empirical*

---

*interpolant*. The spatial integrals over  $dx dy$  in Eq.(1.62) will only depend on the reduced basis (and hence only have to be computed once for a given mirror map) and the parameter variation is handled by the empirical interpolant at a reduced computational cost.

The empirical interpolation method exploits the offline/online computational concept where we decompose the problem into a (possibly very) expensive offline part which allows for a computational cheap online part. In this case, the expensive offline part is in finding the reduced basis and constructing the empirical interpolant. Once the empirical interpolant is found then it can be used for the fast online evaluation of Eq.(1.62). One of the main reasons why the empirical interpolant is used for fast online evaluation of Eq.(1.62) is due to its desirable error properties that makes it superior to other interpolation methods, such as polynomial interpolation. In addition, the empirical interpolant avoids many of the pitfalls of high-dimensional interpolation that would otherwise be encountered (see, e.g. [71]).

### 2.1.2 Affine parameterization

The kernel would ideally be separable for mode parameters  $(\lambda_x, \lambda_y)$  and spatial position  $(x, y)$ . Thus a representation of the kernels would ideally have the form:

$$\begin{aligned}\mathcal{K}(\lambda_x; x) &= a(\lambda_x)f(x), \\ \mathcal{K}(\lambda_y; y) &= a(\lambda_y)f(y).\end{aligned}\tag{2.2}$$

The functions  $a$  and  $f$  are the same irrespective of whether the kernel is a function of  $x$  or  $y$  due to the symmetries of the Hermite Gauss modes. Using the affine parameterization, the coupling coefficient Eq.(1.62) is:

$$k_{nm,n'm'}(q_x, q'_x, q_y, q'_y) = a^*(\lambda_x)a(\lambda_y) \iint_{-\infty}^{\infty} f^*(x)A(x, y)f(y)dx dy, \tag{2.3}$$

## 2. REDUCED ORDER QUADRATURE

---

This affine parameterization thus allows us to compute all the parameter-dependent pieces efficiently in the online procedure as all the  $x - y$  integrals are performed only once for a given mirror map. In general the kernel will not admit an exact affine decomposition as in Eq.(2.2). Using the EIM, the approximation to the kernels will have the form:

$$\begin{aligned}\mathcal{K}(\boldsymbol{\lambda}_x; x) &\approx \sum_i c_i(\boldsymbol{\lambda}_x) e_i(x), \\ \mathcal{K}(\boldsymbol{\lambda}_y; y) &\approx \sum_i c_i(\boldsymbol{\lambda}_y) e_i(y).\end{aligned}\tag{2.4}$$

The sum is over the reduced basis elements  $e_i$  and coefficients  $c_i$  that contain the parameter dependence.

Given a basis  $e_i(x)$ , the  $c_i(\boldsymbol{\lambda}_x)$  in Eq.(2.4) are the solutions to the M-point interpolation problem where it is required that the interpolant is exactly equal to the kernel at any parameter value  $\boldsymbol{\lambda}_x$  at the set of interpolation nodes  $\{X\}_{i=1}^M$ :

$$\mathcal{K}(\boldsymbol{\lambda}_x; X_j) = \sum_{i=1}^M c_i(\boldsymbol{\lambda}_x) e_i(X_j) = \sum_{i=1}^M V_{ji} c_i(\boldsymbol{\lambda}_x),\tag{2.5}$$

where the matrix  $V$  is given by

$$V \equiv \begin{pmatrix} e^1(X_1) & e^2(X_1) & \cdots & e^M(X_1) \\ e^1(X_2) & e^2(X_2) & \cdots & e^M(X_2) \\ e^1(X_3) & e^2(X_3) & \cdots & e^M(X_3) \\ \vdots & \vdots & \ddots & \vdots \\ e^1(X_M) & e^2(X_M) & \cdots & e^M(X_M) \end{pmatrix}\tag{2.6}$$

Thus:

$$c_i(\boldsymbol{\lambda}_x) = \sum_{j=1}^M (V^{-1})_{ij} \mathcal{K}(\boldsymbol{\lambda}_x; X_j).\tag{2.7}$$

---

Substituting Eq.(2.7) into Eq.(2.4), the empirical interpolant is:

$$\mathcal{J}_M[\mathcal{K}](\boldsymbol{\lambda}_x; x) = \sum_{j=1}^M \mathcal{K}(\boldsymbol{\lambda}_x; X_j) B_j(x) \quad (2.8)$$

where:

$$B_j(x) \equiv \sum_{i=1}^M e_i(x) (V^{-1})_{ij} \quad (2.9)$$

and is independent of  $\boldsymbol{\lambda}_x$ . The special spatial points  $\{X_k\}_{k=1}^M$ , selected from a discrete set of points along  $x$ , as well as the basis can be found using algorithm. 1 which is described in the next section.

Note that the kernels  $\mathcal{K}(\boldsymbol{\lambda}_x; x)$  appear explicitly on the right hand side of Eq.(2.8). Because of this, the kernel at the empirical interpolation nodes  $\{X_k\}_{k=1}^M$  must be directly evaluated. Fortunately this is possible in this case as a closed form of the kernels is known. If the kernels were solutions to ordinary or partial differential equations that needed to be evaluated numerically then using the empirical interpolant becomes more challenging, however, this is not required here (see, e.g., [72, 70, 73] for applications of the empirical interpolation method to ordinary and partial differential equation solvers).

### 2.1.3 The empirical interpolation method algorithm (Offline)

The empirical interpolation method algorithm solves Eq.(2.8) for arbitrary  $\boldsymbol{\lambda}_x$ . While it would be possible in principle to use arbitrary basis functions, such as Lagrange polynomials which are common in interpolation problems [74, 75], a different approach is taken that uses only the information contained in the kernels themselves. The selected basis will consist of a set of  $M$  judiciously chosen kernels sampled at points on the parameter space  $\{\boldsymbol{\lambda}_x^i\}_{i=1}^M$ , where  $M$  is equal to the number of basis elements in Eq.(2.8). Because the kernels vary smoothly with  $\boldsymbol{\lambda}_x$  a linear combination of the basis

## 2. REDUCED ORDER QUADRATURE

---

elements will give a good approximation to  $\mathcal{K}(\boldsymbol{\lambda}_x; x)$  for any parameter value [70]. An interpolant is then built using this basis by matching  $\mathcal{K}(\boldsymbol{\lambda}_x; x)$  to the span of the basis at a set of  $M$  interpolation nodes  $\{X_k\}_{k=1}^M$ . The empirical interpolation method algorithm, shown in algorithm 1, provides both the basis and the nodes.

The empirical interpolation method algorithm uses a greedy procedure to select the reduced basis elements and interpolation nodes. With the greedy algorithm, the basis and interpolant are constructed iterative whereby the interpolant on each iteration is optimised according to an appropriate error measure. This guarantees that the error of the interpolant is on average decreasing and—as shown in section 2.1.4—that the interpolation error decreases exponentially quickly. Algorithm 3.1 of [76] is followed which is reproduced in algorithm. 1.

The first input to the algorithm is a *training space* (TS) of kernels - distributed on the parameter space  $\boldsymbol{\lambda}_x$  - and the associated set of parameters. This training space is denoted by  $\mathcal{T} = \{\boldsymbol{\lambda}_x^k, \mathcal{K}(\boldsymbol{\lambda}_x^k; x)\}_{i=1}^N$  and should be densely populated enough to represent the full space of kernels as faithfully as possible. Hence it is important that  $1 \ll N$ . The second input is the desired maximum error of the interpolant  $\epsilon$ . It was found that the  $L^\infty$  norm is a robust error measure for the empirical interpolant and hence  $\epsilon$  corresponds to the largest tolerable difference between the empirical interpolant and any kernel in the training set  $\mathcal{T}$ .

The algorithm is initialised on steps 3 and 4 by setting the zeroth order interpolant to be zero, and defining the zeroth order interpolation error to be infinite. The greedy algorithm proceeds as follows: The basis element on iteration  $i$  is identified to be the  $\mathcal{K}(\boldsymbol{\lambda}_x; x) \in \mathcal{T}$  that maximises the  $L^\infty$  norm with the interpolant from the previous iteration,  $\mathcal{J}_{i-1}[\mathcal{K}](\boldsymbol{\lambda}_x; x)$ . This is performed in steps 7 and 8. On step 9  $X_i$  is selected, the  $i^{\text{th}}$  interpolation node, by selecting the position at which the largest error occurs, and adding that position to the set of interpolation nodes. By definition, the interpolant is equal to the underlying function at the interpolation nodes and so the error

---

**Algorithm 1** Empirical Interpolation Method Algorithm: The empirical interpolation method algorithm builds an interpolant for the kernels Eq.(1.63) iteratively using a greedy procedure. On each iteration the current interpolant is validated against a *training set*  $\mathcal{T}$  of kernels and the worst interpolation error is identified. The interpolant is then updated so that it describes the worst-error point perfectly. This is repeated until the worst error is less than or equal to a user specified tolerance  $\epsilon$ .

---

- 1: **Input:**  $\mathcal{T} = \{\lambda_x^k, \mathcal{K}(\lambda_x^k; x)\}_{k=1}^N$  and  $\epsilon$
  - 2: Set  $i = 0$
  - 3: Set  $\mathcal{J}_0[\mathcal{K}](\lambda_x; x) = 0$
  - 4: Set  $\sigma_0 = \infty$
  - 5: **while**  $\sigma_i \geq \epsilon$  **do**
  - 6:    $i \rightarrow i + 1$
  - 7:    $\lambda_x^i = \arg \max_{\lambda_x \in \mathcal{T}} \|\mathcal{K}(\lambda_x; x) - \mathcal{J}_{i-1}[\mathcal{K}](\lambda_x; x)\|_{L^\infty}$
  - 8:    $\xi_i(x) = \mathcal{K}(\lambda_x^i; x)$
  - 9:    $X_i = \arg \max_x |\xi_i(x) - \mathcal{J}_{i-1}[\xi_i](x)|$
  - 10:    $e_i(x) = \frac{\xi_i(x) - \mathcal{J}_{i-1}[\xi_i](x)}{\xi_i(X_i) - \mathcal{J}_{i-1}[\xi_i](X_i)}$
  - 11:    $V_{lm} = e_l(X_m) \quad l \leq i, m \leq i$
  - 12:    $B_m(x) = \sum_l e_l(x) (V^{-1})_{lm} \quad l \leq i, m \leq i$
  - 13:    $\sigma_i = \max_{\lambda_x \in \mathcal{T}} \|\mathcal{K}(\lambda_x; x) - \mathcal{J}_i[\mathcal{K}](\lambda_x; x)\|_{L^\infty}$
  - 14: **end while**
  - 15: **Output:** Interpolation matrix  $\{B_j(x)\}_{j=1}^M$  and interpolation nodes  $\{X_j\}_{j=1}^M$ . The equivalent interpolant for  $\mathcal{K}(\lambda_y; y)$  is obtained trivially from  $\{B_j(x)\}_{j=1}^M$  and  $\{X_j\}_{j=1}^M$  by setting  $x \rightarrow y$  and  $X \rightarrow Y$ .
- 

at  $X_i$  - which is the largest error on the current iteration - is removed. On step 10 the basis function is normalised. This ensures that the matrix Eq.(2.6) is well conditioned. On steps 11 and 12 Eq.(2.6) and Eq.(2.9) are computed, which are used to construct the empirical interpolant Eq.(2.8). Finally, on step 13 interpolation error  $\sigma_i$  between the interpolant on the current iteration  $\mathcal{J}_i[\mathcal{K}](\lambda_x; x)$  and  $\mathcal{K}(\lambda_x; x) \in \mathcal{T}$  as in step 7 is calculated. The procedure is repeated until  $\sigma_i \leq \epsilon$ .

Once the interpolant for  $\mathcal{K}(\lambda_x; x)$  is found, the equivalent interpolant for  $\mathcal{K}(\lambda_y; y)$  is obtained trivially from  $\mathcal{J}_M[\mathcal{K}](\lambda_x; x)$  by setting  $x \rightarrow y$ .

## 2. REDUCED ORDER QUADRATURE

---

### 2.1.4 Error bounds on the empirical interpolant

Before proceeding to demonstrate the utility of the empirical interpolant for quickly evaluating Eq.(1.62) a brief remark on some of the error properties of the empirical interpolation method is made. A more detailed error analysis of the empirical interpolant can be found in [63]. The empirical interpolant possess a highly desirable property, namely exponential convergence to the desired accuracy  $\epsilon$ . It can be shown [76, 68] that there exists constants  $c > 0$  and  $\alpha > \log(4)$  such that for any function  $f$  the empirical interpolant satisfies

$$\|f - \mathcal{J}_M[f]\|_{L^\infty} \leq c e^{-(\alpha - \log(4))M}. \quad (2.10)$$

This states that under the reasonable assumption that there exists an order  $M$  interpolant that allows for exponential convergence, then the empirical interpolation method will ensure it will converge to this interpolant exponentially quickly. This is an important property as it means that the order of the interpolant,  $M$ , tends to be small for practical purposes. In addition, because the quantity on the right hand side  $c e^{-(\alpha - \log(4))M}$  is set to a user specified tolerance  $\epsilon$  then an *a priori* upper bound on the *worst-fit* of the interpolant can be set. However, one must still verify that the interpolant describes functions outside the training *a posteriori*, although the error bound should still be satisfied provided that the training set was dense enough. In fact, it can be shown [68] that the empirical interpolation method is a near optimal solution to the Kolmogorov  $n$ -width problem in which one seeks to find the best  $M$ -dimensional (linear) approximation to a space of functions.

It is important to recall the integral kernels Eq.(1.63) are interpolated as a function of six free parameters  $\lambda_x$ : two indices  $n$  and  $n'$  and two complex beam parameters  $q_x$  and  $q'_x$ . If the EIM was not used, an alternative way of expressing the  $\lambda_x$ -dependent coefficients in Eq.(2.4) would need to be found. Consider, for example, a case in which

---

a tensor-product splines to describe the coefficients were used: Using a grid of just ten points in each of the six parameters in  $\lambda_x$  would result in an order  $10^6$  spline which would surely be computationally expensive to evaluate. Furthermore, there would be no guarantee of its accuracy or convergence to a desired accuracy.

### 2.1.5 Reduced order quadrature (Online)

Substituting the empirical interpolant Eq.(2.8) into Eq.(2.1) gives the ROQ,

$$k_{nm,n'm'}(q_x, q'_x, q_y, q'_y; A) = \sum_{k=1}^M \sum_{l=1}^M \omega_{kl} \mathcal{K}(\lambda_x; X_k) \mathcal{K}(\lambda_y; Y_l), \quad (2.11)$$

with the ROQ weights  $\omega_{kl}$  given by:

$$\omega_{kl} = \sum_{i=1}^L \sum_{j=1}^L W_{ij} A(x_i, y_j) B_k(x_i) B_l(y_j). \quad (2.12)$$

The ROQ form of the coupling coefficient enables fast online evaluations of the coupling coefficients. Note that because only  $M^2$  operations are required to perform the double sum Eq.(2.11) we expect that the ROQ is faster than the traditional  $L^2$ -term Newton-Cotes integration by a factor of  $L^2/M^2$  provided that  $M < L$ . It is expected in practice that  $M \ll L$  due to the exponential convergence of the empirical interpolation method.

The number of operations in Eq.(2.11) can be compressed further still due to the separability of the empirical interpolant Eq.(2.8) into beam parameters  $\lambda_x$  and spatial position  $x$  that allows us to exploit the spatial symmetry in the HG modes. The HG modes exhibit spatial symmetry/antisymmetry under reflection about the origin. Hence, it is useful to split the  $x$  and  $y$  dimensions into four equally sized quadrants and perform the ROQ in each quadrant separately. For example, when a HG mode is symmetric between two or four of the quadrants then only two or one set(s) of coef-

## 2. REDUCED ORDER QUADRATURE

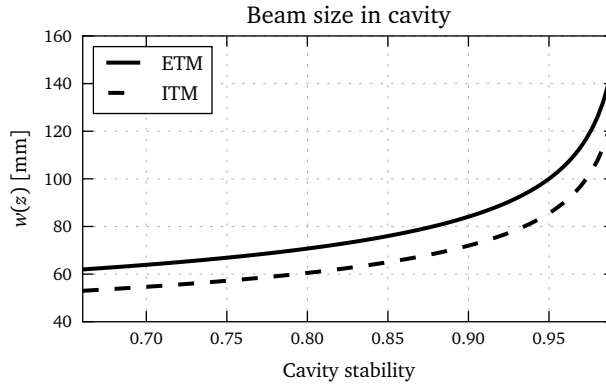


**Figure 2.2:** *Intracavity beam sizes* [64]: The beam size on the ITM and ETM of a LIGO cavity as a function of cavity stability parameter as the mirror RoCs are tuned.

ficients  $\{\mathcal{K}(\lambda_x; X_k)\}_{k=1}^M$  needs to be computed (and likewise for  $\{\mathcal{K}(\lambda_y; Y_l)\}_{l=1}^M$ ). This will speed up the computation of the ROQ Eq.(2.11) by up to a factor of four. Hence, in practice the EI is only built over one half plane for either positive or negative values of  $x$  (or equivalently  $y$ ); the basis spanning the second half-plane by reflecting the basis about the origin is derived. To ensure that this symmetry is exploitable the data points of the map must be distributed equally and symmetrically about the beam axis  $((x, y) = (0, 0))$ . Those points that lie on the  $x$  and  $y$  axes must also be weighted to take into account they contribute to multiple quadrants when the final sum is computed. In the cases where the map data points are not correctly aligned a bilinear interpolation of the data to retrieve symmetric points did not introduce any significant errors. However, higher-order interpolation methods can introduce artefacts to the map data.

## 2.2 Exemplary case: near-unstable cavities and control signals

There are several scenarios when modelling tools can benefit heavily from the ROQ method, of particular interest are cases where the simulation time is dominated by

---

the integration time of the mirror surface maps. One such example is an investigation into the feasibility of upgrading the LIGO interferometers with near-unstable arm cavities. The stability of a Fabry-Perot cavity is determined by its length  $L$  and radius of curvature (RoC) of each of its mirrors and can be described using the parameter::

$$g = (1 - L/R_{c,itm})(1 - L/R_{c,etm}). \quad (2.13)$$

with  $0 \leq g \leq 1$  defining the stable region. Near-unstable cavities are of interest because they result in larger beam sizes on the cavity mirrors (see also figure 2.2) which reduces the coating thermal noise [36], one of the limiting noise sources of the detector. One negative aspect of such near-unstable cavities is that the transverse optical mode separation frequency approaches zero as  $g \rightarrow 0$  or  $1$ . The mode separation frequency determines the difference in resonance frequency of higher-order modes with respect to the fundamental mode. Thus, with a lower separation frequency any defect in the cavity causing scattering into HOMs is suppressed less and can contaminate control signals for that cavity and couple extra noise into the GW detectors output <sup>1</sup>. The optimal cavity design must be determined as a trade-off between these degrading effects and the reduction in coating thermal noise. This is a typical task where a numerical model can be employed to search the parameter space. In this case, each point in that parameter space corresponds to a different beam size in the cavity which forces a re-computation of the scattering matrices on the mirrors. Thus, the new algorithm described here should yield a significant reduction in computing time.

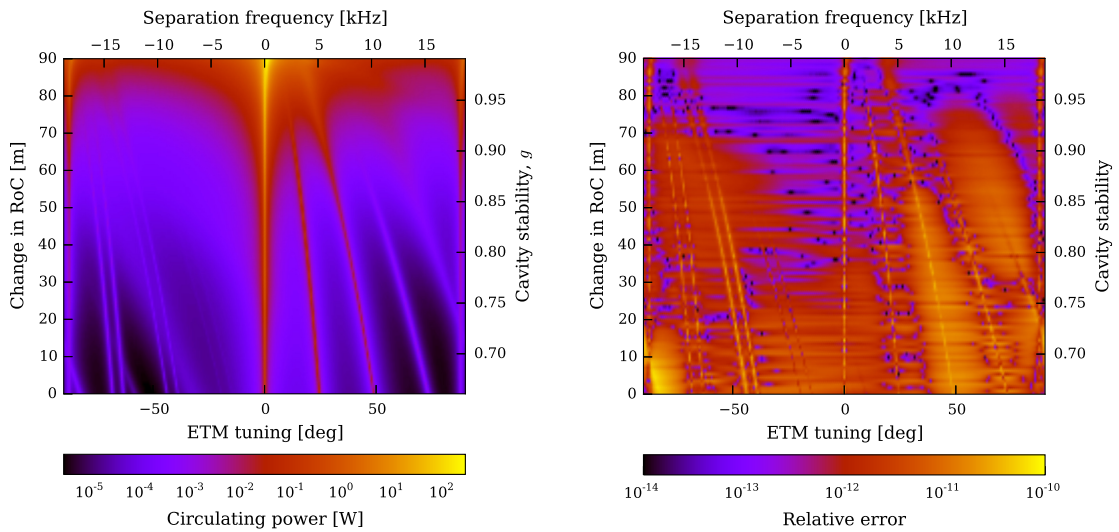
In this section a summary of the test simulation results are given along with how the model was set up. Following this an analysis of the performance of the ROQ algorithm is given. ROQ integration has been implemented in FINESSE and uses the official input parameter files for the LIGO detectors [77]. Below the preliminary investigation

---

<sup>1</sup>Another potential problem is additional clipping or scattering of the beam on the mirrors due to the larger beam sizes which can result in increased round-trip losses of the arm cavity.

## 2. REDUCED ORDER QUADRATURE

of the behaviour of a single Advanced LIGO like arm cavity with a finesse of 450, where the mirror maps for the mirrors ETM08 and ITM04<sup>1</sup> were applied to the high reflective (HR) surfaces is shown. This example is representative for a class of modelling performed regularly for the LIGO commissioning and design where multiple states of an interferometer with varying beam parameters is studied. This provides a concrete and quantitative setup to demonstrate the required steps to use the ROQ algorithm.



(a) Cavity scan as ITM and ETM RoC varied (b) The relative error between ROQ and Newton-Cotes.

**Figure 2.3:** *Near-unstable cavity scan with ROQ* [64]: As the RoC of the ITM and ETM are varied to make the cavity increasingly more unstable. This simulation was run for  $\mathcal{O}_{max} = 10$  and includes clipping from the finite size of the mirrors and surface imperfections from the ETM08 and ITM04 maps. Figure 2.3a shows how the amount of power scattering into HOM changes as  $g \rightarrow 1$ . Also visible here is the reduction in the mode separation frequency with increasing instability. The contribution of the  $TEM_{00}$  mode has been removed to make the HOM content more visible. The reduced basis was built for mode order  $\mathcal{O} = 14$ , to reduce errors, see figure 2.8. The difference in this result when using ROQ compared to Newton-Cotes is shown in 2.3b.

Modelling the LIGO cavity for differing stabilities involves varying the RoC of both the ITM and ETM. The resulting change in  $w(z)$  at each surface means the scattering matrices will need to be recomputed for each chosen state. To view the HOM content

<sup>1</sup>The nominal radius of curvatures of ETM08 and ITM04 are 1934m and 2245m respectively. The optical properties of these mirrors were taken from [51].

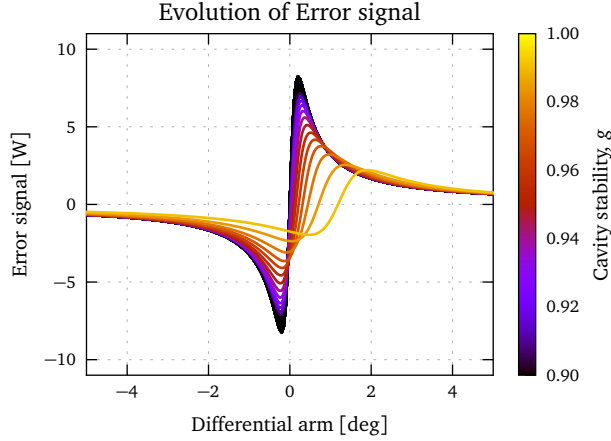


**Figure 2.4:** *Near-unstable cavity error signal* [64]: The Pound-Drever-Hall error signal for the LIGO cavity modelled in figure 2.3. A significant change in zero-crossing position and shape can be seen as the stability of the cavity is reduced ( $g \rightarrow 1$ ).

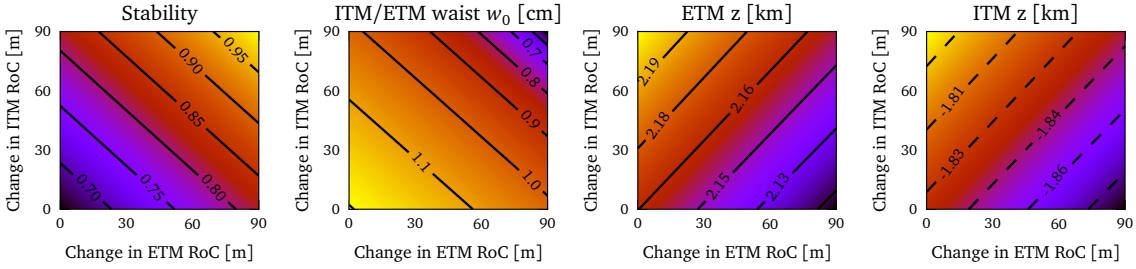


**Figure 2.5:** *ROQ parameter space* [64]: Range of beam parameters needed to model a change in curvature from 0 m to 90 m at the ITM and the ETM. In order to utilise the ROQ to cover this parameter space, the empirical interpolant needs to be constructed using a training set made from kernels Eq.(1.63) densely covering this space.

in the cavity created by the scattering a *cavity scan* can be performed, displacing one of the cavity mirrors along the cavity axis on the order of the wavelength of the laser light,  $\lambda = 1064$  nm, to change the resonance condition of the cavity. The simulation was performed with  $\mathcal{O} = 10$  with Newton-Cotes integration and the ROQ method. The results for cavity scans at different RoCs are shown in figure 2.3a. The dominant mode is the fundamental  $\text{TEM}_{00}$  whose resonance defines the zero tuning, the power in the  $\text{TEM}_{00}$  mode has been removed from this plot to better show the lower power HOM content. For more stable cavities (at the bottom of the plot in figure 2.3a) the HOMs are well separated and not resonant at the same time as the  $\text{TEM}_{00}$ . As the RoC is increased, the stability is reduced and the HOMs can be seen to converge and

## 2. REDUCED ORDER QUADRATURE

---

eventually become resonant at a tuning of 0. At a stability of  $g \approx 0.98$  the cavity mode begins to break down significantly and many modes become resonant. The effect of this on a sensing and control signal used for a Pound-Drever-Hall control system is shown in figure 2.4, where for increasingly unstable cavities the error signal becomes degraded, showing an offset to the nominal zero crossing, a reduced slope and overall asymmetry around the centre. The complete investigation into the feasibility of such cavities was not within the original scope of this test. This would include amongst other issues the quantitative comparison of the control noise from the degradation of the control signals with the reduced thermal noise. The simulation task described above is sufficient to provide a test case for the ROQ method.

### 2.3 Application and performance of new integration method

In this section a complete recipe for setting up and using the ROQ for the LIGO example, using FINESSE and PYKAT, is provided. Along with a discussion of the performance, in terms of speed and accuracy, of the method.

#### 2.3.1 Computing the ITM and ETM empirical interpolants

Firstly the range of beam parameters for the simulation must be determined. Once this is known a training set can be constructed and the empirical interpolant can be computed. The surface distortions that are of interest are those on the HR surfaces of a LIGO arm cavity mirror. Two EIs are required: one for the ITM HR surface and one for the ETM HR surface. This is due to the differing beam parameters at each mirror. The beam parameter range that the training sets should span are determined by varying the radius of curvature of the ITM and ETM to include the range of cavity stabilities that

---

are required to be modelled. The beam parameter ranges are shown in figure 2.5. The required ranges for the ETM are  $4.7 \text{ mm} < w_0 < 12.0 \text{ mm}$  and  $2.11 \text{ km} < z < 2.20 \text{ km}$  and for the ITM  $4.7 \text{ mm} < w_0 < 12.0 \text{ mm}$  and  $-1.88 \text{ km} < z < -1.79 \text{ km}$ , up to a maximum optical mode order of  $\mathcal{O} = 20$ , Newton-Cotes degree of 6,  $L = 1199$ . For this example the maximum tolerable error of the empirical interpolant are set to  $\epsilon = 10^{-14}$ .

Using these ranges the method described in section 2.1.1 can be used to produce the EIs. The offline computation of the basis can have significant computational cost. For very wide parameter ranges the memory required to store the training sets can quickly exceed that of typical machines. For the above parameters, with 100 sample points each in the  $w_0$  and  $z$  range, up to  $\mathcal{O} = 14$  and  $\epsilon = 10^{-14}$  approximately 7GB of memory was required. Running this method on machines with less memory is possible by storing the training set on a hard drive using a suitable data storage format such as HDF5 for access. Computation time of the empirical interpolant is then limited by the read and write times of the media. Using a MacBook pro 2012 model which contains a 2.7 GHz Intel core i7 with 8GB of RAM generating the ITM and ETM reduced basis and empirical interpolant takes  $\approx 4$  hours each. The number of elements in the final reduced basis for the ITM and ETM were  $N = 30$  and  $N = 29$  respectively.

### 2.3.2 Producing the ROQ weights

Once the empirical interpolant has been computed for both ITM and ETM HR surfaces the ROQ weights Eq.(2.12) can be computed by convoluting the mirror maps with the interpolant. The surface maps chosen are the measured surface distortions of the (uncoated) test masses currently installed at the LIGO Livingston observatory, shown in figure 2.1. The maps contain  $L \approx 1200$  samples, thus a theoretical speed-up of  $L^2/N^2 \approx 1200^2/30^2 = 1600$  from using ROQ over Newton-Cotes can be expected. These maps include an aperture,  $\mathcal{A}$ , and the variation in surface height in meters,

## 2. REDUCED ORDER QUADRATURE

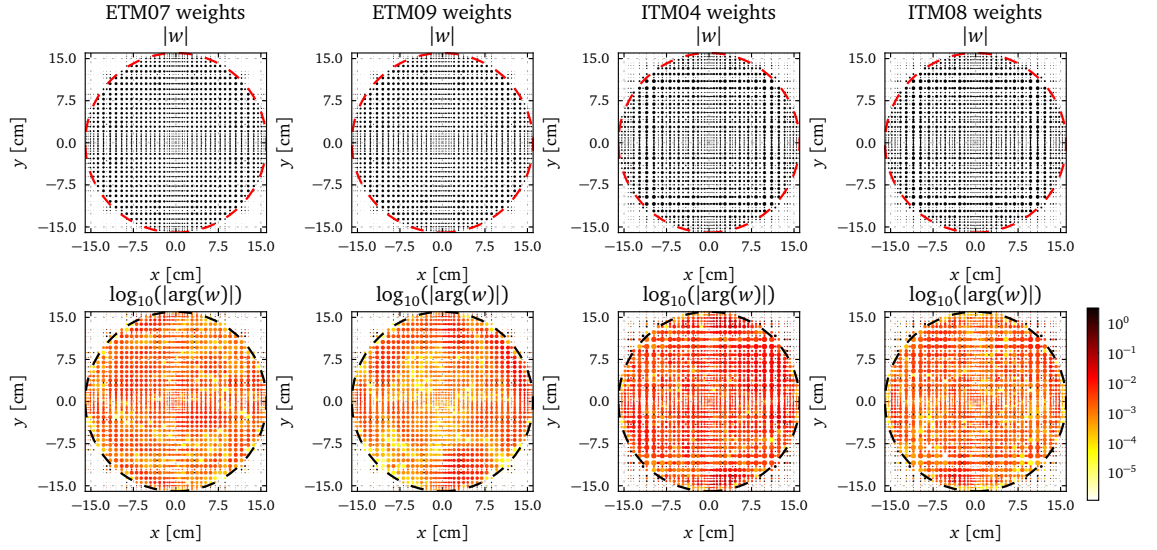


**Figure 2.6:** *Reduced order model of surface maps* [64]: Absolute and argument values of the ROQ weights Eq.(2.12) generated for each of the maps as shown in figure 2.1. Here the final quadrature rule can be visualised. The top plots show the absolute value: The size of the point is proportional to  $|w|$  and the center of each point lies on a specific empirical interpolation node in the x-y plane  $(X_i, Y_j)$  (c.f. Eq.(2.5) and Eq.(2.11)). The bottom plots show  $\log_{10}(\arg(w))$ . The dashed line on each plot shows the mirror surface boundary; outside the boundary the mirror maps are equal to zero. Note that there are non-zero ROQ weights associated with points in the region where the mirror maps are zero. While this may be counter intuitive, it is a consequence of the fact that the empirical interpolant nodes lie within the full x-y plane and, that they are constructed without any knowledge of the mirror maps: the weights still receive no contribution from the region where  $A(x, y) = 0$  as this region does not contribute to the sum in Eq.(2.12). However, the ROQ uses information about the kernels Eq.(1.63) over the entire region, including where  $A(x, y) = 0$ .

$z(x, y)$ . Thus to calculate the HOM scattering on reflection from one of these mirrors with Eq.(1.62) the distortion term is:

$$A(x, y) = \mathcal{A}(x, y)e^{2ikz(x, y)} \quad (2.14)$$

where  $\mathcal{A}(x, y)$  is 1 if  $\sqrt{x^2 + y^2} < 0.16\text{m}$  and 0 otherwise, and  $k$  is the wavenumber of the incident optical field.

Using Eq.(2.14) with equation Eq.(2.12) (with a Newton-Cotes rule of the same degree the empirical interpolant was generated with) the ROQ weights can be computed for each map shown in figure 2.1. This computational cost is proportional to

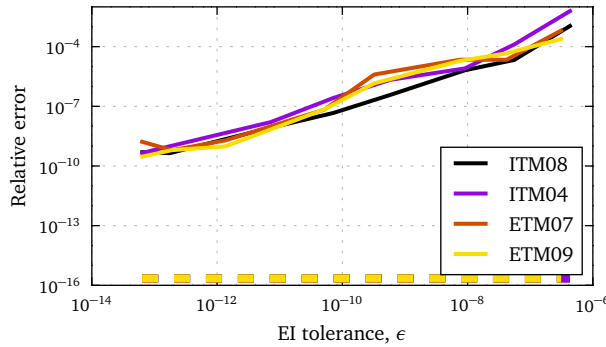


**Figure 2.7:** *Coupling coefficient error* [64]: Relative error in the scattering matrices computed using the ROQ and Newton-Cotes integration (with  $\mathcal{O}_{max} = 10$ ) as a function of the empirical interpolant tolerance  $\epsilon$ . The empirical interpolant was built for maximum coupling  $\mathcal{O}_{max} = 14$ . The error is the minimum (dashed lines) and maximum (solid lines) over the parameter space with which the empirical interpolant was built for, thus represents the worst and best case scenarios. The largest errors are independent of the map data and occur on couplings coefficients which couple the higher order modes included in the empirical interpolant.

the number of elements in the EI,  $M$ , and the number of samples in the map,  $L^2$ . For the LIGO maps this takes  $\approx 10$ s on a 2012 MacBook Pro. The resulting ROQ rule for the maps can be visualised as shown in figure 2.6: the amplitude of the ROQ weights map out the aperture and the phase of the weights varies for different maps because of the different surface structure. The computation of these ROQ weights need only be performed once for each map, unless the range of beam parameters required for the empirical interpolant are changed.

To verify that the process of generating the ROQ rule has worked correctly the scattering matrices with ROQ and Newton-Cotes across the parameter space are generated and compared.  $K(q; \text{ETM07})$  is computed with  $\mathcal{O}_{max} = 10$  using ROQ and then again using Newton-Cotes integration. Computing the relative error between each element of these two matrices the maximum error can be taken for  $q$  values spanning the requested  $q$  parameter range. Figure 2.7 shows how the final error of the EI,  $\sigma_M$ , propagates into an error in the scattering matrix. This shows the maximum (solid line) and minimum (dashed line) errors for any element in the scattering matrix between the two methods. From this it can be seen that building a more accurate empirical

## 2. REDUCED ORDER QUADRATURE

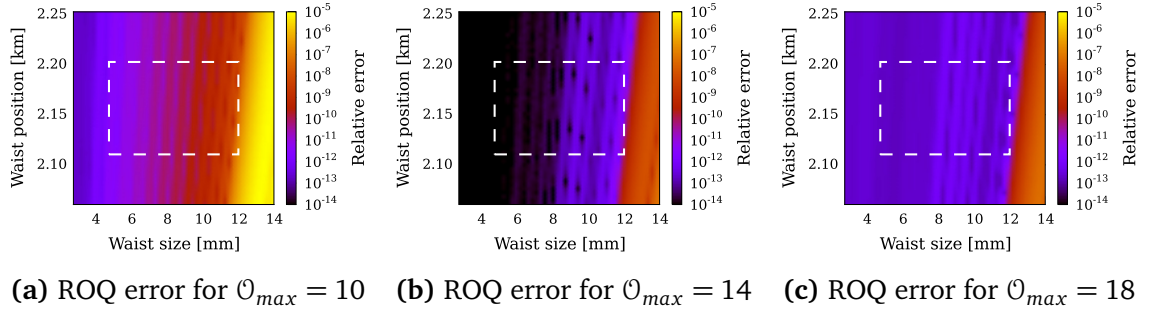


**Figure 2.8:** *ROQ parameter space accuracy and extrapolation* [64]: Maximum relative error between the scattering matrices computed for the ETM07 surface map, with ROQ and using Newton-Cotes, for mode orders up to  $\mathcal{O}_{max} = 18$ . The dashed white area represents the beam-parameter region over which training sets were generated. The subplots illustrate how using an ROQ built for a larger  $\mathcal{O}_{max}$  scattering reduces the maximum error significantly. Also shown is that the ROQ is valid over a larger parameter range than what it was initially generated for, implying that the empirical interpolant can be used for extrapolation in a limited parameter region outside the initial range indicated by the white dashed box.

interpolant results in smaller maximum errors in the scattering matrix. Now, using the most accurate reduced basis the maximum relative error is shown in figure 2.8 over the  $q$  space, where the white dashed box shows the boundaries of the parameters in the training set. Overall the method successfully computed a ROQ rule that accurately reproduced the Newton-Cotes results for scattering up to  $\mathcal{O} = 10$ . It should be noted that the largest errors, as seen in figure 2.7, do not represent the full parameter space but occur only at smallest  $z$  and largest  $w_0$ . It was also found that building a basis including a higher maximum HOM, for example basis of order 14 for scattering computations up to order 10, significantly improved the accuracy of the ROQ. Using a reduced basis constructed for order 14 rather than order 10 only increased the number of elements in the basis by 2, thus, did not significantly degrade the performance. It can also be seen in figure 2.8 that ROQ extrapolates beyond the originally requested  $q$  parameter space and does not instantly fail for evaluations outside of it. A gradual decrease in the accuracy can be seen when using larger  $w_0$  values.

In figure 2.9 the convergence of the empirical interpolant error with respect to the acceptable empirical interpolant error. One can see that the EI error converges

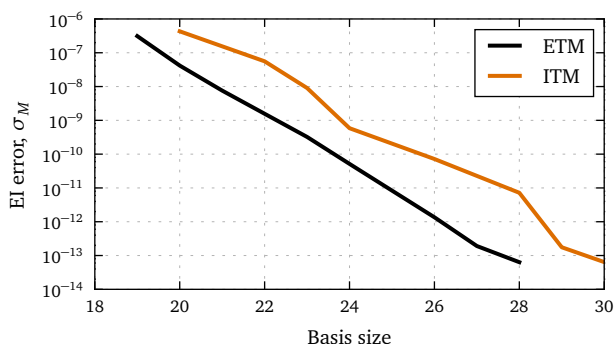


**Figure 2.9:** *Empirical interpolant error* [64]: EI error as a function of the number of basis elements selected by the greedy algorithm (Algorithm 1) for the example described in section 2.3.1. As expected from the error analysis in section 2.1.4, the empirical interpolant error displays exponential convergence with the basis size.

exponentially as described in section 2.1.4.

### 2.3.3 Performance

The time taken to run these FINESSE simulations as  $\mathcal{O}$  is increased is shown in figure 2.10 demonstrating how much more efficient it is to use ROQ over Newton-Cotes for the computation of scattering matrices. Also shown for reference the computation time when no scattering from surface maps is included to give the base time it takes to run the rest of the FINESSE simulation. The overall speed-up achieved can be seen in figure 2.11, reaching  $\approx 2700$  times faster to run the entire simulation at  $\mathcal{O} = 10$ . The overall speed-up then begins to drop slightly as the base time taken to run the rest of FINESSE becomes larger. The dashed line in figure 2.11 shows the speed-up if this base time is removed, again showing an impressive speed-up peaking at 4000 times faster.

Using ROQ enables us to perform such modelling tasks with a far greater efficiency. Running the model to compute the output seen in figure 2.3a required computing 100 different scattering matrices for the various changes in RoC. This took 20.5 hours to compute with Newton-Cotes and 18 minutes with ROQ <sup>1</sup>. The difference in the

<sup>1</sup>Note that the effective speed-up in this case is less than that in figure 2.11. Here the total runtime

## 2. REDUCED ORDER QUADRATURE

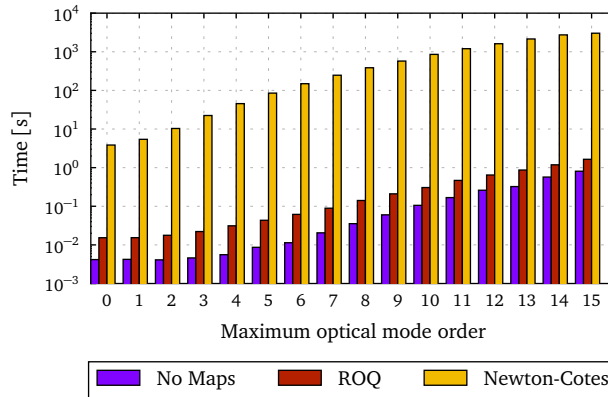


**Figure 2.10: ROQ method timing [64]:** Time taken to run FINESSE to model the steady state optical fields in an LIGO cavity with surface maps on both the ITM and ETM HR surfaces. The timing of running the entirety of FINESSE is used—rather than just the core method—because there are additional speed improvements from having to read and handle significantly less data points, from the  $L \times L$  maps down to  $M \times M$  ROQ weights. Smaller data fits into processor caches better and also reduces disk read times. This plot compares a single computation of the scattering matrices with ROQ Eq.(2.11) and Newton-Cotes. The case with no maps used is also shown to illustrate how much time is spent in FINESSE doing calculations not involving maps, which now becomes the dominant computational cost when using ROQ. A significant improvement is also found for order zero where only one scattering integral need be calculated; this is partly time saved from having to read larger data from the disk and manipulating it in memory. The pre-processing is unavoidable as the FINESSE can accept different types of map, thus it cannot be optimised at runtime until it know what it is dealing with. ROQ helps here as it removes this pre-processing step so it need only happen once. The ROQ pre-processing happens during the computing of the ROQ weights Eq.(2.12). This is a one time cost for each map for a particular EI and is computed outside of FINESSE, thus isn't included in this timing. The computational cost of this is on the order of 5s for each map for the reduced basis used in this example.

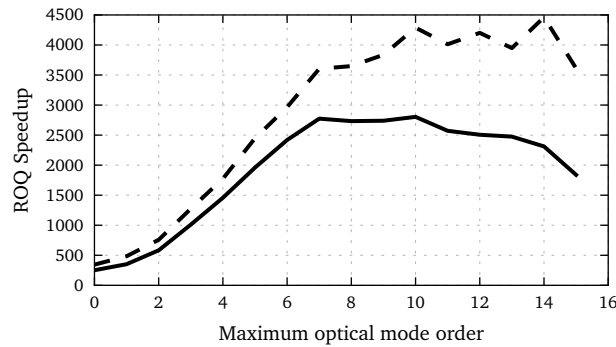


**Figure 2.11:** *ROQ speedup* [64]: The speed-up achieved using ROQ compared to Newton-Cotes as a function of mode order using the timing values in figure 2.10. The dashed line shows the speed-up if the time for initialisation and post-processing is subtracted from both times for Newton-Cotes and ROQ. This demonstrates the improvements just for the computational cost relating to map scattering calculations. Simulations that have a larger computational cost relating to features not related to scattering will show a smaller speed-up. For example, the simulation results shown in figure 2.3 have a total simulation speed-up of  $\approx 80$  but the scattering calculation was reduced from  $\approx 20.5$  Hours  $\rightarrow$  30 s.

final result between ROQ and Newton-Cotes is shown in terms of relative error in figure 2.3b. We have prepared the ROQ input for this example such that the error is significantly lower than 1 ppm (relative error of  $10^{-6}$ ) thereby showing that ROQ can be both much faster and still sufficiently accurate.

## 2.4 Conclusion

Numerical modelling of optical systems plays a vital role for the design and commissioning of precision interferometers. The typical use of the simulation software in this area requires rapid iterations of many simulation runs and manual fine tuning as modelling progresses, which is not well suited for large computer clusters. The scope of current investigations is often limited by the required computation time and thus the development of fast and flexible tools is a priority. Current problems in precision interferometers, such as LIGO, involve the investigation of laser beam shape

---

of the simulation is included. This includes the initialisation and running of the other aspects of FINESSE which took  $\approx 17$  minutes. The actual time taken for just the ROQ calculation is  $\approx 30$  s thus a speed-up in the ROQ vs Newton-Cotes is  $\approx 2500$ .

## 2. REDUCED ORDER QUADRATURE

---

distortions and their effect on the interferometer signal. Frequency-domain simulations using Gaussian modes to describe the beam properties have emerged as fast and flexible tools. However, the computation of the scattering matrix for mirror surface distortions—effectively an overlap integral of measured surface data with Hermite-Gauss modes—has shown to be a limiting factor in improving the computational speed of such tools. A significant reduction in computational time of current numerical tools is required for more efficient in-depth modelling of interferometers including more realistic features such as clipping, optical defects, thermal distortions and parametric instabilities.

In this work it was demonstrated how the empirical interpolation method can be used to generate an optimised quadrature rule for paraxial optical scattering calculations, known as a *reduced order quadrature*. This method removes the prohibitive computational cost of computing the scattering by speeding up the calculation of the steady state optical fields in a LIGO arm cavity by up to a factor of 2750 times, reducing simulation times from days to minutes. Using an exemplary simulation task of near-unstable arm cavities for the LIGO interferometers it has been demonstrated that this method is both accurate and fast for a typical modelling scenario where imperfections in the interferometer have a significant impact on optical performance. A complete recipe to recreate and use the new algorithm is provided and an implementation in FINESSE. Importantly, the reduced order quadrature integration method is generic and can be applied to any optical scattering problem for any surface distortion data.

## Chapter 3

# Optomechanics and parametric instabilities

This chapter outlines the research I have carried out in regards to optomechanical effects that the current and future detectors will experience. Radiation pressure effects and parametric instabilities will limit the future sensitivity and impede the operation of detectors. Due to my work, FINESSE has been developed and significantly extended to allow the modelling of such optomechanical effects. Before this work no generic interferometer simulation tool was available that combined higher order mode scattering and radiation pressure effects. The development of such a tool was needed to enable myself to study more complex systems. The result of this is a new optical scheme that could offer a broadband reduction in parametric instabilities which is reported here. This work is currently being written up for publication: *Daniel Brown et al. Optical suppression of parametric instabilities with extraction cavities. 2015. In preparation.*

In gravitational wave detectors the circulating power in the arm cavities is incredibly high,  $\approx 800$  kW for LIGO, and the force exerted by the intracavity field on the mirrors is non-negligible [79]. These forces can displace the cavity mirrors by multiple

### 3. OPTOMECHANICS

---

wavelengths of the light in some cases. This relatively large displacement, compared to the wavelength of the light and high finesse of the cavity, is problematic in terms of controlling a cavity. However, it is important to note that this type of large dynamic range problem is not dealt with here, or by FINESSE. This type of problem is broadly referred to as *lock acquisition* [80, 81] and can be analysed using non-linear simulation tools such as E2E [82, 83] or SIESTA [17].

What is of interest for my work is the steady state optomechanical effects which are the result of perturbative disturbances to the field. In such cases the interferometer is assumed to be in a well controlled state, thus can be represented in FINESSE. Current and future tasks for commissioning and design will undoubtedly rely on modelling that requires such optomechanical effects to be considered. For example, on the control scheme design of angular alignment instabilities [84, 85], or analysing parametric instabilities; which have already been seen in low power commissioning runs at LIGO LLO [86]. The addition of radiation pressure effects is also key for modelling on future detector design.

*Parametric instabilities* (PIs) [87] are a key topic in this chapter. They are the natural vibrational modes of the mirrors, which once excited, grow exponentially in time. This occurs when positive optomechanical feedbacks are present in the interferometer. Eventually the amplitude of these vibrational modes become large enough that they will cause the interferometer to lose lock.

Two effects are broadly responsible for the susceptibility of current and future generations of detectors to PIs: the increased laser power to reduce shot noise resulting in large radiation pressure forces; and low loss materials used for test masses to reduce thermal noise, resulting in very high quality factor materials, i.e. minimal damping of the mechanical modes. Since 2001 such effects have been measured in various table-top and prototype experiments [88, 89, 90] and recently during low-power commissioning runs of aLIGO [86]. In the latter case a mechanical mode was ringing up to

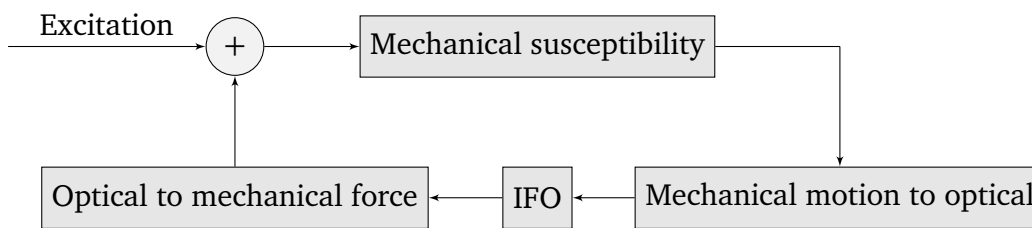


**Figure 3.1:** *Components of radiation pressure:* An overview of the separate elements involved in computing radiation pressure feedback that occurs in the interferometer.

the point where the LLO interferometer’s lock was lost.

As a result of previous theory and experimental evidence of PIs the need for a simulation tool that can model such effects has been apparent. Especially so for potential commissioning issues that may arise in future high-power runs but also for designing future detectors in such a way that may be able to mitigate such problems. An optical configuration is proposed in section 3.2 that demonstrates a setup using optical feedback to reduce the number of unstable PIs. This includes both numerical results and analytic descriptions to describe the setup. Before this the theory of regarding the vibrational modes and radiation pressure effects are outlined in section 3.1.1.

### 3.1 Radiation pressure effects

In this section, the theory involved in computing radiation pressure effects for a suspended mirror including its vibrational modes and any surface distortions present is outlined. The degrees of freedom considered are the longitudinal motion along the surface normal and the individual vibrational modes. Rotational modes can also be considered and have been implemented in FINESSE, the derivations for the pitch and yaw results can be found in appendix C.

Modelling optomechanical effects will be broken down several computational steps as shown in figure 3.1:

- *Mechanical susceptibility*, how the mirror’s modes respond to a particular force

### 3. OPTOMECHANICS

---

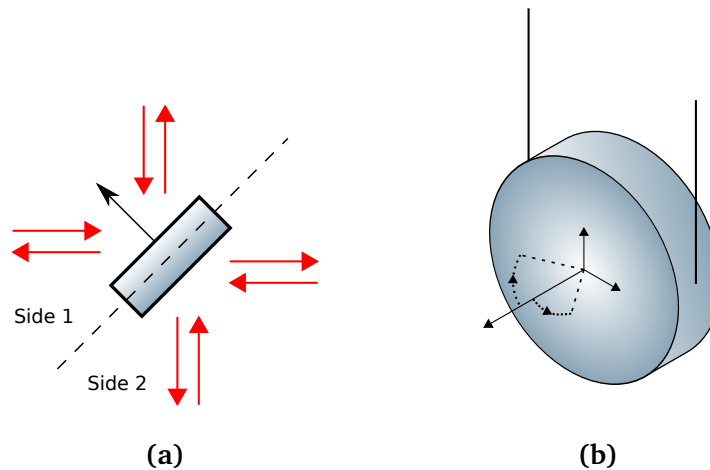


**Figure 3.2:** *Mirror motion degrees of freedom:* The full six degrees of freedom, three rotational and three translational, are not all considered when modelling radiation pressure. Here only the longitudinal motion, normal to the surface and the yaw and pitch motions shown are. In the general case of a mirror at a non-normal incidence there are eight beams that carry momentum into and out of the system.

in section 3.1.1

- *Mechanical motion to optical*, how an arbitrary surface motion of a mirror modulates an incident carrier field in section 3.1.2
- *IFO*, how the scattered optical fields propagate and return to the mirror, as demonstrated in section 3.1.4—although the basis of this is all outlined in chapter 1
- and *Optical to mechanical force*, regarding how the incoming and outgoing optical fields exert a forces on the optic as laid out in section 3.1.3

#### 3.1.1 Mechanics and vibrational modes

The core optics and test masses in a gravitational wave detector are suspended using multi-stage pendulums to reduce ground motion displacing the mirrors. When the interferometer is in a controlled and operational state the magnitude of this motion is very small due to the low resonance frequency of the suspension system. The optics

---

in this case are well approximated as simple harmonic oscillators. The dynamics of a suspended mirror moving along an axis perpendicular ( $\hat{z}$ ) to its surface is:

$$M\ddot{z} = -k_m z - c_m \dot{z} + \Delta F(\tau), \quad (3.1)$$

where the dotted terms are the time derivatives and  $M$  is the mass. The restoring force and damping of the suspension system is then described as a damped spring,  $k_m$  being the spring constant and  $c_m$  the damping coefficient. In Eq.(3.1)  $\Delta F$  is some externally applied force to the test mass, such as radiation pressure, in the direction  $\hat{z}$ . The transient behaviour, assuming no initial velocity or acceleration, can then be computed by taking a Laplace transform of Eq.(3.1):

$$Ms^2 z(s) = -k_m z(s) - c_m s z(s) + \Delta F(s). \quad (3.2)$$

Where  $s = \sigma + i\Omega$ , with  $\sigma$  representing any exponential growth or decay and  $\Omega$  being the angular frequency of an oscillation. The resonant frequency of the suspension is  $\omega_m = \sqrt{k_m/M}$  and the damping coefficient can be reformulated in terms of the damping ratio  $\gamma_m = c_m/(2M\omega_m)$ . The damping of the system can also be stated in terms of the suspension *quality factor*,  $Q_m = 1/(2\gamma_m)$ .

For a given force applied to the test mass the force-to-displacement transfer function is

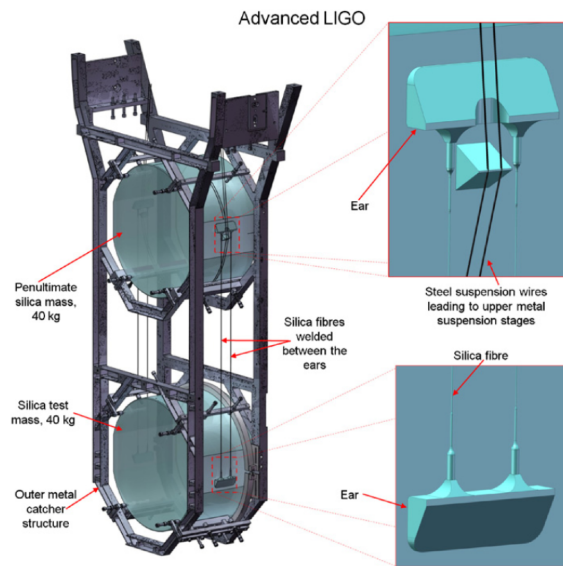
$$H(s) \equiv \frac{z(s)}{\Delta F(s)} = \frac{1}{M(\omega_m^2 + 2\omega_m\gamma_m s + s^2)}. \quad (3.3)$$

The steady-state case is found when  $\sigma = 0$ , thus  $s = i\Omega$ :

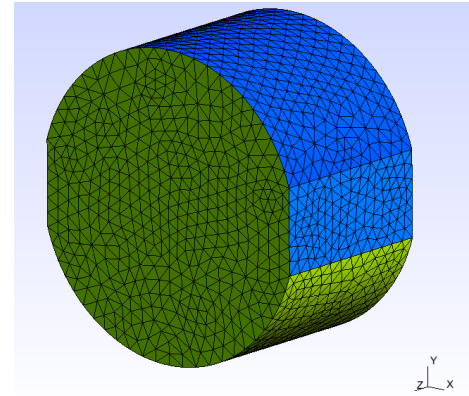
$$H(\Omega) \equiv \frac{z(\Omega)}{\Delta F(\Omega)} = \frac{1}{M(\omega_m^2 + 2i\omega_m\gamma_m\Omega - \Omega^2)}. \quad (3.4)$$

The above is applicable for all degrees of freedom of motion and forces that are described by simple harmonic oscillators.

### 3. OPTOMECHANICS



(a) Illustrative example of the aLIGO suspension stack [32]



(b) Example result from meshing of an aLIGO test mass mirror for use in an FEM model.

**Figure 3.3:** *Suspensions and mirror mesh:* Shown is a picture depicting the aLIGO suspension stack and how the test mass is discretised in an FEM model for processing. In general, the finer the mesh the more accurate the vibrational modes calculated.

#### Vibrational modes

The aim of this section is to outline how to compute the vibrational eigenmodes of the test mass optics. This is a technique typically used in engineering for structural design. To accomplish this the finite-element modelling (FEM) tool COMSOL was used which has specific packages designed for this type of structural study. However, to integrate the data outputted by COMSOL into FINESSE an understanding of what it computes and the values returned is required. Here I shall outline the relevant information and processes needed to do this. The overall steps are: produce a 3D geometry of our object to study; discretise this model into small elements; determine the equations of motion that link these elements together; and finally compute the unforced vibrational modes of the system. These steps are all performed in COMSOL. The final element of the calculation will be to then compute how the vibrational modes are excited due to an external radiation pressure force which will be calculated internally in FINESSE.

---

Parameter	Value
Material	Fused silica
Diameter	35 cm
Depth	20 cm
Mass	40 kg
Poisson ratio	0.17
Young's modulus	73.1 GPa
Density	2203 kg m <sup>-3</sup>

**Table 3.1:** Properties of the aLIGO test mass mirrors used for FEM modelling

Firstly, the geometry of the test masses needs to be constructed and the materials determined for modelling in COMSOL. Using the physical dimensions of the mirror [91] a computer-aided-design tool was used to construct a virtual geometry of the mirror. The mirrors are 20 cm thick with a radius of 35 cm. The sides of the mirror are flattened to provide a surface to bond the suspension to, an illustrative example of which can be seen in figure 3.3a. The final geometry then undergoes a process known as *meshing*, where the 3D object is broken down into a collection of tetrahedrons as shown in figure 3.3b. Each of these tetrahedrons is known as a mass element, where the mass of each is given by its volume times the materials density. The material used for the aLIGO test masses is fused silica. Such a material will be considered as isotropic and at room temperature for our modelling purposes here. The parameters used for the material are listed in table 3.1.

How the test mass responds to both internal and external force is described by the equations of linear elasticity. In normal operating conditions the test masses are not subjected to any stresses that push the material beyond its yield point, thus we always operate in a regime where Hooke's law is applicable. The discrete elements created during the meshing stage can then be modelled as separate masses connected to other nearby masses via *springs*. The spring constant for each of these will be a function of the Young's Modulus and the relative displacements between the mass elements. Such springs also need to take into account the relationship between compression

### 3. OPTOMECHANICS

---

and expansion as given by the Poisson ratio for the material. The calculation of these spring constants is entirely done via COMSOL after the properties given in table 3.1 are inputted.

In general, the resulting equations of motion for each of the mass elements can be written as:

$$\mathbf{M}\ddot{\vec{r}}(\tau) + \mathbf{C}\dot{\vec{r}}(\tau) + \mathbf{K}\vec{r}(\tau) = \vec{F}(\tau). \quad (3.5)$$

Here  $\mathbf{M}$ ,  $\mathbf{C}$  and  $\mathbf{K}$  are the mass, damping and stiffness matrices respectively. The vector  $\vec{r}$  represents the displacement of each mass element and  $\vec{F}$  any forces applied to them in the directions  $\hat{x}$ ,  $\hat{y}$  and  $\hat{z}$ , and  $\ddot{\vec{r}}$  and  $\dot{\vec{r}}$  are the seconds and first derivative in time. The matrices  $\mathbf{M}$ ,  $\mathbf{C}$  and  $\mathbf{K}$  are all symmetric where  $\mathbf{M}$  is also diagonal. To find the vibrational modes the unforced motion of the mass elements is first computed. Each mode is assumed to undergo a harmonic oscillation with some amplitudes  $\psi$  and frequency  $\omega_m$ :

$$\vec{r}(\tau) = \psi e^{i\omega_m t}. \quad (3.6)$$

Substituting this into Eq.(3.5), the unforced equation of motion is

$$\left[ -\omega_m^2 \mathbf{M} + i\omega_m \mathbf{C} + \mathbf{K} \right] \psi e^{i\omega_m t} = 0. \quad (3.7)$$

For non-trivial cases,  $\psi \neq \vec{0}$ , and for any given  $t$ , the new combined matrix must equal zero. This leaves us with solving the characteristic equation of the system to find the eigenvalues:

$$\det \left[ \mathbf{K} - \omega_m^2 \mathbf{M} + i\omega_m \mathbf{C} \right] = 0. \quad (3.8)$$

Solving the Eq.(3.8) is made particularly tricky by the damping terms,  $\mathbf{C}$ , which in general is not a diagonal matrix. It can be assumed at this stage that the damping is weak compared to the inertial and spring constant terms. Thus, this damping should not not affect the eigenvalues much. Assuming a lossless system though will introduce

---

infinities when the mode is driven at its resonance. To stop this the this weak damping can be reintroduced at a later stage by adding any small damping terms into the steady-state equation of motion.

This is an appropriate approximation when the material being described is not lossy. In fact, the reason PIs are problematic in the first place is partly due to producing materials with very low internal losses, for reducing thermal noise; thus this approximation is not an unreasonable one.

With  $\mathbf{C}$  removed from Eq.(3.8) the characteristic equation can be solved. The eigenvalues of this system are given by  $\omega_m^2$ , which are the resonances squared of each mode. The number of eigenvalues that will exist depends on the number of degrees of freedom in our system. In this case it is  $3N_p$  for motions in  $\hat{x}$ ,  $\hat{y}$  and  $\hat{z}$ , where  $N_p$  are the number of mass elements in our mesh.

Using the *mechanical mode frequencies*  $\{\omega_{m,i}\}_{i=1}^{N_p}$  the corresponding *mechanical mode shapes*  $\{\psi_i\}_{i=1}^{N_p}$  are found. The mode shapes are orthogonal over 3D space,  $\langle \psi_i, \psi_j \rangle = D\delta_{ij}$ , where the factor  $D$  depends on the normalisation used. The mode shapes can be organised into the columns of a matrix  $\Psi = [\psi_1, \psi_2, \dots, \psi_{N_p}]$ , which is referred to as the *modal matrix*. This matrix can be thought of as describing the displacement of the mass elements in terms of the mechanical modes rather than in terms of individual elements. Thus we can describe the motion of the optic in this modal basis:

$$\vec{r}(\tau) = \Psi \vec{p}(\tau), \quad (3.9)$$

where  $\vec{p}$  is a vector describing the amplitudes of a particular mode. The equation of motion for each mechanical mode, using Eq.(3.5) (with no damping), is then

$$\mathbf{M}\Psi\ddot{\vec{p}}(\tau) + \mathbf{K}\Psi\vec{p}(\tau) = \vec{F}(\tau). \quad (3.10)$$

Using the orthogonality of the mode shapes, the mass and stiffness matrix can be

### 3. OPTOMECHANICS

---

diagonalised:

$$\Psi^T \mathbf{M} \Psi \ddot{\vec{p}}(\tau) + \Psi^T \mathbf{K} \Psi \vec{p}(\tau) = \Psi^T \vec{F}(\tau), \quad (3.11)$$

where  $\Psi^T \mathbf{M} \Psi \equiv \tilde{\mathbf{M}}$  and  $\Psi^T \mathbf{K} \Psi \equiv \tilde{\mathbf{K}}$  become the diagonalised *modal mass* and *modal stiffness* matrices. This also defines  $\psi_i^T \mathbf{M} \psi_i = \tilde{M}_i$  and  $\psi_i^T \mathbf{K} \psi_i = \tilde{K}_i$  which are the modal mass and stiffness of the  $i^{\text{th}}$  mode, which are just the diagonal elements of the respective modal matrix. The end result of this diagonalisation is that the previously complicated motion of the mirror becomes a set of decoupled equations of motion for the mechanical modes. The motion for the  $i^{\text{th}}$  mode is given by

$$\tilde{M}_i \ddot{\vec{p}}_i(\tau) + \tilde{K}_i \vec{p}_i(\tau) = \langle \psi_i, \vec{F}(\tau) \rangle. \quad (3.12)$$

When using FEM software, such as COMSOL, the outputs from a modal analysis of a structure provides both the mechanical mode shapes and their resonant frequencies. However, there is no unique combination of mode shapes and modal masses, they can be scaled arbitrarily relative to each other [92]. There are several common scalings used in FEM modelling, the most common of which is *modal mass normalisation* which normalises the modal mass to be unitary for each mode. In this case each mode shape is scaled by its modal mass:

$$\hat{\psi}_i \equiv \frac{\psi_i}{\sqrt{\tilde{M}_i}}. \quad (3.13)$$

An example of modes normalised in such a way for an aLIGO like mirror can be seen in figure 3.4. This results in a simplification of the modal masses becoming unity,  $\tilde{M}_i \Rightarrow 1$ , and  $\tilde{K}_i \Rightarrow \tilde{K}_i / \tilde{M}_i = \omega_{m,i}^2$ . The equation of motion is then

$$\ddot{\vec{p}}_i(\tau) + \omega_{m,i}^2 \vec{p}_i(\tau) = \tilde{F}_i(\tau), \quad (3.14)$$

with:

$$\tilde{F}_i(\tau) \equiv \langle \hat{\psi}_i, \vec{F}(\tau) \rangle \quad (3.15)$$

---

defined as the *modal force*. This is an applied force projected onto a particular mode shape. Finally, harmonic forces and motions,  $\tilde{F}_i(\tau) = \tilde{F}_i(\Omega)e^{i\Omega\tau}$  and  $\vec{p}_i(\tau) = \vec{p}_i(\Omega)e^{i\Omega\tau}$ , can be considered in Eq.(3.13):

$$(\omega_{m,i}^2 - \Omega^2)\vec{p}_i(\Omega) = \tilde{F}_i(\Omega). \quad (3.16)$$

Thus for a given modal force the resulting modal motion amplitude is:

$$\vec{p}_i(\Omega) = \frac{\tilde{F}_i(\Omega)}{(\omega_{m,i}^2 - \Omega^2)}. \quad (3.17)$$

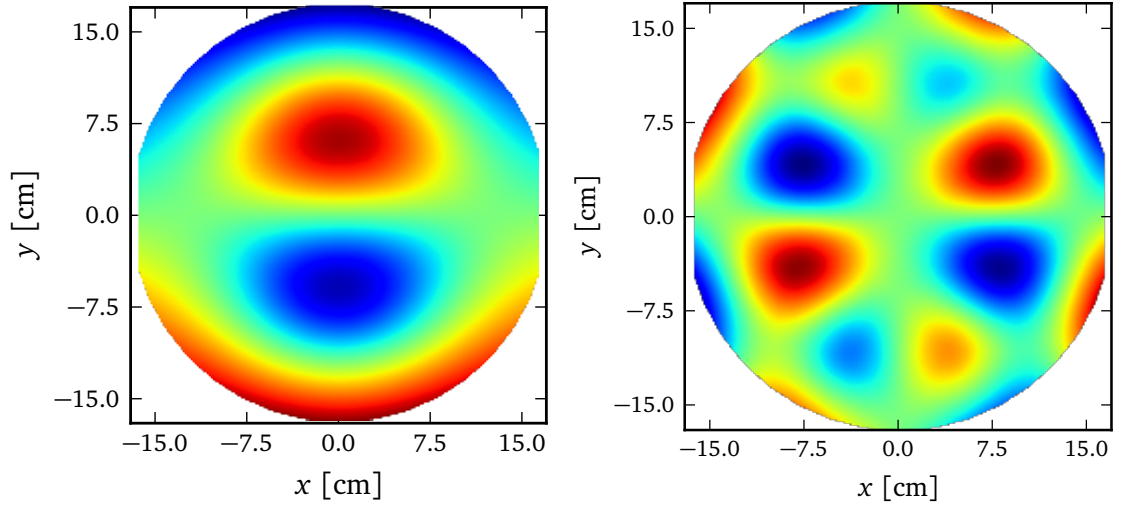
Here we can see the problem with our approximation which removes the damping, forcing at the resonant frequency results in an infinite amplitude.

Structural damping is a complex issue when the systems are particularly lossy [93]. The quality factors for the mechanical modes of the test masses are typically of the order  $Q_m > 10^6$  for fused silica [94]. It is also very high for other materials being considered for future detector upgrades such as silicon with  $Q_m > 10^8$  [94]. In theory this damping should be accounted for in Eq.(3.11) with the term  $\Psi^T \mathbf{C} \Psi$ . It is not necessarily true that  $\Psi$  will diagonalise  $\mathbf{C}$ . With  $\mathbf{C}$  included, Eq.(3.11) does not decouple into a set of separate equations. Including damping would typically introduce cross coupling between various mechanical modes. For this work, it is assumed this is a negligible effect due to the high  $Q_m$  factors. With the weak damping reintroduced, the mechanical susceptibility for the  $i^{\text{th}}$  mechanical mode is

$$H_{s,i}(\Omega) = \frac{\vec{p}_i(\Omega)}{\tilde{F}_i(\Omega)} = \frac{1}{\omega_{m,i}^2 + i \frac{\omega_{m,i}}{Q_{m,i}} - \Omega^2}. \quad (3.18)$$

The lack of any mass term here is because modal mass normalisation is used, which gives a unitary mass values for every mechanical mode.

### 3. OPTOMECHANICS



(a) Mode 37: 15.5 kHz mechanical mode      (b) Mode 140: 28.5 kHz mechanical mode

**Figure 3.4:** Example of the surface displacement for two mechanical mode shapes computed using COMSOL for an aLIGO ETM. Both are modal mass normalised. That shown in 3.4a is thought to have been the cause of recent PIs seen at LLO [86]. The mode number is the index of the mode generated by COMSOL.

In this section I have outlined how the mechanical vibration modes are computed and normalised. This all happens internally within COMSOL, which outputs the mode shapes and resonant frequencies for each mode. However, it must be ensured that the correct modal mass normalisation is used.

#### 3.1.2 Surface motions to optical field couplings

With the mechanical modes of the mirrors understood, the optical scattering that these produce can be derived. The  $i^{\text{th}}$  mechanical mode,  $\hat{\psi}_i(r)$ , describes the harmonic 3D displacement of any given point  $r = \{x, y, z\}$  within the object's volume. As this subsection is only concerned with the scatter from one of the mechanical modes, thus the index  $i$  will be dropped from  $\hat{\psi}_i(r)$  and  $p_i$  for clarity. What must be extracted to compute how the field is scattered is the displacement of the surface from which the beam is reflected from.

The surface motion oscillating at an angular frequency  $\Omega$  is calculated by selecting

---

the component along the incoming beam axis from  $\hat{\psi}$  over the reflecting surface  $S$ :

$$z_s(x, y, \tau) = |p(\Omega)|\hat{\psi}(x, y) \cos(\Omega\tau + \angle p(\Omega)). \quad (3.19)$$

The surface  $S$  is the green front facing surface as seen in figure 3.3b. The surface motion is extracted via a dot product of the mechanical mode in the direction of the beam axis:  $\hat{\psi}(x, y) \equiv \hat{\psi}(r)|_{r=S} \cdot \hat{z}$ . Here  $z_s$  is a 2D surface map that can be used to describe how the phase of the reflected beam will be perturbed by the mechanical mode  $\hat{\psi}(x, y)$ . An example of such surface motion maps can be seen in figure 3.4.

Consider an optical field,  $E_I$ , incident on a mirror with an amplitude reflectivity  $r$ , some static distortion present on its surface,  $z_o$  (given in meters of displacement from a perfect surface), and a surface motion  $z_s$ . The phase of the reflected field,  $E_r$ , will be perturbed by both  $z_o$  and the phase modulated by  $z_s$ :

$$E_r(x, y, \tau) = rE_I(x, y, \tau)e^{i2kz_s(x, y, \tau)}e^{i2kz_o(x, y)}. \quad (3.20)$$

In the case where  $2kz_s(x, y) \ll 1$  the Bessel function expansion (See Eq.(1.51)) can be used to describe this small perturbation with a single pair of sidebands:

$$E_r(x, y, \tau) = rE_I(x, y, \tau)e^{i2kz_o(x, y)} \left[ 1 + ikz_s(x, y, \tau) \left( e^{i\Omega\tau + i\phi_s} + e^{-i\Omega\tau - i\phi_s} \right) \right]. \quad (3.21)$$

### 3. OPTOMECHANICS

---

The TEM<sub>nm</sub> mode of the reflected field is then given by

$$\begin{aligned}
 E_{r, nm}(x, y, \tau) = & r \iint_{-\infty}^{\infty} E_I(x, y, \tau) e^{i2kz_0(x, y)} u_{nm}^*(x, y) dx dy \dots \\
 & + i r k (p(\Omega) e^{i\Omega\tau} + p^*(\Omega) e^{-i\Omega\tau}) \dots \\
 & \iint_{-\infty}^{\infty} E_I(x, y, \tau) e^{i2kz_0(x, y)} \hat{\psi}(x, y) u_{nm}^*(x, y) dx dy,
 \end{aligned} \tag{3.22}$$

$$= E'_{r, nm} + E^+_{r, nm} + E^-_{r, nm}. \tag{3.23}$$

The first integral above,  $E'_{r, nm}$ , is the direct reflection and scattering into HOMs of any incoming carrier or signal field. The other terms,  $E^{\pm}_{r, nm}$ , describe how the incoming field is scattered and modulated into TEM<sub>nm</sub> of the upper and lower signal sidebands as a result of both the surface motion and static surface distortions.

The incoming field will be a mixture of carrier fields and signal sidebands. The incident field is described by HOMs whose amplitudes are  $a_{c, jn'm'}$ , at a frequency  $\omega_j$ :

$$E_I(x, y, \tau) \approx \sum_j \sum_{n', m'} u_{n'm'}(x, y) a_{c, jn'm'} e^{i\omega_j\tau}. \tag{3.24}$$

The resulting TEM<sub>nm</sub> mode of the sidebands are

$$\begin{aligned}
 E_{r, nm}^{\pm} = & i r k A_s^{\pm} \sum_j e^{i(\omega_j \pm \Omega)\tau} \dots \\
 & \left[ \sum_{n', m'} a_{c, jn'm'} \iint_{-\infty}^{\infty} u_{n'm'}(x, y) e^{i2kz_0(x, y)} \hat{\psi}(x, y) u_{nm}^*(x, y) dx dy \right].
 \end{aligned} \tag{3.25}$$

$$= \sum_j a_{s, jnm}^{\pm} e^{i(\omega_j \pm \Omega)\tau} \tag{3.26}$$

Where  $A_s^+ \equiv p(\Omega)$  and  $A_s^- \equiv p^*(\Omega)$ , this is used to simplify the notation regarding the

---

upper sideband using the non-conjugated motion amplitude and vice-versa. Also introduced here is  $a_{s,jnm}^\pm$  which is the upper or lower sideband amplitude for the  $\text{TEM}_{nm}$  mode of the  $j^{\text{th}}$  carrier. The integral above can be separated in two separate coupling coefficient matrices (See section 1.3.3.2):  $\mathbf{K}^o$  being the coupling due to a static distortion and  $\mathbf{K}^s$  the distortion due to the surface motion. The elements of each of the matrices and the final amplitude of each HOM of the sideband,  $a_{s,jnm}^\pm$ , at a frequency  $\omega_j \pm \Omega$  are given by:

$$\mathbf{K}_{nmn'm'}^o = \iint_{-\infty}^{\infty} u_{n'm'}(x, y) e^{i2kz_o(x, y)} u_{nm}^*(x, y) dx dy, \quad (3.27)$$

$$\mathbf{K}_{nmn'm'}^s = \iint_{-\infty}^{\infty} u_{n'm'}(x, y) \hat{\psi}(x, y) u_{nm}^*(x, y) dx dy, \quad (3.28)$$

$$a_{s,jnm}^\pm = i r k A_s^\pm \sum_{n', m'} a_{c, jn'm'} (\mathbf{K}^s \mathbf{K}^o)_{nmn'm'}. \quad (3.29)$$

The challenge now is to find computationally efficient methods for computing the scattering matrix  $\mathbf{K}^s$ . For the lower order motions longitudinal, pitch and yaw (See appendix C for pitch and yaw) analytic solutions can be found to the integrals. However, generic surface motions will rely on numerical integration.

In practice  $\psi(r)$  is calculated at the discrete vertices of the 3D mesh generated by COMSOL. For this the mesh vertices along the high-reflectivity side of the mirror are selected and the component of displacement normal to the surface is taken. The vertices are not typically ordered in a grid or with a sufficient number of samples required to accurately calculate the numerical integral when considering the scattering of high order optical modes. A bilinear interpolator for scattered data points was found to be suitable for generating a finer sampled grid. For many mechanical modes, or cases where the beam parameter changes during a simulation task, it is worth considering using reduced order quadrature (See chapter 2) for accelerating the scattering matrix computation time—as was used in the PI reduction modelling at the end of this

### 3. OPTOMECHANICS

---

chapter.

#### Longitudinal motion

The simplest of the motions to consider is the longitudinal motions, or motion along the surface normal: The shape in which the surface is displaced is then simply  $\hat{\psi}(x, y) = 1$ . Thus solving Eq.(3.28) using the orthogonality of the Hermite polynomials, the resulting coupling coefficients are:

$$\mathbf{K}_{nmn'm'}^s = \delta_{nn'} \delta_{mm'}, \quad (3.30)$$

$$a_{s,jnm}^{\pm} = i r k Z^{\pm} \sum_{n',m'} a_{c,jn'm'} \mathbf{K}_{nmn'm'}^o, \quad (3.31)$$

where, (like  $A_s^{\pm}$ )  $Z^+ \equiv p(\Omega)$  and  $Z^- \equiv p^*(\Omega)$  are introduced for when representing flat longitudinal motions of a surface along the beam axis. This shows that the signal sidebands are just phase modulations of the carrier and have a mode content determined purely by the static surface distortions,  $\mathbf{K}^o$ .

#### 3.1.3 Optical field to surface motion coupling

As described by Maxwell's theory of light, a plane-wave optical field propagating in a vacuum exerts a pressure on over a surface  $A$  proportional to its time averaged Poynting vector [79],  $\langle S(\tau) \rangle$ :

$$F_{rp}(\tau) = \int_A \frac{\langle S(x, y, \tau) \rangle}{c} dA. \quad (3.32)$$

The field consists of  $N_j$  frequencies of light  $\{\omega_j\}_{j=1}^{N_j}$  each of which also has some weak amplitude and phase modulation at a frequency  $\Omega$  described with a pair of sidebands:

$$E(x, y, \tau) = \sum_{j=1}^{N_j} \sum_{n,m}^{n+m \leq 0_{max}} u_{nm}(x, y) (a_{c,jnm} + a_{s,jnm}^+ e^{i\Omega\tau} + a_{s,jnm}^- e^{-i\Omega\tau}) e^{i\omega_j\tau}. \quad (3.33)$$

---

Firstly the radiation pressure force from plane waves will be described, following this how higher order optical modes and mechanical modes will then be described. The time averaged Poynting vector, also the intensity of the beam  $I(x, y, \tau)$ , of such a field points in the direction of propagation and has a magnitude

$$I(x, y, \tau) \equiv \langle S(x, y, \tau) \rangle = |E(x, y, \tau)|^2. \quad (3.34)$$

The intensity will contain the beats of all frequency terms present in the beam. Some of these beats will describe amplitude modulations of the intensity of the light, thus a fluctuating radiation pressure force. What is of interest are the linear steady-state oscillations. This requires making some approximations so that many of the non-linear terms are negligible:

- That DC forces acting on mirror are balanced by control systems acting on the mirror.
- That carrier fields and any modulated sidebands are separated by large frequencies,  $\omega_j \gg \Omega$ . Thus any beating between two carriers or between two different carrier's signal sidebands will be at such a high frequency,  $\approx \omega_j$ , that the mechanical susceptibility, being  $\propto \omega_j^{-2}$ , renders such forces negligible
- There will also be frequency terms oscillating at  $2\Omega$  from the signal sidebands beating with each other; as the magnitude of such sidebands is very small the product between them is also negligible. Thus the only terms remaining are of the carrier beating with its own signal sidebands.

The terms describing the fluctuation in a beam's intensity (that we are concerned

### 3. OPTOMECHANICS

---

with as noted above) is

$$I(x, y, \tau) = \sum_j \sum_{n,m} \sum_{n',m'} (u_{nm}(x, y) u_{n'm'}^*(x, y) a_{s,jnm}^+ a_{c,jn'm'}^* \dots + u_{nm}^*(x, y) u_{n'm'}(x, y) a_{s,jnm}^{-*} a_{c,jn'm'}) e^{i\Omega\tau} + \text{c.c.} \quad (3.35)$$

Integrating over the area in which the beam is incident, the power fluctuations are

$$P(\tau) = \sum_j \sum_{n,m} (a_{s,jnm}^+ a_{c,jnm}^* + a_{s,jnm}^{-*} a_{c,jnm}) e^{i\Omega\tau} + \text{c.c.} \quad (3.36)$$

The above is just for a single beam. The momentum of both the incoming and outgoing fields on both sides of a mirror must be accounted for. The total force on the mirror from the incoming and outgoing beams on both sides of a mirror is

$$F_{\text{rp}}(\tau) = \frac{P_{2i}(\tau) + P_{2o}(\tau) - P_{1i}(\tau) - P_{1o}(\tau)}{c}. \quad (3.37)$$

Here care must be taken with the minus sign convention for the forces. This is decided by which direction the motion is deemed to be *positive* in (See figure 3.2a) <sup>1</sup>.

A subtle point must be mentioned when it comes to computing the power fluctuations with Eq.(3.36). When solving the set of linear coupling equations describing the interferometer only linear operations can be described when using a matrix inversion; the conjugate operation of the lower sideband term is not a linear operation. The process for computing the sidebands describing the carrier perturbations is to firstly compute the carrier fields throughout the interferometer in the static case. Now knowing the amplitude of the carrier at all points in the interferometer, the linear perturbations to it can be described using the upper and lower sidebands. By doing this both  $a_{c,jnm}$  and its conjugate are known values when computing Eq.(3.36).

---

<sup>1</sup>In this work I assume the a positive motion is in the direction of the surface normal on 'side one' of the optic.

---

From 3.36 it at first seems that the four values are required to be solved for  $a_{s,jnm}^{\pm*}$  and  $a_{s,jnm}^{\pm}$ ; in which case would double the number of equations that would need to be solved. However, there is no need to explicitly compute the negative frequency terms in the power fluctuations

$$P(\tau) = P(\Omega)e^{i\Omega\tau} + P(-\Omega)e^{-i\Omega\tau}, \quad (3.38)$$

as  $P(\Omega) = P^*(-\Omega)$ . Thus only

$$P(\Omega) = \sum_j \sum_{n,m} \left( a_{s,jnm}^+ a_{c,jnm}^* + a_{s,jnm}^{-*} a_{c,jnm} \right) \quad (3.39)$$

needs to be explicitly computed. Thus when computing the optical propagation, as laid out in chapter 1, the upper and conjugate of the lower sidebands must be computed.

The frequency spectrum of the radiation pressure force at a frequency  $\Omega$  is then

$$F_{rp}(\Omega) = \frac{2}{c} (-P_{1i}(\Omega) - P_{1o}(\Omega) + P_{2i}(\Omega) + P_{2o}(\Omega)). \quad (3.40)$$

In this model only the positive frequency parts of the optical fields have been considered. As the negative frequency has been ignored, an additional factor of two in Eq.(3.40) is required to correct this.

The final step in translating this force to the resulting steady-state motion requires knowledge of the mechanical susceptibility  $H(\Omega)$  for the longitudinal motion of the mirror, as described in section 3.1.1. For all  $N_F$  longitudinal forces that are acting on a mirror, the oscillatory displacement at a frequency  $\Omega$  is computed with

$$Z_s(\Omega) = H(\Omega) \left[ \sum_n^{N_F} F_{rp,n}(\Omega) + F_{ext}(\Omega) \right]. \quad (3.41)$$

Equation 3.41 is must then be solved simultaneously with the sideband fields Eq.(3.31)

### 3. OPTOMECHANICS

---

as they also depend on  $Z_s$ .

#### Optical field force to surface motions

Once the modal force for a particular mechanical mode is computed using Eq.(3.15), its amplitude is computed with Eq.(3.18). Consider the normal incident beams on a mirror, each beam will exert a force given by Eq.(3.32) over a surface  $S$ . The modal force is then

$$\tilde{F}_i(\Omega) = \langle \hat{\psi}_i, \vec{F}(\Omega) \rangle \quad (3.42)$$

$$= \frac{2}{c} \iiint_V \hat{\psi}_i(r) I(r, \Omega) \delta(r - S) dr. \quad (3.43)$$

Note that the mechanical mode is a displacement in three dimensions, whereas the radiation pressure is only exerted upon the high-reflectivity surface  $S$ , hence the addition of the delta function. This becomes

$$\tilde{F}_i(\Omega) = \frac{2}{c} \iint_S \hat{\psi}_i(x, y) I(x, y, \Omega) dx dy. \quad (3.44)$$

Adding in the intensity fluctuation from Eq.(3.35)

$$\begin{aligned} \tilde{F}_i(\Omega) = \sum_j \sum_{n,m} \sum_{n',m'} \frac{2}{c} \iint_S \hat{\psi}_i(x, y) & (u_{nm}(x, y) u_{n'm'}^*(x, y) a_{s,jnm}^+ a_{c,jn'm'}^* + \dots \\ & u_{nm}^*(x, y) u_{n'm'}(x, y) a_{s,jnm}^- a_{c,jn'm'}) dx dy, \end{aligned} \quad (3.45)$$

the same scattering matrix elements of  $\mathbf{K}^s$  (Eq.(3.28)) for the  $i^{\text{th}}$  mechanical mode can be seen:

$$\tilde{F}_i(\Omega) = \sum_j \sum_{n,m} \sum_{n',m'} \frac{2}{c} (\mathbf{K}_{nmn'm'}^{s_i} a_{s,jnm}^+ a_{c,jn'm'}^* + \mathbf{K}_{nmn'm'}^{s_i*} a_{s,jnm}^- a_{c,jn'm'}). \quad (3.46)$$

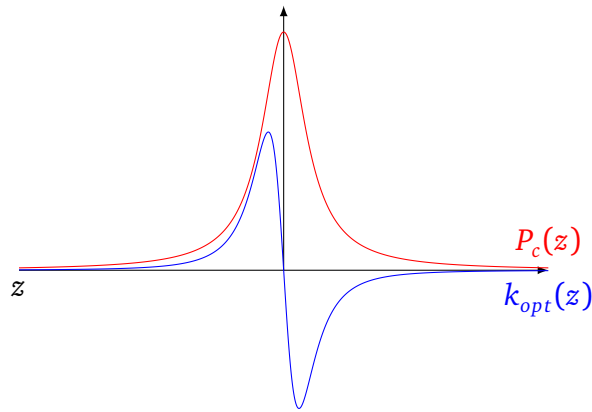


**Figure 3.5:** *Static optical spring:* Illustrative example of the circulating power (red) in a Fabry–Perot cavity. The blue line shows the spring constant (blue). Not to scale.

This final result now allows us to compute how a modulated optical field forces a particular vibrational mode.

### 3.1.4 Optical springs

Now the various components of the radiation pressure effects, as shown back in figure 3.1, they can be combined together to compute the feedback loop. Optical springs are a direct result of this feedback loop. The theory behind optical springs is crucial to understanding the cause of parametric instabilities that are discussed later in this chapter.

Using the optomechanical coupling laid out in the previous sections it will be shown how this feedback process introduces a force that is analogous to a *spring* attached to the mirror. This spring will have a particular resonance frequency and damping coefficient that is determined by the optical and mechanical properties of the interferometer.

Firstly, the simple case of a Fabry–Perot with a single suspended end mirror where the velocity of the suspended mirror is very slow is considered; in this case the optical response to a mirror moving is effectively instantaneous throughout the interferometer. The power circulating in a Fabry–Perot cavity, hence the power incident on the

### 3. OPTOMECHANICS

---

suspended mirror, as a function of a cavity length change  $z$  in meters is:

$$P_c(z) = \frac{P_0 T_1}{1 + R_1 R_2 - 2r_1 r_2 \cos(2kz)}, \quad (3.47)$$

where  $T_1$  and  $R_1$  and the power transmissivity and reflectivity of the input mirror,  $R_2$  the power reflectivity of the end mirror,  $r$  and  $t$  being the relevant amplitude transmissivities and reflectivities of both mirrors,  $2kz$  being the tuning of the cavity length, and  $P_0$  the input light power. This is qualitatively shown in figure 3.5. As the radiation pressure force is  $\propto P_c$  it can be seen that the force will vary with respect to the tuning of the cavity.

A position dependent force is the definition of a spring constant, thus for our optical spring we find

$$k_{opt} = -\frac{dF(z)}{dz} = \frac{d}{dz} \left[ \frac{-2P_c(z)}{c} \right] = \frac{-8P_0 r_1 r_2 k T_1 \sin(2kz)}{c(1 + R_1 R_2 - 2r_1 r_2 \cos(2kz))^2}. \quad (3.48)$$

Plotting the  $k_{opt}$  in figure 3.5 we can see when the cavity is perfectly resonant for the carrier field there is no optical spring, for positive detunings ( $z > 0$ ) a restoring force is found,  $k_{opt} < 0$ , and anti-restoring force,  $k_{opt} > 0$ , with negative detunings,  $z < 0$ .

To compute the full response of a suspended mirror we have to consider the propagation of the sidebands through the optical system. This process of scattering and feedback is represented by the block diagram in figure 3.6. Here we have some force  $F(\Omega)$  acting on a mirror with mechanical susceptibility  $H_s(\Omega)$ . The motion  $z(\Omega)$  combined with the incident carrier field  $a_c$  scatters light into the sidebands  $a_s^\pm$  as described by equation Eq.(3.31). The IFO plant is the optical transfer functions from the port leaving the suspended mirror to the incoming port. Finally, the transformed sidebands,  $a_s'^\pm = \mathbf{G}^\pm(\Omega)a_s^\pm$ , are combined again with the carrier field to compute the radiation pressure force  $F_{rp}(\Omega)$  using Eq.(3.40) which combines with some excitation  $\Delta F(\Omega)$  to feedback into the mirror. For simplicity we'll consider a single carrier with a pair of

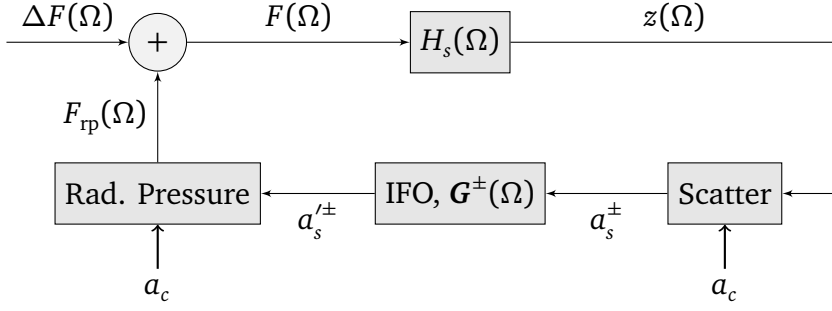


**Figure 3.6:** *Components of radiation pressure, detailed:* A generic view of a closed-loop optomechanical transfer function for a suspended mirror with mechanical susceptibility  $H_\Omega$ . Due to some motion  $z(\Omega)$  of a mirror the light is scattered from the carrier. The IFO plant then describes the optical transfer function of the sidebands propagating through the interferometer and back to the mirror in question. The interference of the propagated fields with the carrier then induces some radiation pressure force which is fed back into the mirror. Here  $a_c$  is the carrier fields at the mirror in question.

sidebands describing a modulation at a frequency  $\Omega$  incident on a suspended mirror with reflectivity  $r$ . The incident optical field and the that reflected, given by Eq.(3.31), assuming  $r^2 \approx 1$  are:

$$a_s'^{\pm} = G^{\pm}(\Omega)a_s^{\pm}, \quad (3.49)$$

$$a_s^{\pm} = a_s'^{\pm} + ikZ^{\pm}a_c. \quad (3.50)$$

The circular dependence on the field can be removed here to find

$$a_s'^{\pm} = \frac{irkG^{\pm}Z^{\pm}a_c}{1 - rG^{\pm}}. \quad (3.51)$$

The radiation pressure force at the frequency  $\Omega$  is given by Eq.(3.40)

$$F_{\text{rp}}(\Omega) = \frac{2}{c} [a_s^+ a_c^* + a_s^{-*} a_c + a_s'^+ a_c^* + a_s'^{-*} a_c] \quad (3.52)$$

$$= \frac{4}{c} [a_s'^+ a_c^* + a_s'^{-*} a_c]. \quad (3.53)$$

Here, only force from the intracavity fields are considered; the beam transmitted

### 3. OPTOMECHANICS

---

through the mirror could also be taken into account, as  $R_2 \approx 1$ . However, the transmitted power is small for a high reflectivity mirror thus contributes little to the force. Substituting the sideband fields into the force we find

$$F_{\text{rp}}(\Omega) = \frac{4i r k P_c}{c} \left[ \frac{G^+ - G^{-*}}{1 - rG^+ - rG^{-*} + RG^+G^{-*}} \right] z, \quad (3.54)$$

$$= \kappa(\Omega)z. \quad (3.55)$$

This shows the radiation pressure force is linearly dependent on  $z$  for an arbitrary interferometer layout described with  $G^\pm$ . The complex valued scaling factor,  $\kappa(\Omega)$ , represents how the dynamics of the suspended mirror is altered. Those terms independent of  $\Omega$  define the stiffness of the optical spring. Terms  $\propto \Omega$  describe any damping, with  $c_{\text{opt}}$  being the optical damping coefficient:

$$\kappa(\Omega) = k_{\text{opt}} + i\Omega c_{\text{opt}}(\Omega) + \mathcal{O}(\Omega^2). \quad (3.56)$$

Depending on the optical feedback, higher order terms in  $\Omega$  can also appear here that can also alter the inertial behaviour terms  $\propto \Omega^2$ .

The above is applicable for a single optical field. In the case of multiple optical fields the sum of the multiple radiation pressure forces must be considered to compute the overall  $\kappa$  value. The result Eq.(3.54) is only applicable when fields are incident on a single side of a high reflectivity mirror. As can be imagined this is particularly time consuming analytically for more detailed cases like a 50:50 suspended beamsplitter, multiple suspended optics, or multiple carrier frequencies with HOMs; hence the desire to be able efficiently model such features using simulation tools.

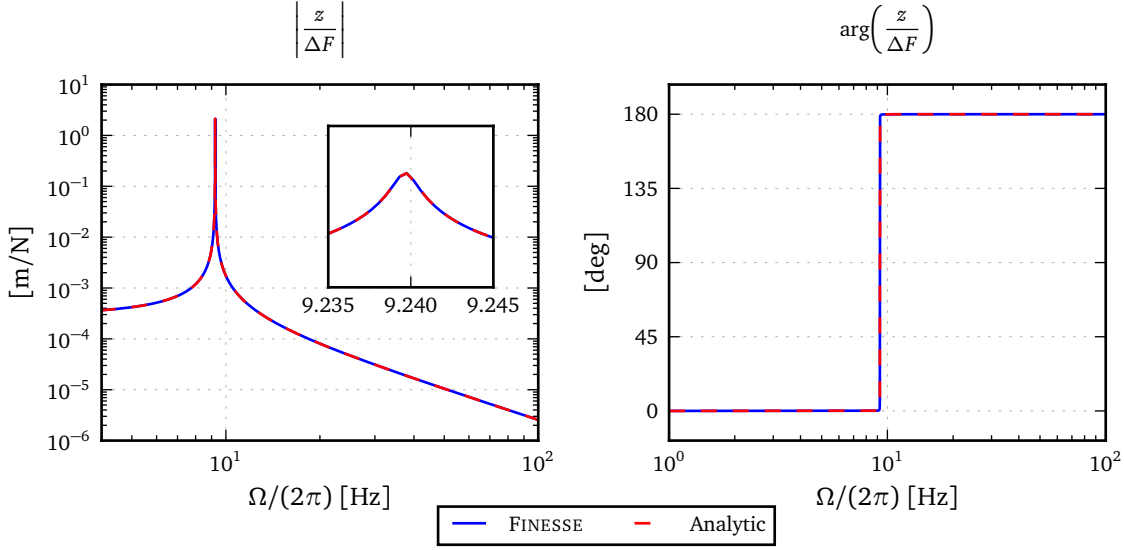


**Figure 3.7:** *Optical spring resonance:* Analytic v.s. numeric (FINESSE) comparison of an optical spring. This is for a fixed input and suspended (free-mass) end mirror. A force is applied to the end mirror and shown is the force-to-displacement of the end mirror transfer function. Inset plot shows zoomed region around the peak which shows a good agreement with the peak shape and position.

### Frequency dependent optical spring in a cavity

Computing the optical spring constant for a suspended cavity is just a case of determining the transfer functions  $G^\pm$ . The optical transfer function describes the propagation of the light reflected from the suspended end mirror, along the cavity length, reflected from the input mirror and back to the field incident upon the end mirror again:

$$G^\pm(\Omega) = r_1 e^{-i2\frac{\Omega}{c}L} e^{i2\phi}. \quad (3.57)$$

Here  $\phi = kz$  is some detuning of the input mirror position. Substituting this into Eq.(3.54)

$$\frac{G^+ - G^{-*}}{1 - r_2 G^+ - r_2 G^{-*} + R_2 G^+ G^{-*}} = \frac{i2r_1 e^{-i2\frac{\Omega}{c}L} \sin(2\phi)}{1 + R_1 R_2 e^{-i4\frac{\Omega}{c}L} - 2r_2 r_1 e^{-i2\frac{\Omega}{c}L} \cos(2\phi)} \quad (3.58)$$

### 3. OPTOMECHANICS

---

the optical spring constant is found:

$$\kappa(\Omega) = -\frac{8kP_c r_1 r_2 \sin(2\phi)}{c} \frac{e^{-i2\frac{\Omega}{c}L}}{1 + R_1 R_2 e^{-i4\frac{\Omega}{c}L} - 2r_2 r_1 e^{-i2\frac{\Omega}{c}L} \cos(2\phi)}. \quad (3.59)$$

When the cavity is on resonance,  $\phi = 0$ , we see no optical spring, likewise when there is no power. Likewise, in the DC limit  $\Omega \rightarrow 0$  an agreement is found with Eq.(3.47). Shown in figure 3.7 is an example of an optical spring force-to-displacement transfer function of the suspended end mirror when a force is applied. It can also be seen in Eq.(3.59) that imaginary component of  $\kappa$ , or optical damping, depends on the propagation delay around the cavity.

#### 3.1.5 The parametric gain: the measure of instability

Consider a mechanical mode of a mirror in some arbitrary interferometer, where the optical field scattered by this mode produces an optical spring. The optical spring differs slightly from Eq.(3.55) in that the scattering and force relations used are the modal ones, Eq.(3.28) and Eq.(3.46). The equation of motion for the mode including the optical feedback is

$$-\tilde{M}\Omega^2 p = -[\kappa_m(\Omega) - \kappa_{\text{opt}}(\Omega)]p + \Delta\tilde{F}(\Omega), \quad (3.60)$$

where the mechanical and optical spring terms are:

$$\kappa_m(\Omega) = k_m + i\Omega c_m, \quad (3.61)$$

$$\kappa_{\text{opt}}(\Omega) = k_{\text{opt}} + i\Omega c_{\text{opt}}(\Omega). \quad (3.62)$$

The combined response of the mode to both the optical and mechanical features is  $\kappa_T = \kappa_m - \kappa_{\text{opt}}$ . This shifts the resonance frequency of the mode and alters the

---

damping ratio from the mechanical values:

$$\omega_T(\Omega) = \sqrt{\frac{k_m - k_{\text{opt}}(\Omega)}{\tilde{M}}}, \quad (3.63)$$

$$\omega_T \gamma_T(\Omega) = \omega_m \gamma_m - \omega_{\text{opt}}(\Omega) \gamma_{\text{opt}}(\Omega), \quad (3.64)$$

where  $\omega_{\text{opt}}(\Omega) = \sqrt{k_{\text{opt}}(\Omega)/M}$ . The various forms of damped harmonic oscillator are applicable here: when  $\gamma_T > 1$  the system is overdamped,  $\gamma_T = 1$  it is critically damped and  $\gamma_T < 1$  it is underdamped. In the case where  $\gamma_T < 0$  an initial oscillation grows exponentially, thus the system is classed as unstable, or a parametric instability. To parameterise this instability the *parametric gain*,  $\mathbb{R}$ , is used [87]:

$$\mathbb{R}(\Omega) \equiv \frac{\omega_{\text{opt}}(\Omega) \gamma_{\text{opt}}(\Omega)}{\omega_m \gamma_m} \quad (3.65)$$

$$\gamma_T(\Omega) = \frac{\omega_m}{\omega_T} \gamma_m (1 - \mathbb{R}(\Omega)). \quad (3.66)$$

When  $\mathbb{R} > 1$  the optomechanical coupling is unstable. Thus any small excitation of a mode—be it from thermal, mechanical or optical—will grow overtime until the mode’s amplitude is large enough to break the interferometer’s lock.

### Extracting the parametric gain from transfer functions

Numerical tools such as FINESSE never explicitly calculate the optical spring constant  $\kappa_{\text{opt}}$ , thus cannot simply output  $\mathbb{R}$ . However, they are an ideal tool for computing transfer functions in which  $\kappa_{\text{opt}}$  and  $\mathbb{R}$  appear and can be extracted from. A general method for computing the parametric gain of a mode is outlined in [95]. Their method relies on computing numerous optical transfer functions for each HOM field for the upper and lower sideband. Such transfer functions could be extracted from the inverted interferometer matrix but it would require a sparse solving of the interferometer matrix for each HOM field in both the upper and lower sidebands. A more efficient method

### 3. OPTOMECHANICS

---

is outlined here which involves a single solution of the sparse matrix.

Using Eq.(3.60) we can compute transfer function:

$$\frac{p(\Omega)}{\Delta\tilde{F}(\Omega)} = \frac{1}{\kappa_T(\Omega) - \tilde{M}\Omega^2} \quad (3.67)$$

$$= \frac{1}{\tilde{M}(\omega_T(\Omega)^2 + i2\Omega\omega_T(\Omega)\gamma_T(\Omega) - \Omega^2)} \quad (3.68)$$

If a modal force is applied that produces a unit modal amplitude, for example  $\Delta\tilde{F} = \Delta p(\Omega)/H_s(\Omega)$ :

$$\frac{p(\Omega)}{\Delta p(\Omega)} = \frac{\omega_m^2 - \Omega^2 + i2\Omega\gamma_m\omega_m}{\omega_T(\Omega)^2 + i2\Omega\omega_T(\Omega)\gamma_T(\Omega) - \Omega^2} \quad (3.69)$$

Inverting and computing the transfer function at  $\Omega = \omega_m$ :

$$\frac{\Delta p(\omega_m)}{p(\omega_m)} = \frac{\omega_T(\omega_m)^2 - \omega_m^2 + i2\omega_m\omega_T(\omega_m)\gamma_T(\omega_m)}{i2\gamma_m\omega_m^2} \quad (3.70)$$

Separating the real and imaginary parts and rearranging with Eq.(3.63) and Eq.(3.64):

$$\frac{\Delta p(\omega_m)}{p(\omega_m)} = 1 - \mathbb{R}(\omega_m) + i\frac{k_{\text{opt}}}{2\tilde{M}\gamma_m\omega_m^2}. \quad (3.71)$$

The transfer function  $\frac{p(\Omega)}{\Delta p(\Omega)}$  is a diagonal element in the inverted interferometer matrix thus is easily extracted in a single sparse matrix solution at the mechanical frequency  $\omega_m$ . Using Eq.(3.71),  $\mathbb{R}$  can be efficiently extracted via the real part of the transfer function. This process is encapsulated in the FINESSE parametric gain detector `pga.ind`. This can also form the basis of a detector which can output  $k_{\text{opt}}$  produced from the feedback of all optical modes if required.

The parametric instability code in FINESSE was validated against analytic calculations (which demonstrated good agreement bar some small numerical differences) but also compared to the experimental results collected by Thomas Corbitt [89]. This

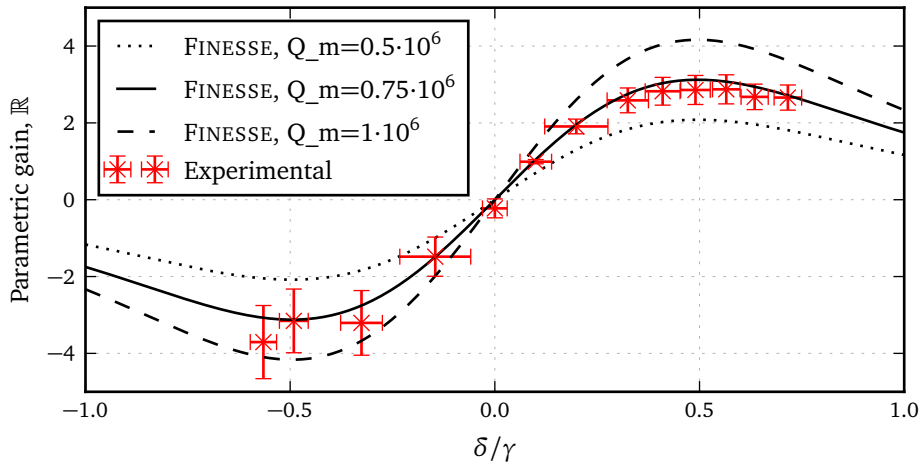


**Figure 3.8:** Corbitt's experimental PI comparison: Using data on the parametric instability experiment conducted by Corbitt [89] a FINESSE model was constructed. The value  $\delta/\gamma$  is the detuning in units of the cavity linewidth. A mechanical drum head mode at 28.188kHz is present in the mirrors used, determined by their own FEM modelling. The data was extracted from figure 3 in the paper using a plot digitiser. Using the modal mass and optical parameters provided in the work a reasonable fit of the data can be seen for the range of Q values that were expected for the drum head mode [96].

is one a few experiments aimed at measuring PI and radiation pressure effects. The mechanical mode of interest in the experiment was the 28.188 kHz mechanical drum-head mode of the mirror. This however can be approximated as just the longitudinal motion of the mirror in our model as no strong optical scattering into modes higher than  $TEM_{00}$  occurs. A simple FINESSE file was constructed for this experiment where  $\mathbb{R}$  is measured at various detunings of the cavity:

### Code 3.1 FINESSE code to replicate Corbitt's experiment

```

const PIfreq 28.188k
const mass 0.25
const Qm 1.5      M

1 11 3 0 n1
m1 Min 0.00631994 0 0 n1 n2
s cav1 1 n2 n3
m1 Mend 0 0 0 n3 dump

```

### 3. OPTOMECHANICS

---

```
# Page 98 in Corbitt's thesis mentions  $g \sim 0.8$   $R_c \sim 0.5$  m
attr Min Rc -0.5125
attr Mend Rc 0.5125

# Add in masses and mechanical resonance of PI
tf susp 1 0 p $PIfreq $Qm
attr Mend m $mass zmech susp

cav c1 Min n2 Mend n3

maxtem 0 # Include up to order 0 optical modes

# Switch on the signal frequency calculations to compute
# parametric gain
fsig force $PIfreq

# Detect gain of longitudinal motion of mirror
pgaind Rz Mend z

xaxis Mend phi lin -0.09 0.09 1000
```

---

Exact details were not provided for all the parameters required, however most were inferred from information in the paper and thesis [97]. Figure 3.8 shows the experimental results overlaying the FINESSE output. The measured mechanical mode quality factor is not explicitly stated in the paper or thesis, a value of  $Q_m = 0.5 - 1 \cdot 10^6$  [96] though provided the fit depicted, which is not an unreasonable value.

#### 3.1.6 Conditions for instability

As shown in Eq.(3.66) the optomechanical coupling of a mode becomes unstable if the system becomes anti-damped,  $\mathbb{R} > 1$ . Although this provides a convenient metric to determine whether the mode is or is not stable it does not offer a clear physical picture of the processes involved. A useful picture though is that of *Stokes and anti-Stokes scattering* as originally used to describe PIs in [87]. This describes the optical

---

scattering as the interaction of the photons in the carrier modes and the phonons of the mechanical mode. The upper and lower sidebands are created when the photons in the carrier field,  $\omega_0$ , interact with the phonons in the mechanical mode,  $\omega_m$ . The energy of the photons in the upper and lower sidebands of the carrier are  $\hbar(\omega_0 \pm \omega_m)$ . The lower sideband photon has less energy than the carrier, thus to conserve energy when one is created, a phonon must be too (this is known as the Stokes mode). When a carrier photon and phonon are combined an upper sideband photon is created (the anti-Stokes mode). When a lower sideband is produced energy is moved from the carrier field into the mechanical mode. The opposite occurs when the upper sideband is created; this is commonly referred to as optical cooling as energy is extracted from the mechanical system. The likelihood of these scattering processes occurring depends on whether the optical system can support scattered optical spatial and frequency modes. If the photons of the lower sideband are resonant in the optical system the mechanical mode is continuously pumped with energy from the carrier, greatly exciting the mode and creating an instability.

These scattering processes are depicted in figure 3.9. The figure shows a contrived setup for illustrating the point. Here a carrier field consisting of mostly  $TEM_{00}$  is resonant in a cavity. There are then two mechanical modes present: one with a mechanical frequency  $\omega_{m_1}$  which scatters  $TEM_{00}$  into  $TEM_{nm}$ , and the another with frequency  $\omega_{m_2}$  scattering  $TEM_{00}$  into  $TEM_{uv}$ . In this scenario, and as depicted in figure 3.9, the lower sideband created with frequency  $\omega_{m_1}$  coincides with the mode separation frequency of spatial mode  $TEM_{nm}$  with which it primarily scatters into. The lower sideband satisfies both the spatial and frequency constraints and is resonant. In this case the  $\omega_{m_1}$  could become unstable. Whether it does or not depends on the optical gain of from the feedback. Note that the upper sideband for this mode is just off resonance, thus a small amount of energy will be extracted from the mode, but not likely enough to counteract the lower sideband. For the other mode we see the spatial and frequency

### 3. OPTOMECHANICS

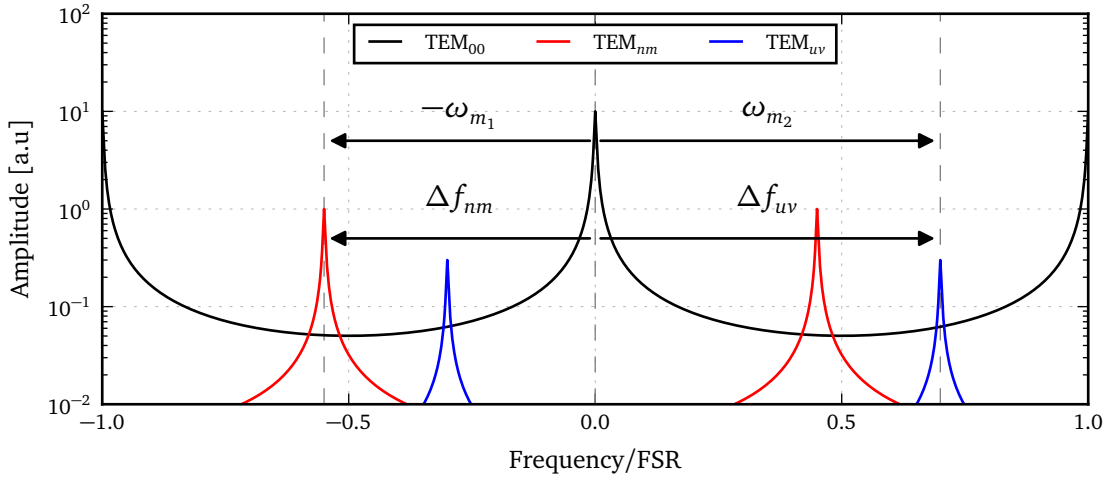


**Figure 3.9:** *Conditions for parametric instabilities:* Depending on the cavity geometry a pair of sidebands are created at a frequency  $\Omega$  can overlap in frequency with a HOM mode separation frequency  $\Delta f$ . If the mechanical mode scatters the pump light into a HOM that overlaps in frequency the optical gain can be large. The three modes shown are: the  $TEM_{00}$  pump field (black),  $TEM_{nm}$  a mode with separation frequency matching the lower sideband (red) and  $TEM_{uv}$  a mode matching the upper sideband. The  $TEM_{nm}$  case would be anti-stokes mode and the  $TEM_{uv}$  a stokes.

modes of upper sideband happens to be resonant, thus in this case the second mode is likely to be significantly damped.

The conditions required for an instability to arise relies heavily on the coincidence of the mechanical and optical properties of the system. Consider the aLIGO arm cavities with  $FSR \approx 37.5\text{kHz}$ ; the resonance frequencies of the mechanical modes span a large range of frequencies covering multiple FSRs as seen in [95]. They considered modes in the range 10–90 kHz of which there were approximately 200 found using FEM modelling. For various potential cavity configurations, such as a change in mode-matching or mirror curvature, they found  $\langle \mathbb{R} \rangle \approx 6$  and the 99% of cases having six or less unstable modes per mirror including up to order 9 HOMs. Thus PIs are expected to be a common occurrence when running at high power. The combination of many mechanical modes, a small FSR and a large parameter space of optical parameters results in a higher chance of PIs occurring. The uncertainty in both the FEM models and our knowledge of the actual experimental parameters means it is not possible to

---

model exactly what modes would be problematic. However, as started in [95], a more statistical outlook should be taken to estimate whether a particular interferometer setup is likely or not to suffer from PIs [98].

## 3.2 Optical suppression of parametric instabilities

Thus far, modelling of parametric instabilities has been on searching for problematic parameter spaces for aLIGO [99, 98, 100] for dual recycled interferometer. This process has also begun for the Einstein Telescope [101, 102]. Potential mitigation of PIs has also been theoretically and experimentally tested [103, 104]. These have predominantly involved using mechanical methods to suppress unstable modes such as modulating the mirror mass using the thermal control system or applying dampeners to the optics to change the resonant modes. Another technique applied in other fields is that of optical cooling. This is achieved by pumping energy from the mechanical mode into the optical field by making the upper sideband resonant within the system. However, for the aLIGO arm cavities the resonances of the mechanical modes are much higher than the cavity linewidth ( $\approx 80$  Hz). Thus to cool the mode by making the upper sideband resonant would require detuning the arm cavity. This would unacceptably reduce the sensitivity of the detector to gravitational waves and disturb it whilst running in science mode. Thus such optical cooling cannot be applied in our case.

However, little research has been conducted on controlling the PIs using purely optical means. Suggestions have been made that specific optical HOMs could be shone on to mirrors to dampening specific modes, which would rely on determining the unstable mode shape quickly and then injecting a suitable enough power level of the HOM to dampen the mode. The question that I will answer here is whether it is possible to design an optical system where some control over the optical transfer functions

### 3. OPTOMECHANICS

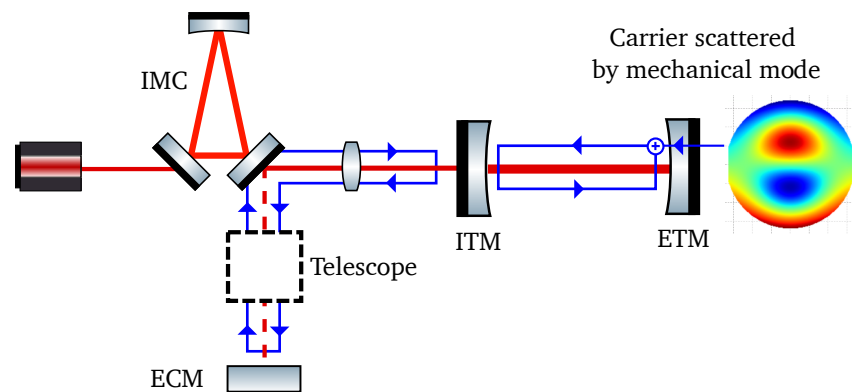


**Figure 3.10:** *Simple extraction cavity:* The basic components required to extract HOMs from a cavity. This involves a mode cleaner to separate the  $TEM_{00}$  of the carrier field that will be resonant in the arm cavity and any HOM that are generated from PIs. An extraction cavity is then formed with the reflection from the mode cleaner.

of the scattered fields can be exerted to reduce the parametric gain. Answering such questions previously would have proven difficult as the necessary features of optical scattering, radiation pressure effects and optical transfer calculations for generic systems did not exist in a complete and tested simulation tool. The work I have accomplished in FINESSE however now makes such studies possible. This section will focus on exploring the idea of using two extra recycling mirrors for the HOMs reflected from the IMC and OMC mirrors, as depicted in figure 3.23. The central idea is that the resonance condition of the HOMs can be tuned in such a way to stop parametric instabilities building up.

In this section I outline a simplified analytic description of the coupled cavity system design and the general effects that arise. Next, I demonstrate that such a scheme does in fact provide broadband reduction in the number of unstable PI.

#### 3.2.1 Extraction cavities

The central idea that will be explored here for the suppression of parametric instabilities is shown in figure 3.10. Here a coupled cavity arrangement is considered to determine if such a configuration offers any potential for PI reduction in the arm cav-

Coupling	Order	$ k_{nm,00} $
Mode 37		
00 $\Rightarrow$ 01	1	0.15258
00 $\Rightarrow$ 03	3	0.0433365
00 $\Rightarrow$ 21	3	0.0248251
00 $\Rightarrow$ 00	0	0.00386493
00 $\Rightarrow$ 02	2	0.00116233
00 $\Rightarrow$ 20	2	0.0010133
Mode 140		
00 $\Rightarrow$ 11	2	0.0838964
00 $\Rightarrow$ 13	4	0.0548791
00 $\Rightarrow$ 10	1	0.00481582
00 $\Rightarrow$ 30	3	0.00245064
00 $\Rightarrow$ 12	3	0.00152063
00 $\Rightarrow$ 31	4	0.00103885

**Table 3.2:** The largest coupling coefficient terms ( $|k_{nm,00}| > 10^{-3}$ ) for scattering of  $\text{TEM}_{00}$  into HOM from the mechanical mode 37 and 140 (See figure 3.4).

ities. It consists of three cavities: the arm cavity which is kept on resonance for the  $\text{TEM}_{00}$  mode; an impedance matched input mode cleaner (IMC) tuned to filter the incoming beam for the  $\text{TEM}_{00}$ ; and the extraction cavity, which is formed between the input mirror of the arm and the extraction cavity mirror (ECM). The key aspect here is that the extraction cavity forms a compound mirror for any fields that are not transmitted through the IMC. When the IMC is tuned to transmit only the  $\text{TEM}_{00}$  of the main carrier field, all of its higher order modes will be reflected. The extraction cavity can then be designed to reduce the optical resonance condition for these fields so that parametric gains can be reduced.

As discussed in the previous sections, a mechanical mode is excited in a mirror when the spatial distribution of the radiation pressure exerted on the mirror surface overlaps well with its shape. Such mechanical modes vary a great deal in shape; like those shown in figure 3.4. The six largest spatial overlaps with optical modes up to order four are shown in table 3.2. Here, it can be seen how much each optical mode

### 3. OPTOMECHANICS

---

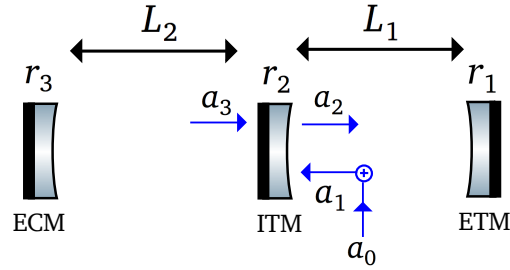


**Figure 3.11:** *Coupled cavity fields:* To compute how a field injected into a coupled cavity system resonates the shown fields need to be considered. Here  $a_0$  is some mode created in the cavity. The field incident on the ITM  $a_1$  is reflected into  $a_2$  as usual. However, in this case the field also circulates in the extraction cavity  $a_3$  which then transmits back through to the arm cavity.

contributes to the excitation of these two mechanical modes, thus lists which modes would need to be suppressed.

Other mechanical modes will have different unique combinations of modes. In reality the mechanical mode shapes are not exactly known and will depend on numerous experimental factors, such as the temperature of the mirror and differences in construction. Thus which mechanical modes will actually become unstable is not known exactly.

For optical suppression to be of much use, an optical layout that suppresses all the higher order modes must be found. Suppressing a single optical mode shape will not suffice, as another mode may also become unstable due to a different set of modes. There is also the issue that the resonant frequencies of the mechanical modes are fairly well distributed in frequency above  $\approx 10$  kHz. If a particular mode  $TEM_{nm}$  happens to overlap well with a mechanical mode at both 20 kHz and 50 kHz, a setup must be constructed to suppress the fields at both frequencies. This is a particularly important criteria as the FSR of future generation interferometers are of the same order of frequencies as the mechanical modes: 37.5 kHz for LIGO and 15 kHz for ET.

---

## Extraction cavity design

Firstly, it will be analysed how an optical mode resonates in a simplified coupled cavity system. In particular an understanding of how any  $\text{TEM}_{nm}$  mode of the lower sideband resonates, as this results in energy being pumped from the main carrier field into the mechanical mode. To compute the intracavity field in the arm the extraction cavity is treated as a compound mirror. The analytic model considered here is shown in figure 3.11. This simplified model assumes the mode cleaner used to separate the higher order modes from the main  $\text{TEM}_{00}$  of the carrier is operating perfectly, thus can be ignored in the analytics. The intracavity field in the extraction cavity is given by

$$a_3 = a_1 \frac{i t_2 r_3}{1 - r_2 r_3 G_2}. \quad (3.72)$$

Here  $G_2$  is the propagator for the scattered field around the extraction cavity being considered. For a higher order mode this will be

$$G_2 = \exp\left(i \left[ \frac{2\Omega L_2}{c} + (n+m)\Psi_{\text{rt},2} + 2\phi \right]\right). \quad (3.73)$$

Here  $\Psi_{\text{rt},2}$  is the round-trip Gouy phase and  $\phi$  is any tuning of the extraction cavity mirror: setting  $\phi = 0$  here ensures that the  $\text{TEM}_{00}$  is resonant. The extraction cavity then alters the reflectivity of the input mirror from the point of view of a field incident from the arm cavity:

$$a_2 = r_2 a_1 + i t_2 a_3, \quad (3.74)$$

$$\frac{a_2}{a_1} = r_2 - \frac{T_2 r_3 G_2}{1 - r_2 r_3 G_2} = \frac{r_2 - r_3 G_2 (R_2 + T_2)}{1 - r_2 r_3 G_2}, \quad (3.75)$$

### 3. OPTOMECHANICS

---

which is assuming the mirrors are lossless  $R_2 + T_2 = 1$ . Given some initial excitation of the mode of interest in the arm cavity,  $a_0$ , the cavity field is then

$$a_1 = \frac{a_0}{1 - r_1 G_1 \left( \frac{r_2 - r_3 G_2}{1 - r_2 r_3 G_2} \right)}. \quad (3.76)$$

Here  $G_1$  is the propagator for the field around the arm cavity. Eq.(3.76) describes how a mode created in the arm cavity resonates within it. The power in this field is

$$|a_1|^2 = \frac{|a_0|^2 |1 - r_2 r_3 G_2|^2}{|1 - r_2 r_3 G_2|^2 + R_1 |r_2 - r_3 G_2|^2 - 2r_1 \operatorname{Re} \{ G_1 (r_2 - r_3 G_2) (1 - r_2 r_3 G_2^*) \}}. \quad (3.77)$$

Note that the relative phase, thus where in the cavity it was created, of the mode does not factor into the resonance condition. The actual magnitude of  $a_0$  will be determined by the scattering matrix for a particular mechanical mode, this merely complicates the equations with no benefit at this stage. It is also assumed that the end mirror is perfectly reflective,  $R_1 \approx 1$ ; as is the case for arms cavities in the gravitational wave detectors.

#### Extraction cavity length

Expanding Eq.(3.77), the circulating power for an excited mode in the arm cavity is

$$|a_1|^2 = |a_0|^2 \frac{1 + R_2 R_3 - 2r_2 r_3 \cos(\angle G_2)}{(R_2 + 1)(R_3 + 1) - 4r_2 r_3 \cos(\angle G_2) - 2r_2(1 + R_3) \cos(\angle G_1) \dots + 2r_3 [\cos(\angle G_1 + \angle G_2) + R_2 \cos(\angle G_1 - \angle G_2)]}. \quad (3.78)$$

$$= |a_0|^2 \frac{S}{D}, \quad (3.79)$$

where  $S$  is the suppression factor and  $D$  the denominator of the above expression. Here  $D$  describes how the mode will resonate in the coupled cavity system. How the resonances behave is analysed later in this section. Ideally for every resonance of the mode as determined by  $D$  there should be an equivalent minimum in  $S$  to suppress it.

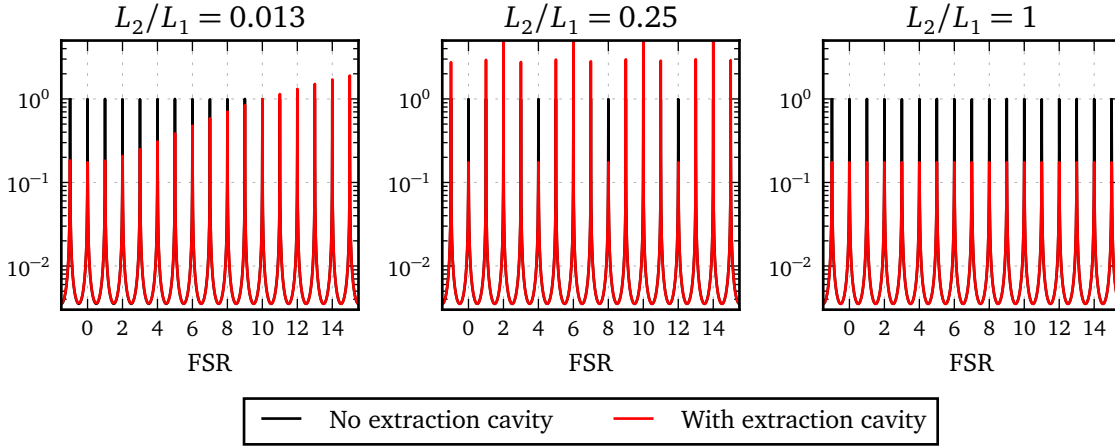


**Figure 3.12:** *Long vs short extraction cavity suppression:* Using Eq.(3.78) the effect of the extraction cavity on the resonance of an optical field in the arm cavity can be seen. This is shown for different extraction cavity lengths. For equal lengths the resonance of the field is suppressed for multiple FSRs, the ideal scenario. For shorter lengths the resonance condition of the extraction suppresses some FSRs but for others increases it. The next preferable case is where the extraction cavity is very short compared to the arm cavity length. In this case the length can be chosen to suppress up to the 10<sup>th</sup> FSR, using a length ratio determined with Eq.(3.82).

Here  $S$  depends purely on the resonant condition of the mode within the extraction cavity; which is minimised when the mode is resonantly enhanced,  $\angle G_2 = 2N\pi$ . By exploring the parameter space of various cavity length ratios,  $L_2/L_1$ , two scenarios were found to be promising: an extraction cavity whose length is some positive and non-zero integer of the arm length,  $L_1 = L_2$ ; and an extraction cavity length which is much less than the arms,  $L_2 \ll L_1$ .

Using an integer ratio of cavity lengths allows the setup to suppress the resonance of a mode at each of its FSRs, as shown in figure 3.12. This is because the FSR of both the arm and extraction cavity are the same. From a practical perspective, as the arm cavity's lengths are already long, having a second cavity even longer is not particularly desirable. However, one that is the same length could in theory be housed within shared vacuum tubes and facilities.

In this case where  $L_2 \ll L_1$ , the bandwidth of the extraction cavity is large enough to encompass multiple FSRs of the arm cavity and suppress them. However, eventu-

### 3. OPTOMECHANICS

---

ally an FSR will be reached where they are no longer suppressed and the resonances become enhanced, such as shown in figure 3.12. The maximum number of FSRs that require suppressing will depend on both the length of the arm cavity (as longer arms means a smaller FSR) and the frequency distribution of the mechanical modes over multiple FSRs present in the mirrors. Once the maximum number of potentially unstable FSRs are known the required length ratio can be computed.

To determine the length ratio required to suppress up to a chosen  $N_{\text{FSR}}^{\text{th}}$  FSR, the resonance of the mode without an extraction cavity ( $r_3 = 0$ ) is compared to one with. From this comparison we can see for a given length ratio how much a particular FSR is suppressed. Using Eq.(3.78) to make the comparison,

$$\frac{1}{D|_{r_3=0}} = \frac{S}{D}. \quad (3.80)$$

we want to solve this for  $\angle G_2$ , which contains the extraction cavity length:  $\angle G_2 = 4\pi f L_2/c$ . As the suppression of mode on resonance is desired, the frequency will be some integer number of FSRs  $f = N_{\text{FSR}} \text{FSR}$ . The FSR in this case being that of the arm cavity,  $\text{FSR} = c/(2L_1)$ . This results in  $\angle G_1 = 2N_{\text{FSR}}\pi$ . By solving Eq.(3.80) and substituting in the above statements, it is found that

$$\angle G_2 = \frac{4\pi f L_2}{c} = 2\pi N_{\text{FSR}} \frac{L_2}{L_1} = \cos^{-1} \left( \frac{r_3(r_2 - 1)}{2} \right). \quad (3.81)$$

Finally, the length ratio that is required to suppress up to the  $N_{\text{FSR}}^{\text{th}}$  FSR resonance must satisfy

$$\frac{L_2}{L_1} < \frac{1}{2\pi N_{\text{FSR}}} \cos^{-1} \left( \frac{r_3(r_2 - 1)}{2} \right) \lesssim \frac{1}{4N_{\text{FSR}}}. \quad (3.82)$$

The approximated version is valid when a high reflectivity ITM is used ( $r_2 \approx 1$ ). An example of this is shown in the first subplot of figure 3.12. Here it was chosen to suppress up to the 10<sup>th</sup> FSR. Obviously if the last FSR requires a reasonable amount

---

of suppression the ratio must be lowered further. The current design in aLIGO has  $\approx 60$  m from the ITM to the IMC which means up to the 16<sup>th</sup> FSR could in theory be suppressed.

### Extraction cavity mirror reflectivity

The next design choice for the extraction cavity is the reflectivity of the extraction cavity mirror (ECM). Choosing the reflectivity simply enables more or less of the light reflected from the mode cleaner to be recycled back into the arm to suppress the mode. It will be shown that the reflectivity of the ECM can produce two different behaviours of the system: of which I will refer to as the *weak* and *strong* coupling regimes.

In the weak coupling regime a mode is resonant at a single frequency. In the strong coupling regime a *frequency split* occurs and the mode will resonate at two distinct frequencies. Such resonance information could be extracted from the denominator of Eq.(3.78): where the differential cosines of  $G_1 \pm G_2$  suggest a splitting could occur. However, extracting such information about the resonant frequencies in this form is not particularly clear.

Performing an eigenvalue analysis of the system allows us to determine the linewidth and resonant frequencies of the system; the real part of the eigenvalue gives the resonant frequency and the imaginary the linewidth. This would involve solving the coupled differential wave equations for the field in both cavities. However, this step is greatly simplified as we already have the solutions to waves propagating in the cavities using our steady-state formalism. The coupled cavity system is described by just two coupled equations:

$$a_1 = a_3 \frac{i t_2 r_1 G_1}{1 - r_1 r_2 G_1} = a_3 A, \quad (3.83)$$

$$a_3 = a_1 \frac{i t_2 r_3 G_2}{1 - r_2 r_3 G_2} = a_1 B. \quad (3.84)$$

### 3. OPTOMECHANICS

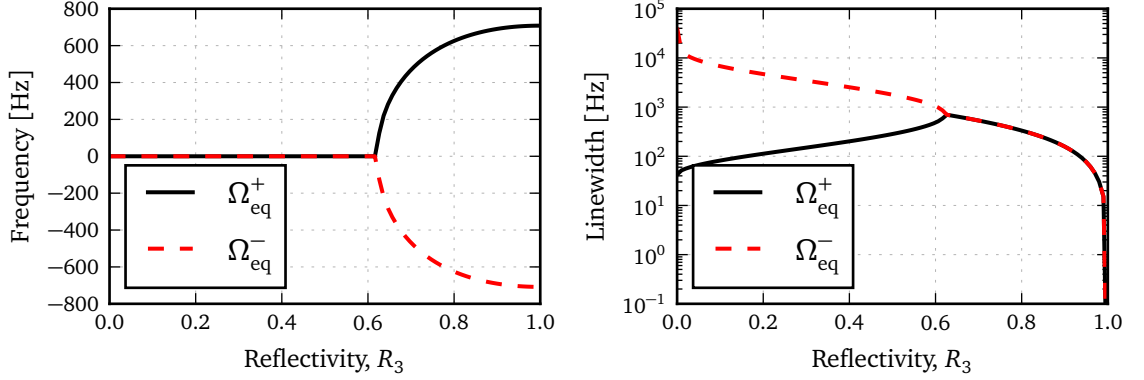


**Figure 3.13:** *Coupled cavity frequency split:* Using Eq.(3.87) the frequency splitting can be seen for an aLIGO like cavity. As the reflectivity reaches the critical value two resonances are then seen and separate further. The linewidth then decreases rapidly, this will correspond to a much higher gain at the particular resonances but the thinner linewidth provides greater suppression of the mode at other frequencies.

The characteristic equation of the system is found with

$$\det \begin{bmatrix} 1 & -A \\ -B & 1 \end{bmatrix} = 0, \quad (3.85)$$

which, after expanding, means solving for  $\Omega$  in

$$r_1 r_2 \exp(-2i L_1 \Omega / c) + r_2 r_3 \exp(-2i L_2 \Omega / c) - r_1 r_3 \exp(-2i \Omega [L_1 + L_2] / c) = 1. \quad (3.86)$$

In general there is not an analytic solution for  $\Omega$  here.

In the case of coupled cavities with equal lengths Eq.(3.86) can be solved for  $\Omega$  directly:

$$\Omega_{\text{eq}}^{\pm} = -\frac{ic}{2\pi L_1} \log_e \left( \sqrt{\frac{r_1 r_2 + r_2 r_3 \pm \sqrt{R_1 R_2 + 2R_2 r_1 r_3 - 4r_1 r_3 + R_2 R_3}}{2}} \right). \quad (3.87)$$

These solutions can be seen in figure 3.13 for an aLIGO like cavity ( $r_1 = 1, r_2 = \sqrt{0.986}, L_1 = 3994.5$  m). Here the splitting can be clearly seen when the extraction cavity reflectivity is increased beyond a critical reflectivity, which is denoted as  $R_c$ . Be-

---

fore this stage there are two resonances at the same frequency, one with an increasing linewidth and one with a decreasing linewidth. The eigenvalues in this regime are purely imaginary as we are looking at the 0<sup>th</sup> FSR resonance, which is defined relative to 0 Hz. At the critical reflectivity the two resonances split, with a linewidth tending to 0 Hz with  $R_3 = 1$ .

The frequency split occurs when the log term in Eq.(3.87) becomes complex, before this we are left with a purely imaginary value. This occurs when the inner square root becomes negative. Solving the quadratic equation for  $r_3$  provides two solutions, one gives  $r_3 > 1$  which is ignored, the other providing the critical reflectivity for equal length coupled cavities:

$$R_c^{\text{eq}} = \left[ \frac{2 - R_2 - 2\sqrt{1 - R_2}}{R_2^2} \right]^2. \quad (3.88)$$

The maximum frequency separation is found by taking the limit of  $r_3 \rightarrow 1$ , which gives

$$f_{\text{sp}}^{\text{eq}} = \frac{c}{4\pi L_1} \tan^{-1} \left( \frac{t_2}{r_2} \right) \approx \frac{c t_2}{4\pi L_1}. \quad (3.89)$$

When the lengths are equal this frequency splitting applies to all of the FSR resonances. This is because  $\Omega_{\text{eq}}^{\pm} + N_{\text{FSR}} \text{FSR}$  is also a solution to Eq.(3.86) for any integer  $N_{\text{FSR}}$ .

In the case where the cavities are not of equal length numerous approximations must be made to find reasonable solutions for  $\Omega$  in Eq.(3.86). The maths undertaken here was done using a symbolic math package. Here a second order expansion in terms of  $\Omega$  for the exponentials is used. A second order expansion is required as two solutions will be present, one for both the positive and negative frequency split. With a small length ratio, the frequency splitting will only occur around FSRs which match between both the arm and extraction cavity.

For the cavities of interest for GW detectors it is also assumed that  $r_1 \approx 1$ ,  $r_2 = \sqrt{1 - T_2} \approx 1 - T_2/2$  for small  $T_2$ , the length ration is also parameterised with  $L_2 =$

### 3. OPTOMECHANICS

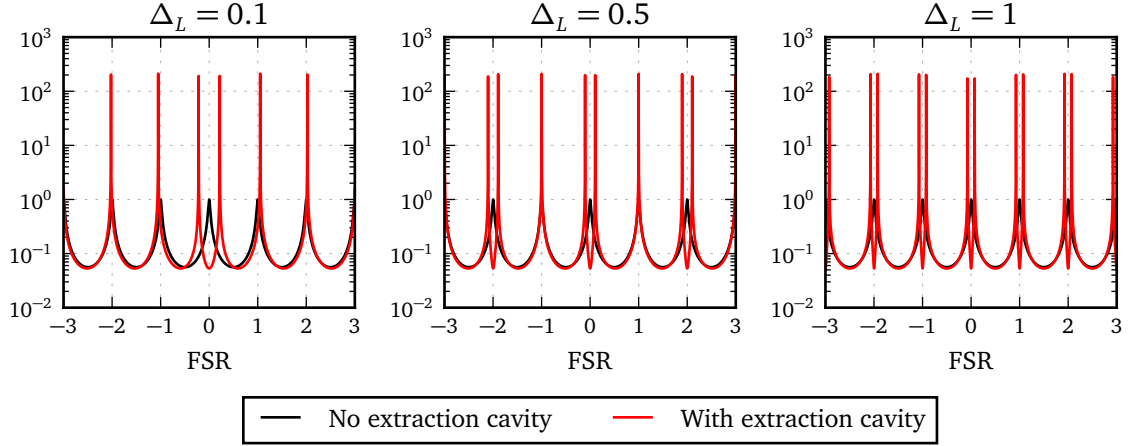


**Figure 3.14:** *Frequency split vs. cavity lengths:* Shown are the resonances of a mode over frequency in the arm cavity for different length ratios. The extraction cavity mirror is perfectly reflective in this case to highlight the frequency splitting. For short length ratios only the 0<sup>th</sup> FSR is affected by the splitting, for equal lengths each FSR is split. The splitting occurs when the resonance of the extraction cavity is aligned with a resonance in the arm, as given by Eq.(3.78).

$\Delta_L L_1$ ; where  $\Delta_L \lesssim 1$ . Expanding and solving Eq.(3.86) provides a second order polynomial in  $\Omega$ . Its determinant of this polynomial controls when the frequency split occurs. Finding the determinant and solving for  $r_3$  the critical reflectivity for such a system is found to be

$$R_c = \left[ \frac{T_2(1 - 3\Delta_L) - 2 + \sqrt{T_2^2(9\Delta_L^2 - 6\Delta_L + 1) + 16\Delta_L T_2}}{2(T_2\Delta_L + T_2 - 1)} \right]^2. \quad (3.90)$$

The maximum frequency split can be approximated by taking the limit of  $r_3 \rightarrow 1$ . Taking this limit and removing negligible terms the maximum frequency split is

$$f_{sp}^{\pm} \approx \pm \frac{c\sqrt{3T_2^2 + 16T_2\Delta_L}}{4\pi L_1(T_2 + 4\Delta_L)}. \quad (3.91)$$

It can be seen that  $f_{sp}$  increases with smaller length ratios. For small  $\Delta_L < 0.1$  Eq.(3.91) the original second order expansion of the exponentials is no longer valid for larger frequencies. However using Eq.(3.86) with similar approximations of small

---

$T_2$  but considering the limits  $\Delta_L \rightarrow 0$  and  $r_3 \rightarrow 1$  the separation tends to value:

$$f_{\text{sp}}^{\pm} \approx \pm \frac{c}{4L_1}, \quad (3.92)$$

which is just half the FSR of the arm cavity. With this frequency offset we no longer have two distinct resonances, as the current and next FSRs positive and negative splitting merge into one. Thus with small the resonances of the cavity can be seen as just shifted in frequency by FSR/2. This was numerically experimented with and found to apply for  $\Delta_L \lesssim 10^{-3}$ .

This subsection has outlined the behaviour of the optical resonances in an equal and short length ratio coupled cavity system analytically. A mechanical mode becoming unstable will only be problematic if it coincides at frequencies where there is also an optical resonance in the system. These formulae show how these resonances behave with respect to multiple variables which can be difficult to extract concisely from numerical simulations. This also helps better understand the numerical results and demonstrate such code is working as expected. The discussion of pros and cons of each regime is discussed in section 3.2.1 where the numerical results are also presented.

### **Extraction cavity stability**

The final design choice regarding the extraction cavity is its geometric stability, or the amount of round-trip Gouy phase accumulated. This must be chosen to ensure that modes of differing orders are suppressed for the same extraction cavity tuning. If this is not the case the suppression of one mode will most likely coincide with an additional excitation of another. A mode circulating in the extraction cavity will accumulate some Gouy phase dependent on its order and some additional mode independent phase from any cavity detuning, which is represented by an ECM tuning of  $\phi$ . The round-trip

### 3. OPTOMECHANICS

---

phase accumulated is then:

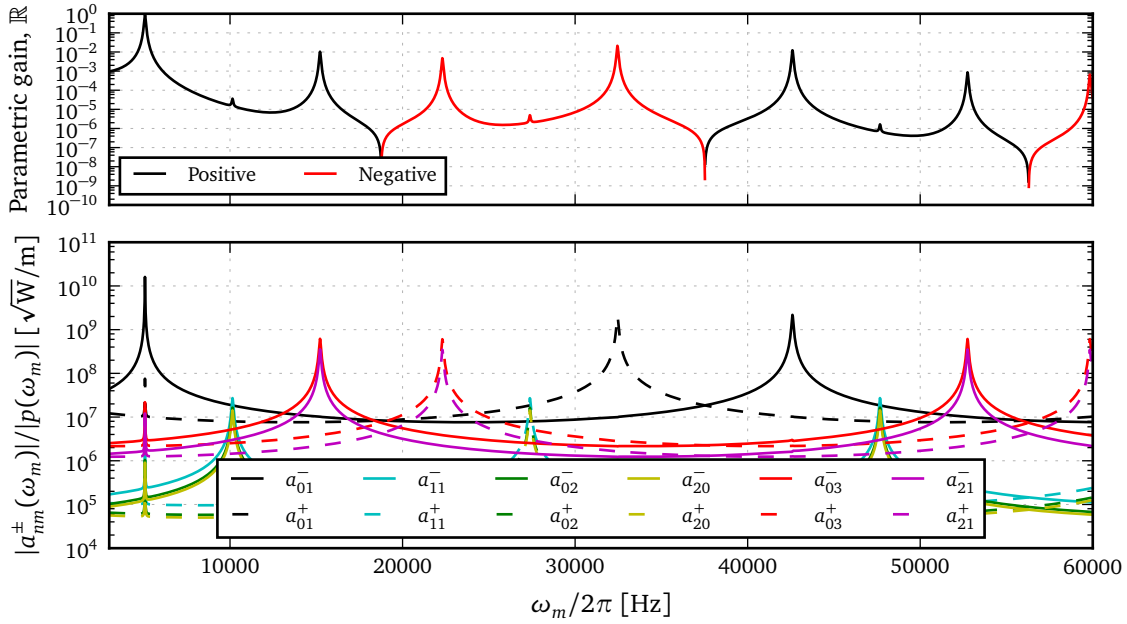
$$\angle G_{2,nm} = \frac{2\Omega L_2}{c} + (n+m)\Psi_{rt,2} + 2\phi, \quad (3.93)$$

For the  $\text{TEM}_{nm}$  mode to be resonant  $\angle G_{2,nm} = 2N\pi$ . This is only possible for any order of HOM if  $\Psi_{rt,2} \approx \pi$ , or in other terminology, the extraction cavity is unstable. To achieve this Gouy phase whilst simultaneously ensuring the above length ratio requirements an extraction mirror telescope will have to be designed. The actual design, whether this involves lenses or mirrors, is not considered here. The models used will force the accumulated Gouy phase a long a space to have the required value.

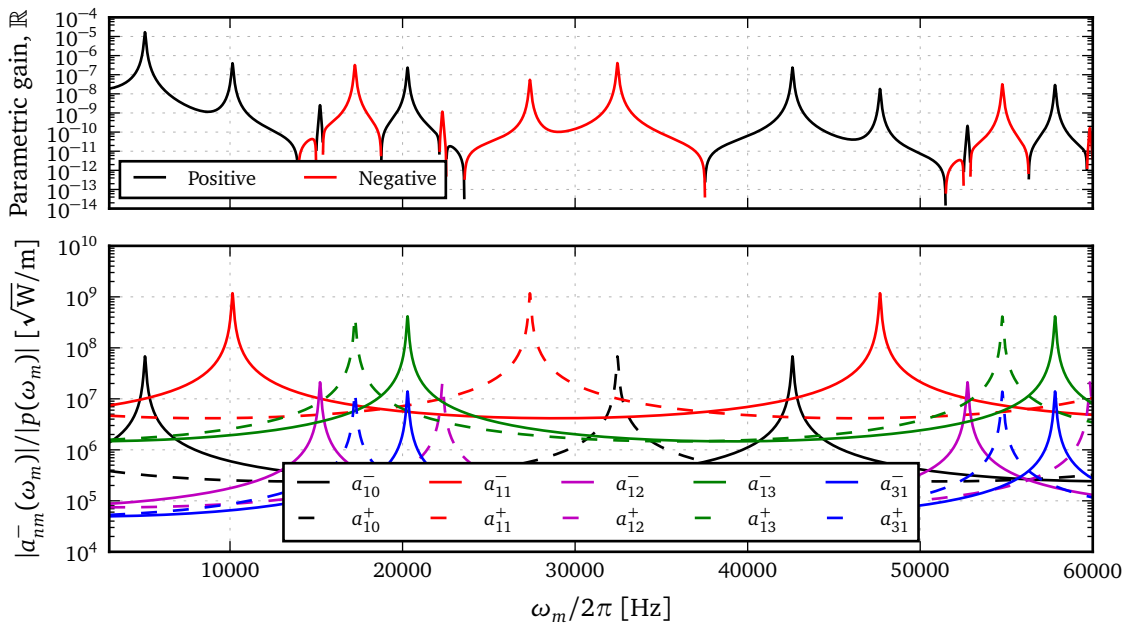
To summarise, an extraction cavity can be designed to feedback fields other than the  $\text{TEM}_{00}$  of the carrier to suppress the resonant build up of such fields. This can be achieved for multiple FSRs and HOMs at the same time using an unstable extraction cavity. The reduced amount of HOM optical fields should in theory reduce the optical feedback via radiation pressure that drives mechanical modes to instability. Thus far only simplified analytics has been shown for the optical fields in a coupled cavity system. To demonstrate the following section will apply this theory in a numerical experiment to demonstrate its workings.

#### 3.2.2 Numerical experiment

The numerical experiments conducted here are all done using the aLIGO IMC and arm cavity design. These are combined as shown in figure 3.10. Some additional lenses are required between the IMC and cavity to mode match the pair. To do this an optimisation routine was employed to maximise the circulating cavity power whilst varying each of the lens' position and focal length. A mode matching setup was found such that the circulating power differed by 1ppm compared to the plane wave case—where mode-matching is not considered. The actual values of the lens and their po-



(a) Mode 37



(b) Mode 140

**Figure 3.15:** *Optical mode resonances and parametric gains:* Using FINESSE the surface motions of a mechanical mode can be applied and the parametric gain modelled. Shown are two modes, 37 and 140, and their respective parametric gains in an aLIGO arm cavity (no ECM) as their mechanical resonance frequency is swept. From the two subplots it can be seen which HOM sideband is causing each of the instabilities, the instabilities occurring for positive gains in the top subplots. The mode separation frequency is  $\approx 5$  kHz, thus features can be seen every such frequency.

### 3. OPTOMECHANICS

---

sitions are not of much importance here as this just ensures that any effects from mode-mismatches are minimised. The length between the IMC and arm containing the lenses though was kept as short as possible, thus allowing for shorter length ratios for the extraction cavity. This setup is then able to pump the arm with  $\text{TEM}_{00}$  laser and various surface motions can be applied to study any unstable modes.

The modes used were generated using COMSOL as discussed in earlier sections. In all around 800 mechanical modes were computed ranging from  $\approx 1\text{--}60$  kHz. The data for these modes can be found in the aLIGO FINESSE Git repository [29], for those that are interested in performing similar simulations. For each of the mechanical modes the surface motion is extracted and converted into a format that FINESSE can read. The maps are then further processed to enable reduced order quadrature as outlined in chapter 2 to greatly speedup the scattering matrix calculations. Here 800 maps will need to be run, without ROQ the runtimes would be excessively long.

To illustrate the behaviour of the two modes the surface motions can be applied in FINESSE using the setup depicted in figure 3.10, but with no ECM to begin with. The mechanical frequency of each mode is swept over an FSR to see where the mechanical modes are excited or damped. For each frequency the mechanical mode is excited by computing how much of each sideband is generated for a unit motion of the surface, then along with this the parametric gain is calculated. The results of this scan for the two modes 37 and 140 are shown in figure 3.15. Enough higher order modes were used to capture the main features from the scattering, which was up to order four for these particular modes. Comparing the resonances to table 3.2 the largest coupling coefficients match with the resonances seen in the figure. It should be noted that by sweeping a mode's mechanical frequency like this we can find which frequencies would be problematic. If in reality the mode were to have a frequency that lies near a positive gain peak, it would then have the potential to become unstable. The respective resonance frequencies for mode 37 and 140 as computed by COMSOL are  $\approx 15.5$  kHz

---

and  $\approx 28.5$  kHz. It can be seen here that mode 37 lies close to a positive 15 kHz peak for the order three modes which is strongly coupled with, thus is a candidate for potential instability. Mode 140 however lies close to a negative gain peak thus is not problematic.

The uncertainty of any given mechanical modes computed frequency compared to its *real* frequency is a considerable obstacle for computing exactly which mode will be unstable. Work has been previously done on comparing 3D FEM tools ability to compute a resonant mode compared to theoretical predictions for a cylindrical mass [105]. Here, it was shown that the accuracy depends strongly on the computational method applied, in some cases the computed value being  $\approx 10^2$  Hz off for higher frequencies. Since writing this there are no procedures that can be used to test the accuracy of the COMSOL modes generated that have been used for this work. However, entirely accurate frequencies are not of importance here as a general suppression of mechanical modes is being studied; a reasonable collection of varied mode shapes and frequency distribution to study if all are suppressed. With no better determinant for whether a mode *could* become unstable, I will class one as having the potential to become unstable if a positive gain peak with  $\mathbb{R} > 1$  exists within  $\pm 2$  kHz of the COMSOL resonant frequency; a similar range was used in [106].

### 3.2.3 Results of PI suppression with the ECM

Including the ECM in the numerical model the effect on the mechanical modes can be studied. Two setups were constructed for equal and short ( $\Delta_L \approx 0.01$ ) length ratios. The setup was mode well mode matched for both by carefully tuning the lenses and lengths between the IMC and arm cavity. In the equal length case the effect the ECM reflectivity has can be seen in figure 3.16. Here, the mechanical frequency of the mode is scanned whilst looking at how the parametric gain is affected. This clearly demonstrates the coupled cavity frequency splitting as discussed analytically:

### 3. OPTOMECHANICS

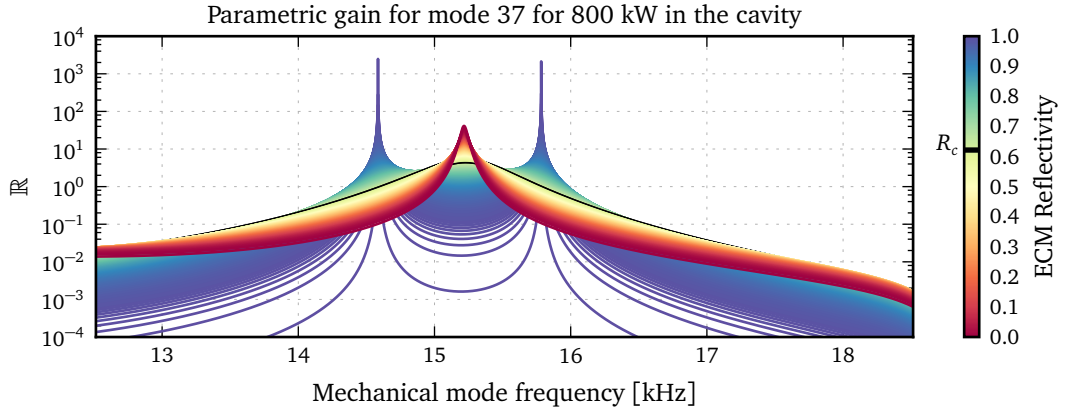


**Figure 3.16:** *Equal length frequency split parametric gain:* For an equal length ratio between the arm and extraction cavity the parametric gain of mode 37 is shown over the mechanical frequency range. COMSOL computes the resonance frequency to be 15.5 kHz for this mechanical mode. Changing the ECM reflectivity has a significant effect on the gain, the coupled cavity resonance frequency split is seen for  $R > R_c$ , and below this a suppression of the resonance and increase in the linewidth.

the critical reflectivity,  $R_c$ , when the splitting begins to occur is marked in the colour bar with the black trace.

In the weak coupling regime the peak in  $\mathbb{R}$  is steadily reduced whilst also increasing in linewidth. Slightly above  $R_c$  the peak in  $\mathbb{R}$  continues to widen whilst decreasing in

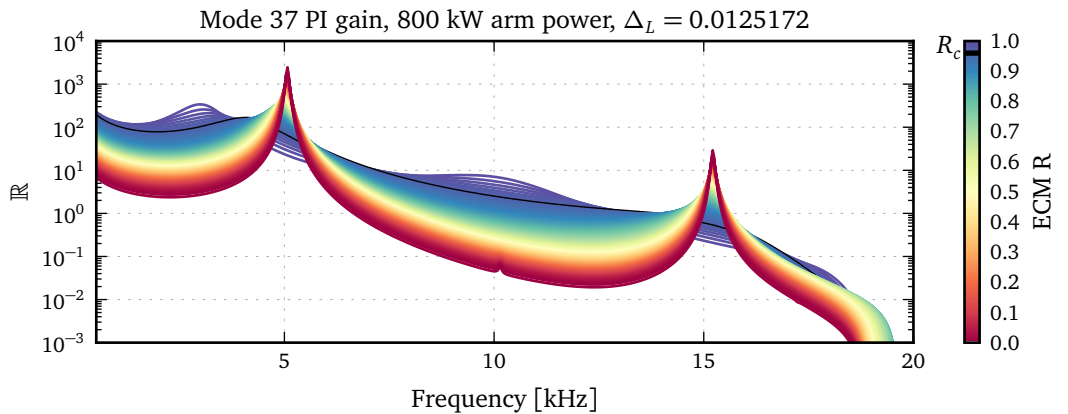


**Figure 3.17:** *Short cavity frequency gain parametric gain:* For a short length ratio between the arm and extraction cavity the parametric gain of mode 37 is shown over the mechanical frequency range. Changing the ECM reflectivity has alters the gain significantly, it can be seen here there is a  $\approx 5$  kHz shift in the resonance peak of the 15 kHz resonance, as predicted by Eq.(3.91). The peak that occurs at 5 kHz is for the resonance of the first order modes that couples strongly with this particular mechanical mode.

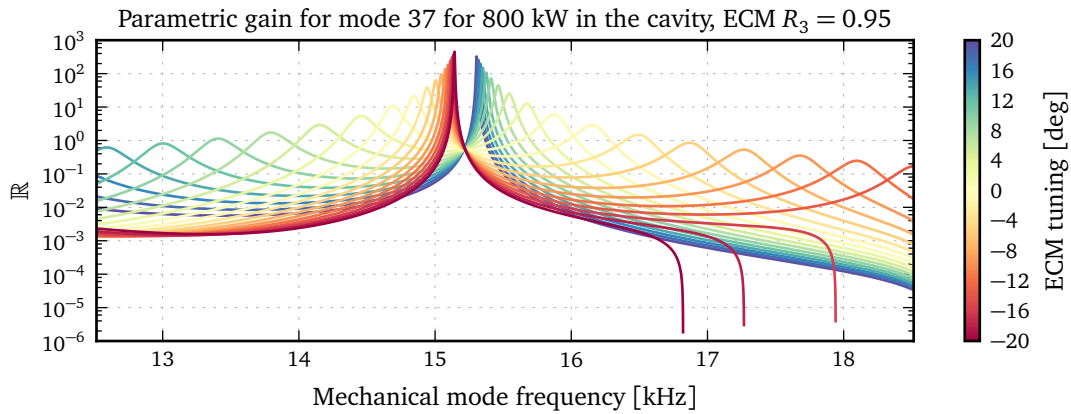


**Figure 3.18:** *Equal length extraction cavity tuning:* For an equal length ratio between the arm and extraction cavity the parametric gain of mode 37 is shown over the mechanical frequency range as the ECM is detuned but with a reflectivity of 0.95.

maximum gain before the split resonances become visible. At perfect ECM reflectivity there exists two narrow high gain peaks corresponding to the new optical resonances of the system. It can be seen in this case that it is essentially impossible to completely remove all instabilities. However, the parametric gain can be shaped.

The ideal choice of ECM reflectivity is perhaps not straightforward. By using a low  $R$  we reduce the original peak's maximum gain without introducing further peaks. Yet the broadening of this peak, resulting in more frequencies where  $\mathbb{R} > 1$ , means that the probability of a mechanical mode finding itself in an unstable frequency range is increased, thus more PIs could exist. Operating with a very low ECM reflectivity whilst keeping the linewidth small does offer a slight reduction in  $\mathbb{R}$ , but such a small change would add additional experimental complexity with more mirrors to control whilst offering little suppression of any unstable modes.

If the broadening of the peaks are thought not to be an issue, the ideal choice would be a reflectivity slightly higher than  $R_c$ ; here the resonance is split but the linewidth of the two merge into an overall wider peak with a lower maximum gain.

The other option is to use the highest reflectivity possible. With this the frequency split in the resonances have much higher peak gains but with much smaller linewidth.

### 3. OPTOMECHANICS

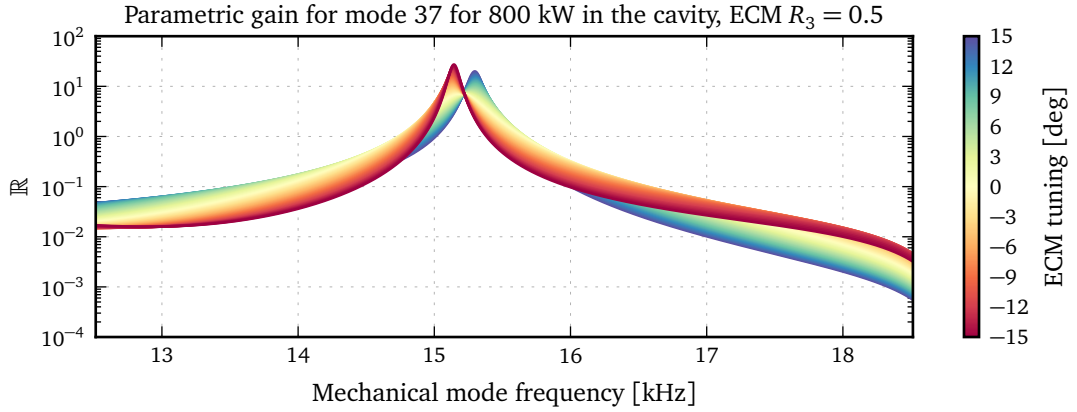


**Figure 3.19:** *Short extraction cavity tuning:* For short length ratio between the arm and extraction cavity the parametric gain of mode 37 is shown over the mechanical frequency range as the ECM is detuned but with a reflectivity of 0.5.

This would reduce the probability that a mechanical frequency would coincide with an optical frequency having  $\mathbb{R}$ , therefore may be a preferable option. Such a narrow linewidth also has the benefit that only small changes in parameters would be needed to shift the resonance frequency of the mode to stop one from being unstable.

Performing the same analysis for the short length ratio the parametric gain behaves as seen in figure 3.17. Here, we do not see any frequency splitting as demonstrated in the analytics. The gain is shown over a larger range here to show how the large frequency shift,  $\approx 5$  kHz, as predicted by Eq.(3.91) effects  $\mathbb{R}$ . Around the actual mechanical resonance frequency, 15.5 kHz, the gain is significantly reduced.

The effect of detuning the extraction cavity shifts the resonance peaks. For high reflectivities as seen in figure 3.18 the direction of the detune decides whether the upper or lower resonant mode is shifted in frequency. Like the use of the thermal control system to shift the mechanical resonance mode, the ECM detuning offers a method to shift which optical frequency is resonant; if a PI was seen to be ringing up then it could be possible to detune the extraction cavity to stop the PI building up further. The only problematic aspect here is that this detuning will affect all optical modes, which could result in other optical modes then becoming co-resonant with mechani-

---

cal modes inducing further instabilities. Detuning in the weak coupling regime as seen in figure 3.19 shifts the peak up or down in frequency whilst increasing the maximum gain. Thus again offering a method for shifting where the largest PI gain is.

Shown in figure 3.20 is the effect that detuning has on mode 37 and 140. For this the largest maximum around 15.2 kHz and 10.2 kHz for each mode respectively is tracked with a peak finder as the ECM is tuned. The top plot shows the dominant optical modes in the lower sidebands resonant in the arm cavity as the mechanical mode is excited. As expected when the EC is tuned to suppress these,  $\mathbb{R}$  is at a minimum. Shown also is the position of the maximum gain, which varies greatest around the minimum. For these results the Gouy phase of the EC was not tuned to demonstrate how the minimum  $\mathbb{R}$  occurs for different EC detunings.

The Gouy phase accumulated between the IMC and ECM was tuned to ensure that  $\pi$  Gouy phase is accumulated between the ITM and ECM in the model, thus ensuring the suppression of each mode. By choosing the EC Gouy phase and its tuning correctly it was possible to suppress any PI that appeared for any mechanical mode. The numerical experiment took each of the 800 mechanical modes and computed the maximum parametric gain in the frequency range  $\pm 2$  kHz around the COMSOL computed resonance mode. This additional range was chosen rather arbitrarily but is to take into account some uncertainty in what exactly the mechanical modes resonance is. These numerical experiments were then ran for multiple ECM reflectivities of equal length coupled cavity system. Similar results were seen for a short length ratio system where equation 3.82 was used to ensure all modes in the frequency range were suppressed. In the short case there was also an absence of frequency splitting seen at high frequencies as demonstrated in figure 3.12.

This analysis was first applied to mechanical modes on the ETM, the results of which are shown in figure 3.21. Here each point represents a positive  $\mathbb{R}$  peak. With 800 kW of power in the arm cavity and no extraction cavity 115 modes were found to

### 3. OPTOMECHANICS

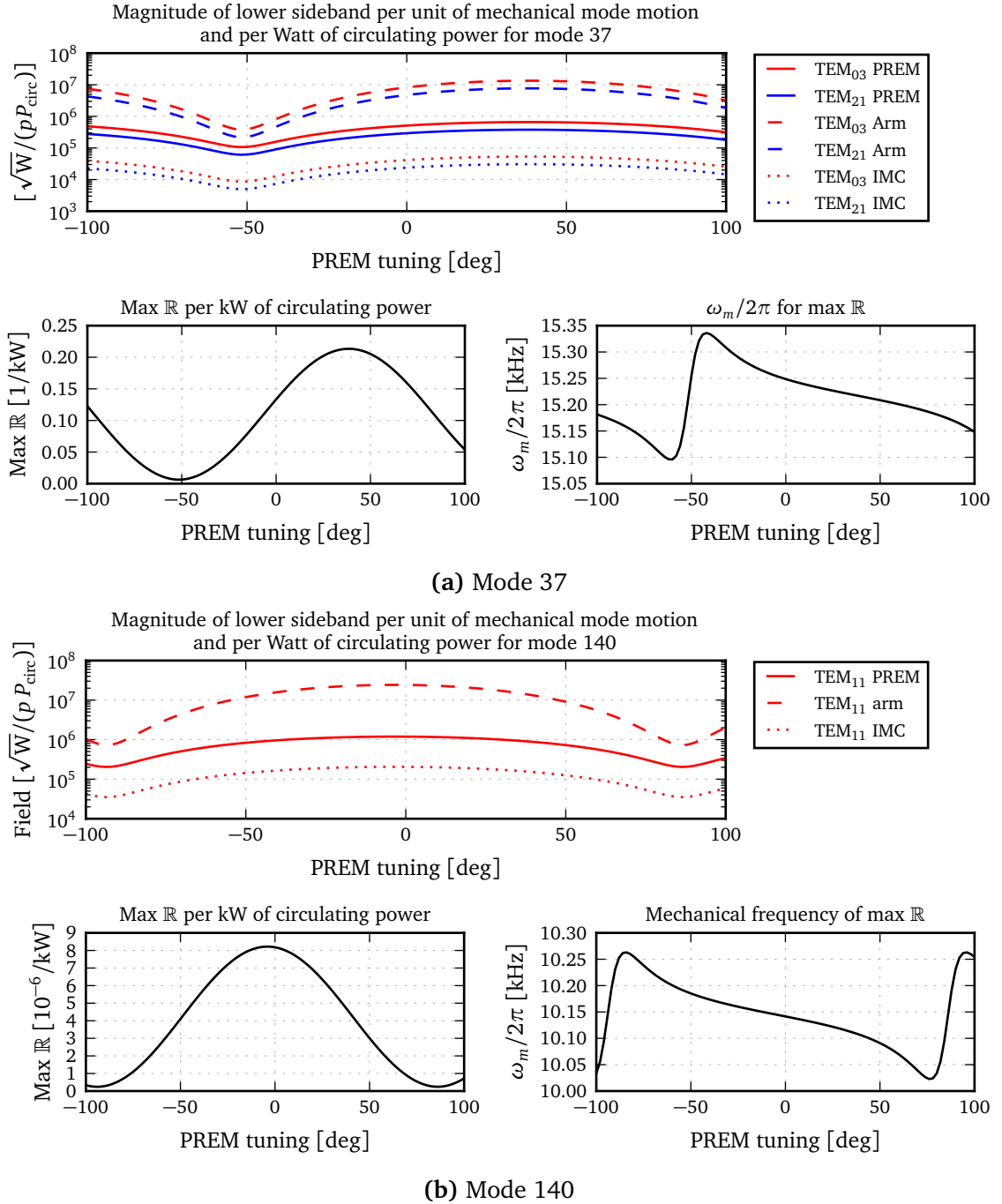


**Figure 3.20:** *Two mechanical modes and an extraction cavity:* The two modes shown in figure 3.4, modes 37 and 140, were placed in the extraction cavity setup shown in figure 3.10. The effect on the HOM of the lower sideband can be seen in the upper subplots as the ECM is detuned. As the ECM is detuned a peak finder records the maximum gain and its position; the effect of which is shown in the lower subplots. As can be seen the lower circulating optical modes that coupled strongly with the mechanical mode corresponds to a lower parametric gain.

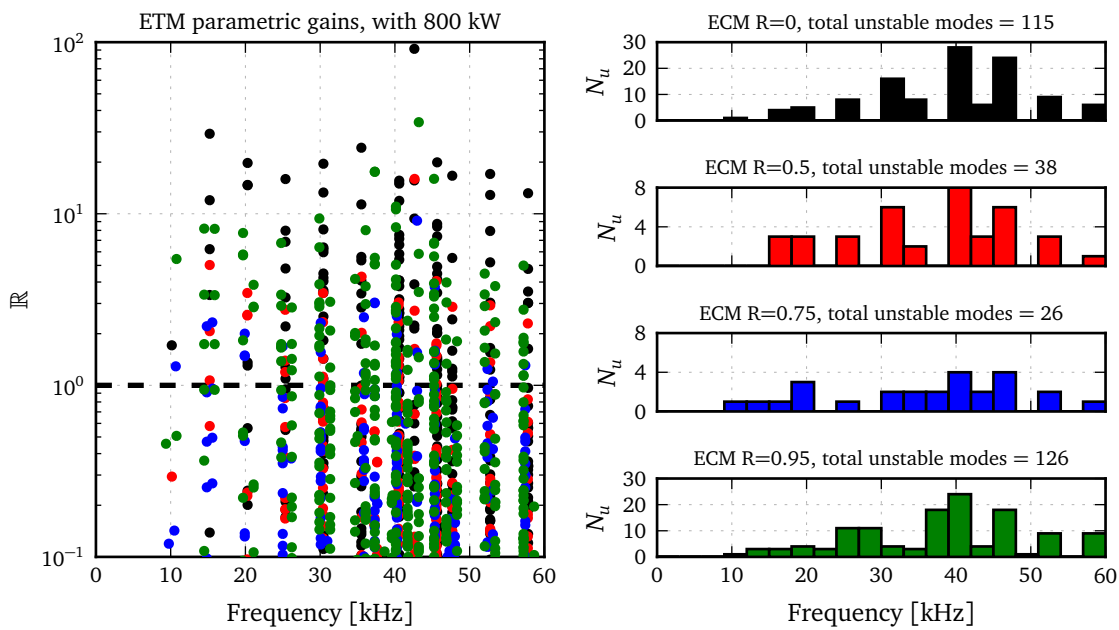


**Figure 3.21:** *ETM parametric instability reduction:* Applying the 800 mechanical modes to the arm’s ETM mirror in the extraction cavity setup its ability to suppress multiple modes can be seen. Each data point relates to a specific mechanical mode that has a positive parametric gain peak within  $\pm 2$  kHz of its COMSOL computed resonance frequency. Here the varying reflectivities of an equal length ratio setup clearly shows a reduction in the peak parametric gain across the full range of modes tested. The FSR of the cavity is  $\approx 37.5$  kHz so we also see a multiple FSR reduction too.

### 3. OPTOMECHANICS

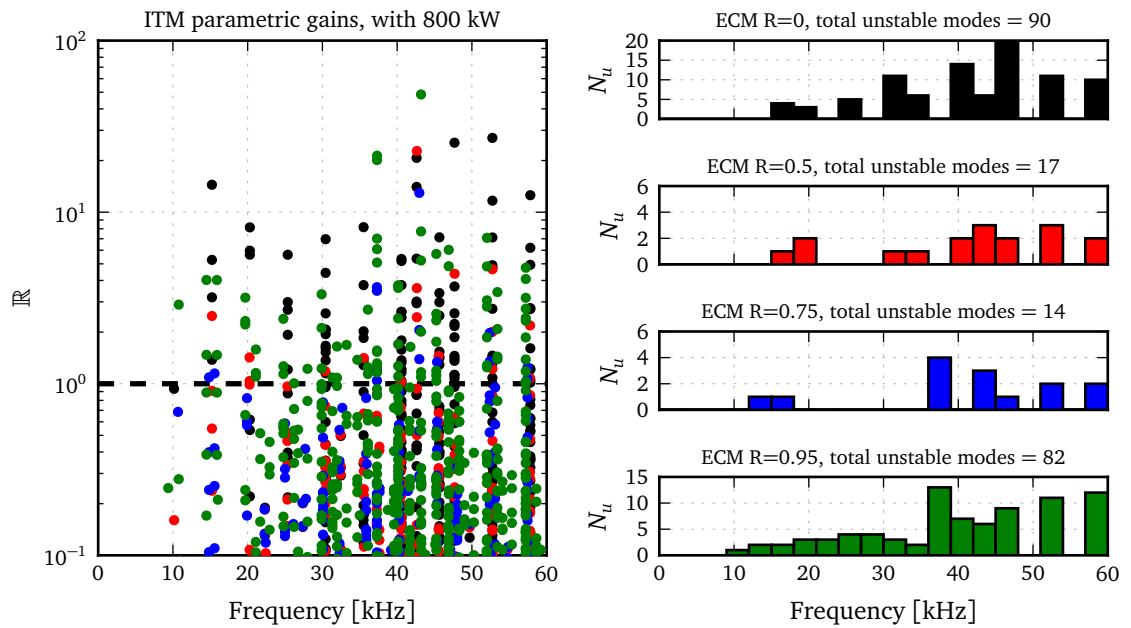


**Figure 3.22:** *ITM parametric instability reduction:* The same as figure 3.21 but applying the parametric instability to the ITM mirror. This shows a reduction in parametric gains for both mirrors.

be unstable in the range 10–60 kHz. Increasing the reflectivity of the ECM the number of unstable modes decrease significantly. The optimum was found to be around  $R \approx 0.75$ , just above  $R_c$ . Increasing it further results in many more modes appearing. This is a direct result of the frequency splitting and the high gain but narrow linewidth. Numerous doublets can also be seen in the plot. It should be noted that this considers the maximum  $\mathbb{R}$  to be a suitable metric for measuring the performance of such a layout. Ideally a probabilistic answer should be attained to suggest the chance that a mode has of becoming unstable. This would be a function of not only the maximum gain but also the frequency range over which  $\mathbb{R} > 1$ . Performing such an analysis however would require assigning likelihoods to the numerous values involved, such as the mechanical mode shape and frequency or optic radius of curvature in a hot state. A similar analysis of the same modes on the ITM also showed a broadband reduction in the number of unstable modes as seen in figure 3.22.

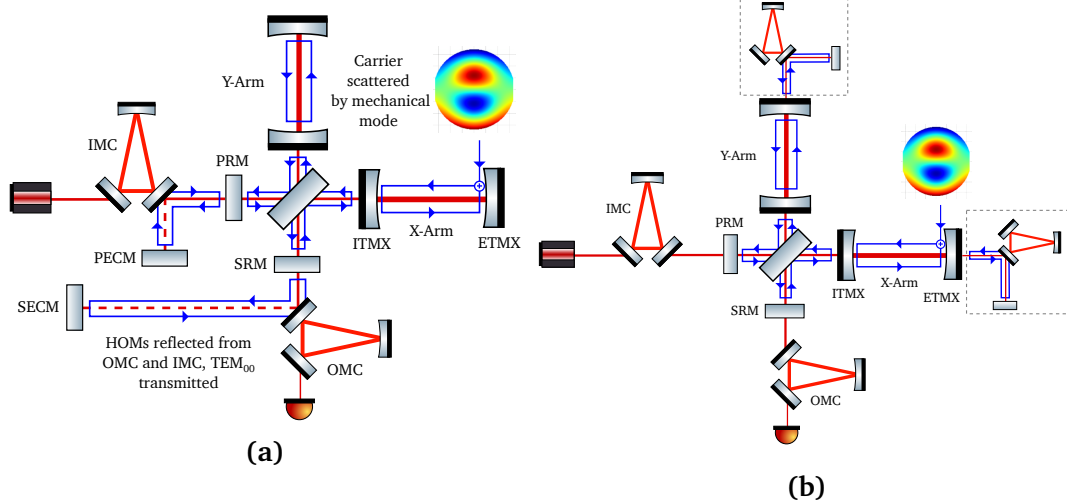


**Figure 3.23:** *Layouts to explore:* When a mechanical mode scatters sidebands at ETMX the generated sidebands (Shown in blue) follow multiple paths throughout the interferometer. The layout shown is a general setup for a dual-recycled interferometer. The recycled HOM content of the sidebands reflected from the IMC and OMC aim to reduce the parametric gain. Shown is another potential approach where each arm cavity has its own extraction cavity after the ETM.

### Ideas for layouts and potential pitfalls

These extraction cavities could be included in interferometer designs in several ways. The first obvious choice would be to use the IMC and OMC as the mode cleaners to separate the beam as they are already present in the design, as shown in figure 3.23. This has the additional benefit that few extra mirrors would be required. In the case that the extraction cavities proved to be more trouble than they are worth after actually running with them they could in theory be easily removed whilst still retaining the rest of the working interferometer. That statement obviously assumes control schemes can be designed that are not affected by their removal. The immediate downside to such a layout is that the two extraction cavities are not operating on a single cavity, instead they would work to reduce common and differential arm PIs. There is also the issue that these modes would have to traverse numerous optics and the PRC and SRC without suffering much loss, so as to ensure the PI gain reduction is significant, and not become distorted enough to no longer affect the original mode that created

### 3. OPTOMECHANICS

---

it. This could prove experimentally to be too challenging. The IMC and OMC will also reflect small amounts of the  $TEM_{00}$  of the carrier which will be affected by the EC and fed-back into the interferometer, this is not ideal and could introduce additional noise couplings. This design would also limit the smallest length ratio possible, dictated by the PRC and SRC lengths.

Other options could be to include a pre-arm mode cleaner between the BS and the ITM. This option would allow for short and equal length ECs easier than using the IMC and OMC. However, the addition of numerous optics on the input side would result in strict requirements to reduce additional noise couplings that would no doubt arise from more optics here. There would then be additional thermal distortion challenges in such a mode cleaner as well as introducing more differential differences between the arms. Such a setup is likely not beneficial.

The last option could be to have the mode cleaner and extraction cavity on the ETM end. This would require a more transmissive ETM which would lower the arm power and sensitivity of the detector. However, if PIs do prove to be enough of a problem during the operation of aLIGO that such extraction cavities are considered, the reduction in arm power would be required anyway to stop PI building up. This option would be ideal in that it also does not affect the operation of the rest of the interferometer. The behaviour of the complicated collection of cavities—the arm, PRC, SRC and ECs—that would then be produced though would require careful investigation.

## 3.3 Conclusion

This chapter has discussed and demonstrated several radiation pressure based effects that will affect advanced gravitational wave detectors. Firstly the theory outlining the optomechanical interaction of suspending optics and the optical fields was outlined and the necessary changes required in FINESSE to enable me to simulate generic inter-

---

ferometric layouts. This was then expanded to higher-order radiation pressure effects which can cause vibrational modes in an optical element to produce negative dampening creating instabilities in the interferometer. Such physical features will be prominent in current and future detectors where high circulating powers are used. The work conducted here ensured that the tools are available to investigate such behaviours in the future commissioning tasks. Using these new tools I investigated one potential idea for reducing the parametric gain for all mechanical modes. This was achieved using a mode cleaner to separate the wanted optical field and those unwanted higher order modes created by the instability, in what I refer to as an extraction cavity. The aim of which is to extract the higher order modes from the arm to reduce the optical feedback to mechanical modes. Thus far only mechanical dampening solutions have been suggested to reduce PIs. Hopefully this work will aid in the study of further designs that could also offer PI reduction via optical means, of which allows multiple mechanical mode gains to be reduced at once.

Whether an optical means of reducing PIs will seem to be an attractive option in the future will depend on the experimental experience of aLIGO as it is pushed to higher powers. If PI are seen to be a limiting or troublesome feature at high power then future upgrades and next generation detectors might want to consider using such an approach as outlined here. The idea laid out here is the beginning of a new method for the reduction of PIs. However, this is not the only metric by which it should be judged. Beyond this work it should be investigated how noise couplings are changed or new ones are introduced, how original control signals for the arms, PRC, SRC and MICH are affected and how the ECs can be controlled.

### 3. OPTOMECHANICS

---

# Chapter 4

## Commissioning and design modelling

At times, the commissioning of the detectors results in unexpected outputs or behaviours from the interferometer. Simulations are used to provide data points for providing a better understanding the physical interferometer. Using the simulation to explore probable parameter spaces allows us to determine whether our theory on why a particular problem has arisen is true, whether certain parameters can be altered to solve it or if not how to minimise it.

Commissioning is a time intensive activity for those scientists undertaking it. The aLIGO FINESSE simulation team exists for commissioners to request particular simulation activities be run to help progress their work. The simulation team is made up of several members with varying experimental and simulation experience. The main members during my PhD have been Paul Fulda, Charlotte Bond and myself. Having a strong link between simulators and experimentalists is crucial for the success of this activity. In general it is easy to simulate *a* result. However, it is not straight forward for those not working directly on the hardware to pickup on fast changes and hands-on knowledge gained by those that do; such details can be key to having accurate models

## 4. COMMISSIONING AND DESIGN MODELLING

---

that provide commissioners with *useful* results. This is why having a link between experimentalists and simulators is crucial. Paul, based at the University of Florida, also works on site at both LLO and LHO.

My place in this team as the lead FINESSE developer was twofold: first performing simulations but also providing the tools and features for the team's ever evolving requirements to achieve its modelling goals. Various work, small and large, was carried out over the years for modelling, here I describe a few highlights.

### **The aLIGO Finesse file**

Before any simulation activity can take place a FINESSE file must be constructed. For aLIGO this file building has been following its progression since the IMC was first installed [107]. Information about the detector is found from various sources primarily technical notes on design from the LIGO DCC and from hands on experience of commissioners and measurements recorded on the LIGO logbooks [108].

An example of a full FINESSE used for modelling activities can be seen in appendix E which is based on design specifications and parameters rather than measured values. This file contains all the core elements of the detectors: IMC, OMC, PRC, SRC, XARM, YARM and the various telescopes to mode match the cavities. It also contains the length sensing photodiodes and control feedbacks for DARM, CARM, SRCL, PRCL and MICH as described by the aLIGO length sensing and control design [60]. Similar files exist for both the LHO [2] and LLO [3] detectors which use measured parameters for the optics [51] and setup. For those interested in learning more about how such files are constructed in more detail, appendix C in [53] reports details regarding setting up and finding operating points of complex interferometer such as these.

---

## 4.1 Lock-dragging modelling technique

When simulating a complex virtual interferometer it is vital that the required operating point is found. What the desired operating point actually is depends on the modelling task at hand. Broadly speaking, the operating point is defined as a particular state of the optics' positions, alignment and thermal state of the mirrors, throughout the entire interferometer. Much of the modelling undertaken for commissioning and design has involved exploring problems where different operating points must be considered [53, 109, 107, 110]. This section outlines the technique called *lock-dragging* that was used in many of these cases. This should provide enough of an overview for interested readers to repeat the process. Code and exemplary usage for this technique can be found in the aLIGO FINESSE Git repository [29].

Some non-exhaustive metrics that must be met for a virtual interferometer to be classed as operational are:

- The carrier field is resonant in the arms and PRC
- The carrier is anti-resonant in the SRC for resonant sideband extraction
- The correct amount of DC DARM offset is applied
- The RF control sidebands are resonant in the required cavities
- All error signals possess a zero crossing corresponding to the relevant optical fields
- That all error signals possess a reasonable linear range around the zero crossing

If a simulation does not produce the above features, it is unlikely to represent the physical interferometer you are aiming to model. It is worth noting that it is possible to use fake error signals that are only available virtually, for example, extracting a particular HOM's intracavity phase or amplitude and using that to ensure a cavity is kept

#### 4. COMMISSIONING AND DESIGN MODELLING

---

on resonance. Although this may simplify locking cavities in the virtual interferometer it will not behave as the real one would. As many commissioning related activities question how error signals look or behave, using fake signals is not desirable. Further information on modelling of control signals in FINESSE for aLIGO can be found in [53].

The problematic aspect of using the same sensing and control scheme as the physical detector is that they can be time consuming and finicky to setup in the model. This is due to tuning the positions of the mirrors by hand and repeatedly running the simulations to ensure all the relevant error signals are appropriate and ensure the relevant optical fields and outputs behave as they should. Cross couplings between a DOF and the other's length sensing outputs complicate this process further, as is usually present between MICH, PRCL and SRCL. Although time consuming, this process is possible for a single state of an interferometer. However, when modelling a problem involving many different states re-tuning the operating point becomes prohibitively time consuming.

This was found to be problematic when modelling the effects of thermal lensing and distortions of the test masses, for example. Both lensing and distortions are a result of optical power being absorbed in the substrate and coatings of the mirrors, the latter being the more dominant effect. The absorbed power in the substrate produces local temperature variations, which due to a temperature dependent refractive index, forms a lens. This acts to mode-mismatch the incoming laser to the eigenmode of the cavity. The thermal distortions refer to how the surface of the mirror is altered, in particular the HR surface. Two effects are present when this happens: an overall change in the radius of curvature of the surface which alters the eigenmode of the cavity; and a smaller residual thermal bump describing higher order surface perturbations. For the LIGO like test masses, at high power, this introduces a thermal bump in the center of the surface of the order of 50 nm high. Both lensing and distortion effects have been modelled extensively using FINESSE [53] and analysed analytically and with FEMs as

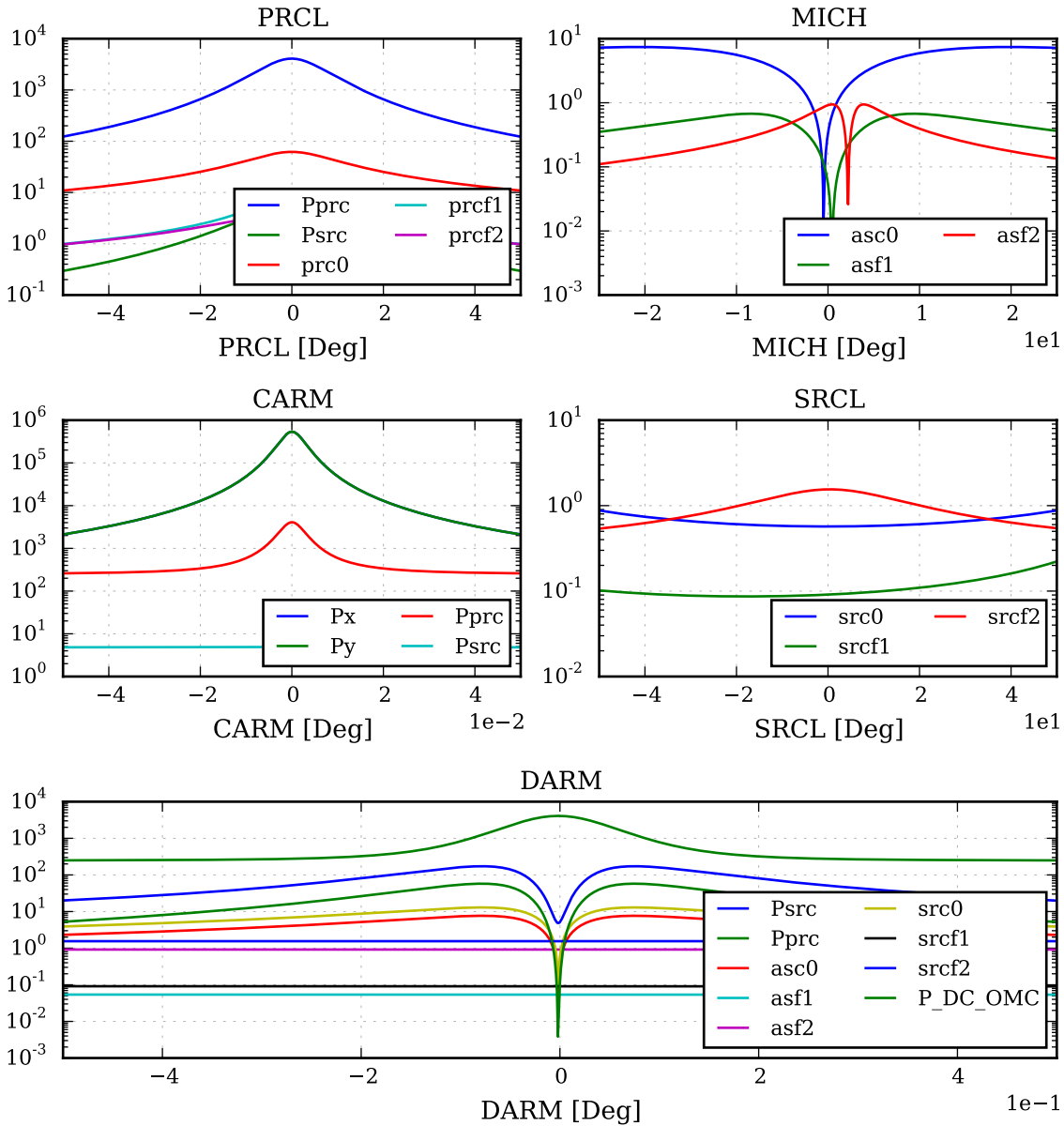


**Figure 4.1:** *ALIGO DOF fields:* This plot shows how these powers and amplitudes vary with the length DOFs of the interferometer. For each DOF there are various optical fields and powers that are of interest as the DOF is changed. No y-axis label are shown here as the relevant unit depends on the trace: those values beginning with 'P' are DC powers in Watts, other values are optical field amplitudes in  $\sqrt{W}$ . Traces ending in '0', 'f1' and 'f2' are the carrier, the 9 MHz RF sideband and the 45 MHz, respectively. From such plots it can be quickly determined whether the relevant fields are behaving as required.

reviewed in [36]. As both of these effects alter the beam shape, they also change the operating point of the interferometer, which must be found for each thermal state of the system.

#### 4. COMMISSIONING AND DESIGN MODELLING

To solve this issue a technique known as *Lock-Dragging* was developed. The idea is to setup the interferometer into an ideal state at first, which must be undertaken by hand (See [53] for more details here). Figure 4.1 and 4.2 show the relevant optical

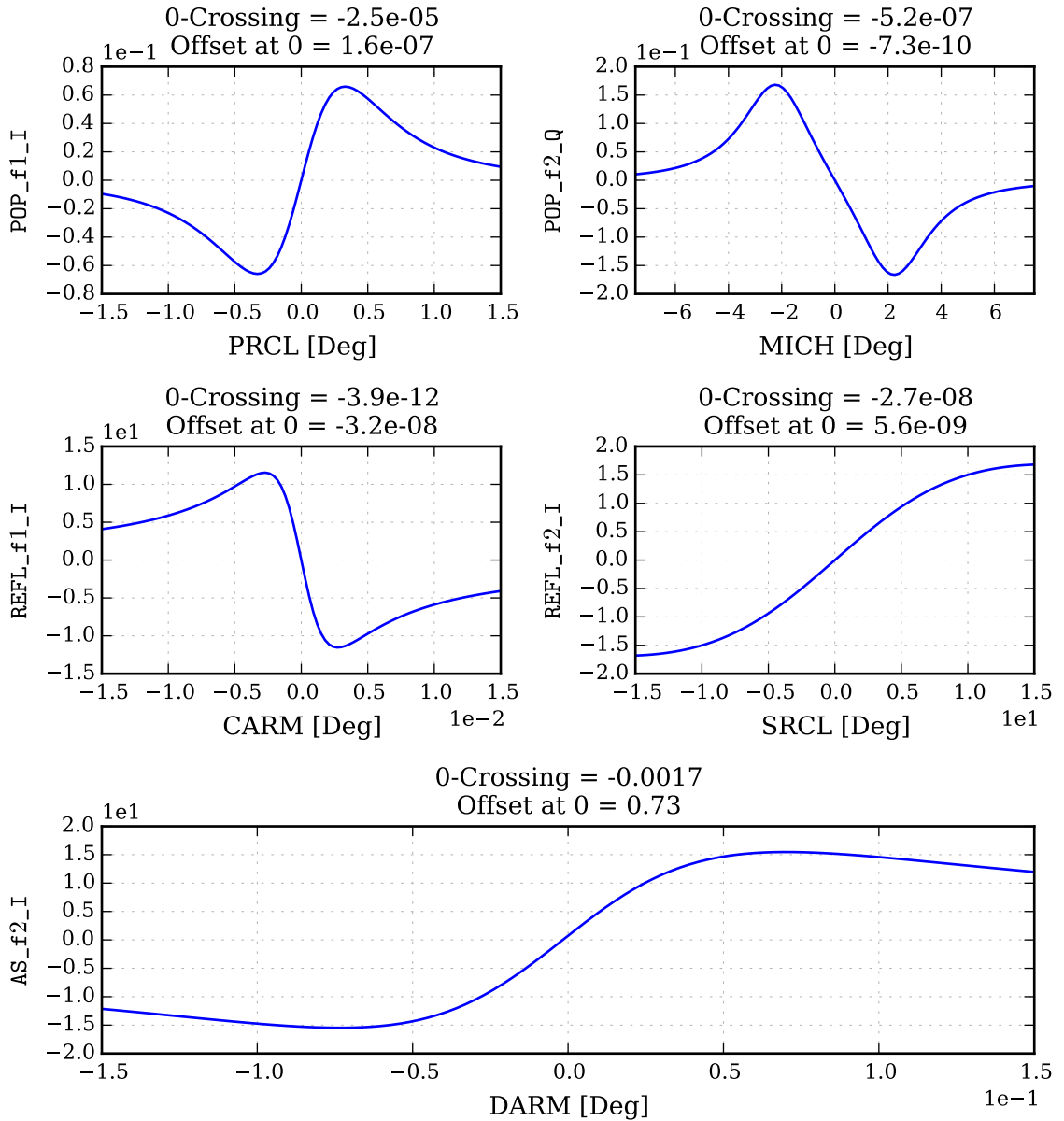


**Figure 4.2:** *aLIGO* length error signals: Shown are the main length sensing error signals for each of the DOFs. This is generated using the AWC (see section 4.4) FINESSE file. This shows the interferometer model is at a reasonable operating point in terms of the error signals: good linear ranges of the signal around a zero crossing. Shown is also the zero-crossing position and the offset at the zero of each DOF. For DARM it can be seen that a large offset is present, this is due to a  $\approx 12$  pm DC offset having been applied.

---

fields and error signals for each longitudinal length DOF for an aLIGO file: this is an example of an ideal operating point to start from. Next, the lock feedback features in FINESSE must be setup, a tutorial regarding which can be found in the appendix A in the FINESSE manual [26]. With the lock feature in FINESSE correctly set up, it will feedback the value of error signal, with some defined gain, to the mirrors for each DOF. This replicates the behaviour of the control systems used to ensure that the error signal is kept zeroed and at a valid operating point. The variable that requires changing must then be stepped in small increments from the initial value to the final value you are interested in. At each small step the locks will adjust the mirror positions keeping the interferometer at a valid operating point and these new positions being outputted and stored in a data file.

The active wavefront control project, as described in section 4.4, is an example of this. Here modelling how the quantum noise limited sensitivity of a detector varies for different strength thermal lenses in the ITMX was required. Before representative sensitivities can be computed for each thermal state, operating points for each must be found. Using a lock-dragging technique the operating points were easily found. It required running a pre-simulation that slowly steps the thermal lens focal length from the initial working operating point to the largest thermal lens required. For each step the mirror positions are recorded and stored in a file. Later this data is the read and used to position the mirrors for a particular thermal lens value and to perform the sensitivity simulation.

A lock-drag of the operating point of the interferometer with a varying ITMX thermal lens can be seen in figures 4.3 and 4.4. The locks in FINESSE are essentially a root finding algorithm, which optimises various mirror positions to zero the error signal within a user-defined accuracy. The change in error signal and the lock output (feedback into the mirror position) is seen in figure 4.3. It can be seen that the error signals are kept below the  $10^{-5}$  accuracy level set in this case. The CARM error signal is being

#### 4. COMMISSIONING AND DESIGN MODELLING

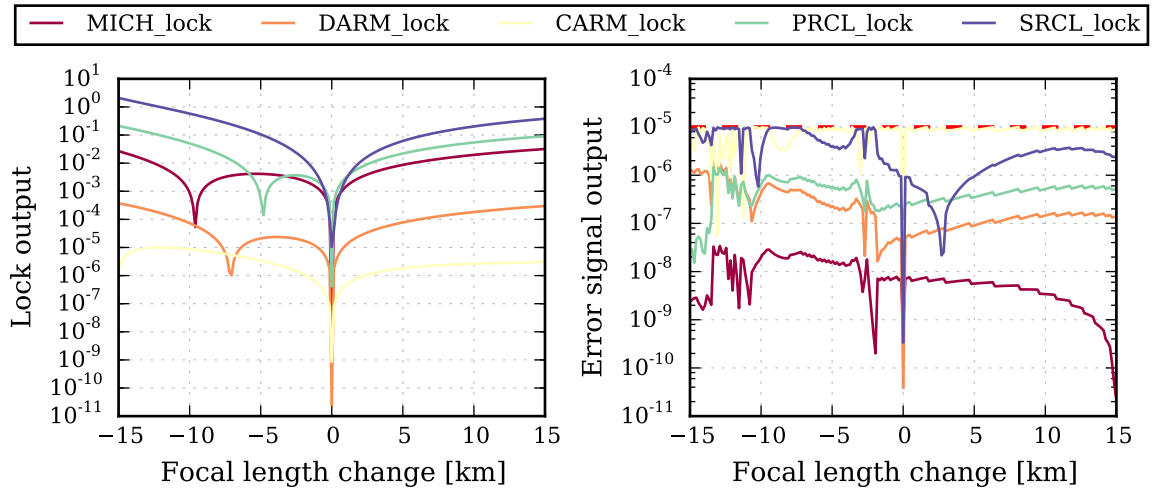


**Figure 4.3:** *Lock-Dragging lock changes:* Shown is the behaviour of the FINESSE locks when varying the ITMX thermal lens: (Left) change in lock output that is fed into the DOF mirrors, (Right) the error signal value for each DOF. The red dashed line shows the lock accuracy.

distorted the most by this thermal lens change which routinely breaches the accuracy level set but is kept in line by the locks. The actual change in the mirror positions can be seen in figure 4.4: this data is the desired result. It shows for a given thermal lens the positions of each mirror.

This lock-dragging however is not foolproof. It is possible that the changes in the interferometer parameters become large enough that error signals become completely distorted: possessing no zero-crossing or too small a linear range. It is also possible that the drag fails due to a large a step in the variable being used. If the step is larger than the linear range of any of the error signals the locking algorithm can lose the lock altogether. There is also the additional issue of cross-coupling between DOFs and their error signals which can cause a lock loss. If the lock-drag fails the first attempt to fix it should be reduce the step size and run it again. Signs that the lock-drag has failed are that the error signals have become much larger than the accuracy level or there are discontinuities in the mirror positions. It is advisable that for each dragged operating point used figures like 4.1 and 4.2 or similar are produced to ensure that the error signals are valid and the zero-crossing matches up with the required optical

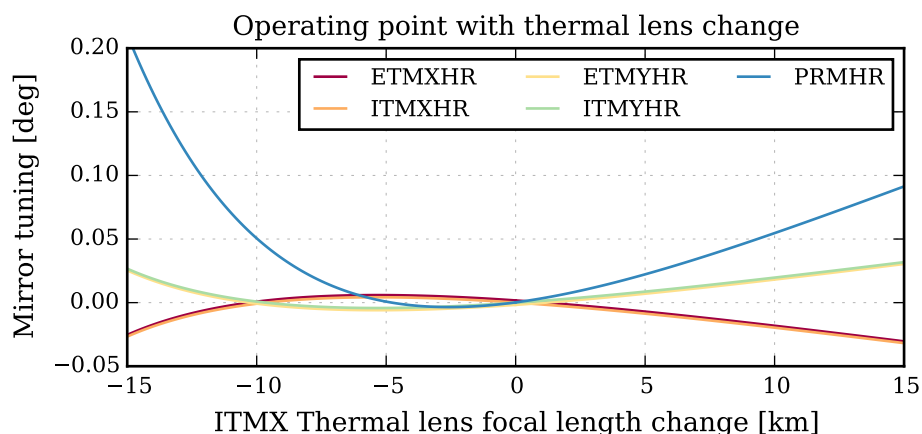


**Figure 4.4:** *Lock-Dragging mirror position changes:* The desired output from the lock-drag are the mirror positions at a particular value of ITMX thermal lens as shown here.

field resonances.

## Outlook

Lock-dragging is currently the only semi-automated technique available for exploring an interferometer's parameter space whilst keeping a valid operating point. It has been used extensively over the past year for commissioning and design problems successfully, saving many hours that would have been wasted hand tuning interferometers files.

There is still much room for improvement in this area though. It is currently unknown whether multiple valid operating points exist, are there others that could be preferable or is there only one? Currently this process relies on finding a usable operating point by hand and sticking with it. Another ideal feature would be the ability to parameterise the operating point to a single, or several, variables which would represent a particular points suitability, or usability. Such variables could then be applied in a searching routine. This in theory could probe a definable parameter space to list potential operating points for a user to investigate further.

### 4.2 Mode Hopping in the LHO SRC

*Mode hopping* is a process where a system jumps between different modes. At LHO whilst commissioning the dual-recycling Michelson (DRMI) (no arm cavities yet) this hopping was seen between resonant higher order modes in SRC when the interferometer was locked [111]. The hops between modes occurred every few seconds. Such a behaviour would be problematic for the detector during a science run, as data is only valid when the SRC is locked to the  $TEM_{00}$  mode which contains the gravitational wave signal. Thus it was asked of the modelling team to simulate the interferometer with various defects to see what might cause such hopping.

At this stage of the detector commissioning only the length control systems were active. The SRC length was being actively controlled when the hops occurred. Hops between which differing higher order modes that are resonant in a cavity will occur if the length error signal possesses multiple zero crossings near one another. Residual oscillations in the length of the SRC could then cause the lock to jump and catch another zero crossing. This was expected to be the main culprit for the hopping as additional higher order modes circulating in the SRC would produce these extra zero crossings. These higher order modes would be present if the system was misaligned or mode-mismatched. The modelling team was asked to experiment with how these effects would distort the SRCL error signal. The work conducted was reported in [112] and presented in [113] to the wider community. This section provides an overview of the results that I contributed towards this work.

The FINESSE file used for modelling the LHO DRMI can be found in version 3 of [2]. To create this file the optical parameters were taken from [51] and positions of the core optics set as specified in [114]. In order to reproduce the SRCL error signal the control scheme as described in [60] was implemented. This uses the 9 MHz and 45 MHz sidebands to sense the length of the PRC, SRC and MICH. For the DRMI

---

Detector	PRCL	SRCL	MICH
REFL 9 MHz I	1.04	0.00	0.01
REFL 45 MHz I	0.26	0.04	0.00
REFL 45 MHz Q	0.00	0.00	0.20

**Table 4.1:** *LHO DRMI length sensing matrix* [112]: Using the model constructed the length sensing matrix for PRCL and SRCL could be observed. A strong cross coupling between from PRCL to SRCL was found.

operation, as noted in [111], PRCL was measured with REFL9I, SRCL with REFL45I and MICH with REFL45Q. Here 'REFL' refers to a photodiode on reflection from the interferometer, i.e. reflection from the PRM. '9' and '45' refer to the demodulation frequency of the photodiode in MHz. 'I' and 'Q' refer to a relative demodulation phase of either 0 or  $\pi/2$  from the optimal demodulation phase.

With these error signals added and optimised the length sensing matrix was computed, shown in table 4.1. The table values denote the gradient of the error signal seen at each detector for a change in each of the DOFs. The larger this value the more a detector will *see* a particular change in a DOF. This showed that a change in PRCL couples  $\approx 6\times$  more to REFL45I than what an SRCL would do. This large coupling means any noise in PRCL would be fed into the SRCL actuators. This coupling would not produce a second zero crossing in the error signal. However, if a second zero crossing were present this additional noise coupling would increase the chance of a hop occurring.

It was found by the commissioners that better initial alignment of the core optics reduced the mode hopping [115]. No alignment control was active at the time when the hopping was first seen, thus alignment would have been able to drift whilst running the interferometer.

Misalignments in the interferometer will also result in slight length changes. Thus to model the types of misalignments expected in the mirror it was important to ensure that a valid operating point was kept in the model. Locks in FINESSE were employed to

#### 4. COMMISSIONING AND DESIGN MODELLING

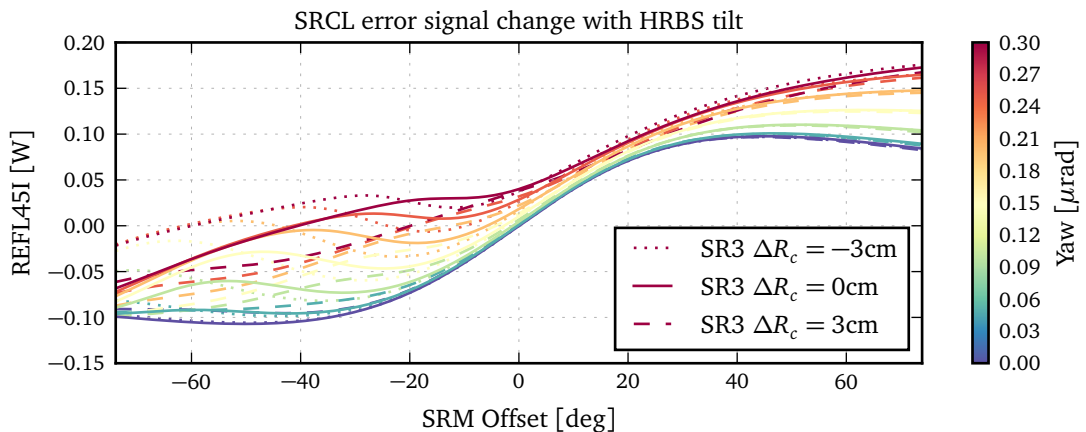


**Figure 4.5:** *SRCL error signal with BS tilt:* Shown is how a yaw tilt of the BS affects the longitudinal SRC length error signal REFL45I. Here SRM offset is in degrees of longitudinal displacement ( $360^\circ = \lambda$ ). This is shown for differing SRC mode separation frequencies, which was altered by changing the SR3 curvature from its original  $\approx 36\text{m}$  ROC.

keep PRC and MICH at their operating points as defined by the REFL9I and REFL45Q error signals. The SRC did not have a lock applied as its length was scanned to output the error signal. For each of the tilts modelled lock-dragging was employed to quickly find valid operating points.

At each of the new tilted state of the interferometer the SRCL length was scanned to compute the REFL45I signal. This was achieved by offsetting the SRM position longitudinally measured in degrees of displacement, where  $360^\circ = \lambda$ . The results of this are shown in figures 4.5 and 4.6 for BS and ITMX tilts. It can be clearly seen here that tilts significantly affect the error signal. In the case of an ITMX tilt an additional zero crossing appeared for  $\approx 35 \mu\text{rad}$  at around a SRCL offset of  $\approx 55 \text{ deg}$ : the zero crossing at  $\approx 35 \text{ deg}$  does not have the same sign slope thus would not be caught by the lock. The *hill* between the two zero crossings plays a part in how likely a hop will occur. If the hill is large then a significant amount of noise or a large glitch in SRCL would be needed to overcome it to reach the next zero crossing. For a low hill the opposite is true and the chance of a hop occurring increases.

As the zero crossing in the error signals relates to the resonance of a particular

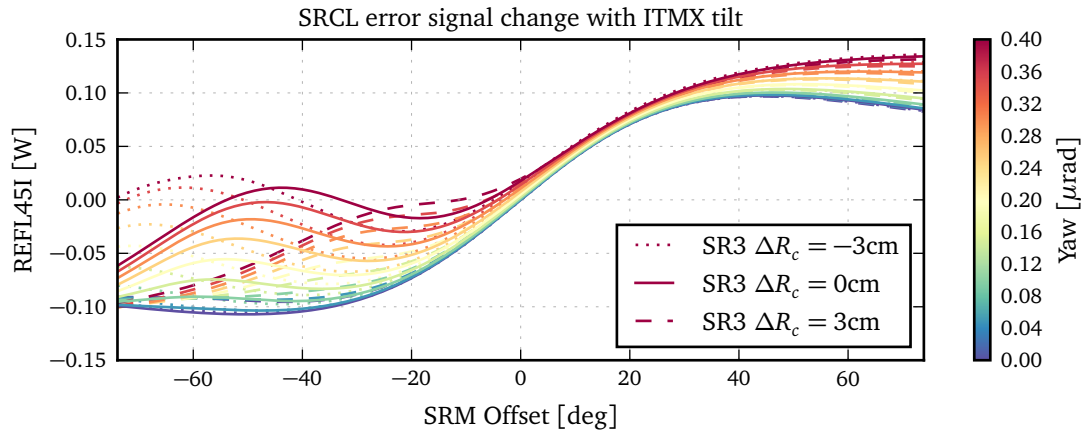


**Figure 4.6:** *SRCL error signal with ITMX tilt:* Similar to figure 4.5, shown is how a tilt in ITMX affects the SRCL error signal REFL45I. This clearly shows how a tilt induces a secondary peak with two extra zero crossings. A change in the SRC mode separation frequency, via a change in SR3 ROC, shows how the zero crossing positions can shift.

higher order mode it's position will be dependent on the SRC round-trip Gouy phase. As some uncertainties exist in exactly what the Gouy phase is for the SRC a range was explored by altering the SR3 ROC. As can be seen in both figures 4.5 and 4.6 the zero crossing is shifted by changing the round-trip Gouy phase of the SRC. Thus, the more unstable the SRC is the more likely hop is to occur.

With the ASC system commissioned at LHO it was possible to measure at which misalignments the hopping began to occur. This was achieved by first locking and aligning the interferometer in a good state, then slowly varying the tilt of a particular optic [116]. The measured tilts for which hopping began to occur is shown in table 4.2. Similar tilts were applied to the model to compute when a second zero crossing appeared in the SRCL error signal. For the BS and ITMX this showed a good agreement.

For misalignments of the SRC mirrors though the results did not agree as well. As can be seen these were larger in general than for the BS and ITMX tilts. Larger tilts would result in beams being clipped more due to the finite size of the SRC mirrors. At the time this was not considered, mostly due to the simulation time required

## 4. COMMISSIONING AND DESIGN MODELLING

---

Optic	Measured	Simulated
BS	$\pm 0.2\mu\text{rad}$	$\pm 0.22\mu\text{rad}$
ITMX	$\pm 0.4\mu\text{rad}$	$\pm 0.36\mu\text{rad}$
SR3	$\pm 0.5\mu\text{rad}$	$\pm 1.2\mu\text{rad}$
SR2	$\pm 4\mu\text{rad}$	$\pm 8.5\mu\text{rad}$
SRM	$\pm 16\mu\text{rad}$	$\pm 70\mu\text{rad}$

**Table 4.2:** *Measured vs. simulated hopping* [112]: A comparison of the measured and simulated tilt of an optic required before mode hopping was seen. For the simulated case this is the tilt at which a second zero crossing appears for a well mode-matched DRMI setup.

for computing the results using many higher order modes and several apertures for varying beam displacements. Here, having the reduced order quadrature scattering calculations, as described in chapter 2, would have proved ideal for such a problem.

### Conclusion

A model representing the DRMI at LHO during the early stages of the interferometer was constructed. This included the MICH, PRCL and SRCL length control schemes. With this, the effect that misalignments in the core optics had on the SRCL error signal were modelled. This was needed to provide a better understanding of why mode hopping was occurring at LHO. During the later stages of commissioning when the alignment control was also included, more precise measurements were made for which misalignments enabled mode hopping. This agreed with simulated results for misalignments of the BS and ITMs. This study work was documented in [112]. Described here is also modelling work examining how Schnupp length, mode-matching and SRM reflectivity also could affect mode hopping; this however was predominantly done by other members of the FINESSE modelling team therefore not discussed here.

---

## 4.3 Beam clipping in the LLO PRC

During the commissioning of the detector at the LLO it was found that the X-arm and Y-arm were not well mode-matched [117]. This was the result of a large differential non-thermal lens present in the substrate of both ITMX and ITMY, 305 km and -82.4 km respectively [118, 119]. This lensing strongly affected the eigenmodes of the SRC and PRC and led to a substantial mismatch of the light returning from the arms. Once the arms were matched, an unexpectedly low power recycling gain of 37 was seen, whereas 57 was expected from models [120]. Here, power recycling gain refers to the ratio between the circulating and the incident power of the PRC. The study undertaken by the FINESSE modelling team demonstrated that this mismatching and larger beams present at the BS resulted in additional clipping losses reducing the PRC gain. This work was reported in both [52] and [53]. My contribution to this work was the development of modal scattering features in FINESSE that were required for computing the clipping within the central interferometer.

When operating at full power, 125 W of input power, the high intracavity power in the arms and the PRC will thermally distort the test masses as they are heated due to absorption [121]. The thermal distortions of the test mass can be modelled with two components [53]: firstly, a thin mirror with variable radius of curvature from heating by the intracavity field; and a thin lens with variable focal length  $f$  to represent the lens formed in ITM substrate, again from absorption. These distortions in cavity geometry significantly reduce the mode-matching between the cavities. The thermal compensation system (TCS) [122] was designed to actuate on the mirrors to correct both effects. To correct the radius of curvatures ring heaters are placed around the AR surface of the test masses; the expansion from heating the mirror applies an opposite change in curvature to that from the absorption of the intracavity field. Secondly, a thermal compensation plate is placed in front of the ITMs which is heated by a CO<sub>2</sub>

#### 4. COMMISSIONING AND DESIGN MODELLING

laser. The heating pattern applied via the CO<sub>2</sub> laser is designed such that the lens forming in the substrate has a negative focal length, compensating the thermal and substrate lens present in the mirrors.

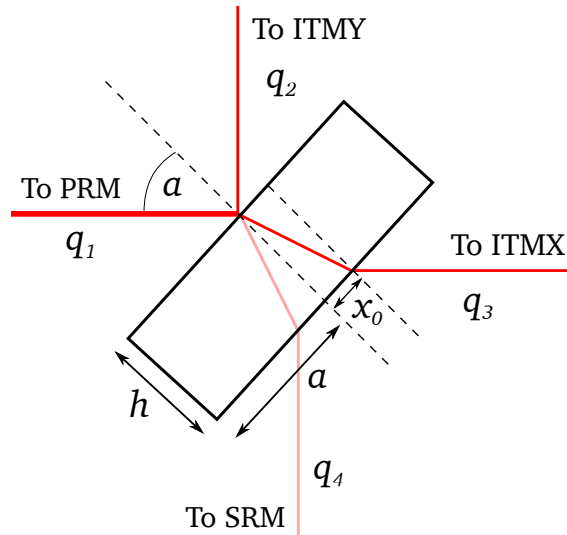


**Figure 4.7:** *HR and AR BS clipping* [52, 53]: Each beam interacting with the main beamsplitter will experience a slightly different clipping due to its finite size. The beam incident on the HR will ideally be centred on the BS face. Those impinging on the AR side however are off-centred from an angled propagation through the BS. The horizontal offset is  $x_0 = 3.35$  cm for a  $45^\circ$  incident beam,  $h = 6$  cm and  $a = 17.5$  cm. The values  $q_{1-4}$  are the beam parameters for the fields travelling in the direction shown by the arrow.

The *cold* state of the mirror curvatures were designed for a 50 km thermal lens present, which should occur with around 12.5 W of input power. As the large difference between the thermal lenses was significant in the installed ITMs, the TCS was employed to correct the ITMX substrate lens from 305 km to -82.4 km to match ITMY. It was whilst doing this the low PRC gain was noted in the experiment when the two arms were matched together. Although the arms were matched, neither were to the PRC; as the PRC was designed with the expectation of positive 50 km lenses. The result of this mismatch meant the size of the beam at the BS was significantly larger than designed for: the design value being 5.3 cm in both  $x$  and  $y$  with 1 ppm clipping loss. Numerically it was found that with the large negative lenses the beam was  $w_x = 6.6$  cm and  $w_y = 7.1$  cm in resulting in 120 ppm of loss. Such an increase in

---

loss would dramatically affect the PRC gain.

To model this loss a realistic beamsplitter was created in the FINESSE model of LLO. The geometry and beams required for this are shown in figure 4.7. The beam makes contact with the BS three times: once on the HR coating in the centre, at the AR coating for the beam heading towards the x-arm and at the AR coating again but towards the SRM. The beamsplitter has a radius of 17.5 cm and a thickness of 6 cm and is constructed from fused silica. Due to the angle  $45^\circ$  of the BS relative to the incoming beams the contact points on the AR side are displaced by  $\approx \pm 3.35$  cm from the centre.

From the incident beams' perspectives the aperture is not a circular one; it is elliptical, with a semi-major axis of  $\cos(45^\circ)17.5\text{cm} \approx 12.4$  cm. Or equally from the beamsplitter's perspective the beam is elliptical with the reciprocal cosine scaling factor.

The differences between the design and LLO clipping seen at the HR and the PRC AR beam is shown in figure 4.8. In this, the beam clipping is shown from the BS's point of view with a stretched beam. Marked is also the boundary within which all but 1 ppm of beam power is contained. As can be seen the larger beam sizes seen at LLO resulted in significantly more clipping loss.

The clipping was modelled as a modal scattering problem, as outlined in section 1.3.3.2. At each of the contact points the finite size of the aperture,  $R_{\text{ap}}$ , the angle of incidence,  $\alpha$ , and any horizontal displacement,  $x_0$ , must be included in the coupling coefficient integral Eq.(1.62). Any light falling outside of the surface is assumed to be lost, therefore the scattering from clipping is treated as an evaluation of

#### 4. COMMISSIONING AND DESIGN MODELLING

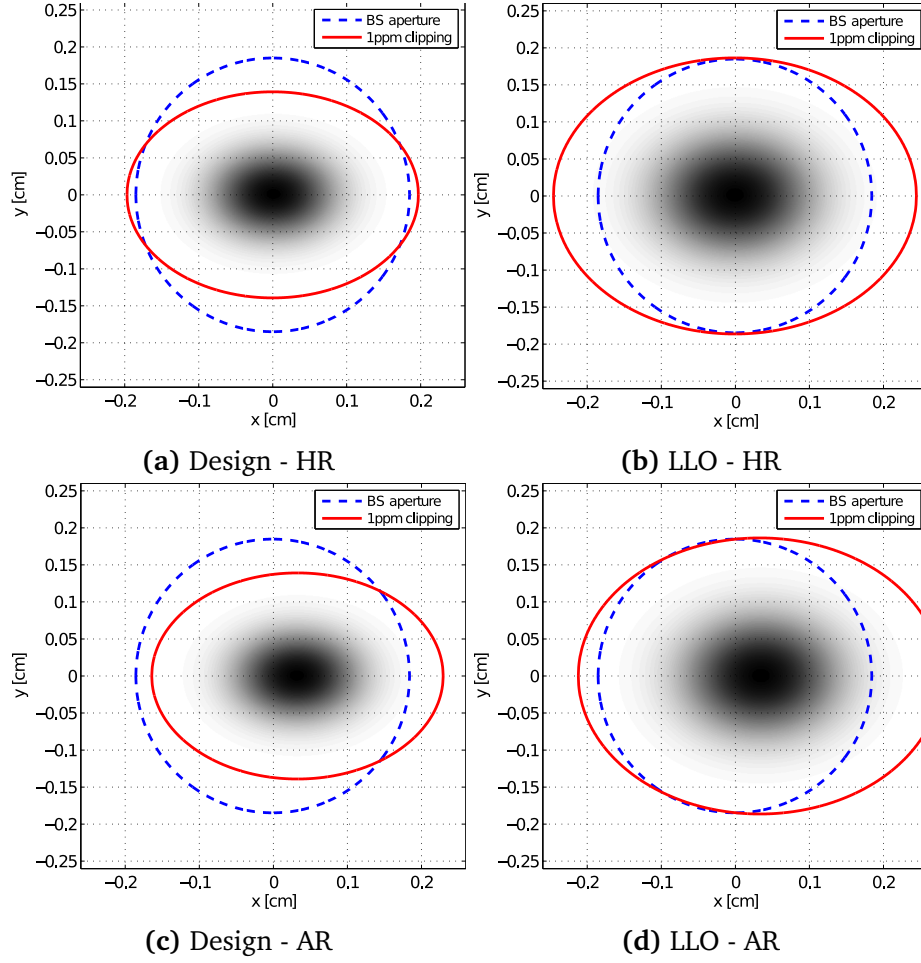


**Figure 4.8:** *Beam clipping at LLO BS* [52, 53]: From the beamsplitters perspective an incident beam is stretched in the horizontal plane. When considering finite apertures these distorted beams will experience additional loss due to the displacement from the centre on the AR side. The comparison shown here is between the designed beam sizes at the beamsplitter and that which was due to the large non-thermal substrate lenses present in the ITMs.

the definite integral Eq.(1.62)

$$\begin{aligned}
 \mathbf{K}_{nm,n'm'}(\mathbf{q}, \mathbf{q}'; \alpha(x - x_0, y; R_{\text{ap}})) = \\
 \cos(\alpha) \int_0^{2\pi} \int_0^{R_{\text{ap}}} \mathcal{K}(\lambda_x; r \cos(\alpha) \cos(\theta) - x_0) \mathcal{K}(\lambda_y; r \sin(\theta)) r dr d\theta. \quad (4.1)
 \end{aligned}$$

The integrand consists of just the kernels Eq.(1.63), which are smooth Hermite Polynomials. The adaptive integration library *Cuba* [65] was used to evaluate this integral in the implementation programmed into FINESSE. The performance of the *Cuhre* rou-

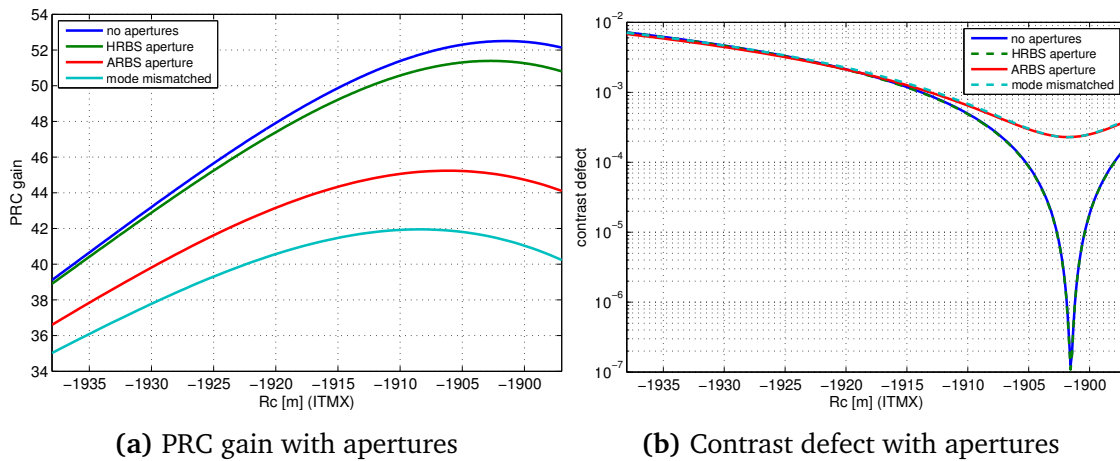


**Figure 4.9:** *Contrast defects and apertures* [52, 53]: By tuning the ITMX radius of curvature to represent the actuation of the TCS, it was possible to simulate how mode-matching and clipping affects both the PRC gain and the contrast defect. In the ideal cases the both the gain and defect occur for the same radius of curvature, i.e. mode-matching is optimised. With apertures this is no longer true, as there exists an optimal beam size that reduces the clipping loss whilst ensuring a reasonable mode-matching.

tine in this library was found to be fast compared to typical Newton-Cotes integration used—reduced order quadrature had not been implemented at this point.

## Results

With clipping calculations allowing for offsets and non-normal angle of incidences implemented in FINESSE an apertured LLO model was constructed. Optical parameters used were taken from measured values of those installed on site [51] and the layout of the optics as defined by the LLO coordinate list [123]. Also included were the aforementioned non-thermal lenses in the ITM substrates.

First, a plane-wave model was used with the measured values of the optics. Here, an idealistic PRC gain of  $\sim 53$  was computed, which involves no mode-matching or clipping effects. This slight deviation from 57 as expected [120] was due to the measured loss values being included for each optic [51]. Such losses represent optic absorptions, non-zero AR coating reflectivities and beams being picked-off for diagnostic and sensing outputs.

#### 4. COMMISSIONING AND DESIGN MODELLING

---

Both the mode matched and mismatched cases were considered in the modelling: Mismatched being that with no thermal actuation on the ITMs, and matched considering when the TCS was used to match the ITMX non-thermal lens to ITMY's. In both cases the TCS was also used to actuate on the ITMX radius of curvature to better match the beams. This is modelled by varying the ITMX RoC. Whilst varying the RoCs it was also important to ensure that the model was still at the correct operating point. This was achieved using the length sensing and control scheme discussed in 1.3.5 and implemented with the FINESSE locking feature.

Figure 4.9 shows the results of including the different apertures present due to the finite size of the BS. It was seen that clipping at the HR surface was minimal, as the beam was well centred. The AR clipping was the dominant source of loss due to the off-centre clipping and larger beam sizes as seen in figure 4.8. The maximum gain in each case was achieved at different ITMX RoC values. This optimal value is a combination of optimised mode matching but minimised clipping loss for the beam contact point on the AR side going towards ITMX. This shift in optimal PRC gain does not correspond to a shift in the minimum contrast defect value; a feature seen experimentally by commissioners. The contrast defect is the ratio of the power incident from each of the arms,  $P_x$  and  $P_y$ , on the beamsplitter and the power at the dark port,  $P_{\text{dark}}$ :

$$\text{CD} = \frac{P_{\text{dark}}}{P_x + P_y}. \quad (4.2)$$

It provides a measure of much differential light is present between the two arms.

Further clipping losses were also present due to the baffles installed around the BS in the experiment to reduce scattered light returning to the beam path. These clippings were also considered and showed another drop PRC gain as seen in figure 4.10a. Values roughly corresponding with the PRC gain of 37 as seen experimentally were then seen. It was shown that the by translating the beam incident on the BS it was

possible to improve the PRC gain, figure 4.10b. Although, this optimises the PRC field by centring the PRC beam at the AS at the expense of the SRC beam being clipped further.

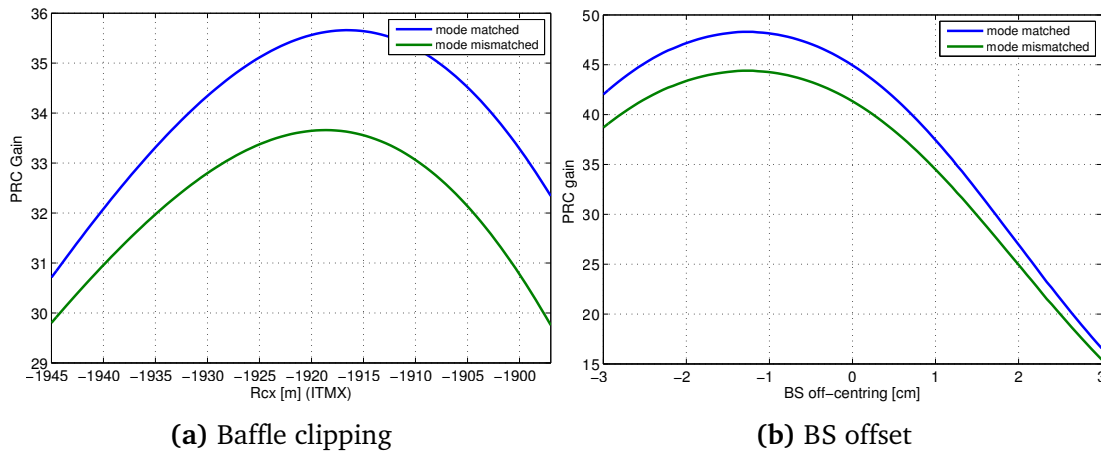


**Figure 4.10:** *Baffles and centring at LLO BS* [52, 53]: The clipping loss present due to the baffles included experimentally was also considered. Here showing another significant reduction in PRC gain. It was also shown that by centring the clipped beams this clipping loss could also be reduced and a significant gain retrieved.

## Conclusion

During the commissioning of LLO unexpected PRC gains were seen and the reasons for this were unclear. The aLIGO FINESSE modelling team was asked to investigate the issue. Upon further study of the mode-matching issues present due to non-thermal substrate lenses clipping of the beams at the beamsplitter and baffles appeared to be the reason for the observed low PRC gains. This study required the inclusion of clipping at the beamsplitter in FINESSE which I implemented. The faster clipping calculations allowed us to model the system and provide the required feedback to the commissioners. This work was reported in the technical note [52].

### 4.4 Active wavefront control modelling

The purpose of the *active wavefront control* (AWC) is to control losses in an interferometer due to mode mismatches of the optical fields. Previous to this effort, mode matching was achieved to be just good enough [124]. Length and alignment sensing and control systems have already been applied, wavefront control is simply the next step up from these, as just good enough can always be improved upon. Achieving this will allow for fewer higher order optical modes, lower loss for squeezing and higher circulating powers within the interferometer.

My contribution to this work was the addition of quantum noise with HOM in FINESSE, PYKAT tools to improve modelling efficiency and performing the modelling of filter cavity mismatches. This work was presented to groups working on the AWC project in August 2015 [109].

The main source of mode mismatches are from thermal lenses, with those in the ITMs being the more extreme. Such issues already arose in initial LIGO and the thermal compensation system was included in aLIGO to combat this by correcting curvatures and thermal lenses in the test masses. This is primarily aimed to actuate on the X and Y arm modes, although it also alters the SRC and PRC modes as they contain the ITM thermal lenses.

To focus efforts, the AWC white paper outlines a roadmap based on both experimental and simulation research that must be conducted [125]. FINESSE is currently the most advanced simulation tool for studying both mode matching and quantum effects for a large interferometer. The aLIGO FINESSE team's experience with this type of modelling fitted the mode matching requirements, sensing scheme and control scheme optimisation stated in the white paper.

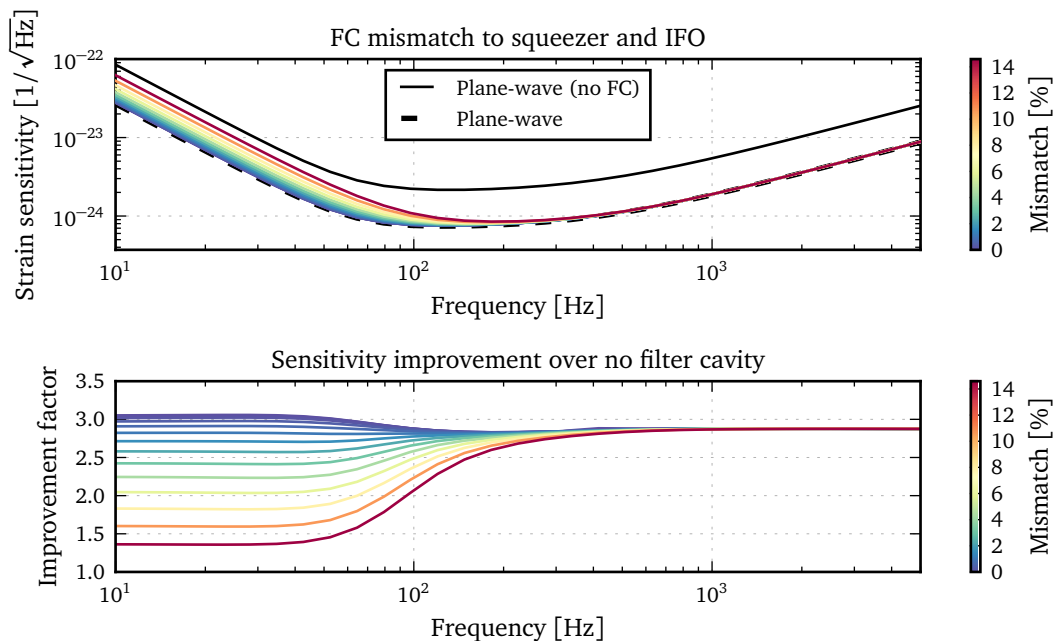


**Figure 4.11:** *Filter cavity mismatching:* Mismatching the filter cavity to both the squeezer and interferometer, which are matched, results in a degradation of the squeezed state for low frequencies. Here a mismatch of 14% still does not degrade the improvement to its original sensitivity. High frequency is unaffected as this does not resonate in the FC and thus does not see the mismatch.

### Filter cavity performance with mode matching

Squeezed light is an intended feature of aLIGO to improve the quantum noise limited sensitivity. By squeezing the phase noise of vacuum, shot noise at high frequency is improved, amplitude squeezing then reduces the low frequency radiation pressure noise. A broadband reduction of both shot and radiation pressure noise is possible by using a frequency dependent squeezed state; ideally low frequency vacuum noise is amplitude squeezed and high frequency with phase.

A frequency dependent squeezed state is achieved using a *filter cavity* [126] (FC). This is a detuned cavity which applies a frequency dependent phase shift to sidebands reflected from it. If correctly designed the phase shift can be made such that a phase squeezed state is rotated to an amplitude squeezed state at low frequencies. This requires a low-loss, high finesse cavity whose pole frequency is chosen so that the

#### 4. COMMISSIONING AND DESIGN MODELLING

rotation is optimised, as stated before, for a broadband reduction in quantum noise.

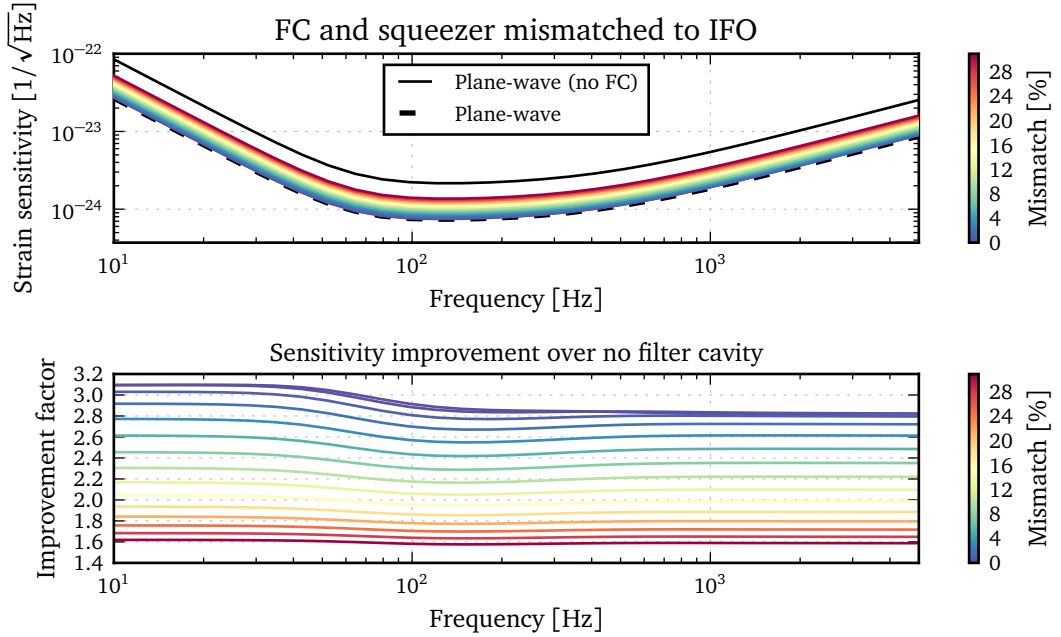


**Figure 4.12:** *Filter cavity mismatching:* Mismatching both the squeezer and FC to the rest of the interferometer results in a broadband loss. A large mismatch still does not degrade the improvement to a state without the filter cavity though.

Figure 4.11 depicts a filter cavity applied and optimised to the AWC aLIGO file. The design of the filter cavity is based on that described in [127]. A linear 16 m confocal cavity was used as stated in the paper, the radius of curvature of both mirrors being 15.9 m; this value was not stated in the paper but was chosen to be less than 16 m to avoid a geometrically unstable cavity. A confocal cavity is ideal as this provides the smallest beam size possible at each of the FC’s mirrors, reducing clipping losses. In all, the real target as stated in [127] is to reach total losses of 1 ppm/m. For this work the actual details of clipping losses are not relevant thus are not included in this model. A perfectly reflective end mirror was used thus the only loss being the input mirror transmission. The exact parameters used were  $T = 61$  ppm for the input mirror with the end mirror tuning of  $\approx -2.6$  pm. These values were found using an optimisation routine with PYKAT to provide the best broadband improvement. The filter cavity was then mode-matched to the output path where a circulator is used to inject

---

the squeezed field into the SRM; mode matching was accomplished by optimising the lengths and two lenses with PYKAT. The exact parameters can be seen in appendix E in the `filtercavity` block of code. Using a plane-wave model (no possible mode mismatches) the resulting reduction can be seen in figure 4.11 showing  $\approx 3\times$  broadband improvement in sensitivity.

There are two distinctive effects from mode-mismatch with the FC. The first is when the squeezed input field and the interferometer are matched but the FC is matched to neither. In this case, the squeezed fields within the FC linewidth are nearly resonant and experience a distortion from the mode-mismatch. The low frequency squeezed fields then experience a loss and a subsequent degradation in the squeezed state. Higher frequencies do not experience this loss as they are not resonant in the FC, thus are unaffected. Secondly, the squeezed input field and FC are matched, but both are mismatched to the interferometer. Here, the squeezed state is optimally rotated. The mode-mismatch between the prepared squeezed field and the interferometer will lead to broadband loss, degrading the squeezed state across the frequency range.

The first case is shown in figure 4.11 and the second in figure 4.12. As the squeezer and FC are matched the rotation of the squeezing works but they experience a loss as they are mismatched to the rest of the interferometer. This is a broadband loss at all frequencies.

There is also a third case, where the FC and interferometer modes are matched but the squeezed field is not. The effect on the sensitivity is a combination of the two above as it is a mismatch with both FC and interferometer.

These results broadly agree with the simplified analytic mismatching model used in [128], which treats mismatches as pure losses. At this stage of the project they simply provide the possible range of effects that mode-mismatching will have on the sensitivity; thus will be eventually used to define how much mode-mismatching can be tolerated.

## 4. COMMISSIONING AND DESIGN MODELLING

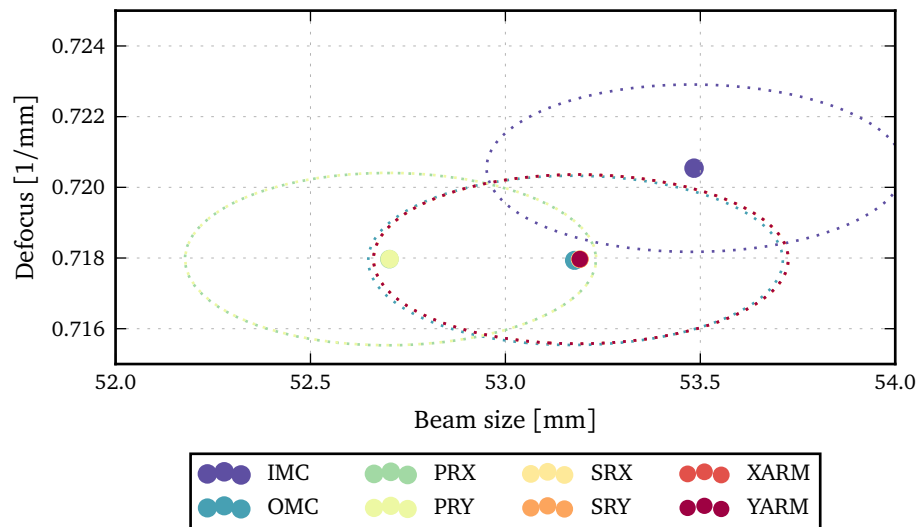


**Figure 4.13:** *Mode-matching of aLIGO cavities:* The AWC aLIGO FINESSE file was well mode-matched by hand, by tuning lengths and radius of curvatures. This shows a beam parameter plot of the default state of the file showing good mode-matching. The circles show the 99.99% region for each of the cavity modes. Defocus is the reciprocal of the beam radius of curvature.

### Beam parameter trajectories

One goal of the AWC project is to enable a graphical representation of the mode-matching between the cavities. Eventually this would become an additional debugging tool for commissioners using realtime data from the interferometer. The principal idea is to produce a plot that displays the relative mode-matching between cavities. This can be achieved by tracing each of the cavity eigenmodes to a common point in the interferometer; the one chosen here is at the main beamsplitter. If two cavities are perfectly matched the beam parameter at the beamsplitter will be the same. Each of the traced cavity eigenmodes will result in a beam parameter at the beamsplitter, the beam waist and defocus is then used to make a scatter plot showing the proximity of each cavity mode to the others.

Using the constructed aLIGO FINESSE file with all the relevant mirror geometries and lengths such plots can be constructed, as shown in figure 4.13. FINESSE has been built in a robust beam tracing algorithm. The required beam parameters are found by enabling the tracing of a single cavity at a time and recording the  $q$  values traced

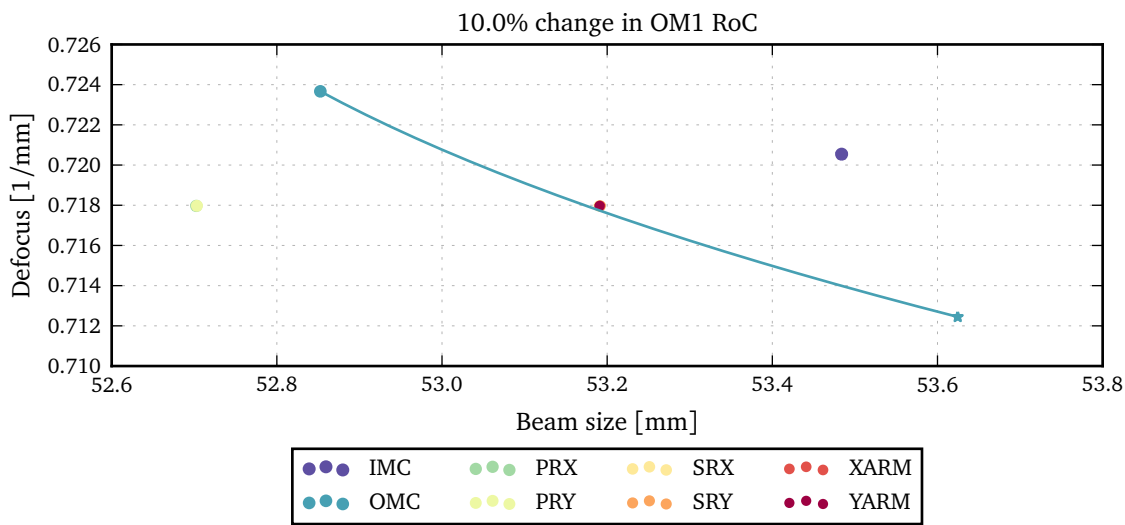


**Figure 4.14:** *OM1 beam parameter trajectory:* Beam parameter traces can show how well mode matched multiple cavities are. Here the cavity modes are all traced to the main beamsplitter and plotted are their defocus (1/RoC) and the beam size. Shown is how a change in OM1’s RoC alters the interferometer mode matching. The range of values is  $-10\%$  (circle) to  $+10\%$  (star) in the RoC. This change only affects the OMC mode as no other beam parameters change.

by FINESSE. The beam parameters found in each cavity can then be compared to its spatial eigenmode to compute an overlap percentage with Eq.(1.74). In the plot the overlap for each cavity is  $\approx 99.99\%$  mismatch levels, which would represent a well matched system.

Such a plotting device allows us to observe how mode-matching changes with variations in an optics geometry. For example, figures 4.14 and 4.15 show how a change in the RoC of OM1 and SR3 mirrors respectively. This is of particular use for exploring potential actuators that will be required to form a control system. Actuators that can control both beam size and defocus separately will be required. Using these models the requirements for the range and precision of actuation can be explored.

## Outlook

The AWC project is one that started towards the end of my PhD. It will be carried on beyond it though by others. Thus, this work represents only the beginnings of the

## 4. COMMISSIONING AND DESIGN MODELLING

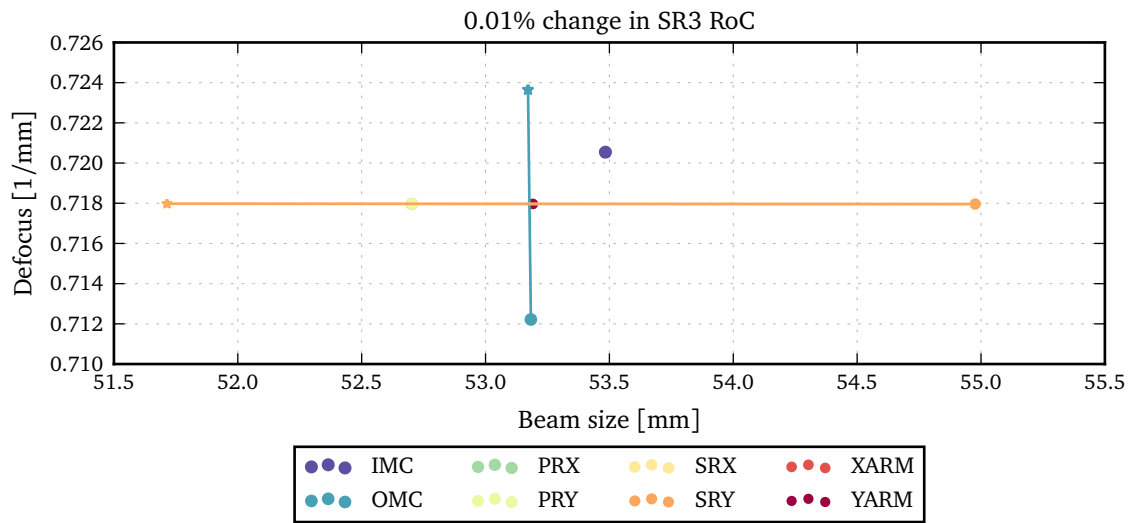


**Figure 4.15:** *SR3 beam parameter trajectory:* Similar to figure 4.14 but varying SR3 to model the effects on mode matching.

modelling required. To ensure that this was possible an AWC FINESSE file was produced with accompanying PYKAT tools to enable efficient modelling of possible AWC actuators and sensors.

The next steps will be to include bullseye detectors [125] for measuring beam size changes to the model. With these we will begin to model an AWC sensing matrix for beam size changes and experiment with feedback to the actuators.

## 4.5 Conclusion

The results presented in this chapter are those highlighting some of the modelling work I undertook for commissioning and design activities. These modelling tasks drove the need for the future development discussed in the first half of the chapter. Highlighted was the lock-dragging technique which enabled the modelling tasks mentioned to be undertaken in an efficient manner when considering multiple operating points. The three modelling tasks were highlighted: how the distortions in the SRCL error signal produced mode hopping; the effect of beam clipping and mismatching on the PRC gain

---

at LLO; and the active wavefront control project. The former two were completed and reported in technical notes as these were requested by commissioners to provide some insight to the particular problems. The AWC project however is still ongoing and the work reported here represents the initial efforts in this direction.

#### **4. COMMISSIONING AND DESIGN MODELLING**

---

## Chapter 5

# Invariance of waveguide grating mirrors to transverse displacement phase shifts

The paper *Invariance of waveguide grating mirrors to transverse displacement phase shifts* [129] was published on the work in this chapter and presented in [43]. The finite-difference time-domain code used for this work was developed by myself during my masters degree [130]. This originally attempted an initial analysis of a waveguide but needed refinement and further analysis. All the simulations performed and the analysis was performed by myself. The plane-wave model provided in the paper was contributed by Daniel Freidrich and general advice was given on gratings structures by Frank Brückner and Andreas Freise. Text and figures from the paper have been used verbatim in this chapter. Some content and formatting has been amended to fit better into this thesis.

The sensitivity of high precision interferometry experiments such as the preparation of entangled test masses [131], frequency stabilisation with rigid cavities [132]

## 5. WAVEGUIDE PHASE NOISE INVARIANCE

---

and gravitational wave detectors [133] are eventually limited by the quantum noise of the interrogating light or the thermal noise of the optical components. The high frequency sensitivity of gravitational wave detectors is limited by quantum shot noise which is typically improved by increasing the laser power circulating within the interferometer, as discussed in chapter 1. This increase in laser power results in more power being absorbed by the high-reflectivity coatings and substrates, inducing substantial thermal distortions. Such distortions affect both the control and performance of the detector [53]. A number of new techniques have been suggested to reduce both the distortions from high power beams as well as thermal noise: the use of non-fundamental beam shapes such as the Laguerre-Gaussian modes [134]; all-reflective interferometer layouts using dielectric gratings [135]; and the use of waveguide grating mirrors (WGM) [136].

The test mass mirrors used in advanced LIGO have approximately 40 sub-wavelength layers applied to them to form their high reflectivity coating. Each layer in the coating introduces additional coating thermal noise [137, 37]. This increase in thermal noise is due to a combination of the mechanical loss from bonding multiple layers together and that the materials used for 1064nm coatings having larger intrinsic mechanical losses than the substrate material (Fused silica). All-reflective grating structures [135] offer lower thermal noise as no coating stacks would be required. The all-reflective nature of such designs mean that alternative materials could be explored which provide preferable thermal noise levels. However, it was found that gratings can couple relative transverse displacements between itself and the incident beam into the phase of the non-zero diffracted orders [138, 139]. This coupling placed stringent requirements on the alignment and stability of gratings and the incident laser beams so as not to induce additional phase noise when used in gravitational wave detectors [140].

Another option being discussed at the time was the use of waveguide grating mirrors to replace more traditional coating stacks. Waveguide grating mirrors would re-

---

place the high reflectivity mirror coating stacks used on fused silica substrates with just two separate layers, reducing their thickness by a factor of 10 to 100. This promised to reduce the Brownian coating thermal noise [133, 141]. However, as WGMs also rely on diffraction into the first order the concern was at the time that the susceptibility to the transverse displacement coupling could negate these benefits.

This work was undertaken to demonstrate that waveguide grating mirrors are not susceptible to this transverse phase coupling. Both a theoretical and numerical argument was published. In this chapter I first provide a simplified plane wave picture of why no transverse to longitudinal coupling should exist in section 5.1. This is then verified by using a rigorous Maxwell equations solver using finite Gaussian beams in section 5.2. The finite-difference time-domain (FDTD) solver of Maxwell's equations was programmed by myself to obtain a clearer understanding of the accuracy and limitations of such a model. This code was also used for the modelling of transverse displacement phase coupling for standard grating structures as part of an experimental project. This work was reported on and published in both [139] and [142].

## 5.1 Waveguide grating mirrors

Waveguide grating mirrors in their most simplistic form consist of two layers: (i) a waveguide layer applied to some substrate material; and (ii) a grating layer which couples the incident laser light into the latter [136]. The grating layer can be etched into the waveguide layer thus creating a lower loss single layer compared to multiple stacks of dielectric coatings [141]. In this case both the waveguide and grating layers are then made from the same high refractive index  $n_h$  material, the substrate material then has a refractive index  $n_l$ . The materials used for 1064nm light are fused silica for the substrate and Tantalum pentoxide for the high refractive index material. A ray picture of an incident plane wave interacting with the WGM is shown in figure 5.1.

## 5. WAVEGUIDE PHASE NOISE INVARIANCE

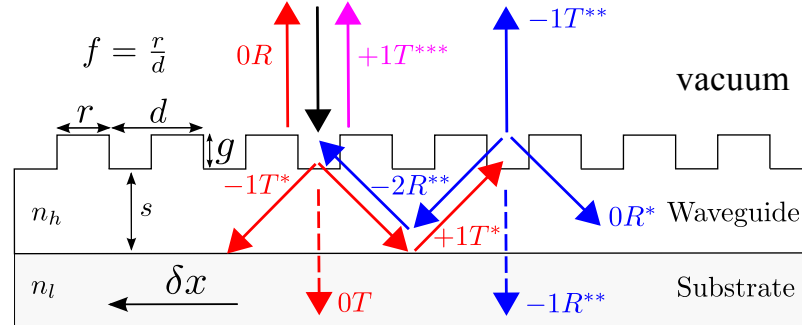


**Figure 5.1:** *The ray picture* [129]: The incident beam (black) is coupled into the waveguide layer by the grating into  $m = \pm 1$ . Orders  $\pm 1T$  propagate along the waveguide coupling back into the vacuum (blue) to interfere with the initially reflected light,  $0R$ , picking up  $\Delta\Phi_m$  phase terms with each interaction with the grating. Further coupling into the vacuum is also possible (magenta) which involved further  $\Delta\Phi_m$  terms. The \* superscript refers to the number of diffractions beam has undergone.  $R$  = Reflection from grating,  $T$  = Transmission from grating, first number is order of diffraction  $m$ .

For given materials and laser light wavelength, the grating period  $d$  must be chosen to form a Littrow configuration, where a normally incident beam is diffracted on transmission into the 1<sup>st</sup> orders within the waveguide layer. The angle at which these modes are diffracted must allow total-internal-reflection (TIR) at the waveguide-substrate boundary to occur (This requires  $n_l < n_h$ ). These reflected modes are then diffracted once again by the grating layer. TIR at the substrate boundary along with the grating create a waveguide in which the  $\pm 1^{\text{st}}$  orders propagate along. These undergo diffraction at the grating multiple times, each time coupling out into the vacuum where it interferes with the reflected laser light. The remaining grating parameters, namely the thickness of the waveguide layer  $s$ , fill-factor  $f$  and groove depth  $g$ , along with the geometrical grating parameters must be carefully chosen to produce a theoretical 100% reflectivity [136, 141] which occurs in the diffracted and specularly reflected light undergo perfect constructive interference.

A transverse displacement  $\delta x$  of a grating structure relative to the incident beam induces a phase shift of [140]:

$$\Delta\Phi_m = 2\pi m\delta x/d. \quad (5.1)$$

---

This phase shift is relative to the phase already accrued by a non-displaced beam diffracted into the  $m^{\text{th}}$  order,  $\Delta\Phi_m = 0$ . For WGMs to experience no transverse to longitudinal phase coupling it must be ensured that any of the rays interfering with the specularly reflected field do not have any phase terms dependent on  $\delta x$ . From figure 5.1 each time a ray is diffracted it picks up an additional  $\Delta\Phi_m$  term. Here an \* is added as a superscript each time this has happened. Examining figure 5.1, the ray  $-1T^{**}$  diffracted into the vacuum has collected two  $\Delta\Phi_m$  terms. The total accumulated phase in the field is then:

$$\Phi_{-1T^{**}} = \Phi_o(s, d, g, f, n_l, n_h) + \Delta\Phi_{+1} + \Delta\Phi_{-1}, \quad (5.2)$$

where  $\Phi_o$  is a collection of the additional phase terms accumulated that depends on the WGM parameters, but not  $\delta x$ .  $\Phi_o$  is tuned by adjusting each parameter to produce 100% reflectivity as required for a WGM to function.

From Eq.(5.1) it can be seen the  $\Delta\Phi_{-1}$  and  $\Delta\Phi_{+1}$  terms cancel. A similar argument is valid for all other rays that couple out to interfere with the directly reflected field, such as  $+1T^{***}$ . Thus, following this simplified picture any of the phase noise effects outlined in [140] for gratings should not apply to WGMs under normal incidence.

## 5.2 Numerical experiment

In order to provide a rigorous and more physically correct model of a finite beam reflected from a WGM, a numerical finite-difference time-domain (FDTD) based algorithm was used. This provided the ability to model a variety of grating structures as well as arbitrary and finite incident electromagnetic field distributions. The simulation tool was coded myself in the *Java* language. It is open sourced and can be found at <http://kvasir.sr.bham.ac.uk/redmine/projects/fdtd>, the code

## 5. WAVEGUIDE PHASE NOISE INVARIANCE

---

itself is based on the work of Taflove who pioneered much of the FDTD field [143]. As only a displacement of the WGM in one direction orthogonal to a normally incident Hermite-Gaussian beam was required, A 2D FDTD simulation also sufficed. To perform the simulation two features were also required for the simulation [143]: *Total-Field Scattered-Field* (TFSF) for separating the incident and reflected beam from the WGM and *complex perfectly matched layers* (CPML) to reduce reflections from the simulation boundaries.

The aim of the simulation was to measure the wavefront of a Hermite-Gaussian beam reflected from a WGM whilst displacing it from  $\delta x = 0 \rightarrow d$ . Along the wavefront the phase can then be deduced and plotted against  $\delta x$  to view any apparent phase shifts. The simulation setup is depicted in Fig.5.2, where a Hermite-Gaussian  $TEM_{00}$  is injected in the  $\hat{x}$  direction along the TFSF boundary and the electric field of the reflected beam is measured along the measurement line  $15\mu m$  away to avoid near-field variations. The *Courrant stability factor* [143] for the simulation was chosen as  $S = c\Delta t/\Delta x = 1/\sqrt{2}$ ; where  $\Delta t$  is the simulation time-step and  $\Delta x = \Delta y = 25nm$  are the size of the 2D discretisation of the simulation space with dimensions  $L_y = 250\Delta y$  and  $L_x = 4000\Delta x$ . The injected beam had a wavelength  $\lambda = 1064nm$  and was positioned such that the waist was at the WGM with size  $w_0 = 800\Delta x = 20\mu m$ . The WGM parameters chosen were  $d = 28\Delta x = 700nm$ ,  $g = 14\Delta x = 350nm$ ,  $f = 0.5$  and  $s = 5\Delta x = 125nm$  which provided a reflectivity of 99.8% for the incident beam (in agreement with [136]). The indices of refraction used were fused silica for  $n_l = 1.45$  and  $Ta_2O_5$  for  $n_h = 2.084$  which are the typical materials used for 1064nm optics.

The phase shift for  $m = \pm 1$  is periodic with displacements of the grating period  $d = 28\Delta x$  as can be seen from Eq.(5.1). Thus, for this effect to be visible the simulation was run multiple times for the offsets  $\delta x = p\Delta x$  with  $p = 0, 1, 2, \dots, 28$ ; 28 samples were used as this ensured integer steps in offset as FDTD is based on discretised space. To compare the phase of the beam for each offset the steady state of the reflected field

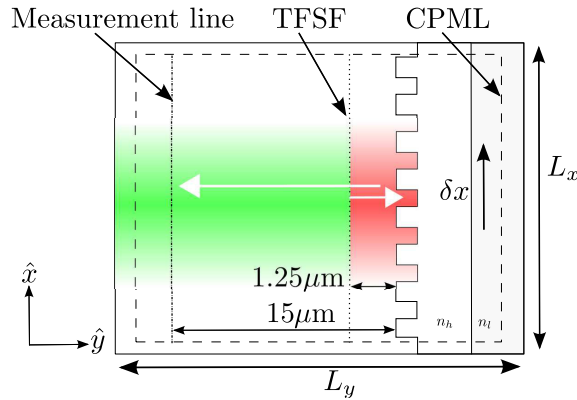


**Figure 5.2:** *Simulation setup* [129]: Schematic layout of 2D FDTD simulation for testing WGM shift invariance. Gaussian beam injected along TFSF boundary onto WGM (Red). The reflected beam (Green) then propagates to the measurement line where the phase is measured. The CPML absorbs outgoing waves to reduce reflections from boundaries.

must be found. Approximately 3000 time steps were required for the reflected beam to reach an approximate steady-state in each simulation. Once reached, 1024 time samples of the electric field,  $E_p(x, t)$ , at each point along the measurement line were taken to extract the phase from. The generalised Goertzel algorithm (based on Fast Fourier Transforms (FFT)) [144] was used to extract both the amplitude  $A_p(x)$  and phase  $\phi_p(x)$  of the reflected beam along the measurement line for the incident laser frequency  $f_0 = c/1064\text{nm}$ .  $\phi_p(x)$  was obtained for each offset  $\delta x = p\Delta x$  of the WGM with the change in phase with displacement defined as  $\Delta\phi_p(x) = \phi_p(x) - \phi_0(x)$ .

The simulation showed that displacement phase shift for WGMs are at least  $10^5$  smaller than for an equivalent grating setup, see figure 5.3. The central plot shows the phase change as a function of the displacement along the beam profile; the satellite plots provide the scale for the central plot. The top plot shows  $\Delta\phi_{14}$  increasing slightly towards the edge of the beam, this is expected to occur when  $A_p(x) \rightarrow 0$ , which degrades any accurate calculation of the phase as the *signal-to-numerical noise* ratio decreases. At the beam's peak intensity the phase change with WGM offset is  $\Delta\phi_p(x = 0) \approx 20\mu\text{rad}$ , this also shows no real dependence on  $\delta x$ . This phase change is five orders of magnitude smaller than what Eq.(5.1) states for displaced grating

## 5. WAVEGUIDE PHASE NOISE INVARIANCE

---

structures. Therefore any coupling from this phase change to the reflected field is small.

To determine whether the oscillations seen in  $\Delta\phi_p(x)$  were near field effects or numerical artefacts, the maximum change in phase,  $\max\{\Delta\phi_p(x)\}$ , over a full grating period displacement was computed at increasing distances from the WGM at the centre of the beam ( $x = -d/2 \rightarrow d/2$ ). As seen in figure 5.4, the near field phase shifts from the initial imprint of the grating can be seen at  $y < 3\mu\text{m}$  decay rapidly with distance. After this a flat noise is present. The accuracy of phase and amplitude information from data using an FFT based method can be improved by using window functions to reduce spectral leakage. Figure 5.4 shows three different FFT windowing functions that were used. These all show similar features for  $y < 3\mu\text{m}$  but each have different noise floors at larger distances; The lowest being  $\max\{\Delta\phi_p(x)\} \approx 10^{-7}$  rad using a *Blackman* FFT window.

Numerical errors present from the FDTD are not thought to be limiting. The approximation errors inherent in the FDTD are dependent on both the spatial and time steps used, finer sampling leads to smaller errors. Increasing the spatial and temporal resolution ( $\Delta x \rightarrow \Delta x/2$ ) did not offer any improvement in the noise levels as seen in figure 5.4. This suggests *spectral leakage* from the FFT is limiting the accuracy of phase measurements and the oscillations present in  $\Delta\phi_p(x)$ . Like those variations seen in  $\Delta\phi_p(x)$  measured at  $15\mu\text{m}$  which are deemed to be purely numerical artefacts. Similar variations were seen at distances from the WGM. There is also the fact that neither the TFSF or CPML are perfect in their own operation; the CPML will always reflect a small amount of light back and the TFSF will not perfectly separate the injected and reflected fields. As the phase variations seen are several orders of magnitude less than what a typical grating would experience further study into the smaller oscillations was not undertaken.

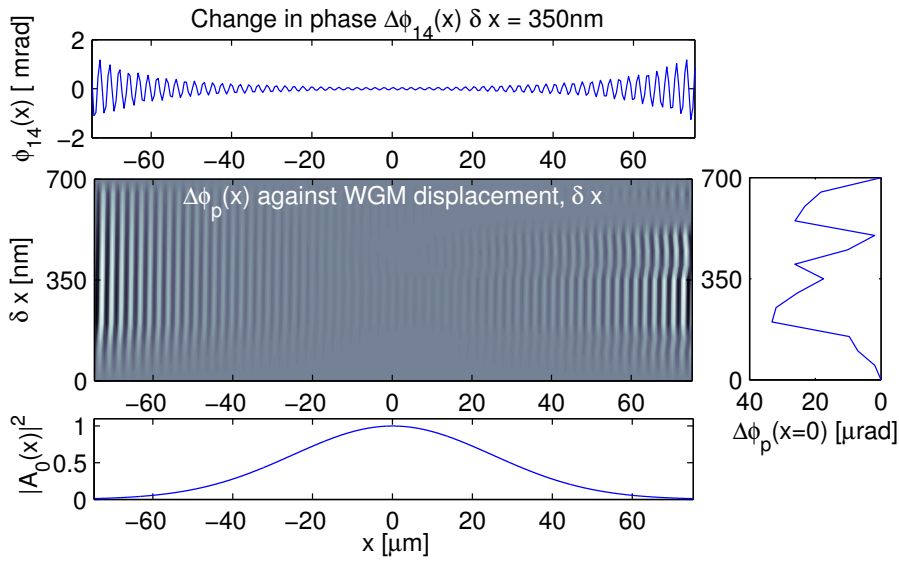


**Figure 5.3:** Waveguide displacement phase shifts [129]: Central plot shows phase change in the reflected beams wavefront  $\Delta\phi_p(x)$  against WGM displacement,  $\delta x$ . Top plot shows cross section of phase at  $\delta x = 350\text{nm}$  where the phase change is maximum. The right plot shows the variation in the phase of at  $x = 0$  against  $\delta x$ . Bottom plot shows the intensity of the reflected beam along  $x$ .

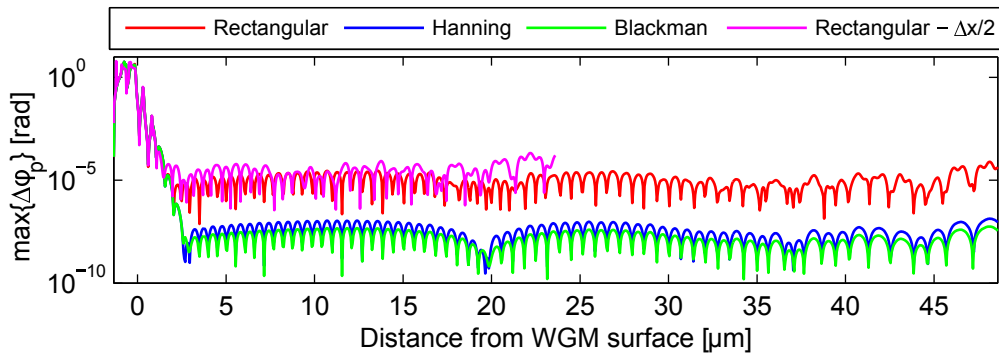


**Figure 5.4:** Numerical noise floor [129]: Maximum change in phase at beam peak intensity as the WGM is displaced from  $\delta x = 0 \rightarrow d$  with increasing distance from the WGM surface and different FFT windowing functions. Large near field phase shifts are seen close to the WGM and then a flat noise. Increasing the spatial and temporal resolution of FDTD  $\Delta x \rightarrow \Delta x/2$  did not appear to offer reductions in numerical noise caused by FDTD.

## 5.3 Conclusion

Before this work no experimental or theoretical work had been published on the waveguide grating mirrors susceptibility to transverse displacement phase noise. This work used a rigorous FDTD simulation to analyse displacement induced phase shifts

## 5. WAVEGUIDE PHASE NOISE INVARIANCE

---

in a reflected Gaussian beam from a waveguide grating mirror. It was found that this coupling did not affect the waveguide grating mirrors for a perfectly normal incident beam, within the precision limit of  $\approx 10^{-7}$  rad set by numerical errors. This limit is seven orders of magnitude lower than the phase noise estimated for previously proposed layouts with diffraction gratings, which raised concerns regarding the stability and alignment [140] of such grating based configurations. Therefore, the absence of this phase shift for WGMs removes one of the concerns for their usage in future high-precision interferometry experiments, motivating further research into such coatings. Since the publication of this work, research elsewhere has continued on the development of WGMs for third generation detectors [145, 146]. Experimental efforts at the Glasgow 10m prototype have also confirmed our results showing no significant transverse to longitudinal couplings to one part in seventeen-thousand [147].

# Chapter 6

## Summary and conclusions

In this thesis I have described the development of new modelling techniques and their application in the study of advanced gravitational wave detectors, in particular for commissioning of Advanced LIGO and the design of future upgrades to LIGO and new detectors such as the Einstein Telescope. It is crucial in the development of numerical models that strong efforts are made to verify them by comparing its predictions with current experimental results. The simulation programme FINESSE, which is at the core of my research work, has been successfully used and verified during the commissioning of gravitational wave detectors by myself and others. I have then used this well tested and vetted code base to develop more powerful modelling techniques and explore new interferometer ideas.

FINESSE is a popular simulation tool capable of modelling steady-state interferometers. It has seen extensive use in previous generations of detectors, table top experiments and prototypes for design and commissioning purposes. As a result of my work, FINESSE's feature set was significantly expanded to accommodate the modelling needs of future detectors. FINESSE was also open sourced and actively maintained across Windows, OSX and Linux during my PhD, whilst responding to queries and bug reports from users across the gravitational wave community and beyond.

## 6. SUMMARY AND CONCLUSIONS

---

Due to advanced detectors using a combination of high laser powers and suspended optics the pressure exerted by the lasers becomes significant within the interferometer. In such cases the interferometer is transformed into an optomechanical system, where its optical and mechanical response is greatly altered by the appearance of optical springs. To enable such effects to be studied I have implemented significant changes to internals of FINESSE. It is now able to model steady-state optomechanical coupling effects—including longitudinal, rotational and higher order surface motions of suspended optics—that are driven by radiation pressure exerted by higher order modes of the lasers light.

In current and future detectors, low loss and high quality factor materials are used for constructing the test masses. The vibrational modes of the test masses coupled with high laser power can result in parametric instabilities; vibrational modes pumped by the optical field that have a growing amplitude. These instabilities are expected to be problematic by causing lock losses and have already been experimentally seen in aLIGO. Here, I develop an idea for an optical configuration that offers a broadband suppression of parametric instabilities. Thus far only mechanical suppression of parametric instabilities acting locally at each mirror have been considered. Although not applicable to LIGO as it is, the scheme proposed could be incorporated into future designs. This work is currently being prepared for publication: *Daniel Brown et al. Optical suppression of parametric instabilities with extraction cavities. 2015. In preparation.*

During my PhD I also actively participated in the commissioning modelling for aLIGO, the work accomplished is reported in chapter 4. As part of a team of simulators we actively maintained an up to date FINESSE script of the LHO and LLO detectors. This was used to respond to requests from commissioners to unexpected behaviours in the interferometers. In this chapter I have highlighted two problems that I contributed towards: the study of error signal distortions that were giving rise to control issues

---

at LHO; and the study of how beam clipping resulted in unexpectedly low power recycling cavity gains. In these cases the work was reported by the modelling team in several technical notes published to the LIGO document control center. A list of technical notes can be seen in the ‘List of publications’ section in the back matter of this thesis.

Throughout my development of FINESSE I have tried to ensure that it remained as fast as possible. Faster simulations allow simulators to respond quicker to commissioning request and generally be more efficient at exploring problems involving high-dimensional parameter spaces. One aspect where significant improvements were made was in the use of reduced order quadrature, as outline in chapter 2. Collaborating with Rory Smith, we created a vastly improved numerical integration algorithm was developed for modelling optical mode scattering. Computational performance of the order of a thousands times were seen, greatly expanding the modelling capabilities of FINESSE. This work has been submitted for publication in: *Daniel Brown, Rory Smith, and Andreas Freise. Fast simulation of gaussian-mode scattering for precision interferometry. Journal of Optics, Sept 2015. Submitted on 2<sup>nd</sup> of September, awaiting feedback.*

Also reported here was is the study I undertook in regards to the use of waveguide grating mirrors and their suitability for use in gravitational wave detectors. These mirror use a grating and waveguide structure to produce a near-perfectly reflective mirror but with a substantial reduction in coating thermal noise compared to dielectric coating stacks. However, there were concerns that the grating structures could introduce a new noise coupling from lateral displacements to the phase of the diffracted orders. Using a numerical finite-difference time-domain code for solving Maxwell’s equations I demonstrated this noise coupling did not affect waveguide grating mirrors, down to levels of numerical and post-processing errors. Thus removing a potential concern for their use in future detectors. This work was published in: *Daniel Brown, Daniel*

## 6. SUMMARY AND CONCLUSIONS

---

*Friedrich, Frank Brückner, Ludovico Carbone, Roman Schnabel, and Andreas Freise. Invariance of waveguide grating mirrors to lateral displacement phase shifts. Opt. Lett., 38(11):1844–1846, Jun 2013.*

### 6.1 Outlook

Looking forward, the modelling of advanced detectors is currently reaching an interesting era. Both of the LIGO detectors have successfully completed their initial commissioning and have now started their first scientific data taking run. Already parametric instabilities have been detected at  $\approx 30$  W of input power. As this is gradually increased in future commissioning efforts parametric instabilities and other radiation pressure will become even more apparent. The FINESSE modelling team is now poised and ready with the necessary tools and experience to play their part in investigating this new and unexplored high power regime.

Also developed and implemented in FINESSE during my PhD were substantial additions to the quantum noise calculations (See appendix D). It is only recently that these features have started to be used in designing new interferometric devices, such as ET and the Glasgow speed meter prototype. These features were also being put to use in studying how mode-matching affects the quantum noise limited sensitivity as part of the active wavefront control project. This project started near the end of my PhD and will be continued by others; the modelling effort started here will enable future research into possible control and sensing schemes for better mode-matching. In the future there also lies interesting modelling possibilities for studying higher order modes in quantum-limited systems, for example, the effects of spatial distortions on balanced homodyne readout, the limits to the effectiveness of squeezed light injection due to spatial distortions and more realistic models of the many new ideas to overcome quantum noise, such as speed meters or active filters. Experimental efforts on

---

both table-top and prototype scales have now started and will provide exciting results which can be used to continue the process of the testing and advancing our numerical models.

## 6. SUMMARY AND CONCLUSIONS

---

# Appendix A

## Interferometer simulation tool:

### Finesse

On their own each of the optical features described in the chapter 1 are not especially complicated. However, great complexity arises when combining all these features together. Calculating the fields by-hand is a time consuming process for systems more complicated than a single cavity: FINESSE was created as a solution to this problem. In 2012 when I took over the development of FINESSE it was already a popular tool within the community. However, it was lacking in several key physical features for modelling advanced detectors: radiation pressure effects, thermal distortions and scattering and quantum noise calculations. These features were desired by the community and actively requested over the years but had unfortunately lacked the developer to accomplish this.

The improvements and additional features added to FINESSE by myself are perhaps the most significant output of my PhD. This is a tool that will be used long after the completion of my PhD for the learning, designing and commissioning of future gravitational wave detectors.

A great deal of time was spent programming and testing the new features. This

## A. INTERFEROMETER SIMULATION TOOL: FINESSE

---

work has enabled both myself and others to accomplish new research. Some examples of where my work has enabled others to study new problems with FINESSE is in the KAGRA OMC design [148], studying thermal correction in GEO600 [149], studying the use of Laguerre-Gaussian beam shapes for thermal noise reduction [150, 151] and thermal distortion effects in aLIGO [53]. These all made use of the new scattering features implemented. The use of quantum noise and radiation pressure effects are currently being used in design work for ET and the speed meter prototype [152]. It is also actively used for aLIGO commissioning simulations and future aLIGO design upgrades, as highlighted later in this chapter, and for studying higher order mode radiation pressure effects, as discussed in chapter 3.

This section will provide an outline of the improvements made over my PhD. Specific aspects of the coding won't be discussed here; the source code is freely available for those wishing to browse the  $\approx 76500$  lines of code at <https://gitmaster.atlas.aei.uni-hannover.de/finesse/finesse>. The FINESSE manual contains more information regarding the technical aspects of features and how to use them [26].

FINESSE is a terminal based, open source (GPL 2) cross platform binary called *kat*. It is written in C and was mostly developed on Unix based systems. *Windows* support was achieved using both the *Cygwin* and *MinGW* projects. It uses a simplified scripting language to produce what is referred to as a FINESSE *file* or a FINESSE *script*. These scripts are then fed into the *kat* binary from a terminal and a text based output file is generated on completion along with a Gnuplot or Python interactive plot of the outputted results.

The scripting language allows the user to define arbitrary interferometer layouts consisting of mirrors, beamsplitters, isolators, modulators, lenses and diffraction gratings. They are then connected together in a *nodal network* by defining the *space* between each component. It operates in either a plane-wave or Hermite-Gaussian beam mode, thus the geometry of mirrors and beamsplitters is also definable.

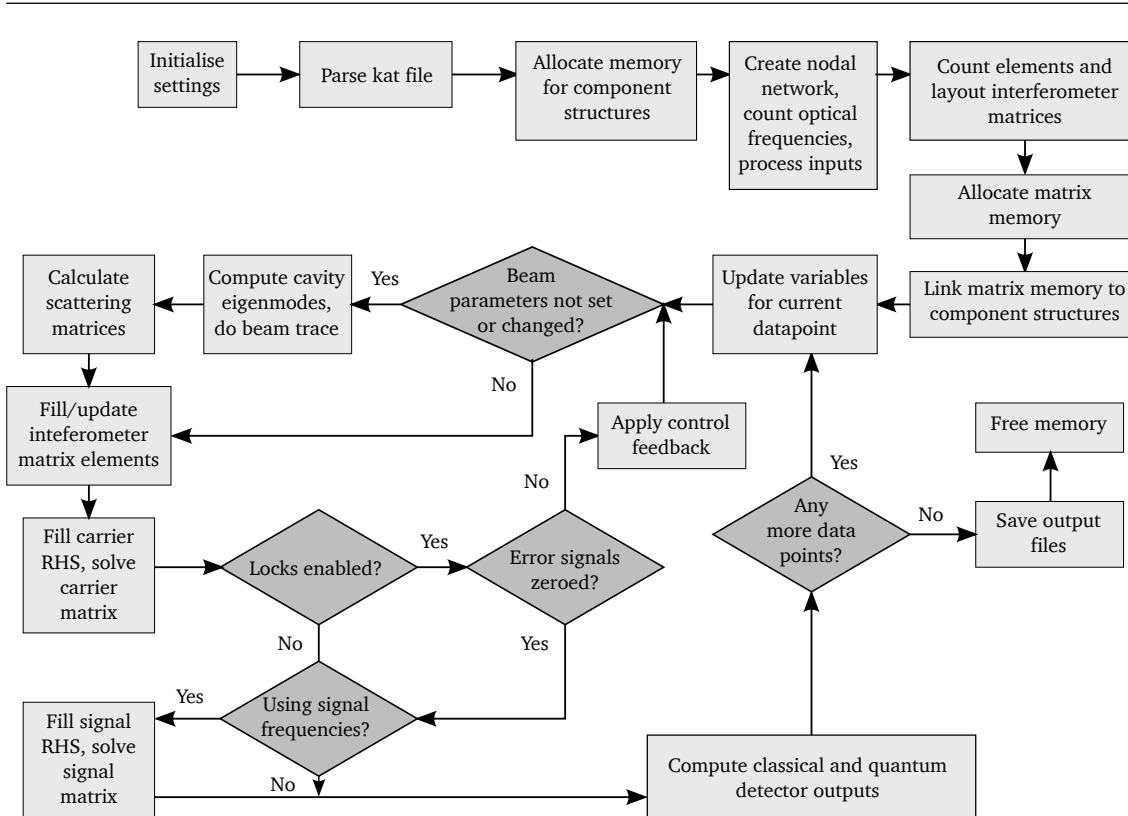


**Figure A.1:** *Flow of FINESSE:* A general overview of the operation when running a given FINESSE file using higher order optical modes.

Once the layout is defined the user can then add a number of different *detectors* to extract information from the simulation. These range from realistic demodulated multi-quadrant photodiodes and CCD cameras to unphysical detectors that directly output the amplitude and phase of a particular HOM at any location.

With the components and detectors set up the file must then state what type of simulation to run. A minimum and maximum range of one or more of interferometer's parameters are then specified to be simulated; then for each of these steps the output of all the detectors specified will be written to an output text file. An overview of the process of running a script is shown in the flow diagram in figure A.1.

### Core matrix solver

One of the largest changes I made to FINESSE was in the way that it handled the interferometer matrix. Originally FINESSE was designed for memory efficiency due to computers having limited amounts of RAM; as large interferometer files can easily end up consuming multiple gigabytes when using a high  $\mathcal{O}_{max}$  with multiple optical frequencies. The shape of the interferometer matrix is identical for each optical frequency, e.g. Eq.(1.59), thus a single matrix propagating a single optical frequency could be created. To solve for the optical fields this matrix was iterated over for each frequency and its elements updated with the appropriate optical frequency.

Although this was ideal for memory usage, it did not allow for either radiation pressure effects or sidebands-of-sidebands [153] to be modelled: a feature of linking sequential optical modulators. This is because both effects require computing the cross coupling between optical fields, something that cannot be achieved if they are solved individually.

The entire matrix construction and filling routines were rewritten for this, the process of which uses the sub-matrix block methods laid out in section 1.3.3. In total two matrices are created in FINESSE now: one for the main carrier and the RF sidebands, the *carrier matrix*; and another for the signal sidebands pairs around each of the carriers and RF sidebands, the *signal matrix*. The carrier matrix represents the steady-state of the main optical fields. The signal matrix then represents small and linear perturbations of each of the carriers at a particular frequency  $\Omega$ , such as those induced by a gravitational wave or noise source. This signal matrix is important for implementing radiation pressure effects and quantum noise calculations.

It was important to ensure these changes still produced the same results for existing files. To do this a Python test server was setup which checked each Git commit pushed to the main FINESSE repository. This takes each commit and builds the corresponding kat binary. A collection of several hundred scripts is then ran and the outputs com-

---

pared to reference outputs to check whether a commit has altered or broken anything. A web interface allows easy viewing of which files were altered and can display the history of which commits produces different values. Overall the differences in all the script outputs tested were better than  $10^{-10}$  in relative error before and after the core matrix solving changes.

## **Maps and scattering**

Before I began developing FINESSE and initial implementation of higher order mode scattering as described in section 1.3.3.2 was included. As noted in the aforementioned section the handling of maps must be done carefully. There were several issues in the way that FINESSE use to handle multiple maps and combining several scattering matrices; these issues were all fixed to operate as described in section 1.3.3.2.

Another technical issue was in efficiently performing the numerical integration for the scattering matrices. The original scattering calculations would take on the order of several hours to days depending on the simulation performed. Chapter 2 outlines the final solution to this issue using reduced order quadrature, which effectively removes the computational cost of evaluating the scattering matrices.

## **Radiation pressure**

With the successful implementation of the new signal matrix construction a linearised model of radiation pressure effects were included in FINESSE. The model used assumes that the actual displacements induced by radiation pressure effects is always  $\ll \lambda$ . The implementation of this requires that the upper and lower audio sidebands can be coupled at a suspended mirror, hence why the new matrix construction was required. More details on the radiation pressure effects implemented are left to discuss in chapter 3.

### **Quantum noise**

Originally FINESSE could only compute the shot noise measured at a demodulated photodiode due to vacuum noise. For future detectors it was required to extend this to include squeezed states of light and how radiation pressure effects due to increased circulating optical field powers altered the noise couplings.

The quantum noise computations I added to FINESSE allowed for computing the full quantum noise effects with radiation pressure effects for general demodulated photodiodes and balanced homodyne detectors. Appendix D provides an overview of how these calculations work. These quantum noise calculations features are now being used for ET and the Glasgow speed meter modelling and for the AWC modelling. Thus far commissioning tasks have not been centred around problems regarding quantum noise. But this will eventually change going forward when the squeezer and filter cavities are designed and installed in planned LIGO upgrades.

## Appendix B

### Pykat: Python wrapper for Finesse

For more advanced FINESSE modelling, along with the core C engine, a Matlab based toolbox SIMTOOLS [154] was available. The core engine of FINESSE is run using a single script file but for more complex modelling tasks that involve iterating over a parameter space, optimising results, or automation of tasks a higher level interface is required. SIMTOOLS was used extensively for all of the commissioning modelling and others that were undertaken in C. Bond's thesis [53].

PYKAT originally started as an experiment for visualising FINESSE scripts: variables used, optical layouts, beam parameters, etc., for easier debugging of long files as shown in appendix E. However, this was supplanted by providing a more feature rich replacement of SIMTOOLS. All the modelling described in this thesis was undertaken using PYKAT (bar some of the commissioning modelling reported).

Python was chosen as it offers all the programmatic features that were required whilst being both free and open sourced. Other simulation tools within the gravitational wave community rely on Matlab and expensive toolboxes, meaning licenses are required just to experiment with them. A particular nuisance is the lack of free access to parallel programming features in Matlab without the designated toolboxes. With ever more complex models being made access to multiple cores was crucial for com-

## B. PYKAT: PYTHON WRAPPER FOR FINESSE

---

missioning and design activities and another driving reason the move to Python was made.

PYKAT was designed with a few key ideas in mind:

- Open source and cross platform support
- Object-orientated design for constructing and manipulating FINESSE files
- Lightweight and succinct interface
- A central repository for helpful tools and functions for FINESSE modelling
- A rolling support of FINESSE features as they are required. Not all features need to have a PYKAT equivalent to use them immediately, a user can always revert back to adding in specific commands by hand.

It is available for both Python versions 2.6+ and 3+ and can be downloaded from [67]. Today PYKAT has displaced SIMTOOLS for advanced modelling tasks with many of its scientifically useful features now ported to Python.

The core part of PYKAT is the `pykat.finesse.kat` class. This will read and parse the commands in a FINESSE file into itself as properties of the class. For example, here the commands to create a plane-wave Fabry-Perot cavity are loaded into PYKAT:

---

### Code B.1 PYKAT example

---

```
import pykat

kat = pykat.finesse.kat() # Create the main Finesse object

kat.parseCommands("""
l l1 1 0 n0           # Input laser
m m1 0.9 0.1 0 n0 n1 # Input mirror
s s1 1 n1 n3
m m2 0.99 0.01 0 n2 n3 # End mirror
```

---

```

pd circ n1          # Circulating power
pd refl n0         # Reflected power
pd trans n3        # Transmitted power
xaxis m1 phi lin 0 180 180 # Scan m1's tuning over half a wavelength
""")

output1 = kat.run() # Run the first simulation...
kat.l1.P = 2        # Access the laser like an object
                  # by changing the power...
output2 = kat.run() # Run again...

# Finally just output the photodiode powers
print(output1["circ"], output1["refl"], output1["trans"])
print(output2["circ"], output2["refl"], output2["trans"])

```

---

When run, the `kat` object reproduces a file that is passed to the FINESSE executable. Parameters of any object can be accessed in a typical object orientated manner, such as the input laser power shown here. Once finished running the data is parsed and outputted into the output objects `output1` and `output2`. From these the calculated values can be accessed, manipulated or saved to file.

Another aim for having this object orientated representation of the script files is to create functions that operate on a FINESSE script file. For example, a function was created that removed subsections of the interferometer when not needed, such as the IMC. In such cases additional mode-matching must be done to ensure the file still works, again an aspect that is automated. Other examples are functions that given some `kat` object of an aLIGO interferometer will proceed to compute a length or alignment sensing matrix. This involves running multiple simulations and collecting results, something which is run multiple times for different interferometer parameters. Lastly having this object representation eases the parallelisation of running multiple FINESSE simulations at once. Built in is support for starting and collecting the results from running many simulations using the *IPython cluster* software. Such a feature was crucial for running parametric instability models as discussed in chapter 3.

## B. PYKAT: PYTHON WRAPPER FOR FINESSE

---

PYKAT also enables other software to interface with FINESSE scripts in new ways. A great example of this is OPTIVIS (<https://github.com/SeanDS/optivis>), a graphical interface for creating interferometer layouts using SVG graphics written by Sean Leavey. Sean and myself worked together to enhance this further, allowing a FINESSE file to be read, displayed and then altered through the graphical interface.

### Outlook

A more ergonomic and powerful wrapper was required for FINESSE to enable more efficient modelling of complicated problems. PYKAT was successful in providing the required features that users demanded of it and is now used exclusively by those doing advanced modelling with FINESSE.

At the end of my PhD PYKAT would be classed as a *beta* version. Overall it is a stable package that greatly enhances the modelling capabilities of FINESSE. A few bugs still remain as well as missing some of the advanced FINESSE features have not yet been wrapped in PYKAT code: such as, maps, FINESSE functions, and various beam tracing outputs. However, in time these will be added as they are required. All the code is open sourced and accessible from <https://gitmaster.atlas.aei.uni-hannover.de/pykat> or via PYPI package manager.

# Appendix C

## Rotational radiation pressure

This appendix outlines the analytic math to compute the scattering matrices for rotational modes of a mirror. These are required for computing optomechanical coupling as outline in chapter 3: thus, this appendix should be read in context with that chapter.

### Yaw and pitch motions

The next order of motion possible after longitudinal motions of rigid object are rotations. When considering any tilting motion the functional form of the surface motion is  $z_s(x, y) = x$  or  $z_s(x, y) = y$ , for yaw or pitch respectively: thus the motion has units of radians. To analytically solve this we will make use of the orthogonality of the Hermite-Gaussian polynomials again, consider the scattering from yaw motion which is represented by  $K^x$ :

$$K_{nmn'm'}^x = \iint_{-\infty}^{\infty} u_{nm}(x, y) x u_{n'm'}^*(x, y) dx dy, \quad (\text{C.1})$$

$$= \int_{-\infty}^{\infty} u_n(x) x u_{n'}^*(x) dx \int_{-\infty}^{\infty} u_m(y) u_{m'}^*(y) dy, \quad (\text{C.2})$$

$$= \delta_{mm'} \int_{-\infty}^{\infty} u_n(x) x u_{n'}^*(x) dx = \delta_{mm'} K_{nn'}^x. \quad (\text{C.3})$$

### C. ROTATIONAL RADIATION PRESSURE

---

Using the 1D Hermite-Gaussian beam of order  $n$ :

$$u_n(x) = \left(\frac{2}{\pi}\right)^{\frac{1}{4}} \frac{e^{i(n+1/2)\Psi(z)}}{\sqrt{2^n n! w(z)}} H_n\left(\frac{\sqrt{2}x}{w(z)}\right) e^{-\frac{x^2}{w^2(z)}} e^{\frac{-ikx^2}{2R(z)}} \quad (\text{C.4})$$

$$= C_n H_n\left(\frac{\sqrt{2}x}{w(z)}\right) e^{-\frac{x^2}{w^2(z)}} e^{\frac{-ikx^2}{2R(z)}} \quad (\text{C.5})$$

and the substitution  $\bar{x} = \sqrt{2}x/w(z)$ :

$$K_{nn'}^x = C_n C_{n'}^* \frac{w_x^2(z)}{2} \int_{-\infty}^{\infty} H_n(\bar{x}) \bar{x} H_{n'}^*(\bar{x}) e^{-\bar{x}^2} d\bar{x}. \quad (\text{C.6})$$

To make use of the polynomial orthogonality we can substitute in another polynomial  $2\bar{x} = H_1(\bar{x})$ :

$$K_{nn'}^x = C_n C_{n'}^* \frac{w_x^2(z)}{4} \int_{-\infty}^{\infty} H_n(\bar{x}) H_1(\bar{x}) H_{n'}^*(\bar{x}) e^{-\bar{x}^2} d\bar{x} \quad (\text{C.7})$$

Using the identity for Hermite products:

$$H_n(x) H_m(x) = \sum_{r=0}^{\min(n,m)} 2^r r! \binom{n}{r} \binom{m}{r} H_{n+m-2r}(x), \quad (\text{C.8})$$

we find:

$$K_{nn'}^x = C_n C_{n'}^* \frac{w_x^2(z)}{4} \sum_{r=0}^{\min(n,n')} 2^r r! \binom{n}{r} \binom{n'}{r} \int_{-\infty}^{\infty} H_1(\bar{x}) H_{n+n'-2r}(x) e^{-\bar{x}^2} d\bar{x}. \quad (\text{C.9})$$

The value of this integral can be found using the orthogonality of the Hermite-Gaussian polynomials,  $\int_{-\infty}^{\infty} H_n(x) H_m(x) e^{-x^2} dx = \sqrt{\pi} 2^n n! \delta_{nm}$ . Applying this result we are left with:

$$K_{nn'}^x = C_n C_{n'}^* \sqrt{\pi} w_x^2(z) \sum_{r=0}^{\min(n,n')} 2^{r-1} r! \binom{n}{r} \binom{n'}{r} \delta_{1,n+n'-2r}. \quad (\text{C.10})$$

The only non-zero terms of the summation are when  $r = (n+n'-1)/2$ . The conditions on  $r$  are that it is a positive integer,  $r$  must be in the range  $0 \leq r \leq \min(n, n')$ , and

$n + n'$  must be odd. These are met only when  $|n - n'| = 1$ . Thus an incoming mode only couples to  $n = n' \pm 1$  for small yaw motions. The only non-zero elements in the scattering matrix are then:

$$\mathbf{K}_{(n'+1)n'}^x = \frac{\sqrt{n'+1}}{2} w_x(z) e^{i\Psi_x(z)} \quad \mathbf{K}_{n'(n'+1)}^x = \mathbf{K}_{(n'+1)n'}^{x*} \quad (\text{C.11})$$

$$\mathbf{K}_{(n'-1)n'}^x = \frac{\sqrt{n'}}{4} w_x(z) e^{-i\Psi_x(z)} \quad \mathbf{K}_{n'(n'-1)}^x = \mathbf{K}_{(n'-1)n'}^{x*} \quad (\text{C.12})$$

This simple result is ideal as it removes a computationally expensive integration required to compute the scattering terms. This is particularly useful in cases where one is interested modelling how changes in beam shapes might affect radiation pressure coupling.

It should be noted that this scattering matrix differs from those examined in section 1.3.3.2, as the elements are not necessarily in the range  $0 \leq |K_{nn'}^x| \leq 1$ . This is due to the fact a linearised version of the equations are used and the magnitude of the motion  $A_s$  has been factored out. Thus, it must be kept in mind that  $|A_s| \ll 1$ . No energy conservation is broken as only very small amounts of power are scattered into these sidebands. It should also be noted that the above result is exactly the same for the pitch motion, only a change in superscript from  $x \rightarrow y$  and subscript  $n \rightarrow m$  is required.

Finally, the coupling from yaw motions,  $A_s \rightarrow \theta_x$ , and pitch,  $A_s \rightarrow \theta_y$ , to the scattered sideband amplitude is:

$$a_{s,jnm}^\pm = \text{irk} \sum_{n',m'} a_{c,jn'm'} \left( \theta_x^\pm (\mathbf{K}^x \mathbf{K}^o)_{nmn'm'} + \theta_y^\pm (\mathbf{K}^y \mathbf{K}^o)_{nmn'm'} \right) \quad (\text{C.13})$$

where as the notation as previously used for longitudinal case means  $\theta_{x/y}^+ \equiv \theta_{x/y}$  and  $\theta_{x/y}^- \equiv \theta_{x/y}^*$ .

## C. ROTATIONAL RADIATION PRESSURE

---

### Optical field to rotation

An optical field can also apply a torque if the beam is off-centred or of some distorted shape. For this we must determine the centre-of-intensity, analogous to a center-of-mass computation. This can be computed by the integration:

$$\Delta x = \iint_{-\infty}^{\infty} \frac{xI(x, y, t)}{P} dx dy \quad (\text{C.14})$$

where  $P$  is the total power of the beam and  $I(x, y)$  is the intensity at a given point. Computing  $\Delta y$  is merely a task of swapping  $x$  for  $y$  in the integrand. Using equation 3.34 we find:

$$\Delta x = \frac{1}{P} \iint_{-\infty}^{\infty} xE(x, y, t)E^*(x, y, t) dx dy, \quad (\text{C.15})$$

$$= \Delta x_{DC} + \Delta x_s(\Omega)e^{-i\Omega t} + \Delta x_s(-\Omega)e^{-i\Omega t} + O(a_s^2) + O(|\omega \gg \Omega|). \quad (\text{C.16})$$

Whereby expanding the  $E^*E$  product we again find multiple frequency components:  $\Delta x_{DC}$  represents DC offsets of a beam and  $\Delta x_s$  represents offsets that are oscillating with frequency  $\Omega$ . We have also truncated some of the terms, namely those that are order  $|a_s|^2$  which are negligibly small and those with a frequency term much greater than the motion frequency  $\Omega$ . This latter truncation is possible because mechanical susceptibility of a suspended mirror is  $\propto \Omega^{-2}$ , thus RF frequency components contribute negligible amounts to the torque applied compared. Therefore, we are concerning ourselves primarily with terms that oscillate at  $\Omega$  as it is assumed DC levels will always be compensated by some active or passive control to keep the static mirror

rotations aligned. Expanding and collecting all  $\Omega$  terms we find:

$$\mathbf{K}_{nmn'm'}^x = \iint_{-\infty}^{\infty} u_{nm}(x, y) x u_{n'm'}^*(x, y) dx dy, \quad (\text{C.17})$$

$$\Delta x_s(\Omega) = \frac{1}{P} \sum_j \sum_{n,m} \sum_{n',m'} (\mathbf{K}_{nmn'm'}^x a_{s,jnm}^+ a_{c,jn'm'}^* + \mathbf{K}_{nmn'm'}^{x*} a_{s,jnm}^{-*} a_{c,jn'm'}) \quad (\text{C.18})$$

The scattering term  $\mathbf{K}_{nmn'm'}^x$  should look familiar, as this is the same as that which we computed analytically previously, see C.11. Our result here can be further simplified knowing that  $\mathbf{K}_{nmn'm'}^x \neq 0$  only when  $|n - n'| = 1$  and  $m = m'$  (A similar argument can be made for  $\mathbf{K}^y$ ):

$$\Delta x_s(\Omega) = \frac{1}{P} \sum_j \sum_{n,m} \gamma_{nm}^x a_{s,jnm}^+ + \gamma_{nm}^{x*} a_{s,jnm}^{-*} \quad (\text{C.19})$$

$$\gamma_{nm}^x = \mathbf{K}_{n(n+1)}^x a_{c,j(n+1)m}^* + \mathbf{K}_{n(n-1)}^x a_{c,j(n-1)m}^* \quad (\text{C.20})$$

$$\gamma_{nm}^y = \mathbf{K}_{m(m+1)}^y a_{c,jn(m+1)}^* + \mathbf{K}_{m(m-1)}^y a_{c,jn(m-1)}^* \quad (\text{C.21})$$

The fluctuating torque applied to the mirror due to radiation pressure is then:

$$\tau_{rp} = \frac{P}{c} \Delta x_s. \quad (\text{C.22})$$

Noting that the  $P$  terms cancel for  $\tau_{rp}$  we are able to calculate the rotational motion:

$$\theta_x(\Omega) = H_{\theta_x}(\Omega) \tau_{rp}(\Omega) \quad (\text{C.23})$$

where  $H_{\theta_x}(\Omega)$  is the mechanical transfer function of the optic for a torque applied to optic.

## C. ROTATIONAL RADIATION PRESSURE

---

# Appendix D

## The quantum kat

This appendix aims to give an overview of quantum noise and later outline the theory behind the FINESSE quantum noise calculations. The beginning of this appendix is a verbatim copy of a section that I wrote on quantum noise for an updated version of: *C. Bond, D. Brown, A. Freise, and K. Strain. Interferometer Techniques for Gravitational-Wave Detection. Living Reviews in Relativity, 13, 2015. Submitted as of August 2015* This text has been altered slightly to fit in with the thesis. The updated article was submitted to Living Review for publication in September 2015.

### Quantum noise sidebands

The two quadratures of the light field, its amplitude and phase, form an observable conjugate pair and thus both cannot be measured simultaneously without some uncertainty in the result [155]. This quantum noise of a single mode laser can be depicted as a phasor with the coherent carrier field and the addition of some stochastic Gaussian distributed noise which affects both its phase and amplitude [156, 157].  $\sigma_\phi^2$  and  $\sigma_a^2$  are the variances that characterise fluctuations in phase and amplitude respectively. The noise present in a light field with an equal minimum  $\sigma_\phi$  and  $\sigma_a$  is known as *vacuum fluctuation* or *vacuum noise*. Vacuum noise can be understood as the photon at

## D. THE QUANTUM KAT

---

all frequencies being incoherently created and annihilated. Therefore vacuum noise is all pervasive, existing at all locations in space, frequency and spatial mode. Such photons also enter our interferometer and limit the sensitivity of any measurement of a field's amplitude or phase.

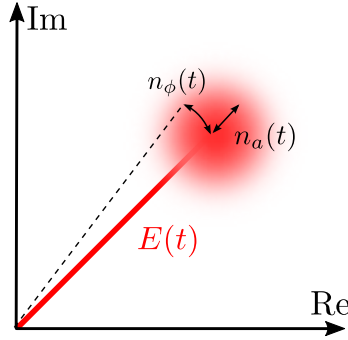


**Figure D.1:** *Ball on a stick* [27]: Phasor diagram of equation D.4 depicting the Gaussian random amplitude and phase fluctuations due to vacuum noise. Here  $n_{a,\phi}(t)$  are random gaussian noises in either the phase or amplitude of the carrier. Shown is only the positive frequency part of the carrier field, as  $E(t)$  is real a conjugate negative frequency term also exists.

Consider a carrier field at one location with amplitude  $a_0$  and frequency  $\omega_0$  along with a continuum of noise fields (the positive frequency spectrum):

$$E(t) = \frac{a_0}{2} e^{i\omega_0 t} + \frac{1}{2} \int_0^{\infty} q(\omega) e^{i\omega t} d\omega + \text{c.c.} \quad (\text{D.1})$$

where  $q(\omega)$  is the Fourier component of a stochastic process, representing the vacuum fluctuation of the electric field.

We can rewrite the continuum of noise in reference to the carrier field frequency:

$$E(t) = \frac{a_0}{2} e^{i\omega_0 t} + \frac{e^{i\omega_0 t}}{2} \int_{-\omega_0}^{\infty} q(\omega_0 + \omega) e^{i\omega t} d\omega + \text{c.c.} \quad (\text{D.2})$$

where we can view our quantum noise fields as sidebands of the carrier instead. For gravitational wave detectors the bandwidth  $B$  of the signals induced by a gravitational wave is of the order of several kHz and thus  $B \ll \omega_0$ . Hence, we can focus on a small

---

range of the noise sidebands that will actually affect our sensitivity:

$$E(t) = \frac{1}{2} \left[ a_0 + \int_{-B}^B q(\omega_0 + \Omega) e^{i\Omega t} d\Omega \right] e^{i\omega_0 t} + \text{c.c.} \quad (\text{D.3})$$

Here  $\Omega$  will be used in notation to refer to frequencies in the signal bandwidth with  $-B < \Omega \leq B \ll \omega_0$ . We can also represent the quantum fluctuations as noise in both amplitude and phase:

$$E(t) = [a_0 + n_a(t)] e^{i\omega_0 t + n_\phi(t)/a_0} + \text{c.c.} = [a_0 + n_a(t) + i n_\phi(t)] e^{i\omega_0 t} + \text{c.c.}, \quad (\text{D.4})$$

with  $n_a$ ,  $n_\phi$  being real amplitudes of the amplitude and phase fluctuations (of the stochastic process) with  $n_a$ ,  $n_\phi \ll 1$ . This equation is represented in the phasor diagram in figure D.1.

We can now relate the amplitude and phase fluctuation to the complex quantum noise  $q(\omega)$ :

$$q(\omega) = n_a(\omega) + i n_\phi(\omega) \quad (\text{D.5})$$

Both  $n_{a,\phi}(\omega)$  of a vacuum noise sideband are characterised by a Gaussian probability density function with mean  $\mu_{a,\phi} = 0$  and variance  $\sigma_{a,\phi}^2$ . Note that the sidebands for the quantum noise are not representing a coherent and deterministic signal.

The variances  $n_{a,\phi}(\omega)$  are limited by the minimum uncertainty in the relation

$$\sigma_\phi \sigma_a \geq \frac{\hbar\omega}{2}, \quad (\text{D.6})$$

which, for an integration time of one second, are  $\sigma_\phi^2 = \sigma_a^2 = \hbar\omega/2$ . As the phase and amplitude of  $q(\omega)$  is random it can only compute its *expected value* or *ensemble value* at a particular frequency:

$$\langle q(\omega) \rangle = \langle \mu_a \rangle + i \langle \mu_\phi \rangle = 0, \quad (\text{D.7})$$

## D. THE QUANTUM KAT

---

which is zero as the mean of the noise is zero, hence on average no sidebands are actually observed. The covariance between any two sidebands at a frequency  $\omega$  and  $\omega'$  can also be considered. As  $q(\omega)$  is a complex value there are multiple ways the covariance can be taken when considering the conjugates of either sideband:  $\langle q(\omega)q^*(-\omega') \rangle$ ,  $\langle q^*(\omega)q(-\omega') \rangle$ , etc.. However as the fluctuations in amplitude and phase at different frequencies are independent, the covariance between any two vacuum noise sidebands are:

$$\langle q(\omega)q^*(\omega') \rangle = \frac{\hbar\omega}{2}\delta(\omega - \omega'), \quad (\text{D.8})$$

$$\langle q(\omega)q(\omega') \rangle = 0, \quad (\text{D.9})$$

The delta function in the covariance signifies that there is no correlation between different frequencies. The auto-covariance is then  $\langle q(\omega)q^*(\omega) \rangle \propto \delta(\omega - \omega) = \infty$ , which may seem odd at a first glance. However, this can be better understood in the time domain picture, as the signal would be measured over an idealistic infinite time span and as our noise is Markovian (and therefore also ergodic), the time average of the power of a signal will be infinitely large.

### Noise power spectral densities

Noise, i.e. a random signal, can be quantified using a *power spectral density* (PSD) which is a measure of the power in a signal per frequency. The definition of a single-sided PSD of some frequency domain value  $x(\omega)$  is:

$$S_{xx}(\omega)\delta(\omega - \omega') = 2\langle x(\omega)x^*(\omega') \rangle, \quad (\text{D.10})$$

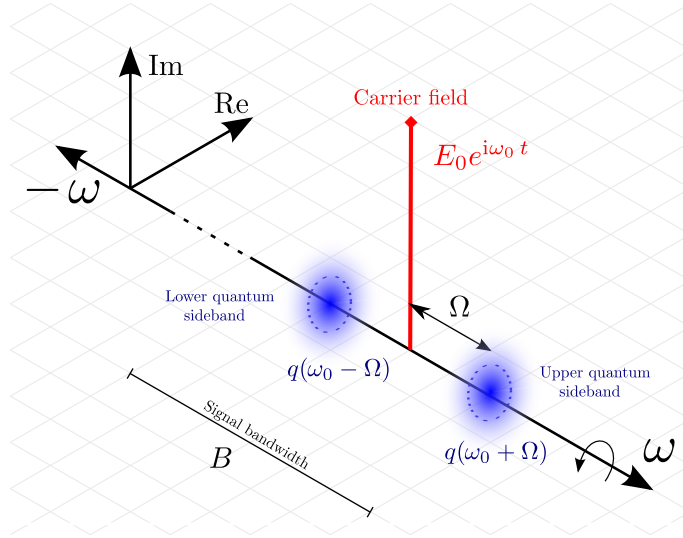


**Figure D.2:** *Quantum noise sideband spectrum* [27]: This diagram depicts a carrier field as shown in figure D.1 but expanded to show the vacuum noise sideband phasors that contribute towards the noise. The amplitude and phase of each sideband is a stochastic Gaussian noise so that its real and imaginary parts are described by some probability distribution depicted by the blue faded region, the dashed circle represents the standard deviation of such fluctuations. The signal bandwidth  $B$  can be imagined as containing an infinite number of such vacuum noise sidebands, each oscillating with a random phase and amplitude. Pictured are two upper and lower sidebands selected from this continuum of vacuum noise. The negative frequency phasors are not shown, they would be the mirrored conjugate versions of the positive phasors.

with units  $[x]^2/\text{Hz}$ . The cross-spectral-density between two values  $x(\omega)$  and  $y(\omega)$  is similarly:

$$S_{xy}(\omega)\delta(\omega - \omega') = 2\langle x(\omega)y^*(\omega') \rangle. \quad (\text{D.11})$$

The eventual physical noise that will be computed is the noise in the demodulated photocurrent of the photodiode measuring the interferometer output signal, here we will consider only photodiodes with 100% quantum efficiency<sup>1</sup>. The photocurrent  $I$  is proportional to the detected light power  $I(t) \sim P(t)$  and the PSD of the noise in the

<sup>1</sup> When measuring squeezed states any additional loss, such as a  $< 100\%$  efficiency, will degrade the squeezed state and introduce further vacuum noise.

## D. THE QUANTUM KAT

---

photocurrent is:

$$S_I(\omega)\delta(\omega - \omega') = s \langle I(\omega)I^*(\omega') \rangle \quad (\text{D.12})$$

The DC and  $\omega \pm \Omega$  terms of the power on a photodiode for a single carrier with quantum noise sidebands is:

$$\begin{aligned} P(t) = E(t)E^*(t) &= |a_0|^2 + a_0^* \int_{-B}^B q(\omega_0 + \Omega)e^{i\Omega t} d\Omega \\ &+ a_0 \int_{-B}^B q^*(\omega_0 + \Omega)e^{-i\Omega t} d\Omega + O(q^2), \end{aligned} \quad (\text{D.13})$$

terms of the order  $q^2$  are assumed to be a negligibly small contribution. The positive half of the photocurrent spectrum for  $0 < \Omega \leq B$  is given by its Fourier transform:

$$I(\Omega) \equiv \mathcal{F}[I(t)] = a_0^*q(\omega_0 + \Omega) + a_0q^*(\omega_0 - \Omega) \quad (\text{D.14})$$

The spectrum for frequencies in the signal bandwidth is thus defined by just quantum noise scaled by the carrier field. From this point on for the sake of brevity we will define the following notation without the carrier frequency, as we are only using a single carrier for this derivation:

$$q(\omega_0 \pm \Omega) \Rightarrow q_{\pm} \text{ and } q(\omega_0 \pm \Omega') \Rightarrow q'_{\pm} \quad (\text{D.15})$$

Using equations D.12 and D.14, the PSD of the photocurrent is:

$$S_I(\Omega)\delta(\Omega - \Omega') = 2P_0(\langle q_+q_+^* \rangle + \langle q_-q_-^* \rangle) + 2a_0^2\langle q_-q_+ \rangle^* + 2a_0^2\langle q_+q_- \rangle. \quad (\text{D.16})$$

---

Now applying equations D.8 and D.9 in equation D.16 the noise PSD for a single carrier field with vacuum noise is:

$$\begin{aligned}
S_I(\omega_0 \pm \Omega)\delta(\Omega - \Omega') &= 2P_0 (\langle q_+ q_+^{*'} \rangle + \langle q_- q_-^{*'} \rangle), \\
&= P_0 (\hbar(\omega_0 + \Omega) + \hbar(\omega_0 - \Omega)) \delta(\Omega - \Omega') \\
S_I(\omega_0 \pm \Omega) &= 2P_0 \hbar \omega_0 \tag{D.17}
\end{aligned}$$

Here we see that the quantum noise of a single carrier field does not depend on the sideband frequency  $\Omega$ . The vacuum fluctuations interfering with our carrier field produces a broadband frequency-independent noise source proportional to the carrier power and frequency. It should also be noted that equation D.17 is the same result as the semi-classical Schottky shot-noise equation. An interesting aspect to note here are the differing reasons for the presence of this quantum or shot noise. The Schottky formula derives this noise from the Poisson statistics of electrons generated in the photocurrent due to the light field power. Whereas the quantum approach reasons that such fluctuations in the photocurrent are in fact due to vacuum noise superimposing itself onto our light fields introducing a noise into our measurements.

## Photodiode demodulation and quantum noise

The quantity that we wish to compute is the noise present in a particular photodiode's output of an interferometer due to quantum fluctuations in the carrier light fields. The power spectral density (PSD) of the noise in the output current for a single carrier field incident on a detector is described by the Schottky formula

$$S_I = 2hfP. \tag{D.18}$$

## D. THE QUANTUM KAT

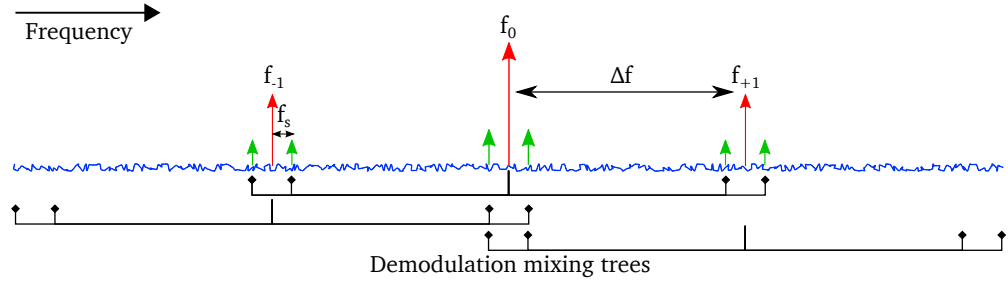


**Figure D.3:** *Demodulated quantum noise spectrum:* Shown is a frequency spectrum consisting of carrier fields (red), signal fields (green) and vacuum noise (blue). The smaller carriers were created by some modulator. This field would then be incident on a photodiode which would then be demodulated. The black tree like structures show which frequency components are mixed together during demodulation. As can be seen signal and noise is mixed with carriers. There is then additional noise at twice the demodulation frequency from the central carrier that also gets mixed in.

Where  $h$  is Planck's constant,  $f$  the frequency of the carrier field and  $P$  is the total power in the field. Here the quantum efficiency of the photodiode has been neglected but could also be included if required. In the case of  $N_c$  discrete carriers incident on a photodiode with frequencies measured by  $\Delta f_i$  from a reference frequency  $f_0$ , the noise PSD is [158, 159],

$$S_I = 2 \sum_i^{N_c} h(f_0 + \Delta f_i) P_i. \quad (\text{D.19})$$

Although the above equations for the noise PSDs appear simple, when information is extracted through demodulation of the photodiode signal greater care must be taken to ensure that coherent and incoherent noise contributions are combined correctly. A method for computing the noise PSD is discussed in [158] in such cases and on which this work is based (see also [160]).

For computing the noise of a demodulated signal the method discussed in [158] is summarised. Firstly given  $N_D$  demodulations of a signal at frequencies  $f_{D,i}$  and phases  $\phi_{D,i}$ ,  $i \in \{0, 1, 2, \dots, N_D - 1\}$  we construct the demodulation frequency matrix  $\mathcal{F}$  with dimensions  $N_c \times 2^{N_D}$  and demodulation phase vector  $\vec{\Phi}_D$  of length  $2^{N_D}$ .  $\mathcal{F}$  contains all

---

the frequency bins that will be mixed due to the demodulation and  $\vec{\Phi}_D$  lists the total demodulation phase of each mix.

$$\beta_{ij} = (-1)^{\lfloor i/2^{N_D-j-1} \rfloor}$$

$$\Phi_{D,v} = \sum_i^{N_D-1} \beta_{vi} \phi_{D,i} \quad (\text{D.20})$$

$$\mathcal{F}_{uv} = f_{c,u} + \sum_i^{N_D-1} \beta_{vi} f_{D,i} \quad (\text{D.21})$$

$$u \in \{0, 1, 2, \dots, N_c - 1\}$$

$$v \in \{0, 1, 2, \dots, 2^{N_D-1}\}$$

This is based on a tree structure of the various demodulations of each carrier field. As the above form is not particularly easy to visualise, here is an example of a double demodulation with frequencies  $\Delta f$  and  $f_s$  with 3 carriers  $f_c = [0, -\Delta_f, \Delta_f]$  (which are relative to a reference frequency  $f_0$ ) which is depicted in figure D.3:

$$\mathcal{F} = \begin{pmatrix} -\Delta_f - f_s & -\Delta_f + f_s & \Delta_f - f_s & \Delta_f + f_s \\ -2\Delta_f - f_s & -2\Delta_f + f_s & -f_s & f_s \\ -f_s & f_s & 2\Delta_f - f_s & 2\Delta_f + f_s \end{pmatrix}. \quad (\text{D.22})$$

Each row in this matrix lists the frequency bins each carrier field is mixed with. Some frequencies are unique but others are shared between multiple carrier fields. To compute the noise PSD the unique frequencies contribute,

$$S_I^U(\mathcal{F}_{ij}) = \frac{h(f_0 + \mathcal{F}_{ij})}{4^{N_D}} |a_{c,i}|^2 \quad (\text{D.23})$$

The set of  $N_s$  indices,  $\{(n, d)\}$ , of the frequency bins that share multiple carrier fields in  $\mathcal{F}$  must be grouped together,  $\{(n_k, d_k)\}_{k=0}^{N_s}$ . For example the frequency bin  $-f_s$  in equation D.22 appears in 2 elements  $\{(1, 2), (2, 0)\}$ . The contribution to the noise PSD

## D. THE QUANTUM KAT

---

of a shared frequency bin is then calculated by

$$S_I^S(\mathcal{F}_{\{(n,d)\}}) = \frac{h(f_0 + \mathcal{F}_{n_0 d_0})}{4^{N_D}} \left| \sum_{k=0}^{N_s-1} a_{c,n_k}^* e^{i\Phi_{D,d_k}} \right|^2 \quad (\text{D.24})$$

where the carriers are added coherently. The total noise PSD is then simply computed as the sum of both these terms for a particular  $\mathcal{F}$  where the set of unique frequency indices is  $\{(m_k, e_k)\}_{k=0}^{2^{N_D}-N_s}$ ,

$$S_I^T(\mathcal{F}) = S_I^S(\mathcal{F}_{\{(n,d)\}}) + S_I^U(\mathcal{F}_{\{(m,e)\}}). \quad (\text{D.25})$$

To calculate the quantum noise PSD for pure vacuum noise from each carrier field, the above equations are all that is required. If however the interferometer contains non-linear behaviour that squeezes the noise—such as radiation pressure effects—the optical transfer functions from each source of quantum noise through the interferometer to the photodiode outputs of interest are required. In this form these equations are not easy to handle for large complex optical systems, an improved form is demonstrated later.

Sources of noise are either laser noise, squeezed vacuum field inputs or optical losses from scattering and absorption. As each source of noise is incoherent with any other, they cannot be included in a single RHS vector input when solving the interferometer matrix—which would imply that they are coherent. Instead each noise source must be propagated separately and combined incoherently at each output required. The number of noise sources,  $N_n$ , scales with optical losses which can be considerable in a realistic model of an interferometer. The total number of times the interferometer matrix would need to be solved for is then  $\propto N_c N_n (\mathcal{O}^2 + 3\mathcal{O} + 2)/2$ , where  $N_c$  is the number of carriers and  $\mathcal{O}$  is the maximum order of HOM we are using in the simulation;  $\mathcal{O}$  is typically in the range 0 – 10. In simulation tools such as OPTICKLE and

---

MIST, this is the method used when modelling quantum noise. With more realistic setups with large  $\mathcal{O}$  the computational load is heavy. This will be referred to as the single-input multiple-output (SIMO) method, as each source can be propagated to all outputs with one calculation.

Next it is outlined how the noise PSD can be computed by instead propagating all the noise sources with multiple-input single-output (MISO). In cases where noise sources greatly outnumber the number of outputs we wish to consider this should reduce the computational load.

### **Propagation of noise sidebands**

As with classical audio sidebands, the propagation of quantum noise sidebands through an interferometer is described by the matrix  $\mathbb{M}_q$ . The matrix,  $\mathbb{M}_q$ , is nearly identical to that generated for describing how the classical audio sidebands propagate. Both these matrices contain the non-linear behaviour created due to radiation pressure effects, thus describe how noise can become squeezed and how injected squeezed light is rotated or degraded.

Consider the graphical depiction of a double demodulation as shown in figure D.3 to illustrate the problem. This shows 3 carrier fields (red), the pairs of signal sidebands for each carrier (green) and a "sea" of vacuum fluctuations (blue); all of which are being demodulated at the frequencies  $\Delta_f$  and  $f_s$ . The tree structures (black) show how each carrier is mixed with the various signal sidebands and in the case of the carriers at frequencies  $f_{\pm 1}$  how they also mix the with pure vacuum noise.

The number of quantum noise frequency bins is typically greater than the number of signal frequency bins, thus at first it may seem that  $\mathbb{M}_q$  would have to include more frequencies than  $\mathbb{M}_s$ . However, those frequencies that are not paired with a carrier field are typically separated from a carrier field by a frequency  $\gg f_s$ . This frequency separation is large enough (on the order of  $\approx$  MHz) that the beating between them

## D. THE QUANTUM KAT

---

will produce negligible radiation pressure effects due to the mechanical susceptibility of the mirrors at high frequency being  $\propto f^{-2}$  and reciprocally will also squeeze noise fields negligibly.

In the case of gravitation wave detectors, the quantum noise at many MHz is far outside the detectors designed bandwidth and thus of little interest. Therefore the carrier-less  $q_s^\pm$  fields can be assumed to be pure incoherent vacuum noise at every output port and do not need to be included in  $\mathbb{M}_q$  reducing the overall number of fields to propagate to those sidebands paired with a carrier. Due to the use of a conjugated lower sideband in  $\mathbb{M}_q$  for the computation of radiation pressure effects (see chapter 3) the upper limit of the simulation frequency bandwidth is in practice limited. The condition for validity of the model is that sideband frequency  $f_s < \min(\{f_{mod}\})/2$ , i.e. that the signal/noise sideband from one carrier does not become the dominant opposite sideband of another carrier.

## MISO method

Typically for large interferometer models the number of noise sources  $N_n$  is much greater than the number of outputs  $N_o$ . In these scenarios it is computationally inefficient to compute the transfer function for each noise source separately by inverting  $\mathbb{M}_q$ . Instead a method is used for solving the transfer functions for all noise sources for a single output which are then combined efficiently for the computation of the noise PSD. Consider the input-output equation for the quantum sidebands, via some rearranging and taking the expectation value we can find the co-variance matrix of

---

the output noise sidebands  $q_{out}$  due to some injected noise sidebands  $q_{in}$ ,

$$\mathbb{M}_q \vec{q}_{out} = \vec{q}_{in} \quad (\text{D.26})$$

$$\mathbb{M}_q \vec{q}_{out} \vec{q}_{out}^\dagger \mathbb{M}_q^\dagger = \vec{q}_{in} \vec{q}_{in}^\dagger \quad (\text{D.27})$$

$$\vec{q}_{out} \vec{q}_{out}^\dagger = \mathbb{M}_q^{-1} \vec{q}_{in} \vec{q}_{in}^\dagger \mathbb{M}_q^{-1\dagger} \quad (\text{D.28})$$

$$\langle \vec{q}_{out} \vec{q}_{out}^\dagger \rangle = \mathbb{M}_q^{-1} \langle \vec{q}_{in} \vec{q}_{in}^\dagger \rangle \mathbb{M}_q^{-1\dagger} \quad (\text{D.29})$$

$$\mathbb{V}_o = \mathbb{M}_q^{-1} \mathbb{V}_i \mathbb{M}_q^{-1\dagger} \quad (\text{D.30})$$

The result here is that through one inversion of  $\mathbb{M}_q$  and 2 matrix products we can compute the variance-covariance matrix  $\mathbb{V}_o$  of the noise sidebands, due to any number of input noise sources, at any output port in the interferometer. However, both  $\mathbb{M}_q^{-1}$  and  $\mathbb{V}_o$  are dense matrices in practice and the requirements for holding these in memory would be too large for most computer systems. Instead we select out the specific values from  $\mathbb{V}_o$  that we require to compute the noise PSD or value using an output specific *selection vectors*  $\{\vec{s}_i\}_{i=0}^{N_o}$ ,

$$\mathbb{V}_o \vec{s}_i = \mathbb{M}_q^{-1} \mathbb{V}_i \mathbb{M}_q^{-1\dagger} \vec{s}_i \quad (\text{D.31})$$

This can be broken down into several steps that are compatible with most modern sparse matrix solvers [161] which typically only offer interfaces for computing the inverted sparse matrix-vector product efficiently: First we compute the weighted contribution of any noise source in the interferometer to the  $i^{\text{th}}$  output,  $\vec{w}_i = \mathbb{M}_q^{-1\dagger} \vec{s}_i$ ; Next we weight the actual input noise sources present,  $\vec{n}_i = \mathbb{V}_i \vec{w}_i$ ; and finally compute how these propagate to the output,  $\mathbb{M}_q^{-1} \vec{n}_i$ .

The obvious question is now how do we select  $\vec{s}_i$ . This is entirely dependent on what combination of variances and covariances are required. The output value must be calculable by some combination of the noise variances with scaling factors included

## D. THE QUANTUM KAT

---

in the selection vector produced by the product  $\mathbb{V}_o \vec{s}_i$ . The elements of the  $\vec{s}_i$  can also be thought of as the optical carrier field on which we project the noise sidebands at the detector. This then defines the amplitude fluctuations present in the field, thus the amount of noise measured by the photodiode.

### Selection vector: photodiode noise PSD

As previously outlined in section D the quantum noise PSD of a demodulated photodiode output is computed using both equations D.23 and . For the frequency bins that are contained in the interferometer matrix  $\mathbb{M}_q$ , these equations can be represented using a specific selection vector  $\vec{s}_{pd}$ . Computing how any number of noise sources affect one particular photodiode's noise PSD should then be calculable with

$$S_I^T = \frac{\vec{s}_{pd}^\dagger \mathbb{V}_o \vec{s}_{pd}}{4^{N_b}}, \quad (\text{D.32})$$

which again relies on a minimal number of matrix inversions and matrix-vector products for fast computation. The vector  $\vec{s}_{pd}$  should be filled with zeros apart from the indices representing the upper and lower sidebands of all the carrier fields. The upper filled with the conjugate of the corresponding HOM and optical frequency carrier amplitude and the lower with the unconjugated. This vector-matrix product will select out the variances multiple with the relevant carrier values, which is akin to both Eq.(D) and Eq.(D.23).

This vector-matrix-vector must be equivalent to equation D.25 which is the contribution to the noise PSD for both unique and shared frequencies for a particular demodulation frequency matrix  $\mathcal{F}$ . However, not all of the optical frequencies in  $\mathbb{M}_q$  are in  $\mathcal{F}$ . These missing frequencies could also be shared or unique contributions in  $\mathcal{F}$ , the sets of indices for these frequencies are respectively  $\{(n', d')\}$  and  $\{(m', e')\}$ . The total photocurrent noise PSD of a demodulated photodiode output for a generic set of

---

incident carrier fields and arbitrary optical setup is then,

$$S_I^T = \frac{\vec{s}_{pd}^\dagger \mathbb{V}_o \vec{s}_{pd}}{4N_D} + S_I^S(\mathcal{F}_{\{(n',d')\}}) + S_I^U(\mathcal{F}_{\{(m',e')\}}). \quad (\text{D.33})$$

## Source injection

An important aspect to using this method correctly is how to build the input noise matrix,  $\mathbb{V}_i$ . This, like the RHS vector when solving the classical interferometer matrix, just describes what the source PSD variance and covariance between every field is; its diagonal elements being the variances and off-diagonal elements the covariances.

Noise sources that must be considered in this input matrix are:

- Open ports
- Component losses
- Squeezing injection
- HOM scattering

The first two are straight forward. Anywhere an open port or component loss exists at a particular node in the model the equivalent amount of noise lost must be injected back in. Squeezed light input requires both variance and covariance between the quantum noise sidebands of the squeezed carrier to be added. When considering HOMs it must be stated which mode is squeezed. Currently FINESSE assumes only TEM<sub>00</sub> is squeezed, the rest are left as pure vacuum noise.

When HOM scattering is present in the model, noise can be both coupled between modes or lost completely. This is due to a finite cut-off in the order of modes included. Thus noise in one mode can be coupled to another, say in the case of a mismatched squeezed field, or it could be lost completely if the mode it is scattered into isn't in the model.

## D. THE QUANTUM KAT

---

This introduces a problem. To converge the results computed many HOMs would need to be included to ensure no noise is lost, giving lower noise levels than it should; however, this slows the simulation down dramatically. Instead it can be assumed that whenever some scattering loss is present, pure vacuum noise is injected back in. For any given scattering matrix,  $\mathbf{K}$ , the total amount of lost power of the  $j^{\text{th}}$  mode is given by the sum of the coupling coefficients:  $L_j = 1 - \sum_{i=0}^N |\mathbf{K}_{ij}|^2$ . This states how much of a particular mode is scattered out of the model. Ideally this value should be 0 if the distortion is completely represented with up to order  $\mathcal{O}_{max}$ .

This lost modal power can then be inserted as a scaled vacuum noise source for each mode in the noise source matrix—just as a normal loss would. Using this technique when scattering of noise was present in the model, it was found that using  $\mathcal{O}_{max} = 0$  gave the same result as before when using a large  $\mathcal{O}_{max}$ . When squeezed light is used enough  $\mathcal{O}_{max}$  should be used to include how the squeezed states are coupled between modes. Otherwise coupled squeezed light will just be replaced with vacuum noise.

### How $\mathbb{M}_q$ differs from $\mathbb{M}_s$

Although both  $\mathbb{M}_q$  and  $\mathbb{M}_s$  propagate the same sideband frequencies and fields through the same interferometric setup, they differ when modelling modulator components. With  $\mathbb{M}_s$  the frequency bins considered are all coherent, whereas in  $\mathbb{M}_q$  the same bins are all incoherent. Consider a single frequency bin of pure vacuum noise, similar to that seen with demodulation, a modulator will couple more noise from other frequency bins that match the modulator's driving frequency into the bin of interest. At the same time it will also take noise from this bin and couple it to others. Overall this has a net result of leaving the same amount of vacuum noise as we began with. Thus if we make the assumption that all incoming carrier fields have only pure vacuum noise present all that will be present at the output is pure vacuum noise. This would not be the

---

case if squeezed fields were present on a carrier or the noise has a larger magnitude than that of pure vacuum. However, such cases are rarely considered in gravitational wave interferometers. Thus in FINESSE the modulator component always assumes pure vacuum noise is input to it.

## D. THE QUANTUM KAT

---

# Appendix E

## aLIGO Finesse file

Here one version of an aLIGO FINESSE is provided for reference. This file was based on the core design file for aLIGO. It was altered to include aspects required for modelling mode matching effects between the numerous cavities. It also contains a 16m filter cavity with 10 dB of squeezing to provide a broadband reduction in quantum noise. This file was developed as part of the AWC project by several members of the aLIGO FINESSE modelling team: Paul Fulda, Charlotte Bond, Antonio Perreca, Andreas Freise and myself.

The file is presented here to give a sense of the level of detail required to model advanced detectors. These files and others are constantly evolving through further use and updates to mirror the real detectors. Thus for up to date versions interested readers should explore the core file folder in the aLIGO FINESSE team Git repository [29] or those files that are uploaded to the LIGO DCC [1, 2, 3].

The usage of *blocks* in large FINESSE files such as this is important for organisational and usage purposes. The blocks contain all the relevant commands for particular subsections of the interferometer. This blocking means a several hundred line file can be navigated with ease. It also allows a degree of automation in particular tasks as blocks can easily be removed if that particular section of code is not required for your

## E. ALIGO FINESSE FILE

---

simulation.

---

### Code E.1 FINESSE file used for AWC simulations

---

```
# -----  
  
# aligo_IFO_maxtem4.kat (Mode matching optimized for ~18W input power)  
#  
# FINESSE kat file for aligo dual recycled michelson with FP arm cavities  
# Tuned for use with maxtem 4 option. Includes a 16m Filter cavity and 10  
# dB  
# of squeezing  
#  
# Parameters are mostly design parameters (see below).  
#  
# To be used as a base file for investigations into active wavefront  
# control  
# requirements, sensing and actuation. Compatible with "awc_tools.py" file  
# for performing automated tasks (zero locks, plot error signals etc.)  
#  
# > This is a file based on aligo_central_IFO.kat where the following  
# features have been added:  
# - Thermal lensing at ITMs (modeled as a thin lens outside  
# the substrate). Default value is 34.5km, corresponding to the lens  
# predicted at ~18W input power with 0.5ppm absorption on ITMs.  
# - SRM thickness;  
# - ROCs and lengths of PRC SRC changed following T0900043 (Table 2) to  
# mode match the cavities with a 34.5km thermal lens in ITMs.  
# - However, PR3 to BS and SR3 to BS are adjusted to maintain overall  
# quoted P/SRC length. These lengths have minimal effect on mode  
# matching.  
# - N.B. the thermal lens quoted in T0900043 is 50km, but this was  
# modeled as being inside the ITM substrate, so in this model the focal  
# length is adjusted by a factor 1/nsilica.  
#  
# FINESSE kat file for aLIGO dual recycled michelson with FP arm cavities.  
#  
# Lengths and Rcs  
# - generally taken from design document T0900043-11 unless otherwise  
# stated  
# - Schnupp asymmetry changed to 8cm (from 5cm)  
# - Average distance between BS and ITMX and ITMY calculated using length  
# of PRC, as not explicitly given (then +/- 4cm on distances to give  
# Schnupp asymmetry)  
# Reflectivities/transmission/losses  
# - also from T0900043-11  
# - transmission of SRM changed to 35% (i.e. see T1300507-v1)  
# - losses at each mirror = 37.5ppm  
#  
# Also use T1000298-T for parameters, (design) control scheme with some  
# updates to match current sensing scheme.  
#  
# https://dcc.ligo.org/LIGO-L1300231  
# https://awiki.ligo-wa.caltech.edu/aLIGO/Finesse%20for%20aLIGO  
# https://alog.ligo-la.caltech.edu/aLOG/index.php?callRep=8102  
#  
# DARM offset adjusted to give 147mW DC offset at 125W input power  
# DARM error signal derived from OMC DC power  
#  
# Charlotte Bond, Daniel Brown, Paul Fulda, Antonio Perreca, Andreas  
# Freise  
# Updated on 2015-09-08  
#
```

```

-----

%% FTblock laser
#
#####

%% FTblock laser
#
#####

l L0 125 0 n0
s lmod1 1 n0 n1
mod mod1 $f1 0.18 1 pm n1 n2
s lmod2 1 n2 n3
mod mod2 $f2 0.18 1 pm n3 n4
s lmod3 1 n4 n5
mod mod3 $f3 0.1 1 pm n5 n6
s mod3toMC1 1 n6 nMC1in

#
#####

%% FTend Laser
%% FTblock IMC
#
#####

# MC1
bs1 MC1 6030u 0.6u 0 44.59 nMC1in nMC1refl nMC1trans nMC1fromMC3
s sMC1toMC2 16.2405708 nMC1trans nMC2in

# MC2
bs1 MC2 5.1u 9.3u 0 0.82 nMC2in nMC2refl nMC2trans dump1
s sMC2toMC3 16.2405708 nMC2refl nMC3in
attr MC2 Rc 27.275

# MC3
bs1 MC3 5845u 0.8u 0 44.59 nMC3in nMC3refl nMC3trans nMCreturn_refl
s sMC3toMC1 0.465 nMC3refl nMC1fromMC3

s sMC3substrate 0.0845 $nsilica nMC3trans nMC3ARin
bs2 MC3AR 0 0 0 28.9661 nMC3ARin dump nMC3ARtrans dump
s sMC3ARtoIM1 0.4282 nMC3ARtrans nIM1in

#
#####

%% FTend IMC
%% FTblock HAM2
#
#####

# IM1 a.k.a. SM1
bs1 IM1 0 0 0 53 nIM1in nIM1refl nIM1HRtrans dump
s sIM1sub 0.02995 $nsilica nIM1HRtrans nIM1ARin
bs2 IM1AR 0 0 0 33.4 nIM1ARin dump5 nIM1ARtrans dump

s IM1ARtonanoscan 3 nIM1ARtrans nIOT2Lnanoscan

#AOE1

```

## E. ALIGO FINESSE FILE

---

```
s sIM1toAOE1 0.1955 nIM1refl nAOE1in
lens AOE1 inf nAOE1in nAOE1trans

# IM2 a.k.a. PMMT1
s sAOE1toIM2 1.0983 nAOE1trans nIM2in
bs1 IM2 0 0 0 7 nIM2in nIM2refl dump dump
attr IM2 Rc 12.8

s sIM2toIM3 1.1704 nIM2refl nIM3in

# IM3 a.k.a PMMT2
#s sIM2toIM3 1.1704 nIM2refl nIM3in
bs1 IM3 0 0 0 7.1 nIM3in nIM3refl dump dump
attr IM3 Rc -6.24

#AOE2
s sIM3toAOE2 1.041 nIM3refl nAOE2in
lens AOE2 inf nAOE2in nAOE2trans

# IM4 a.k.a. SM2
s sAOE2toIM4 0.134 nAOE2trans nIM4in

bs1 IM4 2400u 0 0 45 nIM4in nIM4refl nIM4trans nIM4rettrans
s sIM4toPRMAR 0.4135 nIM4refl nREFL

#
#####

%% FTend HAM2

%% FTblock PR
#
#####

# PRM

# AR surface
m2 PRMAR 35u 4.5u $phi_PRM nREFL nPRMARb

# Substrate
s sPRMsub1 0.0737 $nsilica nPRMARb nPRMHRa

# HR surface
m1 PRMHR 0.03 8.5u $phi_PRM nPRMHRa nPRMHRb
attr PRMHR Rc 11.009

# Distance between PRM and PR2
s lp1 $Lpr1 nPRMHRb nPR2a

# PR2
bs1 PR2 250u $Mloss 0 -0.79 nPR2a nPR2b nPOP dump
attr PR2 Rc -4.545

# Distance from PR2 to PR3
s lp2 $Lpr2 nPR2b nPR3a

# PR3
bs1 PR3 0 $Mloss 0 0.615 nPR3a nPR3b dump dump
attr PR3 Rc 36.027

# Distance from PR3
s lp3 $Lpr3 nPR3b nPRBS

#
#####
```



## E. ALIGO FINESSE FILE

---

```
attr ITMYHR Rc -1934
attr ETMYHR Rc 2245

attr ITMYHR mass 40
attr ETMYHR mass 40

#
#####

%%% FTend Yarm

%%% FTblock Xarm
#
#####

# Distance from beam splitter to X arm input mirror
s lx1 5.0082 nXBS nITMX11

# Thermal lens correction
lens ITMXTL $TL_f nITMX11 nITMXTLtrans
s ITMXt1_null 0 nITMXTLtrans nITMXconstL_in
lens ITMXconstL inf nITMXconstL_in nITMXconstL_trans
s ITMXTL_null2 0 nITMXconstL_trans nITMX1

# X arm input mirror
m2 ITMXAR 20u 0 $phi_ITMX nITMX1 nITMXs1
s ITMXsub 0.2 $nsilica nITMXs1 nITMXs2
m1 ITMXHR 0.014 $Mloss $phi_ITMX nITMXs2 nITMX2
#m1 ITMXHR 0 $Mloss $phi_ITMX nITMXs2 nITMX2

# X arm length
s LXarm 3994.5 nITMX2 nETMX1

# X arm end mirror
m1 ETMXHR 5u $Mloss $phi_ETMX nETMX1 nETMXs1
s ETMXsub 0.2 $nsilica nETMXs1 nETMXs2
m2 ETMXAR 500u 0 $phi_ETMX nETMXs2 nPTX

attr ITMXHR Rc -1934
attr ETMXHR Rc 2245

attr ETMXHR mass 40
attr ITMXHR mass 40

#
#####

%%% FTend Xarm

%%% FTblock SR
#
#####

# Distance to SR3
s ls3 $Lsr3 nSRBS nSR3b

# SR3
bs1 SR3 0 $Mloss 0 0.785 nSR3b nSR3a dump17 dump
attr SR3 Rc 35.972841

# Distance from SR3 to SR2
s ls2 $Lsr2 nSR3a nSR2b

# SR2
bs1 SR2 0 $Mloss 0 -0.87 nSR2b nSR2a dump dump
```

```

attr SR2 Rc -6.406

# Distance from SR2 to SRM
s ls1 $Lsr1 nSR2a nSRMHRa

# Signal recycling mirror SRM-08
m1 SRMHR $T_SRM $L_SRM $phi_SRM nSRMHRa nSRMHRb
s SRMsub 0.0749 $nsilica nSRMHRb nSRMARA
m2 SRMAR 50n 0 $phi_SRM nSRMARA nSRMARb
attr SRMHR Rc -5.6938

#
#####

%% FTend SR

%% FTblock FI
#
#####

# The FI is on a platform delimited by the Input/Output Buffer Assy (I/OBA
)
# The physical distance IBA --> OBA = 0.5034 (D0901920-V13)
# OFI design based on: D0900464, D1002598

# Distance from SRM (AR surface) to the input buffle assy (IBA) in OFI sus
s lIBAIN 0.491516 nSRMARb nIBAIN
m1 IBA 1 0 0 nIBAIN nIBAout

# Distance from IBA to input of OFI (Prism in between not considered)
s lOFIin 0.16 nIBAout nOFIin

# Input Polirizer IP (Silica)
bs1 IP 1 0 0 0 nOFIin dump nIPtrans dump
s lIP 0.019 $nsilica nIPtrans nROTin

# Rotator (TGG)
m1 ROTin 1 0 0 nROTin nROTB
s lROT 0.08285 $nTGG nROTB nROTouta
m1 ROTout 1 0 0 nROTouta nOPa

# Output polirizer OP (Silica)
s lOP 0.019 $nsilica nOPa nOPb

# removed to add in circulator
#m1 OP 1 0 0 nOPb nOFIout

# use new isolator option for injecting the squeezed field
# nOPd is the output towards OMC
# nOPb is the input from SRC
# nOPc is the input from squeezer
isol* OP 100000 nOPd nOPb nOPc # squeezing circulator

# need a bunch of dummy spaces to keep refractive index the same over isol
nodes
# output port of FI where squeezed field is injected
s lOP2 0 $nsilica nOPc nOPe
m1 mOFIout2 1 0 0 nOPe nOFIout2

s lOP3 0 $nsilica nOPd nOPf
m1 mOPinterface 1 0 0 nOPf nOFIout

# Waveplate thickness
s lWP 0.0127 $nCalcite nOFIout nWPa
m1 WP 1 0 0 nWPa nWPb

# Distance from Waveplate to OBA of OFI (Prism in between not considered)

```

## E. ALIGO FINESSE FILE

---

```

s lOBA 0.2098563 nWPb nOBAin
m1 OBA 1 0 0 nOBAin nOBAout
#
#####

%%% FTend FI

%%% FTblock FilterCavity
#
#####

# Mode matching settings:
#   Distance from BS to lens 1:           d1 = 0.541093376854 m
#   Distance from lens1 to lens 2:       d2 = 0.234279382609 m
#   Distance from lens1 to cavity waist: d3 = 8.22462724054 m
#   Focal length of lens1:              f1 = -0.3 m
#   Focal length of lens2:              f2 = 0.55 m
#   Distance from BS to cavity waist:    D_tot = 9.0 m

s lOP_lensFC 0.541093376854          nOFIout2 nlensFC1a
lens lensFC1 -0.3                    nlensFC1a nlensFC1b
s llensFC1_lensFC2 0.234279382609  nlensFC1b nlensFC2a
lens lensFC2 0.55                    nlensFC2a nlensFC2b
s llensFC_FC 0.22462724054          nlensFC2b nIMFC2

# Confocal cavity
attr IMFC Rc -15.999
attr EMFC Rc 15.999
const FLength 16

# using beamsplitters for FC so no need for an isolator
bs1 IMFC 61u 0 0 0 nIMFC1 nIMFC2 nIMFC3 nIMFC4
s lFC1 $FLength nIMFC3 nEMFC1
s lFC2 $FLength nEMFC2 nIMFC4
bs1 EMFC 0 0 -0.000882 0 nEMFC1 nEMFC2 dump dump

s lsqz_FC 0 nsqz nIMFC1

# finally the squeezer...
sq sqz 0 10 0 nsqz

#
#####

%%% FTend FilterCavity

%%% FTblock OMCpath
#
#####

# (Loctions and angles based on the solid work file D1000342-v14 give ~5%
# mismatch. Thus lom1, lom3omc have been adjusted to get ~99.7% overlap at
# the OMC)
# (lom1=2.6334, lom3omc=0.24.8 give 99% overlap at OMC)

# Distance OBA --> OM1
s lom1 2.724 nOBAout nOM1a

#OM1
bs1 OM1 800u $Mloss 0 2.251 nOM1a nOM1b dump dump # T is set for high
# power; Loss is a guess
attr OM1 Rc 4.6

# Distance OM1 --> OM2
s lom2 1.395 nOM1b nOM2a

```

```

# OM2
bs1 OM2 10u $Mloss 0 4.399 nOM2a nOM2b dump dump # T is a guess
attr OM2 Rc 1.7058

# Distance OM2 --> OM3
s lom3 0.631 nOM2b nOM3a
bs1 OM3 0.01 $Mloss 0 30.037 nOM3a nOM3b nOM3trans dump # T is a from
T1200410-v2

# Distance OM3 --> OMC input coupler IC (AR side)
s lom3omc 0.196 nOM3b nOMC_ARIC_in # By design should be ~0.31

# Distance in transmission to OM3 used for testing
#s lomOM3trans 0.1 nOM3trans nOMC_ARIC2_in

#
#####

%% FTend OMCpath

%% FTblock OMC
#
#####

# OMC (as built parameters: D1300507-v1)

# Input Coupler IC (flat mirror)
bs1 OMC_ARIC 1 0 0 4.004 nOMC_ARIC_in dump nOMC_ARIC_trans dump
s subOMC_IC 0.01078 $nsilica nOMC_ARIC_trans nOMC_HRIC_in
bs1 OMC_HRIC 0.0076 10u 0 2.7609 nOMC_HRIC_in dump nOMC_HRIC_trans
nOMC_HRICret
# Distance from IC to OC
s OMC_ICOC 0.2815 1 nOMC_HRIC_trans nOMC_HROC_in

# Output Coupler OC (flat mirror)
bs1 OMC_HROC 0.0075 10u 0 4.004 nOMC_HROC_in nOMC_HROC_refl
nOMC_HROC_trans nOMC_HROC_ret
s subOMC_OC 0.01078 $nsilica nOMC_HROC_trans nOMC_AROC_in
bs1 OMC_AROC 1 0 0 2.7609 nOMC_AROC_in dump nOMC_AROC_trans dump32
# Distance from OC to CM1
s OMC_OCCM1 0.2842 1 nOMC_HROC_refl nOMC_CM1_in

# Curved Mirror CM1
bs1 OMC_CM1 36u 10u 0 4.004 nOMC_CM1_in nOMC_CM1_refl dump dump

# Distance from CM1 to CM2
s OMC_CM1CM2 0.2815 1 nOMC_CM1_refl nOMC_CM2_in
attr OMC_CM1 Rc 2.57321

# Curved Mirror CM2
bs1 OMC_CM2 35.9u 10u 0 4.004 nOMC_CM2_in nOMC_CM2_refl dump dump
attr OMC_CM2 Rc 2.57369

# Distance from CM2 to IC
s CM2OC 0.2842 1 nOMC_CM2_refl nOMC_HRICret

#
#####

%% FTend OMC

%% FTblock Lengths
#
#####

# Calculate lengths of variables so Schnupp asymmetry can be changed
# easily.

```

## E. ALIGO FINESSE FILE

---

```
# Cavity lengths
const Lprc 57.656
#const Lprc 57.645
const Lsrc 56.008
const Lschnupp 0.08

# Individual lengths
# PRC
const Lpr1 16.6107
const Lpr2 16.1647
const Lpr3 19.5381

# SRC
const Lsr1 15.7586
const Lsr2 15.4435
const Lsr3 19.3661

# Arms
const BStickness 0.06873

func Laver = $Lprc - $Lpr1 - $Lpr2 - $Lpr3
noplplot Laver

# x length between BS and ITM
func Lmx = $Laver + 0.5*$Lschnupp - $BStickness * $nsilica - 0.2*$nsilica
noplplot Lmx
put lx1 L $Lmx

# y length between BS and ITM
func Lmy = $Laver - 0.2*$nsilica - 0.5*$Lschnupp
noplplot Lmy
put ly1 L $Lmy

# Lsr3
%func Lasrc = $Laver + $BStickness * $nsilica
%noplplot Lasrc
%func Lsr3 = $Lsrc - $Lsr1 - $Lsr2 - $Lasrc
#noplplot Lsr3
%put ls3 L $Lsr3

#
#####

%% FTend Lengths

%% FTblock Tunings
#
#####

const phi_SRM 90.0068431881324
const phi_PRM 0.000212433947790268
const phi_ITMX 4.36378389012253e-05
const phi_ITMY -4.36378389012253e-05
const phi_ETMX 0.00172458093206306
const phi_ETMY -0.0017617703270198
const phi_BS 0

#
#####

%% FTend Tunings

%% FTblock Constants
#
#####
```

```

const Mloss 37.5u
const T_SRM 0.35
const L_SRM 8.7u

const nsilica 1.44963098985906
const nTGG 1.954
const nCalcite 1.65846
const f1 9099471
const nf1 -9099471
const f2 45497355
const nf2 -45497355
const f3 24000000
const nf3 -24000000

const fM 36397884
const nfM -36397884
const fP 54596826
const TL_f 34.5k

const DARM_DC_offset 0.147303
#
#####

%% FTend Constants
%% FTblock errsigs
#
#####

pd1 REFL_f1_I $f1 101 nREFL
pd1 REFL_f1_Q $f1 191 nREFL
pd1 REFL_f2_I $f2 14 nREFL
pd1 REFL_f2_Q $f2 104 nREFL
pd1 POP_f1_I $f1 101 nPOP
pd1 POP_f1_Q $f1 191 nPOP
pd1 POP_f2_I $f2 13 nPOP
pd1 POP_f2_Q $f2 103 nPOP
pd1 AS_f1_I $f1 0 nSRMARb
pd1 AS_f1_Q $f1 90 nSRMARb
pd1 AS_f2_I $f2 13 nSRMARb
pd1 AS_f2_Q $f2 103 nSRMARb

#
#####

%% FTend errsigs
%% FTblock Powers
#
#####

pd P_DC_AS nSRMARb
pd P_DC_OMC nOMC_HROC_trans
pd PIMCtrans nREFL*
pd Px nITMX2
pd Py nITMY2
pd Pprc nPRMHRb
pd Psrc nSRMHRa*
ad prc0 0 nPRMHRb
ad prcf1 $f1 nPRMHRb
ad prcf2 $f2 nPRMHRb

ad aoc0 0 nOMC_HROC_trans
ad asc0 0 nSRMARb

```

## E. ALIGO FINESSE FILE

---

```
ad asf1 $f1 nSRMARb
ad asf2 $f2 nSRMARb
ad src0 0 nSRMHRa*
ad srcf1 $f1 nSRMHRa*
ad srcf2 $f2 nSRMHRa*

#
#####

%%% FTend Powers

%%% FTblock HOMs
#
#####

cav cavIMC MC2 nMC2in MC2 nMC2refl
cav cavPRX PRMHR nPRMHRb ITMXHR nITMXs2
cav cavPRY PRMHR nPRMHRb ITMYHR nITMYs2
cav cavSRX SRMHR nSRMHRa ITMXHR nITMXs2
cav cavSRY SRMHR nSRMHRa ITMYHR nITMYs2
cav cavXARM ITMXHR nITMX2 ETMXHR nETMX1
cav cavYARM ITMYHR nITMY2 ETMYHR nETMY1
cav cavOMC OMC_HROC nOMC_HROC_refl OMC_HROC nOMC_HROC_in

maxtem 4

#
#####

%%% FTend HOMs

%%% FTblock locks
#
#####

set PRCL_err POP_f1_I re
set MICH_err POP_f2_Q re
set CARM_err REFL_f1_I re
set SRCL_err REFL_f2_I re
set OMC_DC P_DC_OMC re

func DARM_err = $OMC_DC - $DARM_DC_offset

lock PRCL_lock $PRCL_err -2.76232377128 10u
lock MICH_lock $MICH_err 12.0372824217 10u
lock CARM_lock $CARM_err 0.000118716534369 10u
lock DARM_lock $DARM_err -0.00577883583949 1u
lock SRCL_lock $SRCL_err -4.88581756575 10u

func mMICH_lock = 0 - $MICH_lock
func ETMX_lock = $CARM_lock + $MICH_lock + $DARM_lock
func ETMY_lock = $CARM_lock - $MICH_lock - $DARM_lock

put* PRMHR phi $PRCL_lock
put* PRMAR phi $PRCL_lock

put* ITMXHR phi $MICH_lock
put* ITMXAR phi $MICH_lock
put* ITMYHR phi $mMICH_lock
put* ITMYAR phi $mMICH_lock

put* ETMXHR phi $ETMX_lock
put* ETMXAR phi $ETMX_lock

put* ETMYHR phi $ETMY_lock
```

```

put* ETMYAR phi $ETMY_lock

put* SRMHR phi $SRCL_lock
put* SRMAR phi $SRCL_lock

noplot PRCL_lock
noplot SRCL_lock
noplot MICH_lock
noplot DARM_lock
noplot CARM_lock
noplot mMICH_lock
noplot ETMX_lock
noplot ETMY_lock

#
#####

%% FTend locks

%% FTblock ASWFS
#
#####

s lOM3trans2ASWFSBS 0.66 nOM3trans nASWFSBSin
bs ASWFSBS 0.5 0.5 0 45 nASWFSBSin nASWFSBSrefl nASWFSBStrans dump

s lASWFSBS2ASWFSA 0.1 nASWFSBSrefl nASWFSA
attr lASWFSBS2ASWFSA gouy 70

s lASWFSBS2ASWFSB 0.379 nASWFSBStrans nASWFSB
attr lASWFSBS2ASWFSB gouy 160

# AS WFS RF detectors
pd1 ASWFSA_45I_P $f2 0 nASWFSA
pd1 ASWFSA_45Q_P $f2 90 nASWFSA
pd1 ASWFSA_36I_P $fM 15 nASWFSA
pd1 ASWFSA_36Q_P $fM 75 nASWFSA
pdtype ASWFSA_45I_P y-split
pdtype ASWFSA_45Q_P y-split
pdtype ASWFSA_36I_P y-split
pdtype ASWFSA_36Q_P y-split

pd1 ASWFSB_45I_P $f2 0 nASWFSB
pd1 ASWFSB_45Q_P $f2 90 nASWFSB
pd1 ASWFSB_36I_P $fM 65 nASWFSB
pd1 ASWFSB_36Q_P $fM 155 nASWFSB
pdtype ASWFSB_45I_P y-split
pdtype ASWFSB_45Q_P y-split
pdtype ASWFSB_36I_P y-split
pdtype ASWFSB_36Q_P y-split

const f_sig 1

# AS WFS RF detectors double demodulated at signal frequency $f_sig
pd2 ASWFSA_45I_audio_P $f2 0 $f_sig max nASWFSA
pd2 ASWFSA_45Q_audio_P $f2 90 $f_sig max nASWFSA
pd2 ASWFSA_36I_audio_P $fM 0 $f_sig max nASWFSA
pd2 ASWFSA_36Q_audio_P $fM 90 $f_sig max nASWFSA
pdtype ASWFSA_45I_audio_P y-split
pdtype ASWFSA_45Q_audio_P y-split
pdtype ASWFSA_36I_audio_P y-split
pdtype ASWFSA_36Q_audio_P y-split

pd2 ASWFSB_45I_audio_P $f2 0 $f_sig max nASWFSB
pd2 ASWFSB_45Q_audio_P $f2 90 $f_sig max nASWFSB
pd2 ASWFSB_36I_audio_P $fM 0 $f_sig max nASWFSB

```

## E. ALIGO FINESSE FILE

---

```
pd2 ASWFSB_36Q_audio_P $fM 90 $f_sig max nASWFSB
pdtype ASWFSB_45I_audio_P y-split
pdtype ASWFSB_45Q_audio_P y-split
pdtype ASWFSB_36I_audio_P y-split
pdtype ASWFSB_36Q_audio_P y-split
```

```
#
```

```
#####
```

```
%% FTend ASWFS
```

```
%% FTblock commands
```

```
%% FTend commands
```

---

# List of publications

## Papers

- 2015 Daniel Brown et al. Optical suppression of parametric instabilities with extraction cavities. 2015. In preparation
- 2015 Daniel Brown, Rory Smith, and Andreas Freise. Fast simulation of gaussian-mode scattering for precision interferometry. *Journal of Optics*, Sept 2015. Submitted on 2<sup>nd</sup> of September, awaiting feedback
- 2015 Daniel Brown and Andreas Freise. Simulation methods for advanced interferometers. In Peter Saulson and David Reitze, editors, *Advanced Interferometric Gravitational-wave Detectors*. World Scientific, 2015. Chapter submitted in May 2015
- 2015 C. Bond, D. Brown, A. Freise, and K. Strain. Interferometer Techniques for Gravitational-Wave Detection. *Living Reviews in Relativity*, 13, 2015. Submitted as of August 2015
- 2013 Daniel Brown, Daniel Friedrich, Frank Brückner, Ludovico Carbone, Roman Schnabel, and Andreas Freise. Invariance of waveguide grating mirrors to lateral displacement phase shifts. *Opt. Lett.*, 38(11):1844–1846, Jun 2013
- 2013 Deepali Lodhia, Daniel Brown, Frank Brückner, Ludovico Carbone, Paul Fulda, Keiko Kokeyama, and Andreas Freise. Interferometer phase noise due to beam misalignment on diffraction gratings. *Opt. Express*, 21(24):29578–29591, Dec 2013
- 2013 Mengyao Wang, Charlotte Bond, Daniel Brown, Frank Brückner, Ludovico Carbone, Rebecca Palmer, and Andreas Freise. Realistic polarizing sagnac topology with dc readout for the einstein telescope. *Phys. Rev. D*, 87:096008, May 2013
- 2013 Ludovico Carbone, Paul Fulda, Charlotte Bond, Frank Brueckner, Daniel Brown, Mengyao Wang, Deepali Lodhia, Rebecca Palmer, and Andreas Freise. The generation of higher-order laguerre-gauss optical beams for high-precision interferometry. (78), 2013
- 2012 L. Carbone, C. Bond, D. Brown, F. Brückner, K. Grover, D. Lodhia, C.M.F. Mingarelli, P. Fulda, R.J.E. Smith, R. Unwin, A. Vecchio, M. Wang, L. Whalley, and

A. Freise. Computer-games for gravitational wave science outreach: Black hole pong and space time quest. *Journal of Physics: Conference Series*, 363:012057, 2012

2012 P. Fulda, C. Bond, D. Brown, F. Brückner, L. Carbone, S. Chelkowski, S. Hild, K. Kokeyama, M. Wang, and A. Freise. Review of the laguerre-gauss mode technology research program at birmingham. *Journal of Physics: Conference Series*, 363:012010, 2012

### **Presentation, posters and technical documents**

2015 Daniel Brown and Rory Smith. Presentation: Fast simulation of gaussian-mode scattering for precision interferometry, 2015. DCC G1501137. Presented at the Budapest LVC meeting

2015 Paul Fulda, Daniel Brown, Charlotte Bond, Kiwamu Izumi, Lisa Barsotti, and Andreas Freise. Simulation investigation of mode hopping in the h1 signal recycling cavity. Technical Report T1500230, LIGO DCC, June 2015

2015 Daniel Brown, Charlotte Bond, and Andreas Freise. Finesse 2: Radiation pressure and the quantum kat, May 2014. DCC G1400580. Presented at GWADW Takayama

2014 Daniel Brown, Charlotte Bond, Paul Fulda, and Andreas Freise. Update on als alignment modelling and on finesse, Jun 2014. DCC G1400622. Presented to LIGO modelling group

2013 Charlotte Bond, Paul Fulda, Daniel Brown, and Andreas Freise. Investigation of beam clipping in the power recycling cavity of Advanced LIGO using FINESSE. Technical Report T1300954, LIGO DCC, Nov 2013

2013 Ludovico Carbone, Daniel Brown, Charlotte Bond, Paul Fulda, and Andreas Freise. Finesse: a numerical simulation tool for optical design and detector commissioning, Mar 2013. DCC G1300301. Poster at Bethesda LVC meeting

2013 Daniel Brown, Charlotte Bond, Mengyao Wang, Ludovico Carbone, and Andreas Freise. Modelling mirror surface distortion effects in low-loss, near-unstable fabry-perot cavities, Jul 2013. DCC G1300711. Poster at Warsaw Amaldi

2013 Daniel Brown, Charlotte Bond, and Andreas Freise. Finesse: v1.0 and beyond, May 2013. DCC G1300538. Presented at Nice LVC meeting

2013 Charlotte Bond, Daniel Brown, and Andreas Freise. Mode healing in gw interferometers, Jul 2013. DCC G1300711. Poster at Warsaw Amaldi

2013 Charlotte Bond, Daniel Brown, and Andreas Freise. Mode healing in gw interferometers, Jul 2013. DCC G1300711. Poster at Warsaw Amaldi

- 
- 2013 Charlotte Bond, Paul Fulda, Daniel Brown, Andreas Freise, Keiko Kokeyama, Ludovico Carbone, Suresh Doravari, and Koji Arai. FINESSE simulation for the alignment control signal of the aligo input mode cleaner. Technical Report T1300074, LIGO DCC, January 2013
- 2012 Daniel Brown and Andreas Freise. Optical simulations within and beyond the paraxial limit, May 2012. DCC G1200548. Presented at GWADW Hawaii
- 2012 B. Barr, A. Bell, C. Bell, C. Bond, D. Brown, F. Brueckner, L. Carbone, K. Craig, A. Cumming, S. Danilishin, K. Dooley, A. Freise, T. Fricke, P. Fulda, S. Giampsis, N. Gordon, H. Grote, G. Hammond, J. Harms, S. Hild, J. Hough, S. Huttner, R. Kumar, H. Luck, N. Lockerbie, J. Macarthur, I. Martin, P. Murray, S. Reid, S. Rowan, D. Shoemaker, B. Sorazu, K. Strain, S. Tarabrin, K. Tokmakov, and N. Voronchev. Ligo 3 strawman design, team red. Technical Report T1200046, LIGO DCC, Jan 2012

## E. LIST OF PUBLICATIONS

---

# References

- [1] Charlotte Bond, Paul Fulda, Daniel Brown, Andreas Freise, Keiko Kokeyama, Ludovico Carbone, and Antonio Perreca. FINESSE input files for advanced ligo. Technical Report L1300231, LIGO DCC, August 2015.
- [2] Charlotte Bond, Paul Fulda, Daniel Brown, Andreas Freise, Keiko Kokeyama, Ludovico Carbone, and Antonio Perreca. FINESSE input files for lho advanced ligo. Technical Report T1300904, LIGO DCC, June 2015.
- [3] Charlotte Bond, Paul Fulda, Daniel Brown, Andreas Freise, Keiko Kokeyama, Ludovico Carbone, and Antonio Perreca. FINESSE input files for llo advanced ligo. Technical Report T1300901, LIGO DCC, December 2014.
- [4] B.S. Sathyaprakash and Bernard F. Schutz. Physics, astrophysics and cosmology with gravitational waves. *Living Reviews in Relativity*, 12(2), 2009.
- [5] Daniel Brown. Stretch-and-squash, 2009. [http://www.gwoptics.org/processing/stretch\\_and\\_squash/stretchandsquash.php](http://www.gwoptics.org/processing/stretch_and_squash/stretchandsquash.php).
- [6] The LIGO Scientific Collaboration and the Virgo Collaboration. Predictions for the rates of compact binary coalescences observable by ground-based gravitational-wave detectors. *Classical and Quantum Gravity*, 27(17):173001, 2010.
- [7] LIGO Scientific Collaboration and Virgo Collaboration. Narrow-band search of continuous gravitational-wave signals from crab and vela pulsars in virgo vsr4 data. *Phys. Rev. D*, 91:022004, Jan 2015.
- [8] H Lück, M Hewitson, P Ajith, B Allen, P Aufmuth, C Aulbert, S Babak, R Balasubramanian, B W Barr, S Berukoff, A Bunkowski, G Cagnoli, C A Cantley, M M Casey, S Chelkowski, Y Chen, D Churches, T Cokelaer, C N Colacino, D R M Crooks, C Cutler, K Danzmann, R J Dupuis, E Elliffe, C Fallnich, A Franzen, A Freise, I Gholami, S Goßler, A Grant, H Grote, S Grunewald, J Harms, B Hage, G Heinzl, I S Heng, A Hepstonstall, M Heurs, S Hild, J Hough, Y Itoh, G Jones, R Jones, S H Huttner, K Kötter, B Krishnan, P Kwee, M Luna, B Machenschalk, M Malec, R A Mercer, T Meier, C Messenger, S Mohanty, K Mossavi, S Mukherjee, P Murray, G P Newton, M A Papa, M Perreux-Lloyd, M Pitkin, M V Plissi, R Prix, V Quetschke, V Re, T Regimbau, H Rehbein, S Reid, L Ribichini, D I

## REFERENCES

---

- Robertson, N A Robertson, C Robinson, J D Romano, S Rowan, A Rüdiger, B S Sathyaprakash, R Schilling, R Schnabel, B F Schutz, F Seifert, A M Sintes, J R Smith, P H Sneddon, K A Strain, I Taylor, R Taylor, A Thüring, C Ungarelli, H Vahlbruch, A Vecchio, J Veitch, H Ward, U Weiland, H Welling, L Wen, P Williams, B Willke, W Winkler, G Woan, and R Zhu. Status of the geo600 detector. *Classical and Quantum Gravity*, 23(8):S71–S78, 2006.
- [9] Daniel Sigg and the LIGO Scientific Collaboration. Status of the ligo detectors. *Classical and Quantum Gravity*, 25(11):114041, 2008.
- [10] The VIRGO collaboration. Virgo status. *Institute of Physics*, 25(18):184001 (9pp), 2008.
- [11] The LIGO Collaboration. Advanced ligo. *Classical and Quantum Gravity*, 32(7):074001, 2015.
- [12] The VIRGO Collaboration. Advanced virgo: a second-generation interferometric gravitational wave detector. *Classical and Quantum Gravity*, 32(2):024001, 2015.
- [13] Kentaro Somiya and the KAGRA collaboration. Detector configuration of kagra—the japanese cryogenic gravitational-wave detector. *Classical and Quantum Gravity*, 29(12):124007, 2012.
- [14] J.-Y. Vinet, P Hello, C. N. Man, and A. Brillet. A high accuracy method for the simulation of non-ideal optical cavities. *Journal de Physique I*, 2:1287–1303, July 1992.
- [15] Patrice Hello. *Modele physique et simulation de l’antenne interferometrique gravitationnelle virgo*. PhD thesis, Paris-11 Univ., 91 - Orsay (France) ;, 1990.
- [16] H Yamamoto, B. Bhawal, M Evans, Maros E, M Rakhmanov, and R L Jr Savage. End to end simulation program for gravitational-wave detectors. In Seiji Kawamura and Norikatsu Mio, editors, *Gravitational Wave Detection II*, number 32 in Frontier Science Series. Universal Academy Press, 2000.
- [17] B. Caron, L. Derome, R. Flaminio, X. Grave, F. Marion, et al. SIESTA, a time domain, general purpose simulation program for the VIRGO experiment. *Astropart.Phys.*, 10:369–386, 1999.
- [18] STAIC. Software tools for advanced interferometer configurations. <http://www.phys.ufl.edu/LIGO/LIGO/STAIC.html>, 2000. Accessed: 2014-11-18.
- [19] M. Evans and Robert L. Ward. Optickle webpage. <http://www.ligo.caltech.edu/~rward/Optickle/>. Accessed: 2015-07-13.
- [20] Gabriele Vajente. Fast modal simulation of paraxial optical systems: the mist open source toolbox. *Classical and Quantum Gravity*, 30(7):075014, 2013.

- 
- [21] Hiro Yamamoto. SIS: Stationary Interferometer Simulation. Accessed on 10/08/2015: <http://labcit.ligo.caltech.edu/hiro/SIS/>.
- [22] Jerome Degallaix. Oscar a matlab based optical fft code. *Journal of Physics: Conference Series*, 228(1):012021, 2010.
- [23] A Freise, G Heinzl, H Lück, R Schilling, B Willke, and K Danzmann. Frequency-domain interferometer simulation with higher-order spatial modes. *Classical and Quantum Gravity*, 21(5):S1067–S1074, 2004. The program is available at <http://www.gwoptics.org/finesse>.
- [24] A. Freise. FINESSE webpage. <http://www.gwoptics.org/finesse/>. Accessed: 2015-07-13.
- [25] M Punturo, M Abernathy, F Acernese, B Allen, N Andersson, K Arun, F Barone, B Barr, M Barsuglia, M Beker, N Beveridge, S Birindelli, S Bose, L Bosi, S Braccini, C Bradaschia, T Bulik, E Calloni, G Cella, E Chassande Mottin, S Chelkowski, A Chincarini, J Clark, E Coccia, C Colacino, J Colas, A Cumming, L Cunningham, E Cuoco, S Danilishin, K Danzmann, G De Luca, R De Salvo, T Dent, R De Rosa, L Di Fiore, A Di Virgilio, M Doets, V Fafone, P Falferi, R Flaminio, J Franc, F Frasconi, A Freise, P Fulda, J Gair, G Gemme, A Gennai, A Giazotto, K Glampedakis, M Granata, H Grote, G Guidi, G Hammond, M Hannam, J Harms, D Heinert, M Hendry, I Heng, E Hennes, S Hild, J Hough, S Husa, S Huttner, G Jones, F Khalili, K Kokeyama, K Kokkotas, B Krishnan, M Lorenzini, H Lück, E Majorana, I Mandel, V Mandic, I Martin, C Michel, Y Minenkoy, N Morgado, S Mosca, B Mours, H Müller–Eberhardt, P Murray, R Nawrodt, J Nelson, R Oshaughnessy, C D Ott, C Palomba, A Paoli, G Parguez, A Pasqualetti, R Passaquieti, D Passuello, L Pinard, R Poggiani, P Popolizio, M Prato, P Puppò, D Rabeling, P Rapagnani, J Read, T Regimbau, H Rehbein, S Reid, L Rezzolla, F Ricci, F Richard, A Rocchi, S Rowan, A Rüdiger, B Sassolas, B Sathyaprakash, R Schnabel, C Schwarz, P Seidel, A Sintes, K Somiya, F Speirits, K Strain, S Strigin, P Sutton, S Tarabrin, A Thüring, J van den Brand, C van Leewen, M van Veggel, C van den Broeck, A Vecchio, J Veitch, F Vetrano, A Vicere, S Vyatchanin, B Willke, G Woan, P Wolfango, and K Yamamoto. The einstein telescope: a third-generation gravitational wave observatory. *Classical and Quantum Gravity*, 27(19):194002, 2010.
- [26] A Freise, Brown D, and Bond C. *FINESSE 2.0 User manual*. University of Birmingham, 2014.
- [27] C. Bond, D. Brown, A. Freise, and K. Strain. Interferometer Techniques for Gravitational-Wave Detection. *Living Reviews in Relativity*, 13, 2015. Submitted as of August 2015.
- [28] Daniel Brown and Andreas Freise. Simulation methods for advanced interferometers. In Peter Saulson and David Reitze, editors, *Advanced Interferometric*

## REFERENCES

---

- Gravitational-wave Detectors*. World Scientific, 2015. Chapter submitted in May 2015.
- [29] aLIGO FINESSE simulation team. aLIGO FINESSE git repository, 2015. Open access repository containing numerous LIGO based simulation data and files. <http://gitmaster.atlas.aei.uni-hannover.de/aligo-finesse>.
- [30] S Hild, H Grote, J Degallaix, S Chelkowski, K Danzmann, A Freise, M Hewitson, J Hough, H Luck, M Prijatelj, K A Strain, J R Smith, and B Willke. Dc-readout of a signal-recycled gravitational wave detector. *Classical and Quantum Gravity*, 26(5):055012 (10pp), 2009.
- [31] Gwinc: Gravitational wave interferometer noise calculator. Accessed on 08/08/2015: <http://ilog.ligo-wa.caltech.edu:7285/advligo/GWINC>.
- [32] A. V. Cumming, A. S. Bell, L. Barsotti, M. A. Barton, G. Cagnoli, D. Cook, L. Cunningham, M. Evans, G. D. Hammond, G. M. Harry, A. Heptonstall, J. Hough, R. Jones, R. Kumar, R. Mittleman, N. A. Robertson, S. Rowan, B. Shapiro, K. A. Strain, K. Tokmakov, C. Torrie, and A. A. van Veggel. Design and development of the advanced LIGO monolithic fused silica suspension. *Classical and Quantum Gravity*, 29(3):035003, February 2012.
- [33] S Wen, R Mittleman, K Mason, J Giaime, R Abbott, J Kern, B O'ÉCÉReilly, R Bork, M Hammond, C Hardham, B Lantz, W Hua, D Coyne, G Traylor, H Overmier, T Evans, J Hanson, O Spjeld, M Macinnis, K Mailand, D Ottaway, D Sellers, K Carter, and P Sarin. Hydraulic external pre-isolator system for ligo. *Classical and Quantum Gravity*, 31(23):235001, 2014.
- [34] V. B. Braginsky, V. P. Mitrofanov, and K. V. Tokmakov. On the thermal noise from the violin modes of the mass suspension in gravitational wave antennae. *Phys. Letters A*, 186:18–20, 1993.
- [35] Gabriela Gonzalez. Suspensions thermal noise in the ligo gravitational wave detector. *Class. Quantum Grav.*, 17:4409–4435, 2000.
- [36] Jean-Yves Vinet. On special optical modes and thermal issues in advanced gravitational wave interferometric detectors. *Living Reviews in Relativity*, 12(5), 2009.
- [37] Gregory M. Harry, Helena Armandula, Eric Black, D. R. M. Crooks, Gianpietro Cagnoli, Jim Hough, Peter Murray, Stuart Reid, Sheila Rowan, Peter Sneddon, Martin M. Fejer, Roger Route, and Steven D. Penn. Thermal noise from optical coatings in gravitational wave detectors. *Appl. Opt.*, 45(7):1569–1574, 2006.
- [38] Ke-Xun Sun, M. M. Fejer, Eric Gustafson, and Robert L. Byer. Sagnac interferometer for gravitational-wave detection. *Phys. Rev. Lett.*, 76(17):3053–3056, Apr 1996.

- 
- [39] Mengyao Wang, Charlotte Bond, Daniel Brown, Frank Brückner, Ludovico Carbone, Rebecca Palmer, and Andreas Freise. Realistic polarizing sagnac topology with dc readout for the einstein telescope. *Phys. Rev. D*, 87:096008, May 2013.
- [40] P Kwee, C. Bogan, K. Danzmann, M. Frede, H. Kim, P King, J. Pöld, O. Puncken, R. L. Savage, F. Seifert, P. Wessels, L. Winkelmann, and B. Willke. Stabilized high-power laser system for the gravitational wave detector advanced ligo. *Opt. Express*, 20(10):10617–10634, May 2012.
- [41] Patrick Kwee. *Laser Characterization and Stabilization for Precision Interferometry*. PhD thesis, Universitat Hannover, 2010.
- [42] Benno Willke. Pre-stabilized laser design requirements. Technical Report T050036, LIGO DCC, Feb 2009.
- [43] Daniel Brown and Andreas Freise. Optical simulations within and beyond the paraxial limit, May 2012. DCC G1200548. Presented at GWADW Hawaii.
- [44] A.E. Siegman. *LASERS*. University Science Books, 1986. See also: Errata List for LASERS, [http://www.stanford.edu/~siegman/lasers\\_book\\_errata.pdf](http://www.stanford.edu/~siegman/lasers_book_errata.pdf).
- [45] Herwig Kogelnik. On the propagation of Gaussian beams of light through lens-like media including those with a loss or gain variation. *Appl. Opt.*, 4(12):1562–1569, 1965.
- [46] Kenneth A. Strain, Guido Müller, Tom Delker, David H. Reitze, David B. Tanner, James E. Mason, Phil A. Willems, Daniel A. Shaddock, Malcolm B. Gray, Conor Mow-Lowry, and David E. McClelland. Sensing and control in dual-recycling laser interferometer gravitational-wave detectors. *Appl. Opt.*, 42(7):1244–1256, Mar 2003.
- [47] A. Jeffrey and D. Zwillinger. *Table of Integrals, Series, and Products*. Table of Integrals, Series, and Products Series. Elsevier Science, 2007.
- [48] Charlotte Bond, Daniel Brown, and Andreas Freise. Interferometer responses to gravitational waves: Comparing finesse simulations and analytical solutions. Technical Report T1300190, LIGO DCC, March 2013.
- [49] Koji Arai. aligo output mode cleaner: Overview of the realtime model and screens. Technical Report E1500161, LIGO DCC, March 2015.
- [50] GariLynn Billingsley. Etm08 end test mass final polishing data package. Technical Report C1000486, LIGO DCC, Feb 2014.
- [51] G. Billingsley. LIGO core optics reference page. <https://galaxy.ligo.caltech.edu/optics/>. Accessed: 2015-07-13.

## REFERENCES

---

- [52] Charlotte Bond, Paul Fulda, Daniel Brown, and Andreas Freise. Investigation of beam clipping in the power recycling cavity of Advanced LIGO using FINESSE. Technical Report T1300954, LIGO DCC, Nov 2013.
- [53] Charlotte Zoë Bond. How to stay in shape: overcoming beam and mirror distortions in advanced gravitational wave interferometers. July 2014.
- [54] F. Bayer-Helms. Coupling coefficients of an incident wave and the modes of spherical optical resonator in the case of mismatching and misalignment. *Appl. Opt.*, 23:1369–1380, May 1984.
- [55] J. Y. Vinet and the Virgo Collaboration. *The Virgo Book of Physics: Optics and Related Topics*. Virgo, 2001.
- [56] Christopher L Mueller. *TECHNIQUES FOR RESONANT OPTICAL INTERFEROMETRY WITH APPLICATIONS TO THE ADVANCED LIGO GRAVITATIONAL WAVE DETECTORS*. PhD thesis, UNIVERSITY OF FLORIDA, 2014.
- [57] Anthony E. Siegman and R. Arrathoon. Modes in unstable optical resonators and lens waveguides. *Quantum Electronics, IEEE Journal of*, 3(4):156–163, Apr 1967.
- [58] Koji Arai. On the accumulated round-trip gouy phase shift for a general optical cavity. Technical Report T1300189, LIGO DCC, March 2013.
- [59] M.A. Arain and G. Mueller. Design of the advanced ligo recycling cavities. *Optics Express*, Vol. 16, Issue 14:10018–10032, 2008.
- [60] Rich Abbott, Rana Adhikari, Stefan Ballmer, Lisa Barsotti, Matt Evans, Peter Fritschel, Valera Frolov, Guido Mueller, Bram Slagmolen, and Sam Waldman. Advanced ligo length sensing and control final design. Technical Report T1000298, LIGO DCC, June 2010.
- [61] J. Mizuno, K.A. Strain, P.G. Nelson, J.M. Chen, R. Schilling, A. Rüdiger, W. Winkler, and K. Danzmann. Resonant sideband extraction: a new configuration for interferometric gravitational wave detectors. *Physics Letters A*, 175(5):273 – 276, 1993.
- [62] Lisa Barsotti and Matt Evans. Modeling of alignment sensing and control for advanced ligo. Technical Report T0900511, LIGO DCC, June 2010.
- [63] Harbir Antil, ScottE. Field, Frank Herrmann, RicardoH. Nochetto, and Manuel Tiglio. Two-step greedy algorithm for reduced order quadratures. *Journal of Scientific Computing*, 57(3):604–637, 2013.
- [64] Daniel Brown, Rory Smith, and Andreas Freise. Fast simulation of gaussian-mode scattering for precision interferometry. *Journal of Optics*, Sept 2015. Submitted on 2<sup>nd</sup> of September, awaiting feedback.

- 
- [65] T. Hahn. Cuba—a library for multidimensional numerical integration. *Computer Physics Communications*, 168(2):78 – 95, 2005.
- [66] Priscilla Canizares, Scott E. Field, Jonathan Gair, Vivien Raymond, Rory Smith, and Manuel Tiglio. Accelerated gravitational wave parameter estimation with reduced order modeling. *Phys. Rev. Lett.*, 114:071104, Feb 2015.
- [67] Daniel Brown and Andreas Freise. PYKAT webpage. <http://www.gwoptics.org/pykat/>, 2015. Accessed: 2015-07-13.
- [68] Y. Maday, N. C. Nguyen, A. T. Patera, and S. H. Pau. A general multipurpose interpolation procedure: the magic points. *Communications on Pure and Applied Analysis*, 8:383–404, 2009.
- [69] A. Ralston and P. Rabinowitz. *A First Course in Numerical Analysis*. Dover books on mathematics. Dover Publications, 2001.
- [70] Maxime Barrault, Yvon Maday, Ngoc Cuong Nguyen, and Anthony T. Patera. An ‘empirical interpolation’ method: application to efficient reduced-basis discretization of partial differential equations. *Comptes Rendus Mathematique*, 339(9):667 – 672, 2004.
- [71] Jan S. Hesthaven, Benjamin Stamm, and Shun Zhang. Efficient greedy algorithms for high-dimensional parameter spaces with applications to empirical interpolation and reduced basis methods. *ESAIM: Mathematical Modelling and Numerical Analysis*, 48:259–283, 1 2014.
- [72] Max D. Gunzburger, Janet S. Peterson, and John N. Shadid. Reduced-order modeling of time-dependent {PDEs} with multiple parameters in the boundary data. *Computer Methods in Applied Mechanics and Engineering*, 196(4–6):1030 – 1047, 2007.
- [73] B. S. Kirk, J. W. Peterson, R. H. Stogner, and G. F. Carey. libMesh: A C++ Library for Parallel Adaptive Mesh Refinement/Coarsening Simulations. *Engineering with Computers*, 22(3–4):237–254, 2006.
- [74] William H. Press, Saul A. Teukolsky, William T. Vetterling, and Brian P. Flannery. *Numerical Recipes 3rd Edition: The Art of Scientific Computing*. Cambridge University Press, New York, NY, USA, 3 edition, 2007.
- [75] Kendall Atkinson. *An Introduction to Numerical Analysis*. Wiley, 2 edition.
- [76] Tor Øvstedal Aanonsen. Empirical interpolation with application to reduced basis approximations. 2009.
- [77] FINESSE input files for Advanced LIGO. <https://dcc.ligo.org/LIGO-L1300231>, 2015. Accessed: 2015-07-13.

## REFERENCES

---

- [78] Daniel Brown et al. Optical suppression of parametric instabilities with extraction cavities. 2015. In preparation.
- [79] P. Meystre, J. D. McCullen, E. Vignes, and E. M. Wright. Theory of radiation-pressure-driven interferometers. *J. Opt. Soc. Am. B*, 2(11):1830–1840, Nov 1985.
- [80] O Miyakawa and H Yamamoto. Lock acquisition studies for advanced interferometers. *Journal of Physics: Conference Series*, 122(1):012024, 2008.
- [81] M. Evans, N. Mavalvala, P. Fritschel, R. Bork, B. Bhawal, R. Gustafson, W. Kells, M. Landry, D. Sigg, R. Weiss, S. Whitcomb, and H. Yamamoto. Lock acquisition of a gravitational-wave interferometer. *Opt. Lett.*, 27(8):598–600, Apr 2002.
- [82] B. Bhawal, M. Evans, E. Maros, M. Rakhmanov, R. L. Savage, Jr., H. Yamamoto, G. Cella, and S. Klimenko. End-to-End simulation program for interferometric gravitational wave detectors. In *APS Meeting Abstracts*, page 20001, April 2000.
- [83] M. Evans, Mathematics California Institute of Technology. Division of Physics, and Astronomy. *Lock acquisition in resonant optical interferometers*. CIT theses. California Institute of Technology, 2002.
- [84] J. A. Sidles and D. Sigg. Optical torques in suspended Fabry Perot interferometers. *Physics Letters A*, 354:167–172, May 2006.
- [85] Katherine L. Dooley, Lisa Barsotti, Rana X. Adhikari, Matthew Evans, Tobin T. Fricke, Peter Fritschel, Valera Frolov, Keita Kawabe, and Nicolás Smith-Lefebvre. Angular control of optical cavities in a radiation-pressure-dominated regime: the enhanced ligo case. *J. Opt. Soc. Am. A*, 30(12):2618–2626, Dec 2013.
- [86] Matthew Evans, Slawek Gras, Peter Fritschel, John Miller, Lisa Barsotti, Denis Martynov, Aidan Brooks, Dennis Coyne, Rich Abbott, Rana X. Adhikari, Koji Arai, Rolf Bork, Bill Kells, Jameson Rollins, Nicolas Smith-Lefebvre, Gabriele Vajente, Hiroaki Yamamoto, Carl Adams, Stuart Aston, Joseph Betzweiser, Valera Frolov, Adam Mullavey, Arnaud Pele, Janeen Romie, Michael Thomas, Keith Thorne, Sheila Dwyer, Kiwamu Izumi, Keita Kawabe, Daniel Sigg, Ryan Derosa, Anamaria Effler, Keiko Kokeyama, Stefan Ballmer, Thomas J. Massinger, Alexa Staley, Matthew Heinze, Chris Mueller, Hartmut Grote, Robert Ward, Eleanor King, David Blair, Li Ju, and Chunnong Zhao. Observation of parametric instability in advanced ligo. *Phys. Rev. Lett.*, 114:161102, Apr 2015.
- [87] V. B. Braginsky, S. E. Strigin, and S. P. Vyatchanin. Parametric oscillatory instability in Fabry-Perot interferometer. *Physics Letters A*, 287:331–338, September 2001.
- [88] C Zhao, D G Blair, P Barrigo, J Degallaix, J-C Dumas, Y Fan, S Gras, L Ju, B Lee, S Schediwy, Z Yan, D E McClelland, S M Scott, M B Gray, A C Searle, S Gossler,

- B J J Slagmolen, J Dickson, K McKenzie, C Mow-Lowry, A Moylan, D Rabeling, J Cumpston, K Wette, J Munch, P J Veitch, D Mudge, A Brooks, and D Hosken. Gingin high optical power test facility. *Journal of Physics: Conference Series*, 32(1):368, 2006.
- [89] Thomas Corbitt, David Ottaway, Edith Innerhofer, Jason Pelc, and Nergis Mavalvala. Measurement of radiation-pressure-induced optomechanical dynamics in a suspended fabry-perot cavity. *Physical Review A (Atomic, Molecular, and Optical Physics)*, 74(2):021802, 2006.
- [90] John Miller. *On Non-Gaussian Beams and Optomechanical Parametric Instabilities in Interferometric Gravitational Wave Detectors*. PhD thesis, University of Glasgow, 2010.
- [91] Luke Williams. Dimensions for advanced ligo fused silica test masses. Technical Report T040199, LIGO DCC, Feb 2004.
- [92] Brian Schwarz and Mark Richar Dson. Scaling mode shapes obtained from operating data. Technical report, International Modal Analysis Conf. (IMAC XXIV), February, 2003.
- [93] Sondipon Adhikari. *Damping Models for Structural Vibration*. PhD thesis, Cambridge University, Cambridge University, 2000.
- [94] R Nawrodt, A Zimmer, T Koettig, C Schwarz, D Heinert, M Hudl, R Neubert, M Thük, S Nietzsche, W Vodel, P Seidel, and A Tännermann. High mechanical q-factor measurements on silicon bulk samples. *Journal of Physics: Conference Series*, 122(1):012008, 2008.
- [95] M. Evans, L. Barsotti, and P. Fritschel. A general approach to optomechanical parametric instabilities. *Physics Letters A*, 374(4):665 – 671, 2010.
- [96] Thomas Corbitt. Private email from T. Corbitt, August 2015. Requested data on the Q-factor of the mechanical mode from Thomas Cobitt, his reply: "I recall the Q of the drumhead to be in the 5e5 to 1e6 range".
- [97] Thomas Randall Corbitt. *Quantum Noise and Radiation Pressure Effects in High Power Optical Interferometers*. PhD thesis, MASSACHUSETTS INSTITUTE OF TECHNOLOGY, 2008.
- [98] S Gras, C Zhao, D G Blair, and L Ju. Parametric instabilities in advanced gravitational wave detectors. *Classical and Quantum Gravity*, 27(20):205019, 2010.
- [99] V. B. Braginsky, S. E. Strigin, and S. P. Vyatchanin. Analysis of parametric oscillatory instability in power recycled LIGO interferometer. *Physics Letters A*, 305:111–124, December 2002.

## REFERENCES

---

- [100] A. G. Gurkovsky, S. E. Strigin, and S. P. Vyatchanin. Analysis of parametric oscillatory instability in signal recycled LIGO interferometer. *Physics Letters A*, 362:91–99, February 2007.
- [101] S.E. Strigin. The effect of parametric oscillatory instability in a fabry-perot cavity of the einstein telescope. *Optics and Spectroscopy*, 112(3):373–376, 2012.
- [102] S.E. Strigin. Suppression of parametric oscillatory instability in third generation gravitational wave detectors. *Physics Letters A*, 379(2829):1671 – 1674, 2015.
- [103] C. Zhao, L. Ju, J. Degallaix, S. Gras, and D. G. Blair. Parametric Instabilities and Their Control in Advanced Interferometer Gravitational-Wave Detectors. *Physical Review Letters*, 94(12):121102–+, April 2005.
- [104] John Miller, Matthew Evans, Lisa Barsotti, Peter Fritschel, Myron MacInnis, Richard Mittleman, Brett Shapiro, Jonathan Soto, and Calum Torrie. Damping parametric instabilities in future gravitational wave detectors by means of electrostatic actuators. *Physics Letters A*, 375(3):788 – 794, 2011.
- [105] S.E. Strigin, D.G. Blair, S. Gras, and S.P. Vyatchanin. Numerical calculations of elastic modes frequencies for parametric oscillatory instability in advanced {LIGO} interferometer. *Physics Letters A*, 372(35):5727 – 5731, 2008.
- [106] S. Gras, D. G. Blair, and L. Ju. Opto-acoustic interactions in gravitational wave detectors: Comparing flat-top beams with Gaussian beams. *Phys. Rev. D*, 81(4):042001–+, February 2010.
- [107] Charlotte Bond, Paul Fulda, Daniel Brown, Andreas Freise, Keiko Kokeyama, Ludovico Carbone, Suresh Doravari, and Koji Arai. FINESSE simulation for the alignment control signal of the aligo input mode cleaner. Technical Report T1300074, LIGO DCC, January 2013.
- [108] LIGO Lab. aLIGO logbooks, 2015. [alog.ligo-wa.caltech.edu](http://alog.ligo-wa.caltech.edu) and [alog.ligo-la.caltech.edu](http://alog.ligo-la.caltech.edu).
- [109] Daniel Brown, Paul Fulda, Antonio Perreca, Andreas Freise, Anna Green, and Daniel Toyra. Active wavefront control simulation project update. Technical Report G1501039, LIGO DCC, August 2015.
- [110] Paul Fulda, Charlotte Bond, Daniel Brown, and Andreas Freise. Mode matching measurement and modeling update. Technical Report G1400381, LIGO DCC, March 2014.
- [111] Kiwamu Izumi et al. Drmi locked for the first time. Technical Report 14002, LIGO LHO Logbook, September 2014.
- [112] Paul Fulda, Daniel Brown, Charlotte Bond, Kiwamu Izumi, Lisa Barsotti, and Andreas Freise. Simulation investigation of mode hopping in the h1 signal recycling cavity. Technical Report T1500230, LIGO DCC, June 2015.

## REFERENCES

---

- [113] Paul Fulda, Daniel Brown, and Andreas Freise. Sensing and control problems in low finesse cavities, or "how (not) to hop". Technical Report G1500645, LIGO DCC, May 2015.
- [114] Luke Williams. Aligo io h1 master coordinate list. Technical Report E1200616, LIGO DCC, August 2013.
- [115] Shelia Dwyer et al. Drmi locking tonight. Technical Report 14027, LIGO LHO Logbook, September 2014.
- [116] Evan Hall et al. Drmi1f characterization (no arms). Technical Report 15362, LIGO LHO Logbook, December 2014.
- [117] Chris Mueller and Lisa Barsotti. Mode matching investigations at llo. Technical Report G1300909, LIGO DCC, Sept 2013.
- [118] GariLynn Billingsley. Itm04 input test mass final polishing data package. Technical Report C1000472, LIGO DCC, May 2011.
- [119] GariLynn Billingsley. Itm08 input test mass final polishing data package. Technical Report C1000476, LIGO DCC, May 2011.
- [120] Lisa Barsotti et al. Omc mismatching. Technical Report 8192, LIGO LLO Logbook, August 2013.
- [121] Jerome. *Compensation of strong thermal lensing in advanced interferometric gravitational waves detectors*. PhD thesis, The University of Western Australia, 2006.
- [122] R. Lawrence, M. Zucker, P. Fritschel, P. Marfuta, and D. Shoemaker. Adaptive thermal compensation of test masses in advanced LIGO. *Classical and Quantum Gravity*, 19:1803–1812, April 2002.
- [123] Luke Williams. Aligo io l1 master coordinate list. Technical Report E1200274, LIGO DCC, Dec 2012.
- [124] Aidan Brooks, Antonio Perreca, Lisa Barsotti, and Paul Fulda. Active wavefront control, or the story of adaptive higher order mode control (ad hoc). Technical Report G1500372, LIGO DCC, March 2015.
- [125] Aidan Brooks, Antonio Perreca, Lisa Barsotti, Paul Fulda, Rana Adhikari, and Stefan Ballmer. Active wavefront control roadmap. Technical Report T1500188, LIGO DCC, March 2015.
- [126] H. J. Kimble, Y. Levin, A. B. Matsko, K. S. Thorne, and S. P. Vyatchanin. Conversion of conventional gravitational-wave interferometers into quantum nondestruction interferometers by modifying their input and/or output optics. *Physical Review D*, 65(2):022002–+, January 2002.

## REFERENCES

---

- [127] M. Evans, L. Barsotti, J. Harms, P Kwee, and H. Miao. Realistic filter cavities for advanced gravitational wave detectors. *ArXiv*, 2013.
- [128] P. Kwee, J. Miller, T. Isogai, L. Barsotti, and M. Evans. Decoherence and degradation of squeezed states in quantum filter cavities. *Phys. Rev. D*, 90:062006, Sep 2014.
- [129] Daniel Brown, Daniel Friedrich, Frank Brückner, Ludovico Carbone, Roman Schnabel, and Andreas Freise. Invariance of waveguide grating mirrors to lateral displacement phase shifts. *Opt. Lett.*, 38(11):1844–1846, Jun 2013.
- [130] Daniel Brown. Finite-difference time-domain analysis of diffraction and waveguide coating displacement phase shifts. Master’s thesis, University of Birmingham, School of Physics and Astronomy, 2010.
- [131] Helge Müller-Ebhardt, Henning Rehbein, Roman Schnabel, Karsten Danzmann, and Yanbei Chen. Entanglement of macroscopic test masses and the standard quantum limit in laser interferometry. *Phys. Rev. Lett.*, 100:013601, Jan 2008.
- [132] Kenji Numata, Amy Kemery, and Jordan Camp. Thermal-noise limit in the frequency stabilization of lasers with rigid cavities. *Phys. Rev. Lett.*, 93:250602, Dec 2004.
- [133] Gregory M Harry, Andri M Gretarsson, Peter R Saulson, Scott E Kittelberger, Steven D Penn, William J Startin, Sheila Rowan, Martin M Fejer, D R M Crooks, Gianpietro Cagnoli, Jim Hough, and Norio Nakagawa. Thermal noise in interferometric gravitational wave detectors due to dielectric optical coatings. *Classical and Quantum Gravity*, 19(5):897, 2002.
- [134] Simon Chelkowski, Stefan Hild, and Andreas Freise. Prospects of higher-order laguerre-gauss modes in future gravitational wave detectors. *Physical Review D (Particles, Fields, Gravitation, and Cosmology)*, 79(12):122002, 2009.
- [135] Ke-Xun Sun and Robert L. Byer. All-reflective michelson, sagnac, and fabry-perot interferometers based on grating beam splitters. *Opt. Lett.*, 23(8):567–569, Apr 1998.
- [136] A. Bunkowski, O. Burmeister, D. Friedrich, K. Danzmann, and R. Schnabel. High reflectivity grating waveguide coatings for 1064 nm. *Classical and Quantum Gravity*, 23:7297–7303, December 2006.
- [137] Y. Levin. Internal thermal noise in the LIGO test masses: A direct approach. *Phys. Rev. D*, 57:659–663, January 1998.
- [138] S. Wise, V. Quetschke, A. J. Deshpande, G. Mueller, D. H. Reitze, D. B. Tanner, B. F. Whiting, Y. Chen, A. Tünnermann, E. Kley, and T. Clausnitzer. Phase Effects in the Diffraction of Light: Beyond the Grating Equation. *Physical Review Letters*, 95(1):013901–+, June 2005.

- 
- [139] Deepali Lodhia, Daniel Brown, Frank Brückner, Ludovico Carbone, Paul Fulda, Keiko Kokeyama, and Andreas Freise. Interferometer phase noise due to beam misalignment on diffraction gratings. *Opt. Express*, 21(24):29578–29591, Dec 2013.
- [140] A. Freise, A. Bunkowski, and R. Schnabel. Phase and alignment noise in grating interferometers. *New Journal of Physics*, 9:433–+, December 2007.
- [141] Frank Brückner, Tina Clausnitzer, Oliver Burmeister, Daniel Friedrich, Ernst-Bernhard Kley, Karsten Danzmann, Andreas Tünnermann, and Roman Schnabel. Monolithic dielectric surfaces as new low-loss light-matter interfaces. *Opt. Lett.*, 33(3):264–266, 2008.
- [142] Deepali Lodhia. Investigations into phase effects from diffracted gaussian beams for high-precision interferometry. July 2013.
- [143] Allen Taflove and Susan C. Hagness. *Computational Electrodynamics: The Finite-Difference Time-Domain Method, Third Edition*. Artech House Publishers, 3 edition, June 2005.
- [144] Petr Sysel and Pavel Rajmic. Goertzel algorithm generalized to non-integer multiples of fundamental frequency. *EURASIP Journal on Advances in Signal Processing*, 2012:1–8, 2012. 10.1186/1687-6180-2012-56.
- [145] S. Kroker, E.-B. Kley, and A. Tünnermann. Thermal noise of silicon based grating reflectors for high-precision metrology. In *Metrology for Aerospace (MetroAeroSpace), 2014 IEEE*, pages 523–527, May 2014.
- [146] S. Kroker, T. Käsebier, E.-B. Kley, and A. Tünnermann. Investigation on the angular dependent reflectance of coupled high-contrast gratings. In *Society of Photo-Optical Instrumentation Engineers (SPIE) Conference Series*, volume 8995 of *Society of Photo-Optical Instrumentation Engineers (SPIE) Conference Series*, page 0, February 2014.
- [147] S Leavey, B W Barr, A S Bell, N Gordon, C Gräf, S Hild, S H Huttner, E-B Kley, S Kroker, J Macarthur, C Messenger, M Pitkin, B Sorazu, K Strain, and A Tünnermann. Upper limit to the transverse to longitudinal motion coupling of a waveguide mirror. *Classical and Quantum Gravity*, 32(17):175005, 2015.
- [148] Ayaka Kumeta, Charlotte Bond, and Kentaro Somiya. Design study of the kagra output mode cleaner. *Optical Review*, 22(1):149–152, 2015.
- [149] H Wittel, H Lück, C Affeldt, K L Dooley, H Grote, J R Leong, M Prijatelj, E Schreiber, J Slutsky, K Strain, M Was, B Willke, and K Danzmann. Thermal correction of astigmatism in the gravitational wave observatory geo-600. *Classical and Quantum Gravity*, 31(6):065008, 2014.

## REFERENCES

---

- [150] C Bond, P Fulda, L Carbone, K Kokeyama, and A Freise. The effect of mirror surface distortions on higher order Laguerre-Gauss modes. *Journal of Physics: Conference Series*, 363:012005, 2012.
- [151] B Sorazu, P J Fulda, B W Barr, A S Bell, C Bond, L Carbone, A Freise, S Hild, S H Huttner, J Macarthur, and K A Strain. Experimental test of higher-order laguerre-gauss modes in the 10 m glasgow prototype interferometer. *Classical and Quantum Gravity*, 30(3):035004, 2013.
- [152] C Gräf, B W Barr, A S Bell, F Campbell, A V Cumming, S L Danilishin, N A Gordon, G D Hammond, J Hennig, E A Houston, S H Huttner, R A Jones, S S Leavey, H LÄEck, J Macarthur, M Marwick, S Rigby, R Schilling, B Sorazu, A Spencer, S Steinlechner, K A Strain, and S Hild. Design of a speed meter interferometer proof-of-principle experiment. *Classical and Quantum Gravity*, 31(21):215009, 2014.
- [153] Jordan Clarke, Haoyu Wang, Daniel Brown, and Andreas Freise. Revisting sidebands of sidebands in finesse. Technical Report T1300986, LIGO DCC, Dec 2013.
- [154] Andreas Freise, Charlotte Bond, and Daniel Brown. SIMTOOLS webpage. <http://www.gwoptics.org/simtools/>, 2015. Accessed: 2015-07-13.
- [155] C. M. Caves and B. L. Schumaker. New formalism for two-photon quantum optics. I - Quadrature phases and squeezed states. II - Mathematical foundation and compact notation. *Physical Review A*, 31:3068–3111, May 1985.
- [156] Hans-A. Bachor and Peter J. Manson. Practical implications of quantum noise. *Journal of Modern Optics*, 37(11):1727–1740, 1990.
- [157] B. J. Meers and K. A. Strain. Modulation, signal, and quantum noise in interferometers. *Phys. Rev. A*, 44:4693–4703, October 1991.
- [158] J. Harms, P Cochrane, and A. Freise. Quantum-noise power spectrum of fields with discrete classical components. *Phys. Rev. A*, 76(2):023803–+, August 2007.
- [159] C.M. Caves. Quantum-mechanical noise in an interferometer. *Phys. Rev. D*, 23:1693–1708, 1981.
- [160] Malik Rakhmanov. Demodulation of intensity and shot noise in the optical heterodyne detection of laser interferometers for gravitational waves. *Appl. Opt.*, 40(36):6596–6605, Dec 2001.
- [161] T.A. Davis. *Direct Methods for Sparse Linear Systems*, volume 2 of *Fundamentals of Algorithms*. SIAM, Philadelphia, 2006.

- 
- [162] Ludovico Carbone, Paul Fulda, Charlotte Bond, Frank Brueckner, Daniel Brown, Mengyao Wang, Deepali Lodhia, Rebecca Palmer, and Andreas Freise. The generation of higher-order laguerre-gauss optical beams for high-precision interferometry. (78), 2013.
- [163] L. Carbone, C. Bond, D. Brown, F. Brückner, K. Grover, D. Lodhia, C.M.F. Mingarelli, P. Fulda, R.J.E. Smith, R. Unwin, A. Vecchio, M. Wang, L. Whalley, and A. Freise. Computer-games for gravitational wave science outreach: Black hole pong and space time quest. *Journal of Physics: Conference Series*, 363:012057, 2012.
- [164] P. Fulda, C. Bond, D. Brown, F. Brückner, L. Carbone, S. Chelkowski, S. Hild, K. Kokeyama, M. Wang, and A. Freise. Review of the laguerre-gauss mode technology research program at birmingham. *Journal of Physics: Conference Series*, 363:012010, 2012.
- [165] Daniel Brown and Rory Smith. Presentation: Fast simulation of gaussian-mode scattering for precision interferometry, 2015. DCC G1501137. Presented at the Budapest IVC meeting.
- [166] Daniel Brown, Charlotte Bond, and Andreas Freise. Finesse 2: Radiation pressure and the quantum kat, May 2014. DCC G1400580. Presented at GWADW Takayama.
- [167] Daniel Brown, Charlotte Bond, Paul Fulda, and Andreas Freise. Update on als alignment modelling and on finesse, Jun 2014. DCC G1400622. Presented to LIGO modelling group.
- [168] Ludovico Carbone, Daniel Brown, Charlotte Bond, Paul Fulda, and Andreas Freise. Finesse: a numerical simulation tool for optical design and detector commissioning, Mar 2013. DCC G1300301. Poster at Bethesda IVC meeting.
- [169] Daniel Brown, Charlotte Bond, Mengyao Wang, Ludovico Carbone, and Andreas Freise. Modelling mirror surface distortion effects in low-loss, near-unstable fabry-perot cavities, Jul 2013. DCC G1300711. Poster at Warsaw Amaldi.
- [170] Daniel Brown, Charlotte Bond, and Andreas Freise. Finesse: v1.0 and beyond, May 2013. DCC G1300538. Presented at Nice IVC meeting.
- [171] Charlotte Bond, Daniel Brown, and Andreas Freise. Mode healing in gw interferometers, Jul 2013. DCC G1300711. Poster at Warsaw Amaldi.
- [172] B. Barr, A. Bell, C. Bell, C. Bond, D. Brown, F. Brueckner, L. Carbone, K. Craig, A. Cumming, S. Danilishin, K. Dooley, A. Freise, T. Fricke, P. Fulda, S. Giampsis, N. Gordon, H. Grote, G. Hammond, J. Harms, S. Hild, J. Hough, S. Huttner, R. Kumar, H. Luck, N. Lockerbie, J. Macarthur, I. Martin, P. Murray, S. Reid, S. Rowan, D. Shoemaker, B. Sorazu, K. Strain, S. Tarabrin, K. Tokmakov, and

## REFERENCES

---

- N. Voronchev. Ligo 3 strawman design, team red. Technical Report T1200046, LIGO DCC, Jan 2012.
- [173] Adnah Kostenbauder, Yan Sun, and A. E. Sun. Eigenmode expansions using biorthogonal functions: complex-valued hermite–gaussians. *J. Opt. Soc. Am. A*, 14(8):1780–1790, Aug 1997.
- [174] R. G. Beausoleil and D. Sigg. Spatiotemporal model of the ligo interferometer. *J. Opt. Soc. Am. A*, 16(12):2990–3002, Dec 1999.
- [175] Brett Bochner and Yaron Hefetz. Grid-based simulation program for gravitational wave interferometers with realistically imperfect optics. *Phys. Rev. D*, 68:082001, Oct 2003.
- [176] Raymond G. Beausoleil, Eric K. Gustafson, Martin M. Fejer, Erika D’Ambrosio, William Kells, and Jordan Camp. Model of thermal wave-front distortion in interferometric gravitational-wave detectors. i. thermal focusing. *J. Opt. Soc. Am. B*, 20(6):1247–1268, Jun 2003.
- [177] Anthony E. Siegman. Eigenmodes in nonnormal optical systems, 2001.
- [178] Marc Brunel, Guy Ropars, Albert Le Floch, and Fabien Bretenaker. Diffraction losses reduction in multiapertured non-hermitian laser resonators. *Phys. Rev. A*, 55:781–786, Jan 1997.
- [179] Ondřej Haderka. Experimental investigation of eigenmodes of empty optical resonators with apertures. *Appl. Opt.*, 34(33):7656–7661, Nov 1995.
- [180] Richard Rolleigh, Maria E. Bell, Michael Rolleigh, and D. K. Bandy. Effects of finite apertures on transverse eigenmodes of optical resonators. *J. Opt. Soc. Am. A*, 16(11):2669–2674, Nov 1999.
- [181] B Abbott, R Abbott, R Adhikari, P Ajith, B Allen, G Allen, R Amin, S B Anderson, W G Anderson, M A Arain, M Araya, H Armandula, P Armor, Y Aso, S Aston, P Aufmuth, C Aulbert, S Babak, S Ballmer, H Bantilan, B C Barish, C Barker, D Barker, B Barr, P Barriga, M A Barton, M Bastarrika, K Bayer, J Betzwieser, P T Beyersdorf, I A Bilenko, G Billingsley, R Biswas, E Black, K Blackburn, L Blackburn, D Blair, B Bland, T P Bodiya, L Bogue, R Bork, V Boschi, S Bose, P R Brady, V B Braginsky, J E Brau, M Brinkmann, A Brooks, D A Brown, G Brunet, A Bullington, A Buonanno, O Burmeister, R L Byer, L Cadonati, G Cagnoli, J B Camp, J Cannizzo, K Cannon, J Cao, L Cardenas, T Casebolt, G Castaldi, C Cepeda, E Chalkley, P Charlton, S Chatterji, S Chelkowski, Y Chen, N Christensen, D Clark, J Clark, T Cokelaer, R Conte, D Cook, T Corbitt, D Coyne, J D E Creighton, A Cumming, L Cunningham, R M Cutler, J Dalrymple, S Danilishin, K Danzmann, G Davies, D DeBra, J Degallaix, M Degree, V Dergachev, S Desai, R DeSalvo, S Dhurandhar, M Díaz, J Dickson, A Dietz, F Donovan, K L Dooley, E E Doomes, R W P Drever, I Duke, J-C Dumas, R J Dupuis, J G Dwyer,

C Echols, A Effler, P Ehrens, E Espinoza, T Etzel, T Evans, S Fairhurst, Y Fan, D Fazi, H Fehrmann, M M Fejer, L S Finn, K Flasch, N Fotopoulos, A Freise, R Frey, T Fricke, P Fritschel, V V Frolov, M Fyffe, J Garofoli, I Gholami, J A Giaime, S Giampanis, K D Giardina, K Goda, E Goetz, L Goggin, G González, S Gossler, R Gouaty, A Grant, S Gras, C Gray, M Gray, R J S Greenhalgh, A M Gretarsson, F Grimaldi, R Grosso, H Grote, S Grunewald, M Guenther, E K Gustafson, R Gustafson, B Hage, J M Hallam, D Hammer, C Hanna, J Hanson, J Harms, G Harry, E Harstad, K Hayama, T Hayler, J Heefner, I S Heng, M Hennessy, A Heptonstall, M Hewitson, S Hild, E Hirose, D Hoak, D Hosken, J Hough, S H Huttner, D Ingram, M Ito, A Ivanov, B Johnson, W W Johnson, D I Jones, G Jones, R Jones, L Ju, P Kalmus, V Kalogera, S Kamat, J Kanner, D Kasprzyk, E Katsavounidis, K Kawabe, S Kawamura, F Kawazoe, W Kells, D G Keppel, F Ya Khalili, R Khan, E Khazanov, C Kim, P King, J S Kissel, S Klimenko, K Kokeyama, V Kondrashov, R K Kopparapu, D Kozak, I Kozhevator, B Krishnan, P Kwee, P K Lam, M Landry, M M Lang, B Lantz, A Lazzarini, M Lei, N Leindecker, V Leonhardt, I Leonor, K Libbrecht, H Lin, P Lindquist, N A Lockerbie, D Lodhia, M Lormand, P Lu, M Lubinski, A Lucianetti, H Lück, B Machenschalk, M MacInnis, M Mageswaran, K Mailand, V Mandic, S Márka, Z Márka, A Markosyan, J Markowitz, E Maros, I Martin, R M Martin, J N Marx, K Mason, F Matichard, L Matone, R Matzner, N Mavalvala, R McCarthy, D E McClelland, S C McGuire, M McHugh, G McIntyre, G McIvor, D McKechnan, K McKenzie, T Meier, A Melissinos, G Mendell, R A Mercer, S Meshkov, C J Messenger, D Meyers, H Miao, J Miller, J Minelli, S Mitra, V P Mitrofanov, G Mitselmakher, R Mittleman, O Miyakawa, B Moe, S Mohanty, G Moreno, K Mossavi, C Mow-Lowry, G Mueller, S Mukherjee, H Mukhopadhyay, H Müller-Ebhardt, J Munch, P Murray, E Myers, J Myers, T Nash, J Nelson, G Newton, A Nishizawa, K Numata, J O'Dell, G Ogin, B O'Reilly, R O'Shaughnessy, D J Ottaway, R S Ottens, H Overmier, B J Owen, Y Pan, C Pankow, M A Papa, V Parameshwaraiah, P Patel, M Pedraza, S Penn, A Perreca, T Petrie, I M Pinto, M Pitkin, H J Pletsch, M V Plissi, F Postiglione, M Principe, R Prix, V Quetschke, F Raab, D S Rabeling, H Radkins, N Rainer, M Rakhmanov, M Ramsunder, H Rehbein, S Reid, D H Reitze, R Riesen, K Riles, B Rivera, N A Robertson, C Robinson, E L Robinson, S Roddy, A Rodriguez, A M Rogan, J Rollins, J D Romano, J Romie, R Route, S Rowan, A Rüdiger, L Ruet, P Russell, K Ryan, S Sakata, M Samidi, L Sancho de la Jordana, V Sandberg, V Sannibale, S Saraf, P Sarin, B S Sathyaprakash, S Sato, P R Saulson, R Savage, P Savov, S W Schediwy, R Schilling, R Schnabel, R Schofield, B F Schutz, P Schwinberg, S M Scott, A C Searle, B Sears, F Seifert, D Sellers, A S Sengupta, P Shawhan, D H Shoemaker, A Sibley, X Siemens, D Sigg, S Sinha, A M Sintes, B J J Slagmolen, J Slutsky, J R Smith, M R Smith, N D Smith, K Somiya, B Sorazu, L C Stein, A Stochino, R Stone, K A Strain, D M Strom, A Stuver, T Z Summerscales, K-X Sun, M Sung, P J Sutton, H Takahashi, D B Tanner, R Taylor, R Taylor, J Thacker, K A Thorne, K S Thorne, A Thüring, K V Tokmakov, C Torres, C Torrie, G Traylor, M Trias, W Tyler, D Ugolini, J Ulmen, K Urbanek, H Vahlbruch, C Van Den Broeck, M van der Sluys, S Vass,

## REFERENCES

---

- R Vaulin, A Vecchio, J Veitch, P Veitch, A Villar, C Vorvick, S P Vyatchanin, S J Waldman, L Wallace, H Ward, R Ward, M Weinert, A Weinstein, R Weiss, S Wen, K Wette, J T Whelan, S E Whitcomb, B F Whiting, C Wilkinson, P A Willems, H R Williams, L Williams, B Willke, I Wilmut, W Winkler, C C Wipf, A G Wiseman, G Woan, R Wooley, J Worden, W Wu, I Yakushin, H Yamamoto, Z Yan, S Yoshida, M Zanolin, J Zhang, L Zhang, C Zhao, N Zotov, M Zucker, J Zweizig, and LIGO Scientific Collaboration. Observation of a kilogram-scale oscillator near its quantum ground state. *New Journal of Physics*, 11(7):073032, 2009.
- [182] Calum Torrie. *Development of suspensions for the GEO 600 gravitational wave detector*. PhD thesis, University of Glasgow, 1999.
- [183] Hartmut Grote and the LIGO Scientific Collaboration. The status of GEO 600. *Classical and Quantum Gravity*, 25(11):114043 (9pp), 2008.
- [184] Ryutaro Takahashi and the TAMA Collaboration. Status of TAMA300. *Classical and Quantum Gravity*, 21(5):S403, 2004.
- [185] GWIC. Numerical modelling tools for gravitational wave detectors. <https://gwic.ligo.org/simulations>, 2013. Accessed: 2014-11-18.
- [186] Raymond G. Beausoleil, Eric K. Gustafson, Martin M. Fejer, Erika D’Ambrosio, William Kells, and Jordan Camp. Model of thermal wave-front distortion in interferometric gravitational-wave detectors. i. thermal focusing. *J. Opt. Soc. Am. B*, 20(6):1247–1268, Jun 2003.
- [187] ET science team. Einstein gravitational wave telescope conceptual design study. Technical Report ET-0106C-10, 2010.
- [188] Schibli T R, Hartl I, Yost D C, Martin M J, Marcinkevicius A, Fermann M E, and Ye J. Optical frequency comb with submillihertz linewidth and more than 10 w average power. *Nature Photonics*, 2:355 – 359, 2008.
- [189] Susannah M. Dickerson, Jason M. Hogan, Alex Sugarbaker, David M. S. Johnson, and Mark A. Kasevich. Multiaxis inertial sensing with long-time point source atom interferometry. *Phys. Rev. Lett.*, 111:083001, Aug 2013.
- [190] Scott E. Field, Chad R. Galley, Jan S. Hesthaven, Jason Kaye, and Manuel Tiglio. Fast prediction and evaluation of gravitational waveforms using surrogate models. *Phys. Rev. X*, 4:031006, Jul 2014.
- [191] R. Adhikari, K. Arai, S. Ballmer, E K. Gustafson, and S Hild. Report of the 3rd generation LIGO detector strawman workshop. Technical Report LIGO Document T1200031-v3, 2012.
- [192] S Hild, M Abernathy, F Acernese, P Amaro-Seoane, N Andersson, K Arun, F Barone, B Barr, M Barsuglia, M Beker, N Beveridge, S Birindelli, S Bose, L Bosi, S Braccini, C Bradaschia, T Bulik, E Calloni, G Cella, E Chassande

- Mottin, S Chelkowski, A Chincarini, J Clark, E Coccia, C Colacino, J Colas, A Cumming, L Cunningham, E Cuoco, S Danilishin, K Danzmann, R De Salvo, T Dent, R De Rosa, L Di Fiore, A Di Virgilio, M Doets, V Fafone, P Falferi, R Flaminio, J Franc, F Frasconi, A Freise, D Friedrich, P Fulda, J Gair, G Gemme, E Genin, A Gennai, A Giazotto, K Glampedakis, C Gräf, M Granata, H Grote, G Guidi, A Gurkovsky, G Hammond, M Hannam, J Harms, D Heinert, M Hendry, I Heng, E Hennes, J Hough, S Husa, S Huttner, G Jones, F Khalili, K Kokeyama, K Kokkotas, B Krishnan, T G F Li, M Lorenzini, H Lück, E Majorana, I Mandel, V Mandic, M Mantovani, I Martin, C Michel, Y Minenkov, N Morgado, S Mosca, B Mours, H Müller-Ebhardt, P Murray, R Nawrodt, J Nelson, R Oshaughnessy, C D Ott, C Palomba, A Paoli, G Parguez, A Pasqualetti, R Passaquieti, D Passuello, L Pinard, W Plastino, R Poggiani, P Popolizio, M Prato, M Punturo, P Puppò, D Rabeling, P Rapagnani, J Read, T Regimbau, H Rehbein, S Reid, F Ricci, F Richard, A Rocchi, S Rowan, A Rüdiger, L Santamaría, B Sas-solas, B Sathyaprakash, R Schnabel, C Schwarz, P Seidel, A Sintes, K Somiya, F Speirits, K Strain, S Strigin, P Sutton, S Tarabrin, A Thüring, J van den Brand, M van Veggel, C van den Broeck, A Vecchio, J Veitch, F Vetrano, A Vicere, S Vyatchanin, B Willke, G Woan, and K Yamamoto. Sensitivity studies for third-generation gravitational wave observatories. *Classical and Quantum Gravity*, 28(9):094013, 2011.
- [193] P Binev, A. Cohen, W. Dahmen, R. DeVore, G. Petrova, and P Wojtaszczyk. Convergence rates for greedy algorithms in reduced basis methods. *SIAM Journal on Mathematical Analysis*, 43(3):1457–1472, 2011.
- [194] Yvon Maday and Olga Mula. A generalized empirical interpolation method: Application of reduced basis techniques to data assimilation. In Franco Brezzi, Piero Colli Franzone, Ugo Gianazza, and Gianni Gilardi, editors, *Analysis and Numerics of Partial Differential Equations*, volume 4 of *Springer INdAM Series*, pages 221–235. Springer Milan, 2013.
- [195] Scott E. Field, Chad R. Galley, Frank Herrmann, Jan S. Hesthaven, Evan Ochsner, and Manuel Tiglio. Reduced basis catalogs for gravitational wave templates. *Phys. Rev. Lett.*, 106:221102, 2011.
- [196] Sarah Caudill, Scott E. Field, Chad R. Galley, Frank Herrmann, and Manuel Tiglio. Reduced Basis representations of multi-mode black hole ringdown gravitational waves. *Class. Quant. Grav.*, 29:095016, 2012.
- [197] Kipp Cannon, Chad Hanna, and Drew Keppel. Efficiently enclosing the compact binary parameter space by singular-value decomposition. *Phys.Rev.*, D84:084003, 2011.
- [198] Toni Lassila, Andrea Manzoni, Alfio Quarteroni, and Gianluigi Rozza. Generalized reduced basis methods and n-width estimates for the approximation of

## REFERENCES

---

- the solution manifold of parametric pdes. In Franco Brezzi, Piero Colli Franzone, Ugo Gianazza, and Gianni Gilardi, editors, *Analysis and Numerics of Partial Differential Equations*, volume 4 of *Springer INdAM Series*, pages 307–329. Springer Milan, 2013.
- [199] Matthew Evans, Slawek Gras, Peter Fritschel, John Miller, Lisa Barsotti, Denis Martynov, Aidan Brooks, Dennis Coyne, Rich Abbott, Rana X. Adhikari, Koji Arai, Rolf Bork, Bill Kells, Jameson Rollins, Nicolas Smith-Lefebvre, Gabriele Vajente, Hiroaki Yamamoto, Carl Adams, Stuart Aston, Joseph Betzweiser, Valera Frolov, Adam Mullavey, Arnaud Pele, Janeen Romie, Michael Thomas, Keith Thorne, Sheila Dwyer, Kiwamu Izumi, Keita Kawabe, Daniel Sigg, Ryan Derosa, Anamaria Effler, Keiko Kokeyama, Stefan Ballmer, Thomas J. Massinger, Alexa Staley, Matthew Heinze, Chris Mueller, Hartmut Grote, Robert Ward, Eleanor King, David Blair, Li Ju, and Chunnong Zhao. Observation of parametric instability in Advanced LIGO. *Phys. Rev. Lett.*, 114:161102, Apr 2015.
- [200] V.B. Braginsky, S.E. Strigin, and S.P. Vyatchanin. Parametric oscillatory instability in fabry–perot interferometer. *Physics Letters A*, 287(5–6):331 – 338, 2001.
- [201] John Towns, Timothy Cockerill, Maytal Dahan, Ian Foster, Kelly Gaither, Andrew Grimshaw, Victor Hazelwood, Scott Lathrop, Dave Lifka, Gregory D. Peterson, Ralph Roskies, J. Ray Scott, and Nancy Wilkens-Diehr. Xsede: Accelerating scientific discovery. *Computing in Science and Engineering*, 16(5):62–74, 2014.
- [202] Michael Britzger, Daniel Friedrich, Stefanie Kroker, Frank Brückner, Oliver Burmeister, Ernst-Bernhard Kley, Andreas Tünnermann, Karsten Danzmann, and Roman Schnabel. Diffractively coupled fabry-perot resonator with power-recycling. *Opt. Express*, 19(16):14964–14975, Aug 2011.
- [203] Daniel Brown. Finite-difference time-domain code, 2012. <http://kvasir.sr.bham.ac.uk/redmine/projects/fdtd>.
- [204] F. Brückner, D. Friedrich, T. Clausnitzer, O. Burmeister, M. Britzger, E.-B. Kley, K. Danzmann, A. Tünnermann, and R. Schnabel. Demonstration of a cavity coupler based on a resonant waveguide grating. *Optics Express*, 17:163–+, December 2008.
- [205] Oliver Burmeister, Michael Britzger, André Thüring, Daniel Friedrich, Frank Brückner, Karsten Danzmann, and Roman Schnabel. All-reflective coupling of two optical cavities with 3-port diffraction gratings. *Opt. Express*, 18(9):9119–9132, Apr 2010.
- [206] D R M Crooks, P Sneddon, G Cagnoli, J Hough, S Rowan, M M Fejer, E Gustafson, R Route, N Nakagawa, D Coyne, G M Harry, and A M Gretarsson. Excess mechanical loss associated with dielectric mirror coatings on test masses in interferometric gravitational wave detectors. *Classical and Quantum Gravity*, 19(5):883, 2002.

- [207] Daniel Friedrich, Bryan W. Barr, Frank Brückner, Stefan Hild, John Nelson, John Macarthur, Michael V. Plissi, Matthew P. Edgar, Sabina H. Huttner, Borja Sorazu, Stefanie Kroker, Michael Britzger, Ernst-Bernhard Kley, Karsten Danzmann, Andreas Tünnermann, Ken A. Strain, and Roman Schnabel. Waveguide grating mirror in a fully suspended 10 meter fabry-perot cavity. *Opt. Express*, 19(16):14955–14963, Aug 2011.
- [208] J Hallam, S Chelkowski, A Freise, S Hild, B Barr, K A Strain, O Burmeister, and R Schnabel. Coupling of lateral grating displacement to the output ports of a diffractive fabry–perot cavity. *Journal of Optics A: Pure and Applied Optics*, 11(8):085502, 2009.
- [209] Yu. Levin. Internal thermal noise in the ligo test masses: A direct approach. *Phys. Rev. D*, 57:659–663, Jan 1998.
- [210] M. D. Perry, R. D. Boyd, J. A. Britten, D. Decker, B. W. Shore, C. Shannon, and E. Shults. High-efficiency multilayer dielectric diffraction gratings. *Optics Letters*, 20:940–942, April 1995.
- [211] John B. Schneider. Understanding the fdtd method, 2010. <http://www.eecs.wsu.edu/~schneidj/ufdtd/>.
- [212] A. Sharon, D. Rosenblatt, and A. A. Friesem. Resonant grating–waveguide structures for visible and near-infrared radiation. *J. Opt. Soc. Am. A*, 14(11):2985–2993, Nov 1997.
- [213] TAKEOMI SUZUKI and RYUICHI HIOKI. Translation of light frequency by a moving grating. *J. Opt. Soc. Am.*, 57(12):1551–1551, Dec 1967.
- [214] Michael Coughlin and Jan Harms. Upper limit on a stochastic background of gravitational waves from seismic measurements in the range 0.05–1 hz. *Phys. Rev. Lett.*, 112:101102, Mar 2014.
- [215] L Carbone, S M Aston, R M Cutler, A Freise, J Greenhalgh, J Heefner, D Hoyland, N A Lockerbie, D Lodhia, N A Robertson, C C Speake, K A Strain, and A Vecchio. Sensors and actuators for the advanced ligo mirror suspensions. *Classical and Quantum Gravity*, 29(11):115005, 2012.
- [216] Stefan L. Danilishin and Farid Ya. Khalili. Quantum measurement theory in gravitational-wave detectors. *Living Reviews in Relativity*, 15(5), 2012.
- [217] Haixing Miao, Huan Yang, Rana X Adhikari, and Yanbei Chen. Quantum limits of interferometer topologies for gravitational radiation detection. *Classical and Quantum Gravity*, 31(16):165010, 2014.
- [218] S. Chelkowski. *Squeezed Light and Laser Interferometric Gravitational Wave Detectors*. PhD thesis, Universität Hannover, Hannover, 2007.

## REFERENCES

---

- [219] Stefan Ballmer, Valery Frolov, Ryan Lawrence, William Kells, Gerado Moreno, David Ottaway Ken Mason, Mike Smith, Cheryl Vorvick, Phil Willems, and Mike Zucker. Thermal compensation system description. Technical Report T050064, LIGO DCC, April 2005.
- [220] S. Traeger, B. Willke, and K. Danzmann. Monolithically suspended fused silica substrates with very high mechanical  $q$ . *Physics Letters A*, 225(1-3):39 – 44, 1997.
- [221] S Rowan and J Hough. Gravitational wave detection by interferometry (ground and space). *Living Rev. Relativity [Online article]*, 3, 2000.